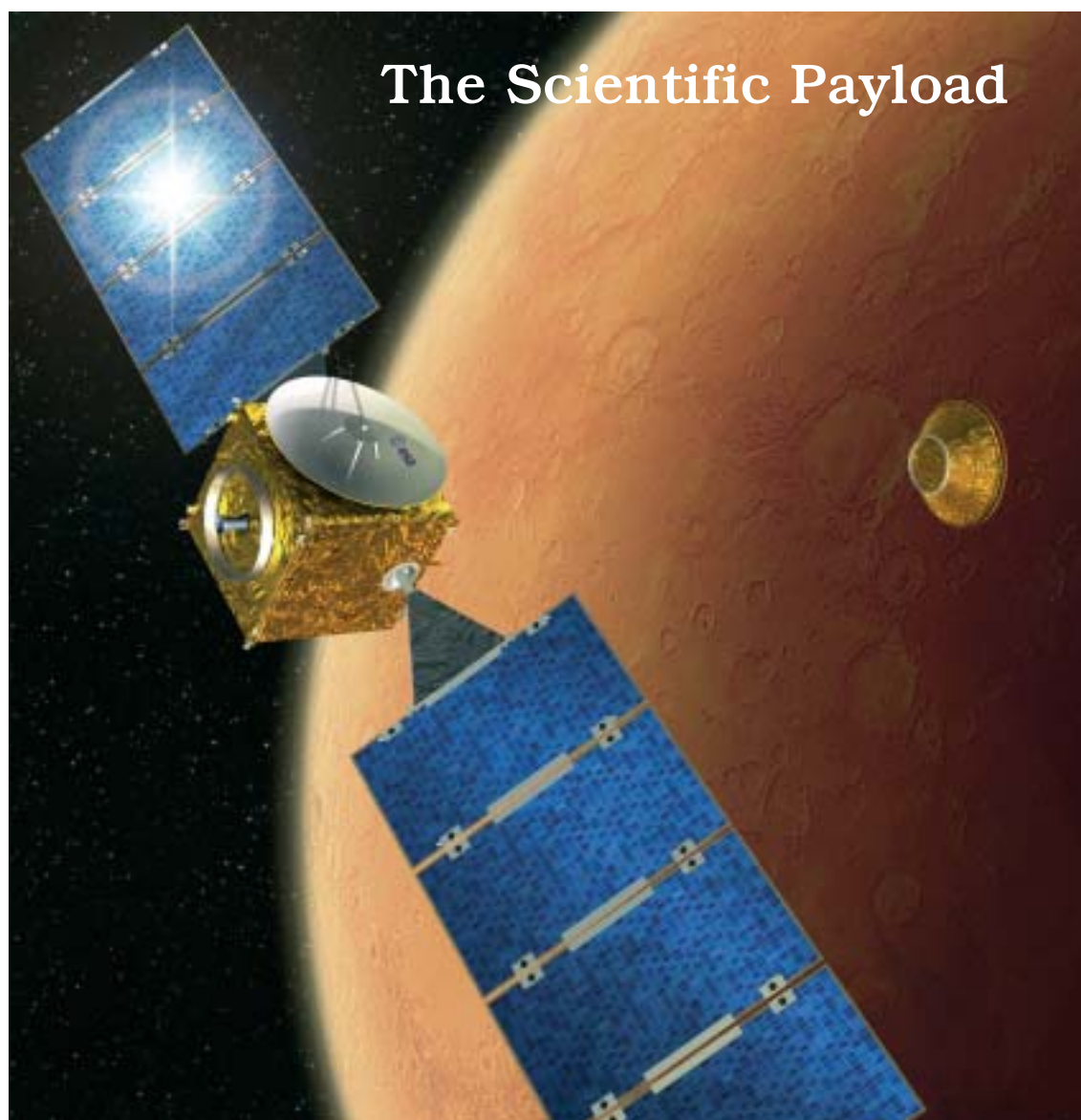




MARS EXPRESS



MARS EXPRESS

The Scientific Payload

SP-1240 'Mars Express: A European Mission to the Red Planet'
ISBN 92-9092-556-6 ISSN 0379-6566

Edited by Andrew Wilson
 ESA Publications Division

Scientific Agustin Chicarro
Coordination ESA Research and Scientific Support Department, ESTEC

Published by ESA Publications Division
 ESTEC, Noordwijk, The Netherlands

Price €50

Copyright © 2004 European Space Agency

Contents

Foreword	v
Overview	
The Mars Express Mission: An Overview	3
<i>A. Chicarro, P. Martin & R. Trautner</i>	
Scientific Instruments	
HRSC: the High Resolution Stereo Camera of Mars Express	17
<i>G. Neukum, R. Jaumann and the HRSC Co-Investigator and Experiment Team</i>	
OMEGA: Observatoire pour la Minéralogie, l'Eau, les Glaces et l'Activité	37
<i>J.-P. Bibring, A. Soufflot, M. Berthé et al.</i>	
MARSIS: Mars Advanced Radar for Subsurface and Ionosphere Sounding	51
<i>G. Picardi, D. Biccari, R. Seu et al.</i>	
PFS: the Planetary Fourier Spectrometer for Mars Express	71
<i>V. Formisano, D. Grassi, R. Orfei et al.</i>	
SPICAM: Studying the Global Structure and Composition of the Martian Atmosphere	95
<i>J.-L. Bertaux, D. Fonteyn, O. Korabely et al.</i>	
ASPERA-3: Analyser of Space Plasmas and Energetic Ions for Mars Express	121
<i>S. Barabash, R. Lundin, H. Andersson et al.</i>	
MaRS: Mars Express Orbiter Radio Science	141
<i>M. Pätzold, F.M. Neubauer, L. Carone et al.</i>	
Beagle 2: the Exobiological Lander of Mars Express	165
<i>D. Pullan, M.R. Sims, I.P. Wright et al.</i>	
US Participation	
US Participation in Mars Express	207
<i>A.D. Morrison, T.W. Thompson, R.L. Horttor et al.</i>	
Acronyms & Abbreviations	215

FOREWORD

Mars, our most Earth-like planetary neighbour, beckons. Its pristine and diverse surface, equal in area to Earth's land surface, displays a long and fascinating history, punctuated by impact events, volcanism, tectonics, and aeolian, fluvial and glacial erosion. A century ago, astronomers believed they were witnessing the last attempts of a dying martian civilisation to cope with the devastating effects of climate change. The notion of an intelligently inhabited Mars was later dispelled, but the expectation that simple life forms could have survived persisted. Today, after sending robotic missions to Mars, our view of the planet retains some striking similarities to those earlier romantic conjectures.

We know from orbiting spacecraft that Mars has undergone dramatic climatic and geologic changes. Water coursing over its surface in the distant past left dramatic evidence in deeply carved channels and fluvial networks. Yet today we find the planet is cold and dry. There is no evidence so far that life exists there now, but primitive life during Mars' warmer, wetter past is a real possibility. So, mysteries remain: how did our Earth-like neighbour arrive at its present parched, cold and almost airless state? Did life evolve and then die out? Did it leave a fossil record? Last but not least, can the changes experienced by Mars teach us something about the dramatic changes being predicted for our own planet?

These and other questions have spurred scientists and engineers to meet the enormous challenge of sending missions to Mars. A Mars-bound spacecraft must survive journeys of more than 6 months, approach the planet from just the right angle and at the right speed to enter orbit, and then operate successfully to return valuable observations. Some missions have failed, but the successes have more than repaid the effort and risk. Our knowledge about Mars has grown dramatically with every successful visit. Four decades of space-based observations have produced more information and knowledge than earlier astronomers with Earth-bound telescopes could have imagined.

Europe joins Mars exploration

Since the Greeks of more than 2000 years ago, many Europeans have made important observations of Mars with the naked eye and through ground-based telescopes, including Nicolaus Copernicus, Tycho Brahe, Johannes Kepler, Galileo Galilei, Christian Huygens, Giovanni Cassini, William Herschel, Giovanni Schiaparelli and Eugene Antoniadi. Europeans have also contributed their fair share of speculation and fantasy about the planet in a fine tradition beginning in 1897 with the publication of *The War of the Worlds* by H.G. Wells, in which hostile martians invade Earth.



The Soyuz launcher and its precious cargo are transported to the launch pad on 29 May 2003.



Mars from 5.5 million km, imaged by the High Resolution Stereo Camera (HRSC). The dark features at top are part of the northern lowlands, where oceans possibly existed billions of years ago. (ESA/DLR/FU Berlin; G. Neukum)

Europe, however, never sent its own spacecraft to Mars – until now. The European Space Agency (ESA) launched the Mars Express orbiter and its small Beagle 2 lander in 2003 on Europe's first mission to any planet. Research institutes throughout Europe provided the instruments onboard the orbiter, some of them first developed for the ill-fated Russian Mars-96 spacecraft. Now upgraded, they provide remote sensing of the atmosphere, surface, subsurface and space environment of Mars to a degree of accuracy never before achieved. The information being gleaned is helping to answer many outstanding questions about the planet.

The mission

Mars Express was successfully launched on 2 June 2003 from Baikonur, Kazakhstan, by a Russian Soyuz rocket. Following a cruise of almost 7 months, the main spacecraft was captured into orbit on 25 December 2003 and soon established a highly elliptical polar orbit with a closest approach to the surface of about 270 km and a period of about 6.75 h. The fate of the Beagle 2 lander, aimed to land in Isidis Planitia, remains unknown. In addition to global studies of the surface, subsurface and atmosphere at unprecedented spatial and spectral resolutions, the unifying theme of the mission is the search for water with all the instruments in its various states everywhere on the planet.

ESA provided the launcher, orbiter and operations, while the instruments were provided by scientific institutions through their own funding. The ground segment includes the ESA station at Perth, Australia, and the mission operations centre at ESOC in Germany. The Mars Express prime contractor was Astrium in Toulouse, France, and a large number of European companies were involved as subcontractors. The ESA engineering and scientific teams are located at ESTEC in The Netherlands. International collaboration, through participation either in instrument hardware or data analysis, is important for diversifying the scope of the mission and improving its scientific return. Collaboration with the NASA Mars Exploration Rovers plays an important role because of the complementary science goals.

Following spacecraft commissioning in January 2004, most instruments began their own calibration and testing, in the process acquiring scientific data. This phase lasted until June 2004, when all the instruments but one began routine operations after the payload commissioning review. The deployment of the MARSIS radar antennas, however, was postponed. The late deployment was initially planned to maximise daylight operations of the other instruments before the pericentre naturally drifts to southern latitudes, which coincides with the nighttime conditions required for subsurface sounding by MARSIS. The nominal lifetime of the orbiter is a martian year (687 days), with a potential extension by another martian year to complete global coverage and observe all seasons twice over.

Early science results

The High Resolution Stereo Camera (HRSC) has provided breathtaking views of the planet, in particular of karstic regions near the Valles Marineris canyon (pointing to liquid water as the erosional agent responsible for modifying tectonic and impact features in the area) and of several large volcanoes (the Olympus Mons caldera and glaciation features surrounding Hecates Tholus). The OMEGA IR mineralogical mapping spectrometer has provided unprecedented maps of water-ice and carbon dioxide-ice occurrence at the south pole, showing where the two ices mix and where they do not. The Planetary Fourier Spectrometer (PFS) has measured atmospheric carbon monoxide variations in each hemisphere and confirmed the presence of methane for the first time, which would indicate current volcanic activity and/or biological processes. The SPICAM UV/IR atmospheric spectrometer has provided the first complete vertical profile of carbon dioxide density and temperature, and has simultaneously measured the distribution of water vapour and ozone. The ASPERA energetic neutral atoms analyser has identified the solar wind interaction with the upper atmosphere and has measured the properties of the planetary wind in Mars'

magnetic tail. Finally, the MaRS radio science experiment has measured for the first time surface roughness by pointing the spacecraft high-gain antenna towards the planet, reflecting the signal to Earth. Also, the martian interior is being probed by studying the gravity anomalies affecting the orbit owing to mass variations of the crust.

Water is the unifying theme of the mission, studied by all instruments using different techniques. Geological evidence, such as dry riverbeds, sediments and eroded features, indicates that water has played a major role in the early history of the planet. It is assumed that liquid water was present on the surface up to about 3.8 billion years ago, when the planet had a thicker atmosphere and a warmer climate. Afterwards, the atmosphere became much thinner and the climate much colder, the planet losing much of its water in the process; liquid water cannot be sustained on the surface under present conditions. Mars Express aims to reveal why this drastic change occurred and where the water went. A precise inventory of existing water on the planet (in ice or liquid form, mostly below ground) is important given its implications for the potential evolution of life on Mars; the 3.8 billion-year age is precisely when life appeared on Earth, which harboured similar conditions to Mars at that time. Thus, it is not unreasonable to imagine that life may also have emerged on Mars and possibly survived the intense UV solar radiation by remaining underground. The discovery of methane in the atmosphere could indicate just that or the presence of active volcanism. From previous orbital imagery, volcanoes on Mars were assumed to have been dormant for hundreds of millions of years. This idea needs a fresh look as the implications of currently active volcanism are profound in terms of thermal vents providing niches for potential ecosystems, as well as for the thermal history of the planet with the largest volcanoes in the Solar System. Mars Express is already hinting at a quantum leap in our understanding of the planet's geological evolution, complemented by the ground truth being provided by NASA's rovers.

Scope of this publication

This ESA Special Publication focuses on the Mars Express scientific instrumentation and its state about a year after launch in order to include some initial scientific discoveries. In spite of the Beagle 2 failure, the lander's payload is also thoroughly described here because it is of the highest scientific value. Furthermore, the orbiter instruments are looking specifically for possible evidence of past or present life. No other mission to Mars since NASA's Viking missions in the 1970s has made exobiology so central to its scientific goals. For further details, both in terms of science results and public outreach, see <http://sci.esa.int/marsexpress/>

Spectacular views

A few spectacular initial results are shown in the next few pages, selected in view of their wide public appeal rather than their intrinsic scientific value. All the scientists involved in Mars Express are now busy submitting papers that include important scientific results, and even a few breakthroughs at this early phase of the mission. The purpose here is to give a visual impression of this early science data.

Agustin Chicarro
Project Scientist, Mars Express
ESTEC, June 2004



This HRSC image was recorded on 14 January 2004. It shows a portion of a 1700 km-long and 65 km-wide swath taken in the south-to-north direction across the huge Valles Marineris canyon. It is the first Mars image of this size at high resolution (12 m pix⁻¹), in colour and in 3-D. (ESA/DLR/FU Berlin; G. Neukum)



This HRSC image was recorded during revolution 18 on 14 January 2004. It shows a vertical view of a mesa in the true colours of Mars. The summit plateau stands about 3 km above the surrounding terrain. Only isolated mesas remain intact after the original surface was dissected by erosion. The large crater has a diameter of 7.6 km. (ESA/DLR/FU Berlin; G. Neukum)



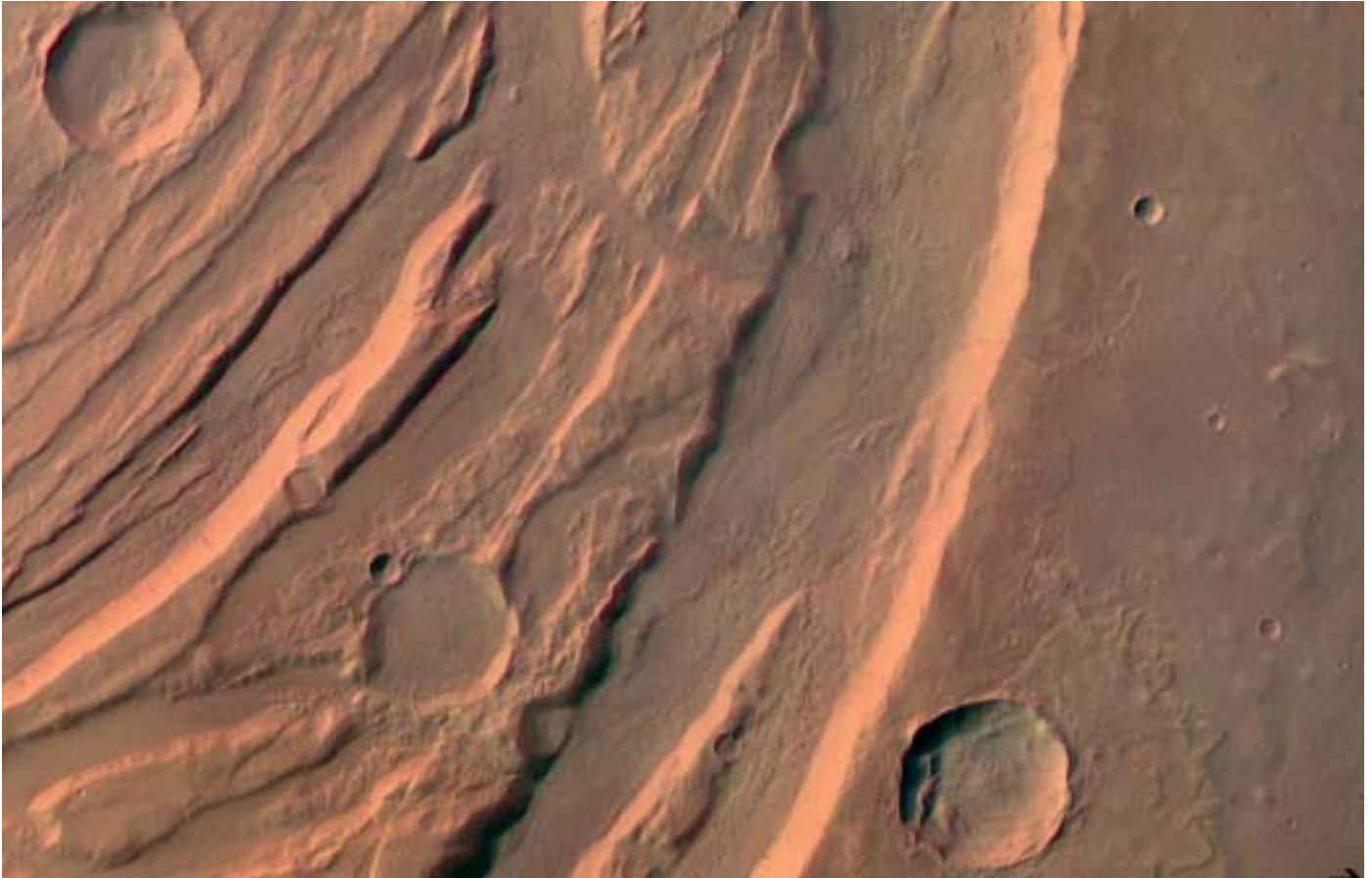
This HRSC image was recorded during revolution 18 on 15 January 2004 from a height of 273 km, east of the Hellas basin at 41°S/101°E. The area is 100 km across, with a resolution of 12 m per pixel. It shows the Reull Vallis, formed by flowing water. North is at top. (ESA/DLR/FU Berlin; G. Neukum)



This HRSC image was recorded during revolution 143 from an altitude of 266 km, providing a perspective view of the western flank of the Olympus Mons shield volcano in the western hemisphere. The escarpment rises from surface level to more than 7000 m. Resolution is about 25 m per pixel. The picture is centred at 22°N/222°E; north is to the left. (ESA/DLR/FU Berlin; G. Neukum)

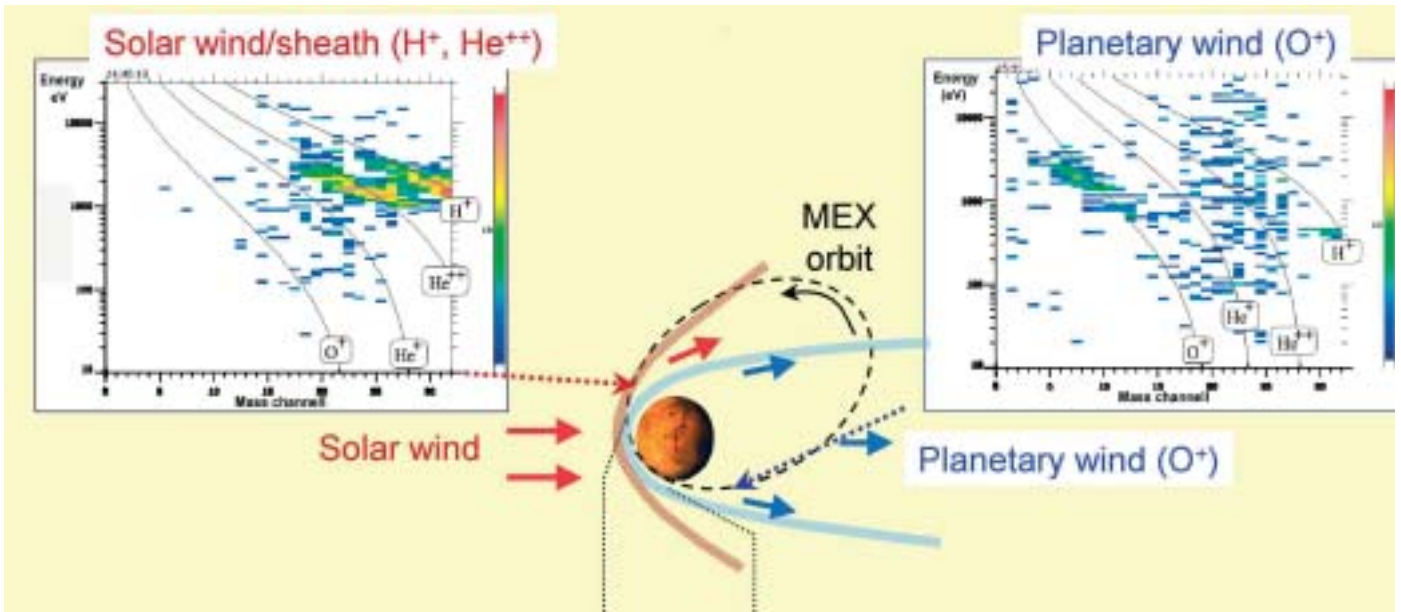


This HRSC vertical view shows the complex caldera at the summit of Olympus Mons, the highest volcano in the Solar System. The average elevation is 22 km; the caldera has a depth of about 3 km. This is the first high-resolution colour image of the complete caldera, taken from a height of 273 km during revolution 37 on 21 January 2004. Centred at 18.3°N/227°E, the image is 102 km across with a resolution of 12 m per pixel; south is at the top. (ESA/DLR/FU Berlin; G. Neukum)

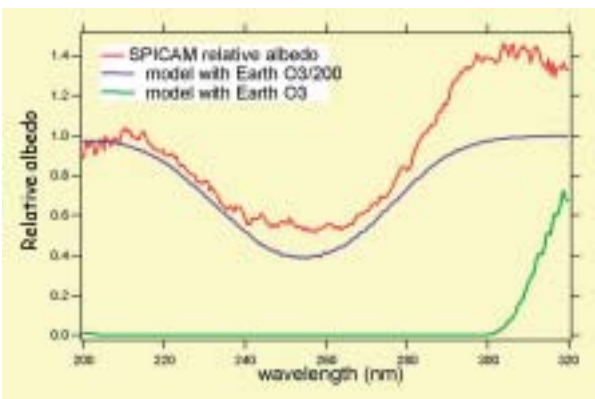


This HRSC image shows the Acheron Fossae region, an area of intense tectonic activity in the past. Acheron Fossae marks the northern edge of the Tharsis plateau; it is part of a network of extensional fractures that radiates from the Tharsis 'bulge', a huge area of regional uplift of intensive volcanic activity. The region is situated at 35-40°N / 220-230°E, about 1000 km north of Olympus Mons. (ESA/DLR/FU Berlin; G. Neukum)

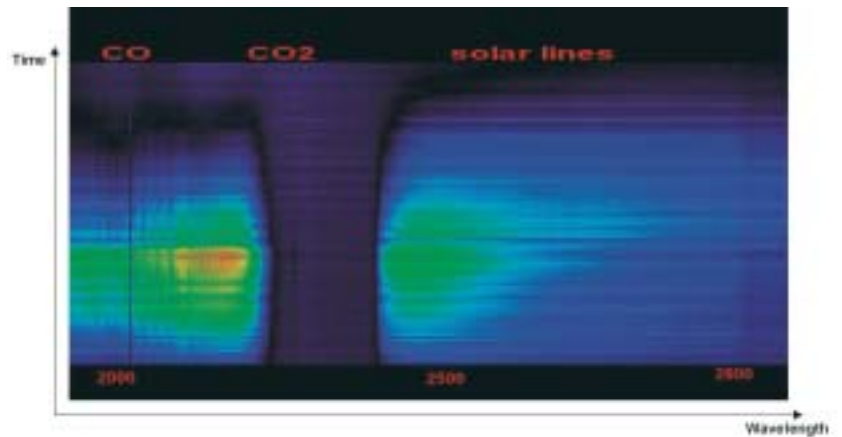
OMEGA observed the southern polar cap of Mars on 18 January 2004, in all three bands. At right is the visible image; in the middle is carbon dioxide ice; at left is water ice. The two types of ice are mixed in some areas but distinct in others. (ESA/IAS, Orsay; J-P. Bibring)



Initial ASPERA results indicate the very different characteristics of two important regions: the impact area of the solar wind with the upper atmosphere and in the Mars tail (planetary wind), confirming the existence of the planetary wind (O⁺ and molecular ions). (ESA/RFI Kiruna; R. Lundin)



SPICAM has provided the first complete vertical profile obtained by an orbiter of the density and temperature of carbon dioxide from 10 km to 110 km above the surface. It has also measured the distribution of water vapour and ozone simultaneously for the first time, indicating that where there is more water vapour there is less ozone. (ESA/CNRS Verrières; J.-L. Bertaux)



PFS initial results indicate that the atmospheric distribution of carbon monoxide is different over the northern and southern hemispheres. The presence of atmospheric methane has also been confirmed by PFS, which opens up new possibilities of there being lifeforms on the planet today. Methane is rather short-lived in the martian atmosphere, so the source(s) that replenish it can have only two origins: volcanic or biologic. (ESA/IFSI Frascati; V. Formisano)

MISSION OVERVIEW

The Mars Express Mission: An Overview

A. Chicarro, P. Martin & R. Trautner

Planetary Missions Division, Research & Scientific Support Department, ESA/ESTEC, PO Box 299, 2200 AG Noordwijk, The Netherlands

Email: agustin.chicarro@esa.int

Mars Express is not only the first ESA mission to the red planet but also the first European mission to any planet. Mars Express was launched in June 2003 from the Baikonur Cosmodrome in Kazakhstan aboard a Russian Soyuz rocket. It included both an orbiter and a small lander named Beagle 2, in remembrance of Charles Darwin's ship. It is the first 'Flexible' mission of ESA's long-term science programme (now known as Cosmic Vision) and was developed in the record time of about 5 years from concept to launch, and in the most cost-efficient manner with respect to any other comparable Mars mission.

Before Mars Express, ESA and the scientific community spent more than 10 years performing concept and feasibility studies on potential European Mars missions (Marsnet, Intermarsnet), focusing on a network of surface stations complemented by an orbiter, a concept that was further developed by CNES in the recently cancelled Netlander mission. The network concept was considered to be a high scientific priority in Europe until the demise of the Russian Mars-96 mission, which included many outstanding European scientific instruments and which may be reconsidered in the future. Mars Express was conceived to recover the objectives concerning the global study of the planet by the Mars-96 mission, and added two major new themes: water and life, following the recommendations of the International Mars Exploration Working Group (IMEWG) and the endorsement of ESA's Advisory Bodies that Mars Express be included in the Science Programme of the Agency.

The scientific investigations of Mars Express closely complement those of recent US orbital missions such as Mars Global Surveyor and Mars Odyssey, as well as the spectacular Mars Exploration Rovers. In addition, very close collaboration was established, in anticipation of future collaboration with Japan, with the Nozomi mission because the scientific objectives and orbital characteristics were complementary. Unfortunately, Nozomi did not reach the planet.

On 2 June 2003 at 17:45:26 UT, a Soyuz rocket with a Fregat upper stage was launched from Baikonur and injected the 1223 kg Mars Express into a Mars transfer orbit. Launch windows to Mars occur every 26 months but 2003 was particularly favourable because it offered the maximum launch mass, a situation that does not repeat for another 16 years. This was important; Beagle 2 could not have been carried in the less-favourable 2005 window.

Mars Express is a 3-axis stabilised orbiter with a fixed high-gain antenna and body-mounted instruments, and is dedicated to the orbital and *in situ* study of the planet's interior, subsurface, surface and atmosphere. It was placed in an elliptical orbit (250 x 10 142 km) around Mars of 86.35° quasi-polar inclination and 6.75 h period, which was optimised for the scientific objectives and to communicate with Beagle 2 and the NASA landers or rovers being launched in 2003-2005.

The spacecraft was captured into Mars orbit on 25 December 2003. Following completion of spacecraft commissioning in mid-January 2004, the orbiter experiments began their own commissioning processes and started acquiring

1. Introduction

2. Mission Overview

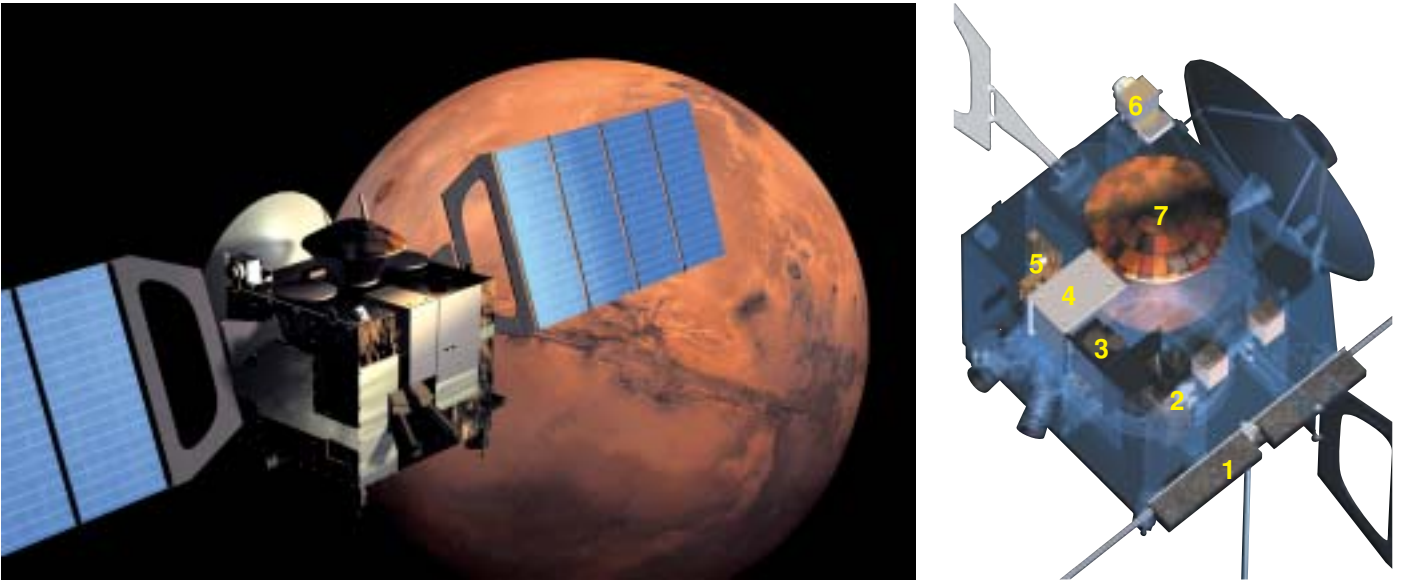


Fig. 1. Mars Express with the Beagle 2 capsule still attached. 1: MARSIS. 2: HRSC. 3: OMEGA. 4: PFS. 5: SPICAM. 6: ASPERA. 7: Beagle 2. (MaRS requires no dedicated hardware).

scientific data from Mars and its environment. The radar antenna was planned to be deployed last in order to maximise early daylight operations of the other instruments, before the natural pericentre drift to the southern latitudes. The optical instruments began their routine operational phase after the Commissioning Review in June 2004. The deployment of the radar antennas was delayed for safety modelling checks. The nominal orbiter mission lifetime is a martian year (687 days), following Mars orbit insertion and about 7 months' cruise. It is hoped that the nominal mission will be extended into a second martian year of operations in order to increase the global coverage of most orbital experiments and, eventually, to allow data-relay communications with potential landers up to 2008, provided that the spacecraft resources allow it.

The Beagle 2 descent capsule was ejected 5 days before arrival at Mars, while the orbiter was on a Mars collision course; Mars Express was then retargeted for orbit insertion. From its hyperbolic trajectory, Beagle 2 entered and descended through the atmosphere in about 5 min, intending to land at $< 40 \text{ m s}^{-1}$ within an error ellipse of $20 \times 100 \text{ km}$. The fate of Beagle 2 remains unknown because no signal was ever received from the martian surface, neither by the UK's Jodrell Bank radio telescope nor by the Mars Express and Mars Odyssey orbiters. All of them made strenuous efforts to listen for the faintest of signals for many weeks following Beagle 2's arrival at Mars. ESA set up a commission to investigate the potential causes of the probable accident and issued a number of recommendations for future missions. The selected landing site was in Isidis Planitia (11.6°N , 269.5°W), which is a safe area of high scientific interest – this impact basin was probably flooded by water during part of its early history, leaving layers of sedimentary rocks. The area is surrounded by geological units of a variety of ages and compositions, from densely cratered highlands to volcanic flows to younger smooth plains. The lander's highly integrated instrument suite was expected to perform a detailed geological, mineralogical and chemical analysis of the site's rocks and soils, provide site meteorology, and focus on finding traces of past or present biological activity. Data from this combination of instruments could have solved the issue of life on Mars. Beagle 2's operational lifetime was planned to be up to 180 sols (about 6 months).

ESA provided the launcher, orbiter, operations and part of Beagle 2, the rest of the lander being funded by a UK-led consortium of space organisations. The orbiter instruments were all provided by scientific institutions through their own funding.



Fig. 2. Mars Express in launch configuration at Baikonur.

Most ESA Member States participated in providing the scientific payload but other countries (including USA, Russia, Poland, Japan and China) have joined in various capacities. The ground segment includes the new ESA station of New Norcia, near Perth, Australia, and the mission operations centre at ESA's European Space Operations Centre (ESOC). A second ESA station at Cebreros, near Madrid, Spain, will be used later in the mission, while NASA's Deep Space Network (DSN) will increase the scientific data return during the whole mission. The orbiter was built by Astrium in Toulouse, France, as prime contractor, together with a large number of European companies as subcontractors in each of ESA's Member States.

The Mars Express orbiter is the core of the mission, scientifically justified on its own merit by providing unprecedented global coverage of the planet, in particular of the surface, subsurface and atmosphere. Beagle 2 was selected through its innovative scientific goals and very challenging payload. The combination of orbiter and lander (Figs. 1 & 2) was expected to be a powerful tool to focus on two related issues: the current inventory of ice or liquid water in the martian crust, and possible traces of past or present biological activity on the planet. The broad scientific objectives of the orbiter are:

- global colour and stereo high-resolution imaging with about 10 m resolution and imaging of selected areas at 2 m pix⁻¹;
- global IR mineralogical mapping of the surface;
- radar sounding of the subsurface structure down to the permafrost;
- global atmospheric circulation and mapping of the atmospheric composition;
- interaction of the atmosphere with the surface and the interplanetary medium;
- radio science to infer critical information on the atmosphere, ionosphere, surface and interior.

The ultimate scientific objective of Beagle 2 was the detection of extinct and/or

3. Scientific Objectives

extant life on Mars, a more attainable goal being the establishment of the conditions at the landing site that were suitable for the emergence and evolution of life. In order to achieve this goal, Beagle 2 was designed to perform *in situ* geological, mineralogical and geochemical analysis of selected rocks and soils at the landing site. Furthermore, studies of the martian environment were planned via chemical analysis of the atmosphere, local geomorphological studies of the landing site and via the investigation of dynamic environmental processes. Further studies to be performed by Beagle 2 included the analysis of the subsurface regime using a ground-penetration tool and the first *in situ* isotopic dating of rocks on another planet.

The description and detailed science goals of the orbiter and lander experiments are presented below; see also Table 1.

3.1 Orbiter scientific instruments

The Mars Express orbiter scientific payload totals about 116 kg shared by six instruments, in addition to a radio-science experiment that requires no additional hardware. The instruments can be listed in two categories: those dealing primarily with the solid planet by observing the surface and subsurface (HRSC super/high-resolution stereo colour imager; OMEGA IR mineralogical mapping spectrometer; MARSIS subsurface sounding radar altimeter), and those studying the atmosphere and environment of Mars (PFS planetary fourier spectrometer; SPICAM UV and IR atmospheric spectrometer; ASPERA energetic neutral atoms analyser). The MaRS radio science experiment will provide insights into the internal gravity anomalies, the surface roughness, the neutral atmosphere and the ionosphere of Mars.

The camera is based on the space-qualified HRSC Flight Model 2 developed for the Mars-96 mission, with the addition of a super-resolution channel. Its major goal is global coverage of the planet at high resolution. The scientific interpretation of the data focuses on the role of water and climate throughout martian history, the timing and evolution of volcanism and tectonics, the surface/atmosphere interactions, the establishment of an accurate chronology, and the observation of Phobos and Deimos. In order to meet these objectives, the imaging capabilities of HRSC allow the characterisation of surface features and morphology at high spatial resolution (about 10 m pix⁻¹ in stereo, colour and at different phase angles), surface topography at high spatial and vertical resolution with dedicated stereo imaging, surface features and morphology using nested images at super resolution (2 m pix⁻¹), terrain classification by multispectral datasets, scattering properties of the regolith and atmosphere by multi-phase angle observations, and atmospheric properties and phenomena by limb sounding and nadir observations. High- and super-resolution are obtained around pericentre, at and above 250 km.

OMEGA, derived from the Mars-96 spare model, is a visible and near-IR mapping spectrometer operating in the wavelength range 0.38-5.1 μm . It will provide global coverage of Mars by the end of the nominal mission at medium resolution (1-5 km) from orbital altitudes between 1000 km and 4000 km, and higher-resolution (a few hundred metres) snapshots of selected areas, amounting to at least a few percent of the surface. OMEGA is characterising the composition of surface materials, studying the time and space distribution of atmospheric CO₂, CO and H₂O, identifying the aerosols and dust particles in the atmosphere, and monitoring the surface dust transport processes. It is contributing greatly to understanding the evolution of Mars from geological time scales to seasonal variations and is giving unique clues for understanding the H₂O and CO₂ cycles throughout martian evolution.

MARSIS is a low-frequency nadir-looking pulse-limited radar sounder and altimeter with ground-penetration capabilities operated. It uses synthetic aperture techniques, two 20 m booms and a secondary receiving monopole antenna to isolate subsurface reflections. It is the first radar sounder to investigate the martian surface and subsurface. Its primary objective is to map the distribution of water (both liquid and solid) in the upper portions of the crust down to 3-5 km varying with geological composition (nightside). The detection of such water reservoirs addresses key issues

Table 1. The Mars Express scientific experiments.

<i>Expt. Code</i>	<i>Instrument</i>	<i>Principal Investigator</i>	<i>Participating Countries</i>
<i>Orbiter</i>			
HRSC	Super/High-Resolution Stereo Colour Imager	G. Neukum <i>DLR/FU, Berlin, D</i>	D, F, RU, USA, FIN, I, UK
OMEGA	IR Mineralogical Mapping Spectrometer	J.P. Bibring <i>IAS, Orsay, F</i>	F, I, RU
PFS	Atmospheric Fourier Spectrometer	V. Formisano <i>CNR, Frascati, I</i>	I, RU, PL, D, F, E, USA
MARSIS	Subsurface-Sounding Radar/Altimeter	G. Picardi <i>Univ. Rome, I</i> & J. Plaut <i>NASA/JPL</i>	I, USA, D, CH, UK, DK, F, RU
ASPERA	Energetic Neutral Atoms Analyzer	R. Lundin & S. Barabash <i>RFI, Kiruna, S</i>	S, D, UK, F, FIN, I, US, RU
SPICAM	UV and IR Atmospheric Spectrometer	J.L. Bertaux <i>CNRS, Verrières, F</i>	F, B, RU, US
MaRS	Radio Science Experiment	M. Paetzold <i>Univ. Köln, D</i>	D, F, US, A
<i>Lander</i>			
Beagle 2	Suite of imaging instruments, organic and inorganic chemical analysis, robotic sampling devices and meteo sensors	C. Pillinger <i>Open Univ., UK</i> & M. Sims <i>Leicester Univ., UK</i>	UK, D, US, F, CH, RU, PRC, A, E

in the geological, hydrological, climatic and possibly biological evolution of Mars, including the current and past global inventory of water, the mechanisms of transport and storage of water, the role of liquid water and ice in shaping the landscape of Mars, the stability of liquid water and ice at the surface as an indication of climatic conditions, and the implications of the hydrological history in the evolution of possible martian ecosystems. Secondary MARSIS objectives include subsurface geologic probing, surface roughness and topography characterisation at scales from tens of metres to km (dayside), and ionosphere sounding (dayside) to characterise the interactions of the solar wind with the ionosphere and the upper atmosphere. At the time of going to press, the radar booms had not been deployed.

The Planetary Fourier Spectrometer, also derived from a Mars-96 model, is a double-pendulum IR spectrometer optimised for atmospheric studies. It covers the wavelength ranges 1.2-5 μm and 5-45 μm with a spectral resolution of 2 cm^{-1} and a spatial resolution of 10-20 km. The main scientific objectives are the global long-term monitoring of the 3-D temperature field in the lower atmosphere, the measurement of the minor constituent variations (water vapour and carbon monoxide) and D/H ratio, the determination of the size distribution, chemical composition and optical properties of the atmospheric aerosols, dust clouds, ice clouds and hazes, and the study of global circulation and dynamics. PFS will also determine the thermal inertia (from the daily surface temperature variations), the nature of the surface condensate and seasonal variations of its composition, the scattering phase function, pressure and height for selected regions, and is studying the surface-atmosphere exchange processes.

SPICAM is a UV and IR spectrometer devoted to studying the atmosphere. It is focusing on atmospheric photochemistry, the density-temperature structure of the atmosphere (0-150 km), the upper atmosphere-ionosphere escape processes, and the interaction with the solar wind. The UV sensor is looking through the atmosphere either at the Sun or stars to obtain vertical profiles by occultation, or to the nadir to obtain integrated profiles, or at the limb to obtain vertical profiles of high-atmosphere emissions. The IR sensor is used only in the nadir-looking mode (column abundances and H₂O, CO₂ and O₃ cycles). SPICAM measurements are addressing key questions into the present state of the atmosphere, its climate and evolution. SPICAM and PFS are highly complementary.

The ASPERA energetic neutral atom analyser is studying plasma domains at different locations along the spacecraft's orbit, focusing on the interaction of the upper atmosphere with the interplanetary medium and the solar wind, and characterising the near-Mars plasma and neutral gas environment. The scientific objectives are being met by studying remote measurements of energetic neutral atoms in order to investigate the interaction between the solar wind and the atmosphere, characterise quantitatively the impact of plasma processes on atmospheric evolution, and obtain the global plasma and neutral gas distributions in the near-Mars environment. *In situ* measurements of ions and electrons complement the energetic neutral atom images; they have never been obtained before and provide undisturbed solar wind parameters. A similar instrument was carried by the Japanese Nozomi mission.

The MaRS radio science experiment does not require dedicated hardware but it is performing radio sounding experiments of the neutral martian atmosphere and ionosphere to derive vertical density, pressure and temperature profiles as a function of height, and the diurnal and seasonal variations in the ionosphere. It is also determining the dielectric and scattering properties of the martian surface in specific target areas with a bistatic radar experiment for the first time, and is determining gravity anomalies in the crust in order to investigate the structure and evolution of the interior. Precise determination of the mass of Phobos and radio sounding of the solar corona during superior conjunction with the Sun are also among the objectives. The experiment relies on the observation of the phase, amplitude, polarisation and propagation times of radio signals transmitted by the spacecraft and received at ground stations on Earth. This experiment has a significant heritage from its equivalent on the Rosetta mission.

Although not considered as part of the scientific payload, two subsystems on the spacecraft were planned to benefit particularly from Beagle 2 operations. The Mars Express Lander Communications (MELACOM) subsystem is the orbiter-to-lander data relay transponder, with the primary mission of providing data services for the lander. Mars Express was scheduled to fly over the landing site every 1-4 sols and was to relay scientific data to the UK-based Lander Operations Centre via ESOC. The Visual Monitoring Camera (VMC) also remained as part of the orbiter. This standalone digital camera imaged the successful separation of Beagle 2 before arrival at Mars.

3.2 Lander scientific instruments

Although Beagle 2 (Fig. 3) did not accomplish its mission because it was most likely lost during the entry, descent and landing, it is still relevant to review the various scientific instruments and robotic tools, given the importance of the investigations and the high standards to which they were built. It is hoped that another opportunity will allow all or some of these instruments to fly again to Mars to undertake the search for life.

The lander's scientific payload totalled less than 10 kg, shared between six instruments and two dedicated tools to sample the surface and subsurface materials of Mars, plus a robotic sampling arm with 5 degrees-of-freedom. Two were mounted directly on the lander platform: the Gas Analysis Package and the Environmental

THE ISSUE OF WATER

Today, liquid water cannot exist on the surface of Mars because of the low atmospheric density (6 mbar). However, there is ample evidence that liquid water flowed freely in the early history of Mars, as witnessed by dry riverbeds in the heavily cratered Noachian southern highlands. The early climate appears to have been warm and wet (although there are renewed doubts about this) until about 3.8 billion years ago, much like the Earth's at about the same age. This was when life appeared on our planet, as evidence from Greenland indicates. So, if the conditions were similar on both planets, it appears reasonable for biological activity to have flourished on Mars as well. Soon after 3.8 billion years ago (in geological terms), surface conditions changed dramatically, creating the cold and dry place of today, as modest erosion rates at the Mars Pathfinder site illustrate. There is also growing evidence that the young smooth northern plains were once covered by a liquid-water ocean extending over a third of the planet. The question is thus: where has all this water gone? Was it lost into space through natural degassing, including atmospheric erosion through large impacts, or is it still somewhere on Mars, probably below the surface in ice form, as in terrestrial permafrost? Recent Mars Odyssey gamma-ray spectroscopy data have revealed a significant concentration of H^+ ions adsorbed to the first



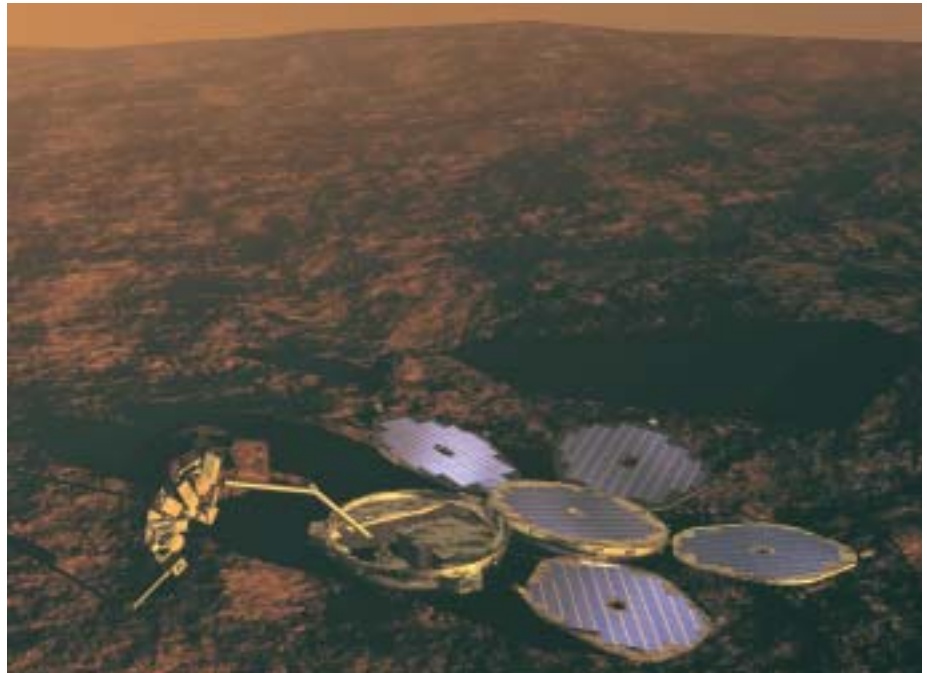
few microns of soil in both polar caps. However, in light of similar results on the Moon from Lunar Prospector, where we know from rock samples there is no water at all, these data only indicate an existing mechanism concentrating H^+ from the solar wind towards the poles. Therefore, most of the Mars Express orbiter instruments are directed towards settling this issue, in particular through radar subsurface sounding (MARSIS), surface mineralogical mapping (OMEGA), establishment of a detailed chronology of geological evolution (HRSC), imaging of atmospheric escape (ASPERA) and the study of the H_2O , CO_2 and dust cycles in the atmosphere (PFS and SPICAM). Never has a mission to Mars been so focused on producing the water inventory of the planet, and never has it been so well equipped to find out.

THE ISSUE OF LIFE

The Mars Express mission planned to address the issue of the emergence of life in the cosmos and, in particular, life signatures on Mars both directly and indirectly. The majority of orbiter instruments are looking for indications of favourable conditions for the existence of life, either at present or during the planet's past, and particularly for traces of liquid, solid or gaseous water. The HRSC camera is imaging ancient riverbeds, the OMEGA spectrometer is looking for minerals with OH^- radicals formed in the presence of water, the MARSIS radar will look for subsurface ice and liquid water, the PFS and SPICAM spectrometers are analysing water vapour in the atmosphere, and ASPERA and MaRS are studying neutral-atom escape from the atmosphere, in particular O_2 coming from water and carbonates. The instruments on Beagle 2 were designed to look for the presence of water in the soil, rocks and atmosphere, and in particular to look for traces of life with direct measurements, such as the presence of a larger amount of the light C^{12} isotope compared to the heavier C^{13} ,

which would have indicated the existence of extinct life, or even the presence of methane, indicative of extant life together with other organic compounds. Results from a single instrument will most likely not allow the issue of life on Mars to be settled, but all the measurements taken together will allow us to build a scenario pointing, or not, in the direction of present or past life on Mars. Either way, the cosmobiological implications would be far-reaching: we would know if life is a common occurrence in the Universe or not. In this debate, comparing the geological evolutions of Earth and Mars is obviously a fruitful exercise because the planets share seasons, polar caps, a transparent atmosphere and aeolian activity, for example. Our other planetary twin neighbour, Venus, must not be forgotten in view of its similarities with Earth in terms of internal activity and recent resurfacing. Comparative planetology is the key to our understanding of Solar System evolution, including cosmobiology. Since NASA's Viking missions in 1976, it is the first time that the exhaustive search for life is so central to a space mission to Mars, even after the failure of Beagle 2.

Fig. 3. Beagle 2 operating on the surface of Mars.



Sensor Suite. The others were housed within an innovative structure called the Payload Adjustable Workbench (PAW) at the end of the robotic sampling arm: the Stereo Camera System, Microscope, X-ray Spectrometer and Mössbauer Spectrometer, together with a set of tools that included the Rock Corer Grinder, the PLANetary Underground TOOL and other support equipment such as a sampling spoon, a torch and a wide-angle mirror. The PAW also carried one of the ESS sensors. The science-payload-to-landed-structure ratio is about 1/3, the highest so far of any planetary lander.

The Gas Analysis Package (GAP) is designed for quantitative and qualitative analysis of sample composition and precise isotopic measurements. It can process atmospheric samples and soil or rock chippings acquired by the sampling tools. These are deposited via an inlet system into one of eight miniaturised ovens. Gases are analysed directly (such as those present in the atmosphere), after their release from samples by heating, or those resulting from a byproduct of chemical processing (e.g. CO₂). GAP is very flexible and can investigate processes dealing with atmospheric evolution, circulation and cycling, the nature of gases trapped in rocks and soils, low-temperature geochemistry, fluid processes, organic chemistry, formation temperatures and surface exposure ages, and can also assist in isotopic rock dating.

The Environmental Surface Suite (ESS) contributes to the characterisation of a landing site and to meteorological studies through the measurements from 11 parameter-sensors scattered around the lander platform and PAW. Measurement of the UV and radiation flux at the surface together with the oxidising capability of the soil and atmosphere provides insights into exobiological investigations. In addition, the measurement of atmospheric temperature, pressure, wind speed and direction, dust saltation and angle of repose complements the *in situ* environmental experiments.

The Stereo Camera System (SCS) consists of two identical CCD cameras and integrated filter wheels. A primary engineering objective of the Beagle 2 SCS was the construction of a Digital Elevation Model (DEM) of the landing site from a series of overlapping stereo image pairs. The DEM was to be reconstructed on Earth and used to position the PAW with respect to target rocks and soils. The investigation of the landing site included 360° panoramic imaging, multi-spectral imaging of rocks and

soils to determine the mineralogy, and close-up imaging of rocks and soils to infer the texture. Observations of the day and night sky, Sun, stars and Deimos and Phobos allow the identification of atmospheric properties such as optical density, aerosol properties and water vapour content. The SCS also supports the determination of the landing site location by providing panoramic and celestial navigation images. Furthermore, the observation of lander surfaces and atmospheric effects allows the identification of dust and aerosol properties in the atmosphere.

The Microscopic Imager (MIC) investigates the nature of martian rocks, soils and fines at the particulate scale (few mm). Such studies would have provided important data to fulfil Beagle 2's exobiological objectives in the form of direct evidence of microfossils, microtextures and mineralisations of biogenic origin, if present. In addition, identifying the physical nature and extent of the weathering rinds/coatings on rocks and soils contributes to the geological characterisation of a landing site. Atmospheric and global planetary studies also benefit from detailed knowledge of dust morphology. The MIC was the first attempt to image and assess directly individual particles of sizes close to the wavelength of scattered light on another planet. The acquisition of complete sets of images for each target allows the 3-D reconstruction of sample surfaces in the visible and UV.

The primary goal of the X-Ray Spectrometer (XRS) is to determine, *in situ*, the elemental composition and, by inference, the geochemical composition and petrological classification, of the surface material at the landing site. Major elements (Mg, Al, Si, S, Ca, Ti, Cr, Mn, Fe) and trace elements up to Nb are detectable. The instrument employs X-ray fluorescence spectrometry to determine the elemental constituents of rocks, using a set of four radioisotope sources (two ^{55}Fe and two ^{109}Cd) to excite the sample. Crude radiometric dating of martian rocks *in situ* was to be performed using the $^{40}\text{K}/^{40}\text{Ar}$ method. For this, the XRS needs to make a precise measurement of K on a 'fresh' sample of rock. The Ar component is determined by the GAP as part of a suite of experiments performed on a core sample extracted from the same specimen.

The Mössbauer Spectrometer (MBS) allows a quantitative analysis of Fe-bearing materials in rock and soil materials. The Fe-rich nature of martian deposits enables relative proportions of Fe in olivine and pyroxene to be determined using the Mössbauer technique, together with magnetite in basalts. Owing to the abundance of Fe-bearing minerals on Mars and their formation being linked to the history of water on the planet, MBS measurements are particularly important. Also, these results provide information about rock weathering in general, and oxidation in particular. The MBS uses gamma rays from the decay of ^{57}Co to ^{57}Fe . The generated spectra allow the characterisation of the mineralogical make-up of rocks and soils, and hence their petrological classification. In conjunction with the X-ray spectrometer, the Mössbauer spectrometer complements the *in situ* geochemical and petrological work, and provides support for the GAP measurements.

The Rock Corer Grinder (RCG) on the PAW is a combined tool that addresses the scientific prerequisite that all the PAW instruments have access to pristine material on a suitably prepared rock surface to avoid the effects of weathering rinds and geometric effects that can seriously compromise instrument performance. The RCG removes the altered material and produces a flat, fresh surface suitable for both types of spectrometer measurements. After the *in situ* analyses have been completed, a sample from the ground patch is extracted by the coring action of the device, and delivered to the GAP inlet port for chemical analysis.

The PLUTO (PLanetary UndergrounD TOol) is another PAW tool to retrieve soil samples from depths down to about 1.5 m and, depending on the terrain, from under a large boulder. This capability is very important for exobiological investigations because materials preserving traces of biological activity would be found at depth within the soil or rocks, where they would be unaffected by solar-UV radiation. In addition to its main function as a soil sample-acquisition device, PLUTO allows *in situ* temperature measurements as a function of time and depth as it travels below

the surface. The ground-intrusion behaviour also allows the mechanical properties and layering of the soil to be estimated.

Coordination between Mars Express orbital observations and Beagle 2 experiments had to be carefully planned, so that the lander could provide ground truth to the orbiter through its detailed geological and chemical analysis, and the orbiter could provide the landing site regional context for the Beagle 2 experiments. Detailed studies of the Beagle 2 landing site have also been carried out.

4. Science Operations

The 'G3-UB' baseline orbit of Mars Express has a quasi-polar inclination of 86.35°. In order to fine-tune observation parameters such as illumination, a manoeuvre was performed to transition from a G3-U to a G3-B orbit a few weeks after Mars orbit insertion. The total number of orbits during the nominal mission is 2293, which corresponds to slightly more than 3 orbits per sol. Good illumination conditions for a systematic coverage of the whole surface is a major requirement for the global coverage strategy. Priorities are dictated by scientific goals (e.g., polar coverage, regions of interest, targets of opportunity) and, at the beginning of the mission, by the need to fly over the lander site in the Isidis Planitia area. Beagle 2 communication contacts were repeatedly attempted for more than a month, and were expected to vary between once a week to once a day during nominal Beagle 2 operations. The lander lifetime, a main driver of the orbiter's early science operations, was estimated to be about 6 months as a result of decreasing illumination and dust building up on the lander panels.

Mars Express is recording science data onboard and dumping it during ground station passes. The daily data volume varies throughout the year from less than 1 Gbit to about 6 Gbits, via the single New Norcia ground station with its 35m antenna and 8 h daily coverage. The use of NASA's Deep Space Network is planned in order to increase the capacity.

As one of the various actors in Mars Express science operations, the Payload Operations Service (POS) was established at the Rutherford Appleton Laboratory, (Chilton, UK) to support the Mars Express Project Scientist Team (PST), the Principal Investigators (PIs), the Mission Operations Centre (MOC) and the Lander Operations Centre (LOC). The POS carried out the development, implementation, testing and operations of the system and tools required to support Mars Express science operations under contract from ESA. The PST and PIs compile the Master Science Plan (MSP) to schedule the acquisition of science data by the spacecraft in a way that is consistent with the scientific objectives and the resources available during the observation time. The MSP represents the basis of all payload operations timeline planning during the various phases of the mission. The high-level scientific planning is performed by the Science Operations Working Group (SOWG), which includes representatives of all the PI teams. PST and POS both interface with the MOC, the PI institutes and the LOC.

4.1 Data distribution

To further the potential use of the Mars Express scientific data, as well as to benefit from a new scientific perspective, ESA established a participating programme for Interdisciplinary Scientists (IDSs) and Recognised Cooperating Laboratories (RCLs). The six selected IDSs (half being non-European) bring their expertise in various multidisciplinary fields, such as the space environment, surface-atmosphere interactions, geological evolution or cosmobiology, in order to support various PI teams by typically combining data from several instruments into investigations from a fresh viewpoint. The RCLs have IDS guidance to prepare themselves for interpreting the data when they become available to the public after the 6-month proprietary period and distributing them further into the geoscience community and/or country they represent, as these RCLs have been selected to encourage scientific groups from areas new to space activities to participate in ESA planetary

missions. In addition, ESA is building a scientific data archive for all planetary missions as a repository of European planetary data after the 6-month proprietary period (see below).

4.2 Data archiving

The Planetary Science Data Archive (PSA) is an online archive that provides data search and access via the Internet of ESA's planetary missions, data-formatted to NASA's Planetary Data System (PDS) standards. Following the request by Mars Express PI teams for the archive to offer additional functionality on top of the delivery of PDS-compliant data sets, the reuse of an existing astronomy scientific data archive architecture was adopted because it offered significant cost benefits over developing an entirely new system. This archive will be located at the European Space Astronomy Centre (ESAC), Villafranca, Spain, while expertise exists in the PST at ESTEC. Detailed requirements have been defined for the PSA by representatives from a wide variety of disciplines, who will support the testing and overall future functionality of the PSA. The PSA will support scientists looking for data on specific topics, particular instruments or given locations on the planet, as well as helping the general public and educators, interested in visually appealing or easy-to-interpret data.

International collaboration beyond the ESA Member States, through participation in either instrument hardware or scientific data analysis, is important for diversifying the scope and quality of the mission's scientific return. Three major partners are contributing to the mission: USA, Russia and Japan. NASA provided a major share of MARSIS and is supporting Co-Investigators in most of the scientific payloads. NASA is also making its DSN available to increase the science data download throughout the mission, including critical manoeuvres. Russian scientists are involved in most of the orbiter experiments as many of these originated on Mars-96 as joint collaborations between European and Russian institutes. Other non-ESA countries participating in the mission include Poland and China.

Collaboration with Japan is a special case, although the high expectations were unfortunately not met. Turning the malfunction of the Nozomi spacecraft soon after launch in 1998 into a positive event, the Mars Express and Nozomi Science Working Teams began a close collaboration because both missions were then expected to reach Mars at the same time. In the end, however, Nozomi could only fly past Mars because its technical difficulties could not be overcome to enter orbit. This collaboration included scientific data exchange and analysis, as well as the ongoing exchange of scientists from all the instrument teams. The missions were highly complementary in terms of orbits and scientific investigations, with Nozomi focusing on the atmosphere and in particular its interaction with the solar wind from a highly-elliptic equatorial orbit, while Mars Express is devoting a large share of its mission to the surface and subsurface from polar orbit. Never before was a planet expected to be simultaneously observed from two different geometries by two orbiters of different space agencies. This tandem exploration was planned to pave the way for even closer cooperation in the future between Europe and Japan to other targets, such as Mercury.

Further details on the Mars Express mission and its Beagle 2 lander can be found at <http://sci.esa.int/marsexpress/> and <http://www.beagle2.com/>

5. International Collaboration

SCIENTIFIC INSTRUMENTS

HRSC: the High Resolution Stereo Camera of Mars Express

G. Neukum^{1,4}, R. Jaumann² and the HRSC Co-Investigator and Experiment Team³

¹*Freie Universität Berlin, Department of Earth Sciences, Institute of Geosciences, Remote Sensing of the Earth and Planets, Malteserstr. 74-100, Building D, D-12249 Berlin, Germany*
Email: gneukum@zedat.fu-berlin.de

²*German Aerospace Center (DLR), Rutherfordstrasse 2, D-12489 Berlin, Germany*
Email: ralf.jaumann@dlr.de

³see Tables 2 & 3

⁴until 2002: *German Aerospace Center (DLR), Rutherfordstrasse 2, D-12489 Berlin, Germany*

The High Resolution Stereo Camera (HRSC), originally developed for the Russian-led Mars-96 mission, was selected as part of the Orbiter payload for ESA's Mars Express mission. The HRSC is a pushbroom scanning instrument with nine CCD line detectors mounted in parallel in the focal plane. Its unique feature is the ability to obtain near-simultaneous imaging data of a specific site at high resolution, with along-track triple stereo, four colours and five different phase angles, thus avoiding any time-dependent variations of the observational conditions. An additional Super-Resolution Channel (SRC) – a framing device – will yield nested images in the metre-resolution range for detailed photogeologic studies. The spatial resolution from the nominal periapsis altitude of 250 km will be 10 m px⁻¹, with an image swath of 53 km, for the HRSC and 2.3 m px⁻¹ for the SRC. During the mission's nominal operational lifetime of 1 martian year (2 Earth years) and assuming an average HRSC data transfer share of 40%, it will be possible to cover at least 50% of the martian surface at a spatial resolution of ≤ 15 m px⁻¹. More than 70% of the surface can be observed at a spatial resolution of ≤ 30 m px⁻¹, while more than 1% will be imaged at better than 2.5 m px⁻¹. The HRSC will thus close the gap between the medium- to low-resolution coverage and the very high-resolution images of the Mars Observer Camera on the Mars Global Surveyor mission and the *in situ* observations and measurements by landers. The HRSC will make a major contribution to the study of martian geosciences, with special emphasis on the evolution of the surface in general, the evolution of volcanism, and the role of water throughout martian history. The instrument will obtain images containing morphologic and topographic information at high spatial and vertical resolution, allowing the improvement of the cartographic base down to scales of 1:50 000. The experiment will also address atmospheric phenomena and atmosphere-surface interactions, and will provide urgently needed support for current and future lander missions as well as for exobiological studies. The goals of HRSC on Mars Express will not be met by any other planned mission or instrument.

1. The Challenge

Europe will make a major contribution to the international programme of Mars exploration with the launch of Mars Express in 2003. The scientific objectives of the orbiter include the significant task of completing the high-resolution reconnaissance of Mars from orbit and the partial recovery of the scientific objectives of the lost Russian Mars-96 mission.

Imagery is the major source for our current understanding of the geologic and climatologic evolution of Mars in qualitative and quantitative terms. It has the potential to enhance our knowledge of Mars drastically and is an essential prerequisite for detailed surface exploration. Therefore, a prime objective of the Mars Express orbiter is the photogeologic analysis of the martian surface at high resolution. For this task, the existing second flight model of the High Resolution Stereo Camera (HRSC) developed for Mars-96 was selected. This pushbroom camera will provide simultaneously high-resolution, stereo, colour and multiple phase-angle coverage and thus will acquire imaging data of unprecedented scientific quality. In response to the urgent demands for very high-resolution imagery in the metre-range, a complementary Super-Resolution Channel (SRC) was added. This boresighted channel serves as the 'magnifying lens' by providing image strips nested in the wider swath of the HRSC stereo and colour scanner.

The reconnaissance task is quite challenging: in only 2 Earth years – the nominal operational lifetime of Mars Express – at least half of the martian surface shall be covered at a pixel resolution better than 15 m, three quarters of the surface at 30 m per pixel and almost the entire surface at least at 100 m px⁻¹. In addition, about 1% will be observed at about 2 m px⁻¹. The images will allow surface distances, heights and the colours of different rocks to be measured. During imaging, the camera is 250 km or more above the martian surface. The camera processes internally up to 9 million pixels per second; the output data rate (after on-line compression) to the spacecraft memory depends on the altitude and can reach up to 25 Mbit s⁻¹, i.e. 200 Mbit of memory are filled with compressed data within several minutes. Each and every bit acquired by the camera is extremely valuable because most of the covered regions will be overflowed only once at the highest resolution.

Such data will not be acquired by any other current or planned mission. The HRSC image data have a high potential for unravelling the geologic and climatologic history of Mars. It will also provide the required database for the preparation and planning of future sample-return missions, as well as other robotic and human exploration.

2. The Science

The HRSC directly addresses two of the main scientific goals of the Mars Express mission (high-resolution photogeology and surface-atmosphere interactions) and significantly supports another two (atmospheric studies and mineralogical mapping). In addition, the imagery will make a major contribution to characterising the landing site geology and its surroundings for the Mars Express and other Mars missions (e.g. NASA's Mars Exploration Rovers). The scientific objectives and measurement goals have been formulated by an international team of 45 Co-Investigators (Co-Is) from 10 countries under the leadership of the Principal Investigator (PI). The image data will focus on:

- characterisation of the surface structure and morphology at high spatial resolution of ≥ 10 m px⁻¹;
- characterisation of the surface topography at high spatial and vertical resolution;
- characterisation of morphological details at super-resolution of up to 2 m px⁻¹;
- terrain classification at high spatial resolution by means of colour imaging;
- refinement of the geodetic control network and the martian cartographic base;
- characterisation of atmospheric phenomena;
- characterisation of physical properties of the surface through multi-phase angle measurement;
- observation of Phobos and Deimos.

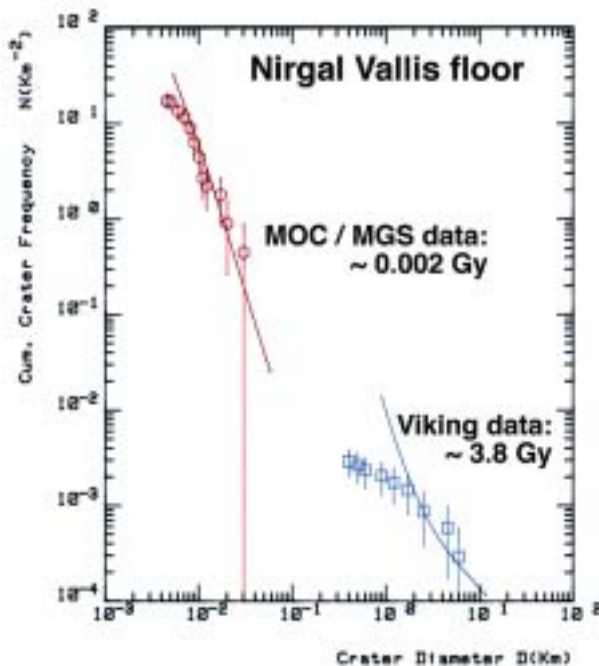


Fig. 1. Nirgal Vallis floor surface ages. Cratering counts on MOC data reveal the near-recent aeolian activity at the floor of Nirgal Vallis, while the formation of the valley more than 3.8 Gy ago can be roughly constrained based on Viking data. Note the obvious gap in spatial resolution to be closed by the HRSC. (counts by D. Reiss, DLR)

These will dramatically increase our knowledge about the planet with special emphasis on:

- the geologic evolution of the martian surface;
- the evolution of volcanism and its influence on the martian environment;
- information on the past climate, its variability and the role of water through martian history;
- the structure of the martian crust and the elastic response of the lithosphere;
- surface-atmosphere interactions (variable features, frost) and aeolian processes and phenomena;
- analysis of atmospheric phenomena (dust devils, cloud topography, aerosol content);
- characterisation of past, present and future landing sites and support for lander experiments;
- support for exobiological studies.

Looking at the previous martian imagery and the expected performance of cameras and altimeters aboard current and planned missions, HRSC's imaging data will close the gap between medium- to low-resolution coverage and the very high-resolution images of the Mars Observer Camera (MOC) on Mars Global Surveyor, as well as the *in situ* observations and measurements by landers. It will substantially increase the very high-resolution image coverage. Such data will not be provided by any other instrument on any other planned mission. The experiment will also contribute significantly to the scientific objectives of past, current and future Mars lander modules (e.g. Mars Pathfinder; the lander missions of 2003 with the Mars Exploration Rovers; sample-return missions) by providing context information on the geological setting of the landing sites. Landing site characterisation will address geological and topographic mapping for scientific interpretation, as well as landing safety and mobility characteristics of future sites.

Orbital imagery in the 10 m px^{-1} range, as obtained by the HRSC, is an essential prerequisite to detailed surface exploration and to solving many of the open questions such as volcanic evolution or the role of water throughout martian history. The

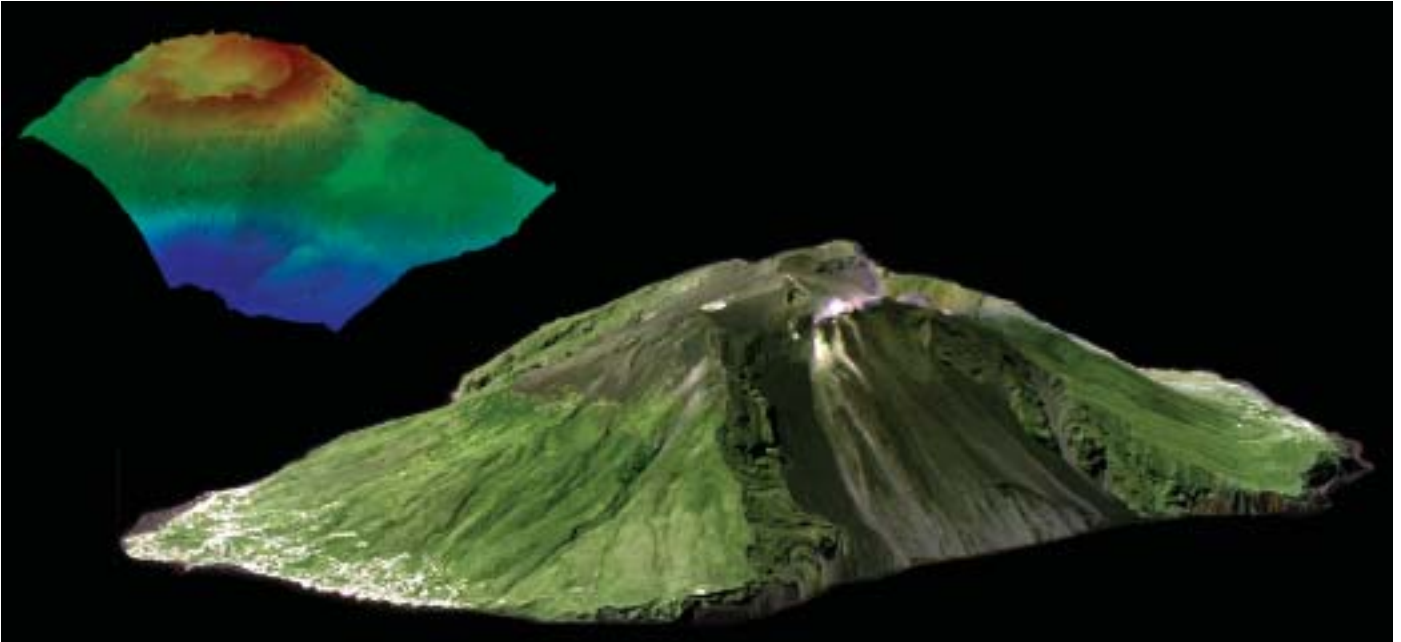


Fig. 2. An example of the expected data return from the HRSC. During standard operations, the HRSC will provide stereo and colour information as shown in this example from the airborne HRSC experiment at the Aeolian island of Stromboli. Here, spatial and vertical resolutions of 40 cm were obtained (main image). For Mars, resolutions in the 10 m range are expected. For comparison, a Digital Terrain Map (DTM) of Arsia Mons in the available DTM resolution of 1 km px^{-1} , derived from Viking data with a resolution of 170 m px^{-1} , is shown (top left).

zoom-in capability of the SRC channel for targeted observations in the metre-range will follow-up these questions at even greater detail.

The ability to study morphologic surface features in more detail by photogeology is complemented by the possibility of deriving ages even for small features like valley floors, surfaces of former lakes, and debris aprons from creep or lavaflows. High-resolution imagery enables the counting of craters much smaller than the features themselves and is essential for reconstructing the geologic history and sequencing of events. The reconstruction of the martian cratering record requires the ability to determine the crater-size frequency distribution at all scales. This is impossible at the moment because 10 m resolution is insufficient and there is little coverage available in the metre-range (see Fig. 1). Closing this gap is a major objective for the HRSC.

The stereo and colour capabilities will both significantly enhance the interpretation of the imaging data (Figs. 1 and 2). For instance, the accurate determination of erosion rates, the modelling of various geologic processes such as water flow, ice-abetted creep, and emplacement of lava flows, is presently limited by the lack of information on local elevation differences. The colour information will be important for terrain classification, detecting compositional layering, variations in surface materials and their composition, and recognising different surface processes.

A key aspect in the evolution of Mars is the role of water in the different epochs. Valley networks and outflow channels provide ample evidence of the existence of liquid water or ice on or in the ancient surface of the planet. Small gullies discovered in MOC images might indicate rather young or even recent erosional activity by water. The present surface, however, is essentially water-free (with the exception of the small residual water ice caps on the poles), and the atmosphere contains only minor amounts of water vapour. Though some water might have escaped into space, the question of water on the surface and where it is now is one of the great unanswered questions in the exploration of Mars.

Permafrost and ground water are considered as the most likely candidates for large water reservoirs in the subsurface. The past or present existence of ground ice is indicated by various morphologic surface features, e.g. rampart craters, terrain softening, and features from the interaction of magma and permafrost. The latitudinal variation of the depth of permafrost has been inferred from the minimum diameter of

craters with fluidised ejecta flows (rampart ejecta). Future topographic and morphologic information must be detailed enough to map the exact distribution of ejecta and to determine precisely its volume. If a substantial amount of subsurface ice is present, a terrain can be degraded, or 'softened', by gravity-induced viscous creep of surface material. The degree of such terrain softening can be accurately determined only if the topographic data have spatial and vertical resolutions high enough to discriminate between undisturbed and softened ground (e.g. sharp *vs.* broad slope inflections; concave *vs.* convex slope segments). In a similar manner, the volume of surface features (e.g. thermokarst depressions) caused by the interaction of ground water or ground ice with magma can be calculated only on the basis of sufficiently precise stereo information with horizontal and vertical resolutions better than that of the addressed features (typically of the order of tens or hundreds of metres).

A variety of mechanisms has been invoked to explain the origin of valley networks and outflow channels, including surface water runoff, glacial processes, groundwater sapping and mass wasting. Runoff implies a warmer, denser atmosphere, which places important constraints on the evolution of the atmosphere as a whole. It is a cornerstone not only for the development of Mars' aqueous history but also for the question of life having ever existed on Mars. A critical unknown in the development of valleys and channels is the amount of water needed to create these features and the maximum discharge rates. These can be computed only if reliable cross-sectional profiles through the channels are available; the longitudinal slope of the channel floor also needs to be known.

The existence of ancient palaeolakes and sedimentary basins in the northern lowlands of Mars is one of the most debated topics in martian geology. If ocean-sized bodies of water or mud ever persisted on Mars, they would have had a substantial impact on the atmosphere and global climatic conditions. Even though a lot of effort has been spent in trying to identify evidence for such terminal lakes, into which the outflow channels would have spilled their load of water and sediment, the work suffers from the lack of extended high-resolution imaging data. Lacustrine features that would prove the existence of lakes are very subtle and only a few could be definitely identified in high-resolution Viking Orbiter images. MOC data show evidence for layered deposits in many impact craters, suggesting that standing bodies of water occurred in these locations. Such features are abundant and widespread over the entire planet. If there were lakes, their extent will be determined only by continuous high-resolution coverage to trace faint wave-generated shorelines surrounding them. Once a shoreline has been identified, the volume of water in a lake can be derived from topographic information only. This will help to decide whether lakes periodically covered as much as a quarter of the planet or were comparable in size to the volumes discharged by individual floods. This, in turn, will significantly improve our understanding of the martian water inventory and palaeoclimate.

Mars has had a long and varied volcanic history. Based on Viking data, the youngest volcanic deposits were thought to occur at Olympus Mons. Evidence from crater counts and martian meteorites suggest that Mars could be volcanically active even today. MOC images then revealed a number of young lava flows (as young as a few million years) in several volcanic provinces such as Olympus Mons, Tharsis, Elysium and Amazonis Planitia. Models of the formation of Mars indicate that, at the end of heavy bombardment, the global heat flow was about five times the present value and was even higher during heavy bombardment. Such high heat flows imply high rates of volcanism early in the planet's history, yet available morphologic evidence for volcanic activity in this period is rather sparse because the older terrains are highly modified and much of the earlier history is not visible in available images. A multitude of volcanic features reflecting a variety of volcanic processes has been found on the martian surface, which can be divided into central cones and volcanic plains. More than 60% of the surface is covered by plains units of all types. Some are certainly volcanic and some are undoubtedly of other origin. In many cases, however,

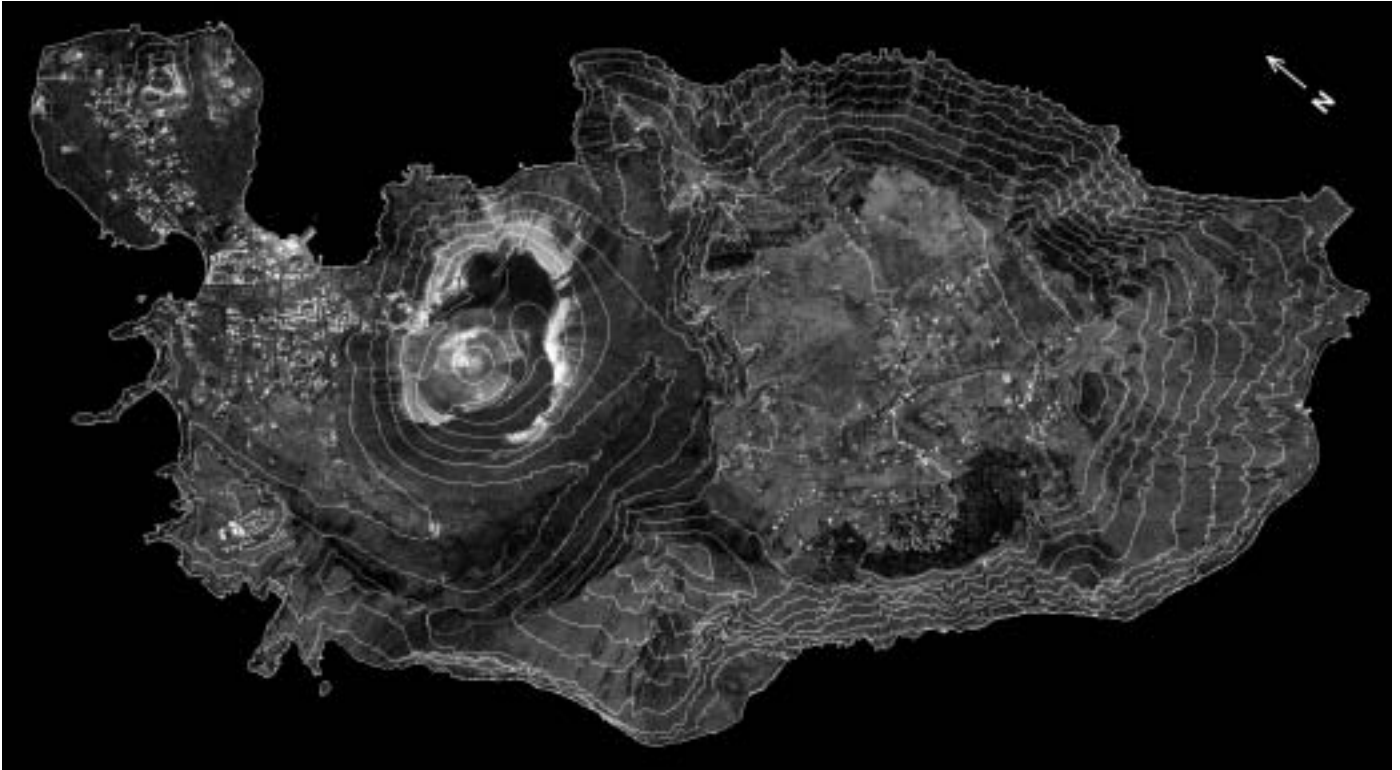


Fig. 3. HRSC orthoimage mosaic of Vulcano Island (I) with 50 m contour lines derived from HRSC stereo data. Obtained during the HRSC flight campaign of May 1997 at an altitude of 5000 m with a spatial resolution of 20 cm px⁻¹ for the nadir and 40 cm px⁻¹ for the stereo lines.

their origin is interpreted controversially. Volcanic edifices were classified into three different categories based on their morphologies: with shield volcanoes, domes (tholi) and composite cones, and highland paterae. Lava flow deposits are associated with most of the volcanoes. Their morphology suggests high fluidity, which corresponds to a mafic to ultramafic composition by terrestrial analogy. This interpretation is confirmed by the chemical analysis of the SNC meteorites. The results of Mars Pathfinder indicate the presence of more silicic volcanic materials, which implies a higher degree of crustal fractionation than previously thought. The different environmental conditions on Mars, however, with lower gravity and lower atmospheric pressure, could be responsible for a larger amount of explosive activity than on Earth, assuming similar mafic composition and similar volatile content. High-resolution imaging and topographic information is essential for a better understanding of the formation processes and the evolution of volcanic features. The volcanic history is intimately tied to the climatic history and the history of internal processes. Volcanic activity, especially on the Tharsis bulge, could also explain the occurrence of outflow events and the formation of thermokarst features. From Viking imagery we know that a spatial resolution of about 10 m px⁻¹ is sufficient to recognise single lava flows within the complex flows found on the flanks and around the shield volcanoes. Quantitative models to estimate the diffusion rate, yield strength and composition of lavas are based on the length, width and volume of a single lava flow as well as on the local topography. The recognition of explosive deposits requires the detailed analysis of erosional features, while many small possible volcanic features like the domes in the lowlands remain enigmatic without higher resolution imagery or have not yet been discovered with existing data.

Wind has played a major role in shaping the martian surface and is still active. Both erosional and depositional landforms are widespread features. The most prominent features are dunes occurring either in large dune fields or as isolated patches. Other aeolian features are wind streaks, yardangs, pits and grooves. It is not clear if dunes



Fig. 4. Example of an HRSC data product. Vulcano Island in a perspective view based on a Digital Elevation Model from HRSC-A stereo and multispectral data. The resolution is 25 cm from 6 km flight altitude.

are still active despite some hints in MOC data. High-resolution imagery and the possibility of analysing the population and degradational state of small craters over a large area are essential for a better understanding of dune formation and evolution.

Atmospheric studies are a prime objective for the cameras aboard the NASA Mars Surveyor missions, which will have increased our knowledge of atmospheric circulation and the cycles of volatiles and dust before the launch of Mars Express. A high-resolution, multicolour and multiphase stereo instrument, however, will make a significant contribution to our understanding of atmospheric phenomena on Mars, especially of cloud properties, local wind regimes, dust devils, variations in aerosol content and the vertical structure of the atmosphere.

Detailed mapping (geology, morphology, topography, composition, etc.) is the prerequisite for the proper characterisation and selection of areas of interest for lander missions, mobile surface activity and sample return. An imaging instrument gathering high-resolution, stereo and colour imagery (Figs. 3 and 4) of large parts of the martian surface will provide the required database. One of the surprising results from MOC/MGS was the discovery that the martian surface appears completely different in images with different spatial resolution. Surfaces that seem smooth at typical Viking scales ($60\text{-}100\text{ m px}^{-1}$) show a rough morphology at the very high resolution of MOC (few m px^{-1}) and vice-versa. MOC, however, is observing only a small fraction of the martian surface and much more image data at similar resolution are needed.

Finally, Mars Express will encounter Phobos several times during the nominal mission, when the node of its orbit on the equatorial plane is at the Phobos distance from Mars. There will be periods of about a week when close flybys will occur naturally, with little impact on mission operations. At these times, the HRSC Co-I Team is interested in imaging Phobos at high- and very high-resolution, as well as in colour and stereo. These images will be of higher resolution than the Viking images and will provide an excellent opportunity for detailed geological, compositional, regolith and orbital studies.



Fig. 5. HRSC Flight Model.

3. The Camera

The HRSC instrument (Fig. 5; Table 1) consists of the camera unit containing the HRSC stereo colour scanner and the Super-Resolution Channel (SRC), and of the digital unit. The unique capability of the HRSC stereo colour scanner is to obtain quasi-simultaneously high-resolution images in three-line stereo, in four colours and at five phase angles. The combination with the SRC makes it a five-in-one camera:

- the along-track acquisition of stereo imagery avoids changes in atmospheric and illumination conditions which so far have caused severe problems in the photogrammetric evaluation of stereo images acquired at well-separated times;
- the triple stereo images permit robust stereo reconstruction, yielding Digital Terrain Models (DTMs) at a vertical resolution similar to the high pixel resolution of the nadir sensor, with 10 m px^{-1} at 250 km altitude (periapsis);
- the colour images (Fig. 6) enable terrain classification and provide information on compositional variations and surface weathering as a complement to the more specific (but with lower spatial resolution) mineralogical information obtained by the imaging spectrometer of Mars Express;
- the multiphase imagery will address the physical properties of the martian soil (roughness, grain size, porosity) via photogrammetric data evaluation by providing a second stereo angle triplet (in essence quintuple stereo);
- the super-resolution imagery, nested in the broader swath of the scanner with a spatial resolution of 2.3 m px^{-1} at periapsis, will serve as the magnifying lens to analyse surface morphology at even greater detail.

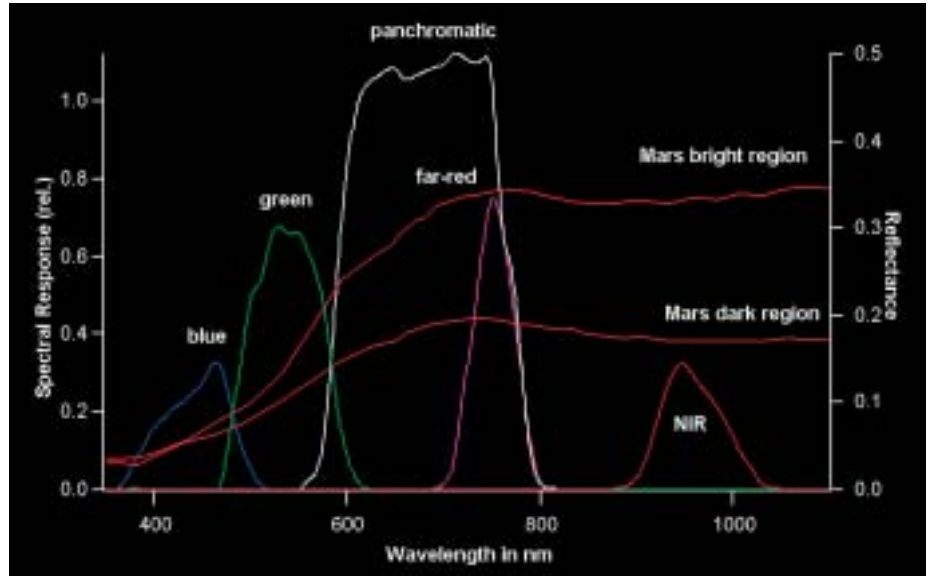
The HRSC stereo colour scanner is a multi-sensor pushbroom instrument, with nine CCD line sensors mounted in parallel delivering nine superimposed image swaths. Originally, it was developed as the HRSC instrument for the Russian Mars-96 mission. Two fully tested and calibrated Flight Models were prepared, and only minor modifications to the remaining version were required to satisfy the Mars Express interface requirements.

The stereo colour scanner comprises a baffle, optics, optical bench, spectral filters,

Table 1. HRSC characteristics and performance.

	<i>HRSC stereo colour scanner</i>	<i>SRC</i>
<i>Mechanical and Electrical Parameters</i>		
Camera Unit envelope	515 x 300 x 260 mm (height x width x length)	
Digital Unit envelope	222 x 282 x 212 mm (height x width x length)	
Mass	19.6 kg	
Power consumption ^a	45.7 W during imaging	3.0 W during imaging
Radiation shielding	10 krad	
<i>Electro-optical Performance</i>		
Optics, focal length	Apo-Tessar, 175 mm	Maksutov-Cassegrain, 975 mm
F number	5.6	9.2
Stereo angles	-18.9°, 0°, +18.9°	in-track FOV 0.543°
Cross-track field of view	11.9°	0.543°
Number of CCD lines	9: on 3 plates with 3 lines each	1 area array sensor
Detector type	THX 7808B	KODAK KAI 1001
Sensor pixel size	7 x 7 µm	9 x 9 µm
Pixel size on ground	10 x 10 m at 250 km altitude	2.3 x 2.3 m at 250 km altitude
Field of view per pixel	8.25 arcsec	2 arcsec
Active pixels per sensor	9 sensors at 5184 pixels	1024 x 1032
Image size on ground ^b	52.2 km x [# of lines] at 250 km	2.3 x 2.35 km at 250 km
Radiometric resolution	8-bit entering compression	14-bit or 8-bit selectable
Sensor full well capacity	420 000 e ⁻	48 000 e ⁻
Gain attenuation range	10.5 dB to 62 dB in 3 dB steps	–
Spectral filters ^c	5 panchromatic and 4 colour	–
Pixel MTF at 50 lp/mm	at nadir: 0.40; at 20° off nadir: 0.33	
SNR for panchromatic lines ^d	>>100 (without pixel binning)	>>70
SNR for colour lines	>80, blue >40 for 2x2 macro pixels	
<i>Digital Features</i>		
On-line compression	yes, DCT: table-controlled JPEG	
Mean output data rate	peak rate 25 Mbit s ⁻¹ after compression	
<i>Operations</i>		
Pixel exposure time	2.24 ms to 54.5 ms	0.5 ms to 8 s
Pixel binning formats	1 x 1, 2 x 2, 4 x 4, 8 x 8	–
Compression rates	2...20, nominal: 6...10, bypass possible	
Typical data volume	≈1 Gbit/day (compressed data)	
Duty cycle	every orbit; several times/orbit	
Internal data buffer	no	8 x 8 bit or 4 x 14 bit images
Typical operations duration	3 – 40 min	
Expected coverage	≥50% at about 15 m px ⁻¹	≥1% at about 2.5 m px ⁻¹
Operational lifetime	> 4 years	
<i>Notes</i>		
a: including 12 W maximum heating power. b: image size is defined by the swath width times the number of acquired image lines, and depends on available downlink capacity. c: nadir, outer stereo (2), photometric (2) 675±90 nm; blue 440±45 nm; green 530±45 nm; red 750±20 nm; near-IR 970±45 nm. d: worst-case scenario (30° solar elevation angle and dark Mars region)		

Fig. 6. The HRSC colour filter spectral characteristics.



CCD sensors lines, sensor electronics and thermal control system. The technical design is defined by:

- single-optics design;
- CCD line arrays with 5272 pixels each;
- nine detectors for simultaneous stereo and colour imaging, and for multi-phase angle measurements;
- CCDs and sensor electronics implemented in high-reliability hybrid, low-noise and low-power technology;
- implementation of the CCD-control unit in ASICs.

The SRC is a framing device and uses an interline CCD detector to cope with the very short exposure and read-out times. It is based on an instrument development for the Rosetta Lander and the design is characterised by:

- CCD area array interline detector with 1024 x 1032 pixels;
- highly miniaturised and low-power detector and control electronics;
- compact 3D multi-chip module technology using thin-film multilayer metallisation, dycostrate, plasma-etching and chip-on-wire technology;
- selectable dynamic range of 8- and 14-bit per pixel;
- internal data buffer to store eight 8-bit (or four 14-bit) images;
- lightweight Maksutov-Cassegrain telescope with a focal length of 975 mm.

The HRSC scanner and the SRC are boresighted and mounted in a common instrument structure. The common Digital Unit contains a power converter, spacecraft interface, processor for instrument control, data compression unit and heater control unit. It is based on the Digital Unit developed for the Mars-96 mission. Modifications include a lighter housing box, a new camera control processor based on the Mars-96 telemetry controller unit, and new spacecraft interfaces derived from existing parts.

The HRSC is operated in individual imaging sequences. A typical sequence consists of nine HRSC stereo colour scanner images covering the same area on the ground. Image data will be taken during every orbit that offers sufficient illumination conditions for 4-30 min. Data will be compressed on-line by JPEG-based compression hardware with an average (selectable) compression factor of 6-10 and with throughput rates of up to 450 lines s^{-1} in four parallel signal chains (each serving

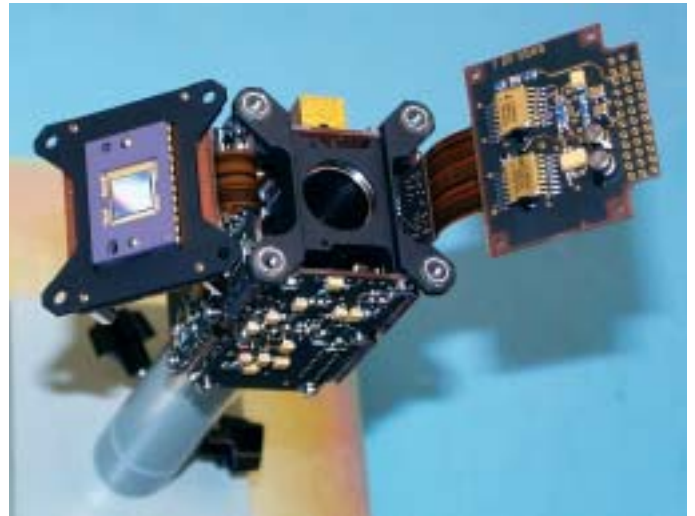


Fig. 7. Above left: SRC optics (Maksutov Cassegrain, focal length 975 mm, optics length 210 mm). Above right: the SRC electronics and detector section.

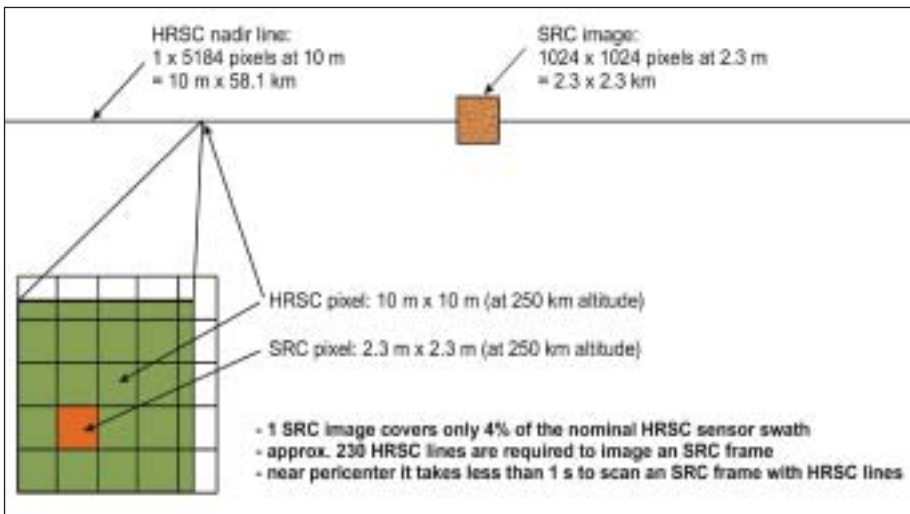


Fig. 8. HRSC scanner and SRC footprints.

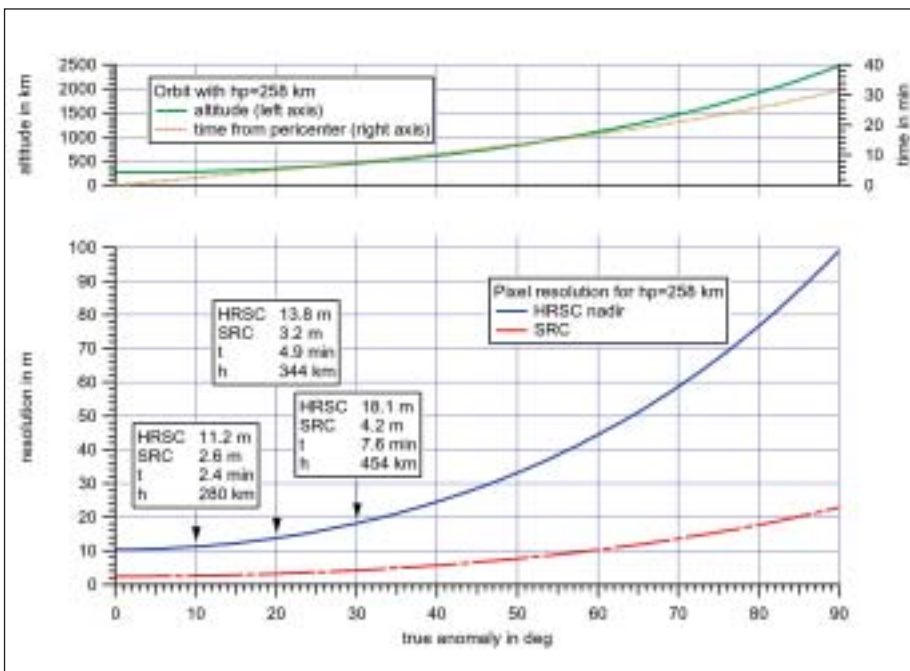
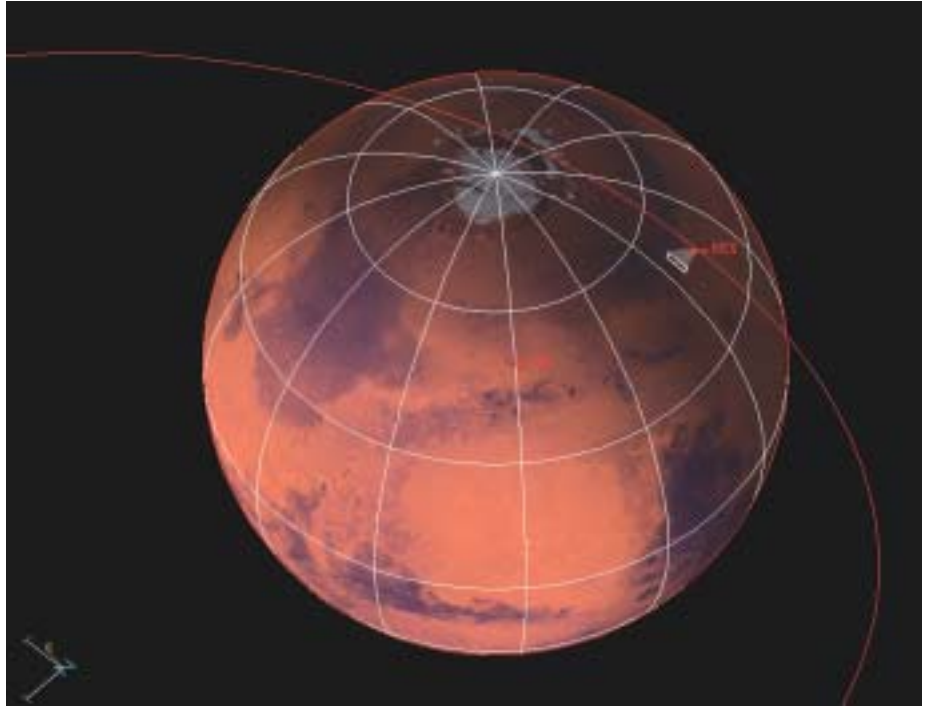


Fig. 9. HRSC and SRC pixel resolution for the nominal Mars Express orbit with 258 km periastron altitude.

Fig. 10. The Mars Express orbit, with HRSC's field of view near periapsis.



a part of the nine CCD lines). Bypassing the compression is possible. Data compression techniques have been used successfully on previous planetary missions (e.g. on the US Clementine mission to the Moon based on hardware similar to the HRSC chip-set) and for current Earth remote-sensing and deep-space missions. Up to date, a specific implementation of the JPEG algorithm, namely the Discrete Cosine Transform (DCT) compression, has been applied in most of the cases. Before its implementation in the HRSC, the DCT algorithm was thoroughly tested. No appreciable loss of 'science' arising from this particular method could be detected within the expected compression rates.

The SRC (Fig. 7) is used for targeted observations. It will operate mostly in parallel with the scanner to generate nested super-resolution images in order to avoid any location problems and to obtain the contextual information and the precise position (Figs. 8 and 9).

SRC imaging will be carried out in one of two modes. In the 'internal' mode, up to eight 8-bit images or four 14-bit images can be acquired during one session. The images are stored in an SRC internal buffer and transferred to the spacecraft memory via the digital unit after compression. There are no restrictions on scanner operations for this mode. In the 'connected' mode, one of the four HRSC signal chains is devoted to SRC. This means that, in addition to spot and raster images, contiguous image strips can be formed. However, this requires a reduction in resolution or in the number of operated lines of the scanner.

The operational profile foresees imaging preferably near periapsis and at solar elevation angles of 15-90°. With the Mars Express reference orbit, this will be possible during the first 3 months (January to March 2004) of the mapping phase and after one year with the periapsis in the dark again starting in March 2005. However, high-altitude imaging is also envisaged and solar elevation angles down to a few degrees will be used for specific tasks. The high flexibility in instrument operations (e.g. pixel summation, compression ratio, windowing, integration time) allows optimisation of data acquisition with respect to the scientific goals, the available spacecraft resources and orbital constraints. Multiple imaging sequences during one orbit revolution are being considered for optimum coverage strategies.

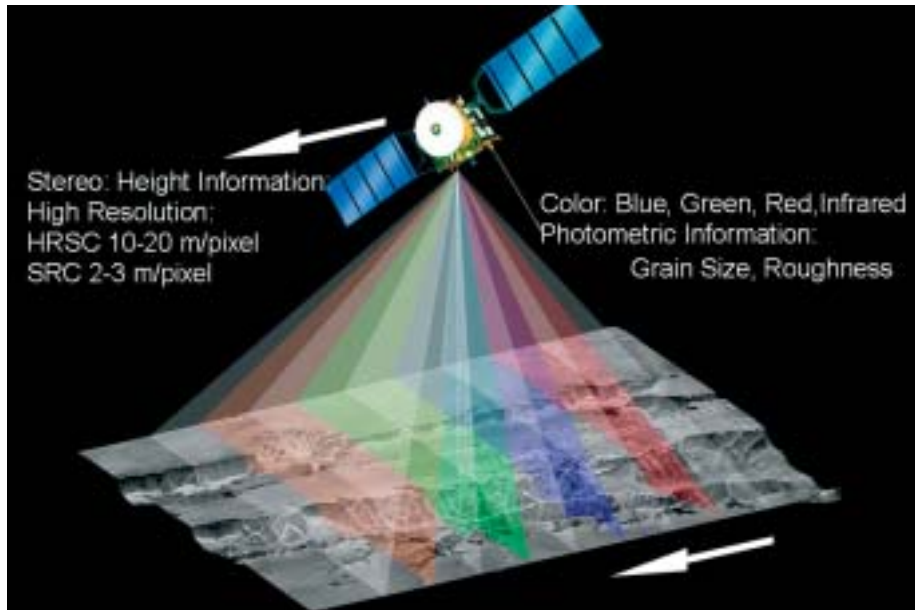


Fig. 11. The HRSC operating principle and viewing geometry of the individual CCD sensors.

The highest image quality is attained by providing accurate spacecraft attitude and orbital data. Combined with geometrical calibration data, they allow the derivation of digital terrain models. Radiometric precision is maintained by thorough on-ground calibration and by periodic in-flight verification over near-uniform targets such as dust storms.

The achievable surface coverage is not restricted by the HRSC instrument but has to be traded-off between available telemetry rates, telemetry sharing and orbit characteristics (Fig. 10). During the nominal mission lifetime of 2 Earth years and within the given mission constraints, at least 50% of the surface will be covered at a spatial resolution of $\leq 15 \text{ m px}^{-1}$ and about 1% at a spatial resolution of 2.5 m px^{-1} .

The camera is designed to sustain an operational lifetime of more than 4 Earth years in orbit, consistent with the envisaged mission extension of another martian year.

The martian surface is 'scanned' by the nine CCD lines of the stereo colour scanner at frequencies of up to 450 Hz (Fig. 11). Single spot observations by the SRC are gathered at specific times from periapsis while continuous observations are performed at a constant frequency. After internal signal processing and on-line data compression, HRSC data are transferred to the spacecraft mass memory at output rates of up to 25 Mbit s^{-1} .

Instrument operations control (housekeeping and command echo monitoring, data consistency checks) is performed by the DLR Institute of Planetary Research in concurrence with the PI and his project group at FU Berlin.

During the cruise phase, the camera will be operated only for internal health checks (i.e. no imaging will be provided, with the exception of looking back at the Earth-Moon system for a 'farewell' picture). During the approach to Mars, HRSC-SRC images of Mars will be obtained for the first time.

For nominal imaging, camera operations focus on the configuration of the camera channels (CCD lines, signal electronics, use of the SRC) and of the on-line data compression. Various imaging strategies will be realised by setting different resolutions for each of the nine CCD lines via pixel summation formats. Pixel summation (or 'macropixel') formats of 1x1, 2x2, 4x4, 8x8 (first factor: in-flight direction pixel summation, realised by exposure time variations; second factor: across-flight direction pixel summation, digitally realised by pixel summation/averaging in the Digital Unit) are possible independently for each line. Thus, under certain restrictions it is possible to read out all nine CCD lines by three signal chains

and to devote the remaining one to the read-out of SRC data. The number of possible configurations has been grouped into 64 basic camera macro formats. The macro format is selected by commands and remains constant during one imaging sequence. A number of internal parameters (e.g. sensor integration time for taking into account imaging altitudes, sensor on/off delays for covering the same area on the ground, as well as window size and compression parameters for reducing the data rate, timing for SRC observations) are set depending on the selected imaging strategy. All of them are constant during one imaging sequence (except the sensor integration time, which is automatically adopted according to the orbit profile) but may be changed via commands for subsequent sessions.

4. Relation to Other Mars Express Instruments

The HRSC is a standalone instrument – it does not require operational interactions with other instruments. There are no restrictions regarding simultaneous operations with other instruments except probably the electric ambient field of MARSIS.

The surface- and atmosphere-oriented instruments of Mars Express are highly complementary. DTMs and images derived from the HRSC will allow registration and map projection with the results of the OMEGA IR mapping spectrometer and the MARSIS subsurface radar to a common reference surface. The combined evaluation of HRSC images and topographic data with the gravity measurements obtained by the MaRS radio science experiment will allow an improved investigation of the martian crust. The HRSC will also produce improved spacecraft orbit and attitude information from high-precision stereo models, which will be shared with the Mars Express project and the other instruments for their data reduction.

While OMEGA will provide surface mineralogy at about 100 m resolution, HRSC's colour capability will detect compositional variations in the OMEGA subpixel range, leading to a better understanding of terrain boundaries and spectral mixing characteristics. The topographic information derived from MARSIS can be used to verify or calibrate the HRSC terrain models and vice-versa.

5. Relation to Other Missions

In order to better understand and validate the achievements and scientific return expected from the HRSC, the instrument has to be placed in a broader context of former, current and planned missions. Almost every planetary mission carries an imaging system for observing planetary surfaces and atmospheres (Fig. 12). In addition, Mars Global Surveyor is carrying a laser altimeter (MOLA) around Mars for the first time.

What will HRSC achieve in comparison with other Mars missions?

The Viking missions provided near-global (95%) coverage at 200 m px⁻¹ and 28% coverage at ≤ 100 m px⁻¹, but only 0.3% was observed at ≤ 20 m px⁻¹. The Mars Observer Camera (MOC, initially developed for the failed Mars Observer mission, now on Mars Global Surveyor) provides global coverage with its wide-angle camera at a spatial resolution of 225 m px⁻¹. The MOC narrow-angle camera yields a spatial resolution of up to 1.4 m px⁻¹, but only for a small amount of the martian surface even after the extension of the MGS mission. The spatial resolution of the SRC is comparable to MOC and it will be possible to increase the 2 m-resolution coverage significantly, which is especially important for future lander missions.

Mars Climate Orbiter (MCO) aimed at covering about 80% of the surface at 40 m px⁻¹, but its loss resulted in a major gap in martian imagery. HRSC can fill that gap. Mars Odyssey arrived in orbit in October 2001 and provides a spatial resolution of 20 m px⁻¹. However, the number of images that can be transferred to Earth is severely limited and no more than about 7% of the surface will be covered. The Mars Surveyors carry single-line sensors that lack intrinsic geometrical control. Only Mars Express and HRSC data will close the gap in the high-resolution reconnaissance imagery and provide the link between MOC's small images at very high-resolution and the medium- to low-resolution data of former missions.

Moreover, the HRSC is the only dedicated stereo camera planned for flight. Some

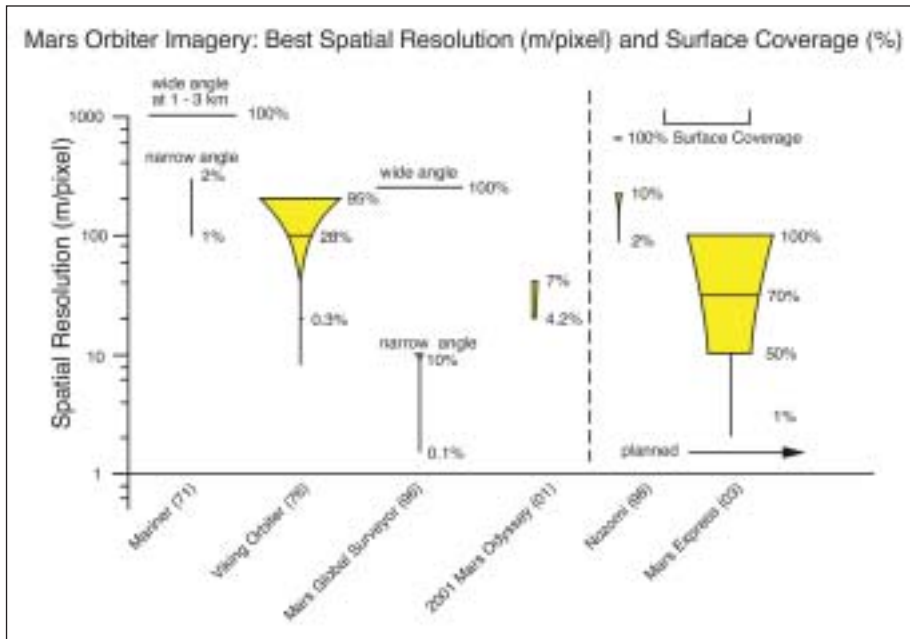


Fig. 12. Best spatial resolution and surface coverage for past, present and planned Mars missions.

high-resolution stereo imagery has been obtained but only by multiple coverage at different times and for a very small part of the surface. From Viking data, a global DTM with 1 km resolution was obtained; better resolution was achieved only locally. MGS has provided stereoscopic coverage with its wide-angle camera at 225 m px^{-1} . Mars Odyssey is focusing on colour imagery and has no dedicated plans for stereo coverage.

A second source for topographic information is the MOLA laser altimeter on MGS. It has produced global topographic coverage with a spatial resolution of about $300 \times 1000 \text{ m}$ at the equator, and better near the poles. The HRSC with a (nominal) resolution of 10 m is a significant improvement. Furthermore, the individual laser return points (though these cannot be seen in images) can be entered as control information in the HRSC image adjustment procedures to calibrate for absolute heights. The MOLA altimeter and the HRSC stereo information are thus highly complementary.

The Viking cameras were sensitive only in the visible wavelength range. Near-global coverage with 2-3 colours was achieved at 900 m px^{-1} and only a small amount of the surface at 100 m px^{-1} ($\sim 1\%$). The MGS/MOC instrument has only a 2-colour capability for the wide-angle camera, while the narrow-angle camera has no colours at all. The THEMIS camera of Mars Odyssey has five colours, with a maximum resolution of 20 m px^{-1} . With the ability to transfer 15 000 images in total, no more than about 7% of the surface can be covered. The HRSC colour capability will drastically improve the multispectral coverage of the martian surface. Owing to its higher spatial resolution (ratio $\sim 1:5$), it will support the spectrometer data obtained by Mars Express and Mars Odyssey.

Furthermore, the HRSC is the only instrument with the ability to obtain near-simultaneous images with multiple phase angles of the surface. Similar information by other cameras/missions has and will be obtained only by multiple coverage with large time differences, producing severe problems in photometric modelling arising from variations of atmospheric conditions, variable surface features etc. The unique multi-angle capability of the HRSC will also support its stereo capability by providing not only a stereo triplet but also a stereo quintuplet.

In conclusion, the orbital reconnaissance of the martian surface is not met by any other instrument or set of instruments. The HRSC is a unique instrument in the international Mars exploration effort and will close the existing gaps and provide the required imaging and cartographic products for future missions.

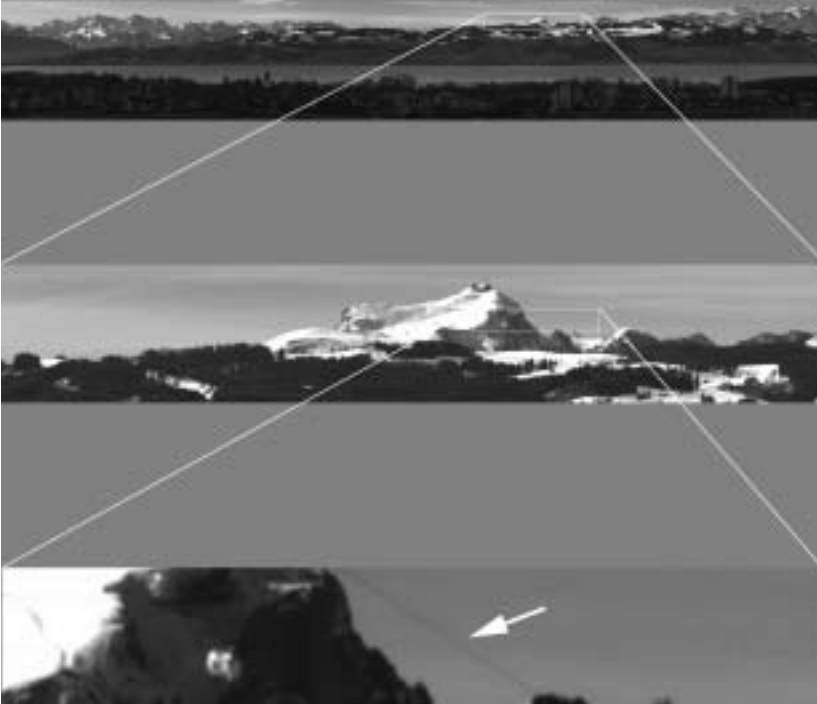


Fig. 13. This test image, looking across Lake Constance in March 1995, illustrates HRSC's resolution. The cable car rope (diameter 10-15 cm) is imaged from a distance of 40 km. The pixel resolution at this range is 1.6 m.



Fig. 14. HRSC test image of Mount Etna lava flows from a flight altitude of 10 km. Resolution is 40 cm px⁻¹.

6. The Test Campaign

The HRSC instrument and its ground data system were extensively tested in March 1995 at Lake Constance (Fig. 13), as well as during airborne experiments near Mount Etna (Fig. 14), Stromboli and Vulcano, Sicily, in May 1997. The tests included the HRSC Flight Model and demonstrated the resolving power and the radiometric quality of the instrument, as well as the reliability of the fully operational software. The airborne campaign verified the entire system in an end-to-end test, including the ground data system. The HRSC Qualification Model was mounted on a stabilising platform and the volcanoes were covered from a flight altitude of 10 km with a spatial resolution of 40 cm px⁻¹, in triple stereo, in colour and at multiple phase angles. These targets were selected specifically for their relevance to comparative planetology. Comparative analysis of volcanic morphologies will shed important light on the origin and mechanisms of volcanic activity on both planets. Images from Etna (Fig. 14) were analysed for their potential to recognise and map surface features typically associated with volcanoes, such as lava flows.

The dataset of the Stromboli airborne test is available in Planetary Data System (PDS) standard format on CD-ROM along with stereo processing software and calibration data.

A further result of this test and other multiple airborne flight campaigns with the Qualification Model was the demonstration of the robustness of the camera system under severe environmental conditions. During these tests, the camera produced excellent imagery which allowed the qualitative and quantitative validation of the camera performance parameters. Since 1997, the HRSC airborne camera has been widely used for Earth remote-sensing applications.

Additional tests have been conducted in order to identify ageing and degradation effects; none has been found. For Mars Express, the HRSC instrument underwent comprehensive and full-scale tests before integration on the spacecraft.

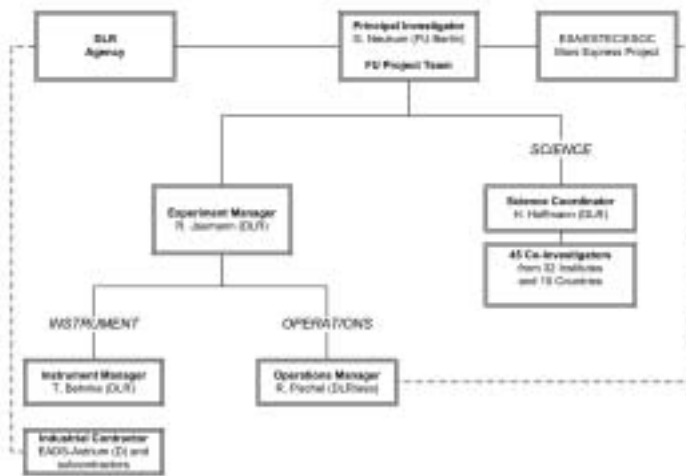


Fig. 15. The HRSC project team structure.



Fig. 16. The Science Team structure.

Mars Express scientific data will be transmitted to Earth daily. After receipt in Perth, Australia (or at station of the NASA Deep Space Network) and primary decoding and formatting, the image data will be processed at the DLR Institute of Planetary Research, Berlin (D) to a certain level.

The data reduction will be performed in consecutive steps consisting of systematic and scientific data processing. For Mars-96, a fully operational software package for scanning instruments was developed. A modified version of this software that takes into account framing camera characteristics (SRC) has been applied and tested for analysis of Viking Orbiter, Clementine and Galileo images. Only minor modifications to Mars Express-specific needs are necessary.

The results of the systematic data processing step are radiometrically and geometrically calibrated and map-projected images. These data will be transferred to the database of the PI at FU Berlin. After validation by the PI, they will be released electronically to the Science Team at the individual home institutes of the Co-Is. They will be distributed to the Science Team members and the science community. The scientific data processing by the Science Team involves chiefly the photogrammetric and cartographic processing and colour image production, and will result in higher level products, including DTMs, orthoimages, image mosaics, cartographic products (e.g. image maps, topographic maps, thematic maps) and a refined geodetic control network.

After the processing phase, the data will be released as individual images in electronic version or through hardcopy, as offset-printed maps and CD-ROM archives in PDS formats for further use by the general planetary science community and the public. The stereo images are expected to have a great potential for public relations activities.

The processing software was tested and refined as an additional result of the HRSC airborne campaigns. Data handling and data management were also exercised. The amount of data processed for airborne projects since 1999 exceeds the expected Mars data volume by a factor of 10-100.

The HRSC experiment organisation is divided into three functional teams (Science Team, Instrument Team, Operations Team) under the direction and responsibility of the PI, supported by his project team at FU Berlin (Fig. 15; Table 2). The Science Team (Fig. 16) is subdivided into working groups by discipline to meet the

7. The Data Processing Tasks

8. The Team

Table 2. HRSC Co-Investigators.

J. Albertz¹, G. Bellucci⁶, J.-P. Bibring²², M. Buchroithner³; E. Dorrer⁴, H. Ebner⁵, E. Hauber², C. Heipke⁷, H. Hoffmann², W.-H. Ip⁸, R. Jaumann², H.-U. Keller⁸, P. Kronberg¹⁹, W. Markiewicz⁹, H. Mayer⁴; F.M. Neubauer¹⁰, J. Oberst², M. Pätzold¹⁰, R. Pischel², G. Schwarz¹¹, T. Spohn¹², B.H. Foing¹³, K. Kraus¹⁴, K. Lumme¹⁵, P. Masson¹⁶, J.-P. Muller¹⁷, J.B. Murray¹⁸, G. Gabriele Ori¹⁹, P. Pinet²⁰, J. Raitala²¹, A.T. Basilevsky²², B.A. Ivanov²³, R. Kuzmin²², M.H. Carr²⁴, T.C. Duxbury²⁵, R. Greeley²⁶, J.W. Head²⁷, R. Kirk²⁸, T.B. McCord²⁹, S.W. Squyres³⁰, A. Inada³¹

1. TU Berlin, Photogrammetry and Cartography, EB 9, Straße des 17. Juni 135, D-10623 Berlin, Germany
2. DLR Berlin, Institute of Planetary Research, Rutherfordstrasse 2, D-12489 Berlin, Germany
3. TU Dresden, Institute of Cartography, Helmholtzstr. 10, D-01062 Dresden, Germany
4. Universität der Bundeswehr, Institut für Photogrammetrie und Kartographie, Werner-Heisenberg-Weg 39, D-85577 München, Germany
5. TU München, Photogrammetrie und Fernerkundung, Arcisstr. 21, D-80290 München, Germany
6. Istituto di Fisica Spazio Interplanetario (INAF), I-00133 Rome, Italy
7. Universität Hannover, Institut fuer Photogrammetrie und Ingenieurvermessungen (IPI), Nienburger Str. 1, D-30167 Hannover, Germany
8. Max-Planck-Institut für Aeronomie, Postfach 20, D-37191 Katlenburg-Lindau, Germany
9. TU Clausthal, Leibnizstr. 16, D-38678 Clausthal-Zellerfeld, Germany
10. Universität Köln, Institut für Geophysik und Meteorologie, A.-Magnus-Platz, D-50923 Köln, Germany
11. DLR Oberpfaffenhofen, Institute of Remote Sensing Methods, D-82234 Wessling, Germany
12. Westfälische Wilhelms-Universität, Institut für Planetologie, Wilhelm-Klemm-Str. 10, D-48149 Münster, Germany
13. ESA Research & Scientific Support Department, ESTEC, P.O. Box 299, NL-2200 AG Noordwijk, The Netherlands
14. TU Wien, Institut für Photogrammetrie und Fernerkundung, Gußhausstraße 27-29, A-1040 Wien, Austria
15. University of Helsinki, Observatory and Astrophysics Lab., PO Box 14, FIN-00014 Helsinki, Finland
16. Lab. de Géologie Dynamique de la Terre et des Planètes (ERS CNRS 0388), Univ. Paris-Sud (bât. 509), F-91405 Orsay Cedex, France
17. Department of Geomatic Engineering, University College London, Gower St., London WC1E 6BT, UK
18. Department of Earth Sciences, The Open University, Walton Hall, Milton Keynes, Buckinghamshire MK7 6AA, UK
19. Dipartimento di Scienze, Università d'Annunzio, Viale Pindaro 42, I-65127 Pescara, Italy
20. GRGS, Observatoire de Midi-Pyrénées, 14 Avenue Edouard Belin, F-31400 Toulouse, France
21. Astronomy Space Institute, University of Oulu, FIN-90401 Oulu, Finland
22. Vernadsky Institute of Geochemistry and Analytical Chemistry, Russian Academy of Science, Kosygin Street 19, Moscow 117975, Russia
23. Institute of Dynamics of Geospheres, Russian Academy of Science, Leninskij Prospect 38, Moscow 117979, Russia
24. US Geological Survey, Branch of Astrogeology, 345 Middlefield Rd., Menlo Park, CA 94025, USA
25. Jet Propulsion Laboratory, California Institute of Technology, MS 301-429, 4800 Oak Grove Drive, Pasadena, CA 91109, USA
26. Department of Geology, Arizona State University, Box 871404, Tempe, AZ 85287-1404, USA
27. Department of Geological Science, Brown University, Box 1846, Providence, RI 02912, USA
28. Astrogeology Team, US Geological Survey, 2255 N. Gemini Dr., Flagstaff, AZ 86001, USA
29. Planetary Science Division/SOEST, University of Hawaii, 2525 Correa Road, Honolulu, HI 96822, USA
30. Center for Radiophysics and Space Research, Space Sciences Building, Cornell University, Ithaca, NY 14853-6801, USA
31. Graduate School of Science and Technology, Kobe University, 1-1 Rokkodai Nada, 657-8501, Kobe, Japan
32. Institut d'Astrophysique Spatiale, CNRS, F-91405 Orsay, France

Table 3. HRSC Experiment Team.

FU Berlin: T. Denk, O. Fabel, S. van Gasselt, C. Georgi, S. Huber, G. Mygiakis, G. Neukum (PI), S. Preuschmann, B. Schreiner, S. Werner, W. Zuschneid;

DLR: T.Behnke, U. Carsenty, K. Eichentopf, J. Flohrer, B. Giese, K. Gwinner, E. Hauber, H. Hirsch, H. Hoffmann, A. Hoffmeister, R. Jaumann, D. Jobs, U. Köhler, K.-D. Matz, V. Mertens, J. Oberst, S. Pieth, R. Pischel, C. Reck, E. Ress**, D. Reifl, T. Roatsch, F. Scholten, G. Schwarz, I. Sebastian*, S. Sujew*, W. Tost, M. Tschentscher, M. Wählisch, I. Walter, M. Weiss, S. Weifle, M. Weiland, K. Wesemann;

Subcontractors: A. Zaglauer, U. Schönfeldt, K. Eckhardt, J. Krieger, D. Tennef, S. Govaers, A. Kasemann, M. Langfeld (DLR/Anagramm), E. Rickus (Levicki microelectronic), J. Schöneich (Jena-Optronik)

*left project, **retired

experiment objectives (Geosciences, Photogrammetry/Cartography, Spectrophotometry, and Atmosphere). The Instrument and Operations Teams, led by the Experiment Manager, include engineers and scientists from the DLR Institute of Planetary Research. The industrial contractor is Astrium (D), who built, assembled, tested and verified the HRSC for Mars-96.

The DLR Institute of Planetary Research provides a competent Instrument Team that was especially trained for a similar task in the Mars-96 HRSC experiment, covering the development of the sensor electronics, compression, electrical and optical ground support equipment, mission planning, instrument operations, target acquisition, calibration, data processing and data management. The DLR Institute is in charge of the assembly, verification and testing, for the system integration qualification, testing and calibration, and of the camera system integration with the spacecraft. Astrium (D) was responsible for the development of the Digital Unit and the integration and testing of the instrument subunits.

The PI and Co-Is are responsible for the scientific outcome of the experiment, and the Co-Is have individual responsibilities in areas such as calibration support, data processing, assessment of imaging scenarios, and photogrammetric data processing. All public relations efforts are a primary responsibility of the PI, who also has the primary data rights. The PI will actively support ESA in PR matters.

The Instrument Team includes engineers and scientists from the DLR Institute of Planetary Research and industry (all of whom have built and flown space instruments) and was recruited from the former HRSC Mars-96 Team. Similarly, the Operations Team from the DLR Institute of Planetary Research has extensive experience in running planetary missions and processing, archiving and the delivery of data products; it originally developed the HRSC ground data system on Mars-96.

OMEGA: Observatoire pour la Minéralogie, l'Eau, les Glaces et l'Activité

J-P. Bibring¹, A. Soufflot¹, M. Berthé¹, Y. Langevin¹, B. Gondet¹, P. Drossart², M. Bouyé², M. Combes², P. Puget², A. Semery², G. Bellucci³, V. Formisano³, V. Moroz⁴, V. Kottsov⁴ and the OMEGA Co-I team: G. Bonello¹, S. Erard¹, O. Forni¹, A. Gendrin¹, N. Manaud¹, F. Poulet¹, G. Poulleau¹, T. Encrenaz², T. Fouchet², R. Melchiori², F. Altieri³, N. Ignatiev⁴, D. Titov⁴, L. Zasova⁴, A. Coradini⁵, F. Capacionni⁵, P. Cerroni⁵, S. Fonti⁶, N. Mangold⁷, P. Pinet⁸, B. Schmitt⁹, C. Sotin¹⁰, E. Hauber¹¹, H. Hoffmann¹¹, R. Jaumann¹¹, U. Keller¹², R. Arvidson¹³, J. Mustard¹⁴ & F. Forget¹⁵

¹*Institut d'Astrophysique Spatiale (IAS), Bâtiment 121, F-91405 Orsay Campus, France*

Email: jean-pierre.bibring@ias.u-psud.fr

²*Laboratoire d'Etudes Spatiales et d'Instrumentation en Astrophysique (LESIA), Observatoire de Paris/Meudon, F-92195 Meudon, France*

³*Istituto di Fisica dello Spazio Interplanetario (IFSI-INAF), I-00133 Rome, Italy*

⁴*Institute for Space Research (IKI), 117810 Moscow, Russia*

⁵*Istituto di Astrofisica Spaziale (IASF-INAF), I-00133 Rome, Italy*

⁶*Department of Physics, University of Lecce, I-73100 Lecce, Italy*

⁷*Orsay Terre, F-91405 Orsay Campus, France*

⁸*Observatoire de Midi-Pyrénées, F-31000 Toulouse, France*

⁹*Laboratoire de Planétologie de Grenoble, F-38400 Grenoble, France*

¹⁰*Laboratoire de Planétologie et de Géodynamique, Université, F-44322 Nantes, France*

¹¹*DLR Institute of Planetary Research, D-12489 Berlin, Germany*

¹²*Max-Planck-Institute für Aeronomie, D-37191 Katlenburg-Lindau, Germany*

¹³*Department of Earth and Planetary Sciences, Washington Univ., St. Louis, MO 63130, USA*

¹⁴*Department of Geological Sciences, Box 1846, Brown University, Providence, RI 02912, USA*

¹⁵*Laboratoire de Météorologie Dynamique (LMD), IPSL, Université Paris 6, F-75252 Paris, France*

The OMEGA visible and near-IR mapping spectrometer will reveal the mineralogical and molecular composition of the surface and atmosphere of Mars through the spectral analysis of the diffused solar light and surface thermal emission. It will provide global coverage at medium resolution (2-5 km) for altitudes from 1500 km to 4000 km, and high-resolution (< 350 m) spectral images of selected areas.

OMEGA (Observatoire pour la Minéralogie, l'Eau, les Glaces et l'Activité) is a visible and near-IR mapping spectrometer, operating in the spectral range 0.38-5.1 μm . Combining imaging and spectrometry, it will study the mineralogical and molecular composition of the surface and atmosphere of Mars through the spectral analysis of the diffused solar light and surface thermal emission. OMEGA will provide global coverage at medium-resolution (2-5 km) for altitudes from 1500 km to 4000 km, and high-resolution (< 350 m) spectral images of selected areas, amounting to a few percent of the surface, when observed from near-periapsis (< 300 km altitude). OMEGA will:

1. Introduction

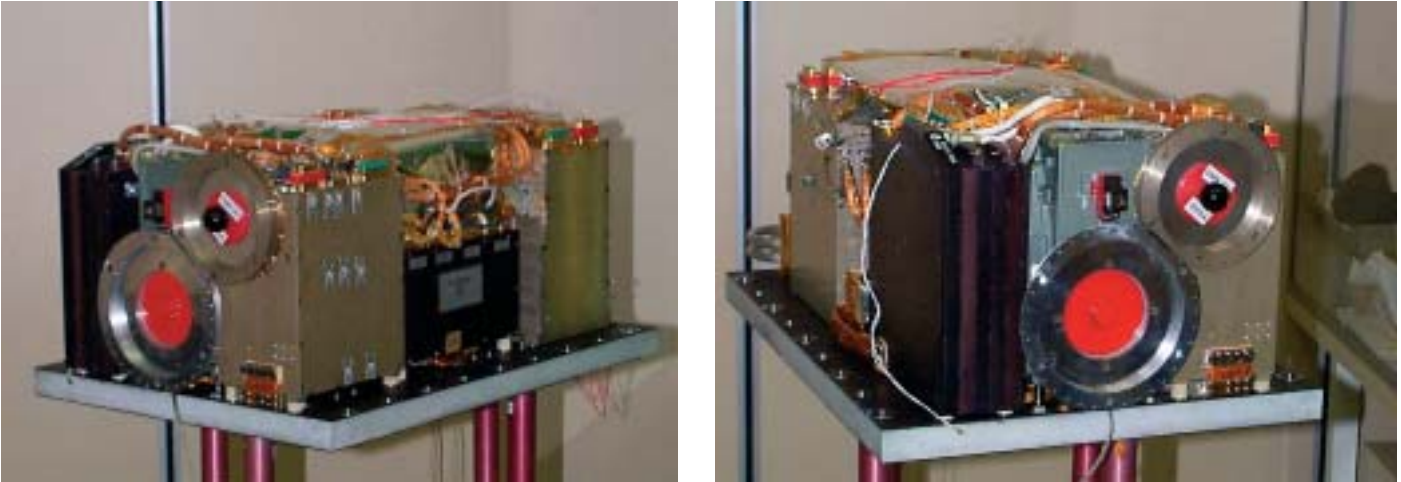


Fig. 1. The Flight Model of OMEGA.

- characterise the composition of surface materials, identifying the composition and the spatial and temporal distributions of the various classes of silicates, hydrated minerals, oxides and carbonates in soils and rocks, and of ices and frosts;
- study the spatial and temporal distributions of atmospheric CO₂, CO, H₂O and aerosols.

OMEGA will therefore address major questions concerning internal structure, geological and chemical evolution, past activity and present surface variegation. It will greatly contribute to understanding the evolution of Mars, ranging from geological timescales to seasonal variations. In particular, it will provide unique clues for understanding the H₂O and CO₂ cycles over martian history. It will play a major role in identifying areas of interest for future *in situ* exploration.

OMEGA was developed for the Russian Mars-96 mission. A spare unit was fully integrated and calibrated for that mission, and served as the basis for the Mars Express flight unit (Fig. 1). The major change was the complete redesign of the Main Electronics. OMEGA is managed as it was for Mars-96, between France, Italy and Russia, involving the following Institutions: IAS (Institut d'Astrophysique Spatiale, Orsay, France), LESIA (Laboratoire d'Etudes Spatiales et d'Instrumentation en Astrophysique, Observatoire de Paris/Meudon, France), IFSI (Istituto di Fisica dello Spazio Interplanetario, Rome, Italy) and IKI (Institute for Space Research, Moscow, Russia). The Principal Investigator and the Experiment Manager are both from IAS.

2. Scientific Objectives

The highly inclined (86°) and eccentric (0.6) orbit of Mars Express offers variable ground-track spatial sampling and latitude drift of the periapsis to produce near-global coverage. Consequently, OMEGA will achieve global coverage at medium resolution from medium altitudes, and will acquire high-resolution spectral images, for a fraction of the surface, with full selection flexibility, when operating close to periapsis. With its instantaneous field of view (IFOV) of 4.1 arcmin (1.2 mrad), global coverage should be attained in one martian year, at 2-5 km resolution, from altitudes of 1500-4000 km, while the highest resolution at periapsis should reach a few hundred metres.

2.1 Mineralogy

OMEGA will map the surface in order to identify the minerals of the major geological units. The goal is to study the evolution of Mars caused by internal activity, meteoritic impacts and interaction with the atmosphere.

Viking Orbiter and Mars Global Surveyor images indicate strong albedo variations down to subkilometre scales. Spectral images from the ISM mapping spectrometer on the Phobos mission in the near-IR also show large compositional variations at kilometre scales. Although large amounts of transported soil with uniform properties cover parts of the surface, all geological units exhibit part of their uncovered bedrock at these scales. OMEGA should therefore reveal the diversity of the global surface, inferring compositional variations directly related to planetary evolution.

In addition, OMEGA's high-resolution observations close to periapsis will:

- increase the sensitivity for detecting constituents with restricted geographical extension. For example, the continuing failure to detect carbonates might be directly linked to limited instrumental resolution. High-resolution snapshots of areas more likely to have accumulated sedimentary carbonates might lead to a positive detection of fundamental value;
- map mineralogical boundaries between geological units, in particular recent plains and older regions with a high density of impact craters, thus helping to understand Mars' hemispherical asymmetry;
- identify the composition of deposits and reveal possible gradients in the hydration minerals near features associated with fossil water flows;
- monitor features associated with wind transportation.

As for the spectral range and spectral sampling, OMEGA will operate within 0.38-5.1 μm using 352 contiguous spectral elements (spectels), 7-20 nm wide. It will identify, through their diagnostic spectral features, the major classes of silicates and other important minerals (such as carbonates), oxides and hydrates. Moreover, OMEGA is capable of measuring the content of OH radicals within the surface soil and rocks, so as to identify possible genetic relationships of hydrated minerals with major structural units such as volcanoes or canyons. In addition, fluidised ejecta around impact craters is likely to indicate that the underlying bedrock contains ice mixed with rocks. It is then plausible that ejecta experienced hydration. The spectral features of hydrated minerals (clays) are readily observable in the near-IR.

Alteration processes transformed martian mafic rocks into ferric-bearing minerals. In order to understand when this process took place (via volcanic activity, interaction with the atmosphere or flooding water), it is essential to relate these minerals with geological structures. OMEGA will detect these altered minerals through their signatures at 0.5-0.8 μm .

It is plausible that the martian CO_2 reservoir is dominated by carbonates. The detection and localisation of these minerals would be of key importance for understanding the past activity of the planet. OMEGA should unambiguously detect them, even at very low concentrations, through their absorption features at 3.4-4.0 μm .

2.2 Polar caps and frosts

OMEGA will determine the spatial evolution of the two polar caps, by observing CO_2 and H_2O , and the layered deposits. It will enable discrimination between the permanent (residual) ice, at both poles, and the seasonal frosts. It will thus monitor the cycle of sublimation/condensation, and identify the relative contributions of the two major atmospheric constituents as a function of time and location. OMEGA will also identify dust within the polar ices; its composition indicates its origin and thus reveals the transportation processes.

At lower latitudes, the condensation of frost will be mapped over time, for both CO_2 and H_2O . In addition, OMEGA is capable of detecting minor species containing carbon or nitrogen; no such molecules have yet been observed, and their discovery would be of major interest for understanding the overall chemical evolution.

If there are permafrost layers, they may appear at the surface in a few regions. OMEGA would detect such icy-rich rocky sites. By identifying the borders of these underlying permafrost layers, the global distribution of ice within the crust can be evaluated, complementing the subsurface sounding by the MARSIS radar instrument

of Mars Express. Identification of the sites and phases where most of the water resides is a major goal, in particular when searching for the most favorable sites for possible past organic activity, and assessing water resources for future exploration.

2.3 Atmospheric evolutionary processes

OMEGA is well-suited for monitoring some of the atmospheric parameters with key roles in martian meteorology: total pressure, column densities of the H₂O and CO minor constituents, content of aerosols, and, in some cases, vertical temperature distribution. It complements the PFS and SPICAM investigations, with lower spectral sampling but at much higher spatial resolution. The ISM/Phobos imaging spectrometer, which mapped part of the martian surface in February-March 1989, demonstrated the ability of IR spectroscopy, even at low spatial sampling (21 km), to retrieve the altimetry of Mars (100 m vertical resolution) accurately. The observations of CO₂ absorption bands with OMEGA will provide, as did ISM/Phobos, a measurement of the ground pressure. As the altimetry of Mars is now of higher quality, thanks to continuing MOLA/Mars Global Surveyor measurements, OMEGA will study local pressure variations, as induced by baroclinic wave pattern at mid-latitudes, by passing over the same regions at different times. The expected variations of a few percent in atmospheric pressure will be measured easily by OMEGA (the design goal is 1% in accuracy), in the absence of global dust storms.

OMEGA will monitor the CO and H₂O partial pressure for each resolved pixel. The spatial distribution of these minor constituents is still a field of great interest, following the ISM/Phobos discoveries of unexpected variations in their mixing ratios from volcano areas and surrounding plains.

OMEGA has four major advantages over ISM/Phobos for atmospheric studies:

- about double the spectral resolving power. This is important for improved retrieval of the H₂O and CO total column densities;
- extension of the spectral range up to 5.1 μm. The 3.2-5.1 μm range accesses the thermal emission of the martian disc for most of the dayside regions (surface temperature higher than about 240K). It will be possible to infer the thermal profile from the inversion of the strong CO₂ ν₂ band at 4.3 μm. In addition, new information, complementing that obtained from the diffuse solar spectrum, will be obtained on the CO abundance from its absorption bands at 4.7 μm;
- an IFOV 2.9 times higher, leading to a spatial sampling 70 times higher at periapsis;
- greatly extended planetary coverage, because of the near-polar orbit instead of the equatorial orbit of the Phobos mission.

Another important atmospheric parameter is the aerosol content. It has a key role in the general circulation, because the dust modifies the radiative properties of the atmosphere through its heating and cooling rates. As the atmospheric dust content shows very strong variations, both on a local scale and over a seasonal cycle, continuous monitoring is as necessary as knowing the local thermal profile. The analysis of ISM/Phobos data has shown that the aerosol abundance can be estimated from the slope of the reflected component of the spectrum. The same information will be derived by OMEGA over the whole martian disc. Moreover, OMEGA will be able to identify the aerosols through their composition (silicate and/or icy-rich particles), and assess their distribution with altitude and time, in addition to their optical properties. In particular, these measurements can be correlated with surface and climatic seasonal properties, towards an integrated (surface, atmosphere, aerosols) database of unique meteorological value.

Observations by the Short Wavelength Spectrometer (SWS) of ESA's Infrared Space Observatory (ISO) provided a high-quality IR spectrum of Mars, which is helping to prepare for OMEGA observations. In particular, it demonstrated the feasibility of retrieving dust opacity from the strong 2.7 μm CO₂ band. The detection

of faint fluorescence emission in CO₂ at 4.3 μm by ISO provides another objective: OMEGA will confirm and study the spatial variation of these emissions, which give information on the highest part of the stratosphere.

The capabilities of OMEGA can be summarised as:

- imaging: 128 contiguous IFOVs of 1.2 mrad (4.1 arcmin) each, corresponding to < 350 m surface sampling at periapsis;
- spectral: 352 (or 400, depending on the summing mode chosen for the visible channel) contiguous spectels to acquire the spectral range 0.38-5.1 μm for each resolved pixel, with 96 (or 144) spectels to cover the 0.38-1.05 μm range, with a spectral sampling of 7 nm (or 4.5 nm), 128 spectels to cover 0.93-2.73 μm, with 13 nm spectral sampling, and 128 spectels to cover 2.55-5.1 μm, with 20 nm sampling;
- photometric: S/N > 100 over the full spectral range, allowing the identification of absorptions and thermal variations to the percent-level.

The high sensitivity of OMEGA and its high spectral and spatial sampling capabilities should allow the unambiguous detection and compositional identification, on each resolved pixel, of the surface minerals and their OH/H₂O content, the atmospheric major and minor constituents, and the aerosols. For example, if there are carbonates at concentrations of a few percent, they should be readily detected. At the same spatial scale of a few hundred metres, the surface temperature will be mapped with an accuracy of better than 1K.

Such performance will provide an unprecedented harvest of results in a wide variety of Mars and planetary science fields such as: geology, tectonic and chemical planetary evolution, climatology and meteorology, atmospheric processes and exobiology.

4.1 Instrument concept

OMEGA is a mapping spectrometer, with coaligned channels working in the 0.38-1.05 μm visible and near-IR range (VNIR channel) and in the 0.93-5.1 μm short wavelength IR range (SWIR channel). The data products constitute three-dimensional (x, y, λ) 'image-cubes', with two spatial and one spectral dimensions.

The VNIR channel uses a bi-dimensional CCD detector, operating in a pushbroom mode. The telescope's focal plane provides one cross-track line corresponding to the entire 8.8° FOV, defined by an entrance slit; the second dimension of the image is provided by the motion of the spacecraft. Each line is spectrally dispersed along the columns of the array, the slit being imaged through a concave holographic grating.

The SWIR channel operates in the whiskbroom mode. Each imaged pixel is focused by an IR telescope on a slit, followed by a collimator. The beam is then split towards two separated spectrometers, to acquire the IR spectrum of each resolved pixel on to two InSb linear arrays of 128 spectels each, working at 0.93-2.73 μm and 2.55-5.1 μm. A scanning mirror in front of the telescope provides cross-track swaths 16-128 pixels wide, for a maximum FOV of 8.8° (matching the VNIR FOV). The spacecraft motion provides the second spatial dimension. The images are built as shown in Fig. 5. Each array is cooled to 70K by a dedicated cryocooler, while the entire spectrometer is cooled to 190K by a conductive link to a passive radiator.

The typical IR integration time, defined by the spacecraft ground-track velocity and the spatial sampling chosen, is 2.5 ms or 5 ms. The corresponding VNIR integration times are 50-200 ms, depending on the swath width (and hence the altitude). With such integration times, an S/R of > 100 is specified over the entire spectral range.

OMEGA comprises two distinct units, coupled by a 0.7 kg electrical harness:

- a Camera unit (OMEGA Camera, or OMEC), carrying the VNIR and SWIR

3. OMEGA Performance

4. Instrument Description

Fig. 2. VNIR optical layout.

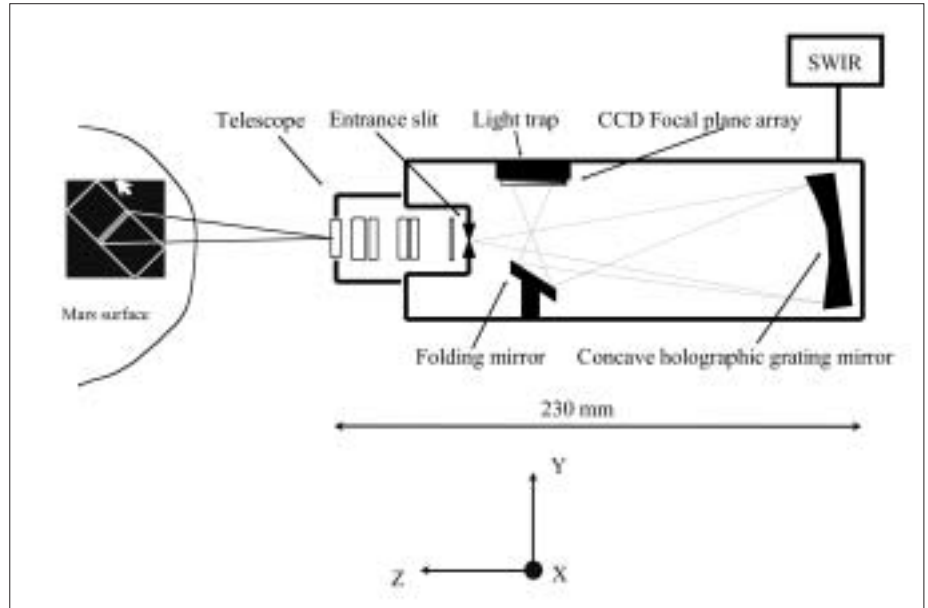
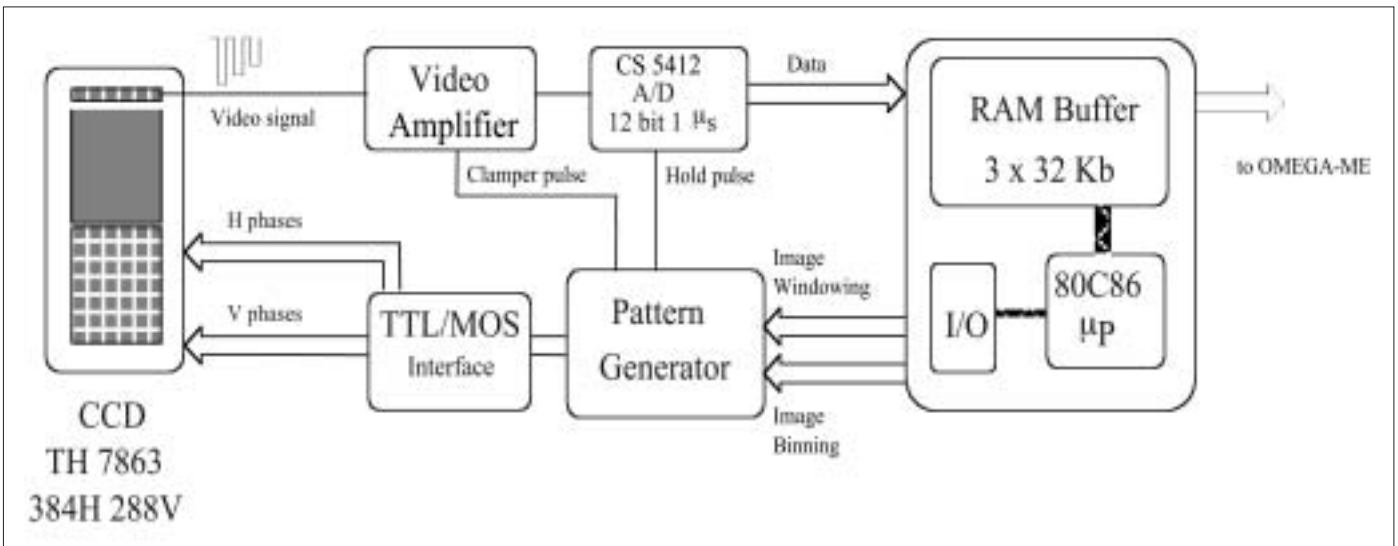


Fig. 3. VNIR electronics.



spectrographs, their associated electrical devices, and an electronics assembly for controlling the camera. All units are integrated on a common baseplate. The mass and size of OMEC are, respectively, 23.5 kg, and 290x180x150 mm;

- a Main Electronics module (OMEGA-Me, or OMEM), for the data processing and the general management of the instrument. Mass is 4.6 kg.

OMEGA's power requirement is 27.4 W during the ~2 h cooling of the focal planes, and 47.6 W peak power during observation.

4.2 VNIR

VNIR comprises two optical subsystems: a focusing telescope with its focal plane on a slit, and a spectrometer to spread the slit image in the spectral dimension. It provides image data in the spectral range 0.38-1.05 μm, achieving a maximum spatial sampling of 0.4 mrad and a maximum spectral sampling of 50 Å.

The optical layout and major components of VNIR are summarised in Fig. 2 and

Table 1. OMEGA's VNIR characteristics.

<i>Element/Parameter</i>	<i>Description/value</i>
Telescope	Double Gauss objective
Field of view	8.8°
Spectrometer	concave holographic grating mirror
Detector	CCD Thomson TH 7863 384×288 pixels
Detector size	8.8×6.6 mm
Pixel size	23×23 μm
Spectral range	0.38-1.05 μm
Spectral resolution	70-200 $\lambda/\Delta\lambda$
Dynamics	12-bit

Table 2. VNIR telescope and spectrometer optical parameters.

Aperture	15.6 mm
Focal length	57.6 mm
Field of view	8.8°
F number	3.7
Scale factor	1°/mm
Entrance slit width	50 μm
Grating type	concave holographic grating mirror
Grooves/mm	65
Dispersion	1071 Å/mm
Wavelength range	0.38-1.05 μm
Grating size	40 x 10 mm
Material	Silica
Manufacturer	Jobin Yvon

Table 1. A refractive telescope focuses the image on to a slit placed on the Rowland circle of an aberration-corrected concave holographic grating mirror. This element reflects and disperses the light on a CCD detector tangent to the Rowland circle. The detector used is the TH7863 frame-transfer CCD produced by Thomson. The grating mirror creates a flat image at the focal plane, matching the flat detector matrix to the grating without other optical components. Each row of the CCD frame contains an image of the slit at a given wavelength, while each column contains the spectrum of a point along the slit. The bi-dimensional image of the surface is obtained by the pushbroom technique, in which the spacecraft's movement along its orbit scans the slit across the planetary surface. The electrical signal from the detector is amplified and then digitised by a fast 12-bit analogue/digital converter (ADC). Following conversion, all data are processed within the OMEGA Main Electronics module.

In order to decrease the detector noise, the VNIR channel is cooled to 190K by conduction to the SWIR mechanical unit.

Refractive optics are preferred over reflective because of the large (8.8°) field of view requirement. The telescope has a 6-element objective similar to that of a modern commercial photographic camera. The shape of the elements and the types of optical glass were chosen to obtain the best chromatic aberration corrections over the entire spectral range. The last element serves as a field lens which matches the entire objective with the grating to avoid light losses. To avoid stress in the lenses at the working temperature, the two doublets are not cemented. The two glasses, FK54 and fused silica, have very different expansion coefficients of $8 \times 10^{-6} \text{ K}^{-1}$ and $0.55 \times 10^{-6} \text{ K}^{-1}$ at room temperature. The entrance aperture of 15.6 mm is defined by a diaphragm between the two doublets.

An aberration-corrected concave holographic grating is placed 142.7 mm from the entrance slit (which is in the focal plane of the telescope). The grating is tilted to form the spectrum at an angle of roughly 6° from the optical axis. This angle does not allow CCD insertion near the entrance without beam obscuration, so a folding mirror deflects the beam toward the side of the assembly, where the CCD can be mounted with ample clearance. The zero-order spectrum, at 4.5° from the folded optical axis (lying in the y-z plane), is directed into a light trap to prevent degradation of the image. The first-order spectrum ranges in angle from 6° at 0.35 μm to 10° at 1.05 μm. The second- and higher order spectra can, in principle, also degrade the data. Their contributions depend both on the grating efficiency and the spectral distribution of the incident radiation. For this reason, a dedicated filter is mounted in front of the detector. The concave, spherical, holographic grating in a Rowland mounting – where the entrance slit and the spectrum are on radii of curvature of the grating – makes the spectrometer compact, light and simple. In

fact, no collimator or camera lens is required and the spectrometer has only one element. Moreover, the focal plane image is flat, matching the planar CCD sensors. Since the concave holographic grating is obtained by recording a perfect optical pattern with groove spacing absolutely constant, it has no ghosts. Stray light is also at a much lower level than the best ruled gratings. Therefore, concave holographic gratings generally have a much higher signal to noise ratio than classically ruled gratings.

The optical performances were computed by ray tracing. In the focal plane, the spot diagram is about the pixel size ($23 \times 23 \mu\text{m}$). For off-axis propagation (4.4°), the total spot size is about 2 pixels in the sagittal direction (the z direction, see Fig. 2). More precisely, on axis and at $0.7 \mu\text{m}$, 98.8% of the energy falls within a $23 \times 23 \mu\text{m}$ pixel; at 4.4° off-axis and $0.4 \mu\text{m}$, 74% of the energy falls within a CCD element. When the light propagates off-axis, the spot size is smaller for the shorter wavelengths.

The block diagram of the VNIR electronics is shown in Fig. 3. The Pattern Generator (PG) determines the CCD integration time, and generates the timing signals necessary to transfer an image from the light-sensitive area to the masked zone and then to the output shift register of the CCD. The output of the CCD is then amplified and converted by a fast 12-bit ADC under control of the PG.

The timing of the instrument imposes a relatively high frequency for CCD operation. In fact, depending on the distance from the planet and hence on the spacecraft speed, the time T_R between consecutive frames can be chosen as: 50, 100, 200, 400 or 800 ms. During the T_R period the integration, readout and data transmission processes must occur. To save time, integration and transmission of the previous frame are overlapped. Because the maximum data value that can be transmitted during T_R is limited to 12 288 bytes, it is not possible to read the total frame of 384×288 pixels, corresponding to 110 592 bytes. We are forced to read only a subframe, or to reduce the number of pixels by summing them on chip. The combination of different scientific requirements, integration times and hardware limitations led us to the definition of 40 operation modes, which can be selected through commands sent to the spacecraft, ranging from the nominal (spatial \times spectral) mode (128×96 with summation of 3×3 pixels), to the high spectral resolution mode (64×144), to the high-speed mode (16×96). Summation along columns and rows decreases the spatial and spectral resolution, but increases signal-to-noise ratio considerably. The implementation of mode 16×74 is the most critical owing to the short time available to complete all the operations ($T_R = 100$ ms). For this reason, the Pattern Generator provides two values for the pixel readout frequency: $f_{slow} = 500$ kHz when the pixel voltage has to be digitised and $f_{fast} = 4$ MHz when the pixel is simply read from the CCD output register without any digital conversion.

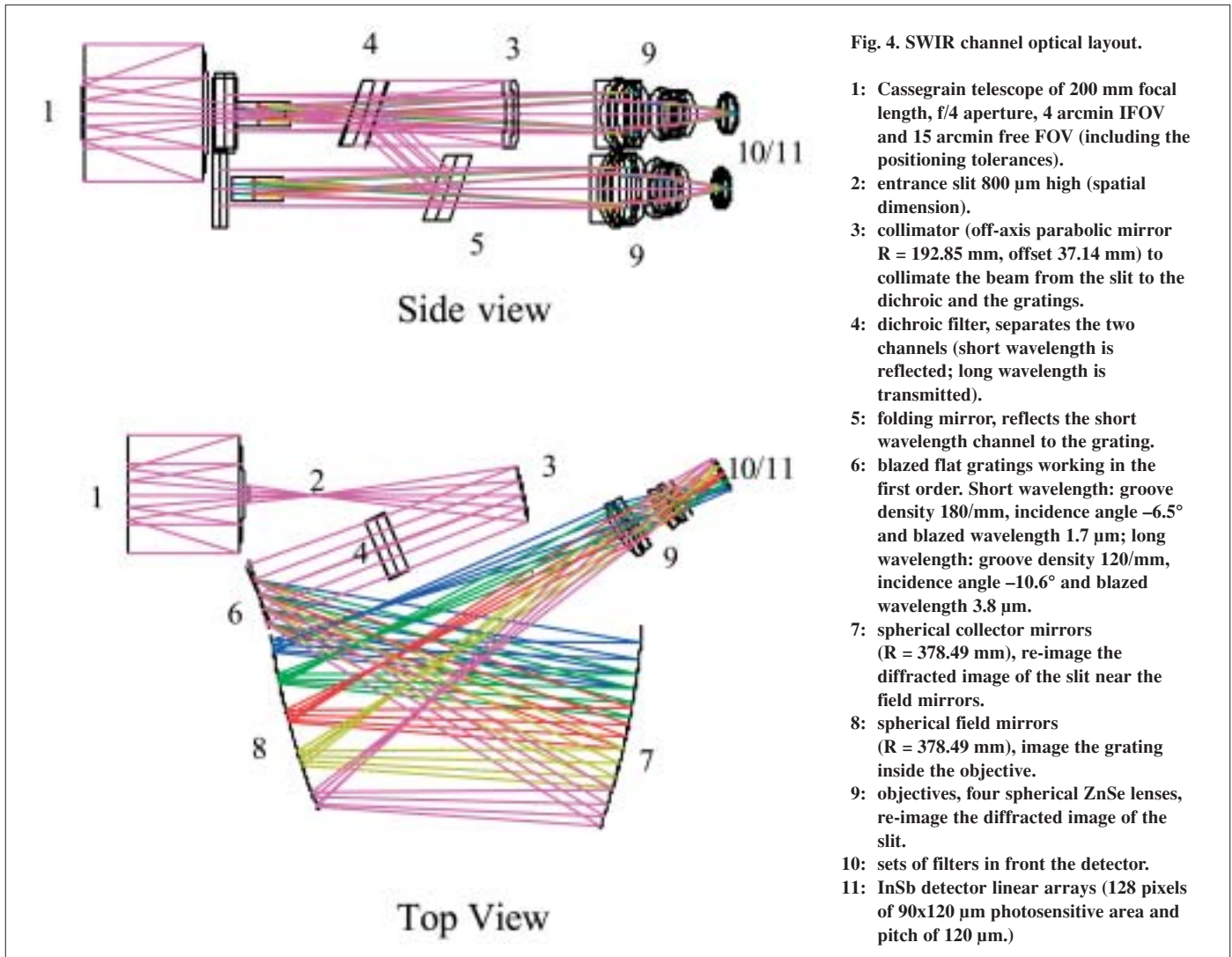
4.3 SWIR

The SWIR channel consists of a telescope and its fore-optics, a beam splitter and two spectrometers, each with its detector array actively cooled (Fig. 4).

The telescope is a Cassegrain of 200 mm focal length, an $f/4$ aperture, leading to a 1.2 mrad (4.1 arcmin) IFOV and a 15 arcmin free FOV (including the positioning tolerances). The distance between the primary and secondary mirrors is 51 mm; between the secondary mirror and the image plane is 82 mm.

In front of the telescope, a fore-optics system has the primary goal of providing a cross-track scanning of the IFOV. It includes two mirrors, moving and fixed. The total scanning angle is $\pm 4.4^\circ$ (FOV = 128 IFOV), and is adjusted to the OMEGA viewing direction. The control of the scanning mechanism is performed by a dedicated FPGA-based electronic subsystem.

Focused by the telescope on an entrance slit, through a shutter, the beam is first collimated, then separated, by a dichroic filter with its cut-off wavelength at $2.7 \mu\text{m}$ towards two spectrometers, operating at $0.93\text{-}2.73 \mu\text{m}$ and $2.55\text{-}5.1 \mu\text{m}$. Each spectrometer includes a blazed grating working at its first order, and an optical



reflective system, then a field mirror and a refractive refocusing system that gives a large aperture on the detection block ($f/1.6$). It images the spectrum on to a 128-element InSb linear array, cooled to $< 80\text{K}$, and multiplexed by a charge transfer device. Sets of filters are implemented in front of the detector to reject the contribution of other orders from the grating.

The InSb photodiodes were manufactured by SAT (F). The dimensions of each photosensitive element is 90×120 μm , with a pitch of 120 μm . All elements of the focal planes are hybridised on a ceramic with two electric circuit layers to connect the elements. The ceramic is glued to a titanium baseplate and covered by a titanium frame that holds the filters.

An internal calibration source controls potential shifts of the overall spectrometer transmission and calibrates the relative response of each pixel. The tungsten lamp, operated as a black body, is heated to different temperatures. The calibration beam is reflected towards the spectrometer by diffusion on the back side of the entrance slit.

SWIR requires accurate thermal control, at three levels:

- the electronics and the cryocoolers heads are internally linked by heat pipes and coupled to a 280K radiator.

Table 3. Typical OMEGA observing sessions.

Maximum altitude (km)	300	1500	4000
True anomaly	0	60	95
Pixel size	< 360 m	< 1.8 km	< 4.8 km
Track width (px)	16	64	128
Track width (km)	5-7	60-120	300-600
Track length (px)	~ 7500	~ 2000	~ 1000
Track length (km)	~ 3000	~ 3000	~ 3000
Session duration (min)	~ 12	~ 12	~ 24
Data volume (Mbit)	~ 200	~ 200	~ 200

Table 4. OMEGA total data budget.

<i>Investigation</i>	<i>Global Mapping (100% coverage)</i>	<i>High-Resolution (5% coverage)</i>	<i>Seasonal Variation (5% coverage)</i>
Required number of non-overlapping contiguous sessions	250	500	500
Total data volume	~ 50 Gbit	~ 100 Gbit	~ 100 Gbit

- the spectrometer must be cooled to $\leq 190\text{K}$, to minimise the thermal background and to enable the detectors to reach their operational temperature ($< 80\text{K}$). This is achieved by copper links to a spacecraft radiator;
- the IR detectors must be cooled to $< 80\text{K}$, controlled with an accuracy of better than 0.1K . This is done by using copper heat links to two cryocoolers, one for each array: Inframetrics 13000-series integral Stirling cycle coolers controlled by dedicated electronics. Their guaranteed lifetimes are $> 2500\text{ h}$;

4.4. OMEGA Main Electronics

The main electronics power and control the instrument, acquire and compress all scientific data on-line, and interface with the spacecraft telecommand/telemetry system. The entire system is cold-redundant. Within OMEga-Me, the Command and Data Processing Unit (CDPU) has the following tasks:

- acquisition of all scientific data from VNIR and SWIR;
- formatting for realtime data compression;
- wavelet-based data compression, followed by formatting of processed data;
- reception and formatting of housekeeping data;
- forwarding of all data to the spacecraft telemetry system.

The CDPU is based on a TSC21020 Temic processor, and integrated, together with a 6 Mbyte SRAM, into a 3D-packaged highly miniaturised cube, inherited from the ÇIVA instrument aboard the Rosetta mission.

5. Ground Calibration

OMEGA was fully calibrated before its delivery and integration with the spacecraft. The calibration plan included spectral, geometric, photometric, sample and functional tests, with the following goals:

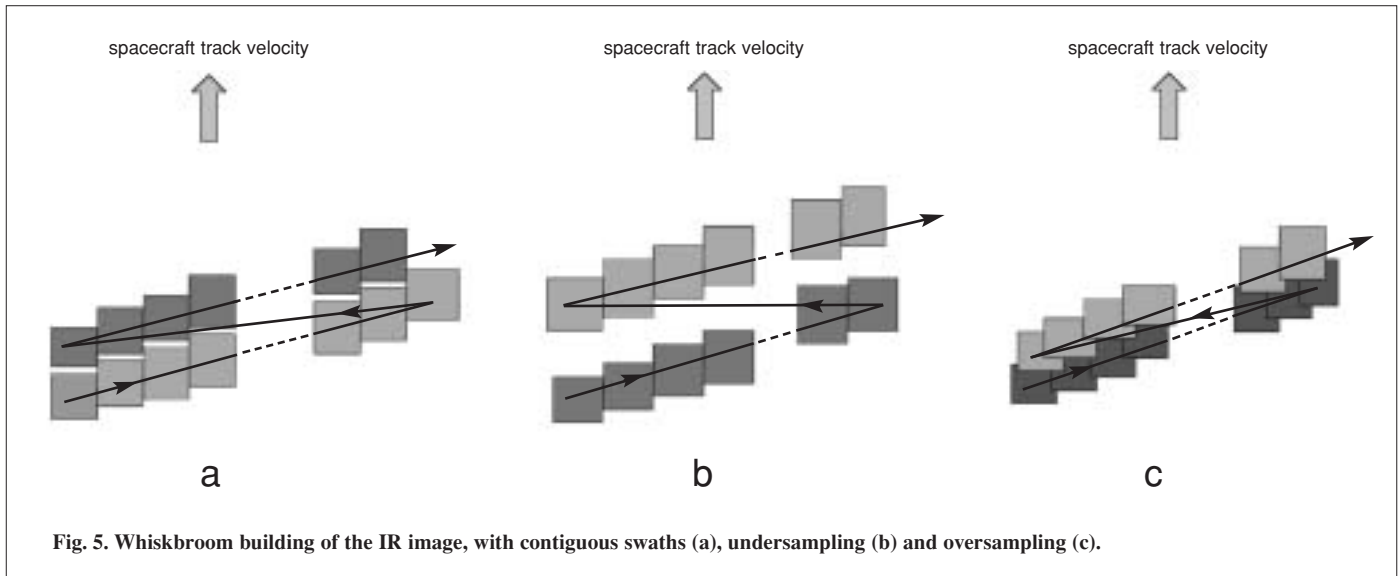


Fig. 5. Whiskbroom building of the IR image, with contiguous swaths (a), undersampling (b) and oversampling (c).

- spectral calibration: determination of the spectral centre position and width of each spectel, with an accuracy of better than 1/5 of the spectel width, within the entire FOV;
- photometric calibration: determination of the Data Number (DN) value of each spectel for a given incident power. Accuracy: better than 1% spectel-to-spectel (relative) and better than 20% in absolute terms;
- geometric calibration: determination of the IFOV and FOV of each channel, their spatial response in azimuth and declination, and their relative coalignment;
- sample calibration: determination of the actual response of OMEGA when imaging targets with minerals and mixtures of known composition;
- functional calibration: determination of the instrumental response for all programmable parameters and modes.

A dedicated calibration facility was built at IAS, comprising two major components:

- an ultra-clean vacuum chamber, where OMEGA was installed on a stage remotely movable in two angular directions around the entrance pupil of the instrument. The chamber's thermal screens and regulated platforms cool the spectrometers to any temperature within the range 300-150K, while maintaining OMEGA-Me at a different and higher temperature. The incident beam, from the optical bench, passes through a large sapphire window to illuminate OMEGA;
- an optical bench, purged with dry nitrogen, containing a 4 m focal length and 400 mm-diameter collimator, imaging one of the following four sources on to OMEGA: a monochromator, a black body with temperature stabilised up to 1200°C, a point source (1/3-pixel) illuminated by a high-temperature (2500°C) ribbon black body, and a cold black body (down to 70K).

During calibration, OMEGA was operated through its Electrical Ground Support Equipment (EGSE) and spacecraft simulator, while the facility (vacuum chamber and optical bench) was controlled by a dedicated computer, acquiring all relevant parameters (monochromator wavelength, angular positions of the moving stage, temperatures), and acting as the slave in a master/slave configuration with the EGSE, ensuring synchronous acquisition with OMEGA scientific data.

6. Operations

Given the global Mars Express orbital and downlink constraints within the nominal (one martian year) duration of operations, the OMEGA science goal of complete planetary coverage cannot be achieved at the highest possible resolution, obtained close to periapsis. Thus, the OMEGA investigation is divided into three global modes:

- global (100% complete) coverage at 2-5 km spatial resolution, acquired from altitudes of 1500-4000 km;
- high-resolution (< 350 m) coverage of a fraction (> 5%) of the surface, with high flexibility of site selection (longitude and latitude), acquired close to periapsis;
- seasonal monitoring of surface and atmospheric composition at given locations, with wide flexibility of site selection (longitude and latitude).

These investigations will be conducted using different operational and instrumental modes. With a fixed IFOV, OMEGA has the flexibility to accommodate operations from a variety of altitudes, through a number of acquisition times, swath widths and data compression modes. As the IR maps will be built by contiguous cross-track swaths (Fig. 5) in a wiskbroom mode, the displacement of the spacecraft track during the acquisition of a swath should be as close as possible to the pixel size (5a) in order to avoid both undersampling (5b) and oversampling (5c).

At periapsis, where the orbital ground velocity is about 4 km s^{-1} , the nadir track shifts by one IFOV in less than 100 ms. This duration corresponds to acquiring cross-track swaths 16 pixels wide, with a nominal integration time of 5 ms. Thus, the nominal OMEGA high-resolution mode, operated from altitudes of < 350 km, will build maps 16 pixels wide. For medium-resolution modes, 32-pixel swaths will be chosen when operating from altitudes of 350-700 km, and 64 pixels from altitudes up to about 1500 km. From 1500 km to 4000 km, OMEGA will provide global coverage: it will use the full 128-pixel FOV, for which one swath is acquired, with nominal integration time, in 640 ms. However, at these altitudes, the ground-track velocity is less than 2 km s^{-1} , and the spacecraft ground-track shifts by one pixel (one IFOV) in 1-2.5 s. In order to avoid oversampling, OMEGA will sum several (up to 4) contiguous swaths. This is illustrated in Table 3, indicating three typical session sizes, with the assumption of a (pessimistic) compression factor of 3, and spatial summing of two contiguous swaths for the global coverage mode. The non-overlapping sessions required to achieve the three objectives quoted above are covered in Table 4. These budgets are based on building maps with non-overlapping sessions and performing limb observations. These require the availability of dedicated spacecraft pointing modes:

- nadir pointing, either along the track, or with a constant off-track angle (up to 30°), for all surface mappings;
- 3-axis inertial pointing, for a few atmospheric studies and some specific surface observations.

The data, as soon as they are received at ESOC on the Data Distribution System (DDS) are transferred to IAS, on a dedicated server, where they are decompressed, PDS formatted and archived. Each cube of data is submitted to a quick-look analysis (for both scientific data and housekeeping) to validate its completeness and the quality of the downloaded data. In parallel, orbital and spacecraft attitude parameters are received from ESOC via ESTEC, out of which geometric cubes are built, first as predicted values and then after proper reconstruction. These cubes are in-house PDS-formatted in a manner identical to the scientific ones, to enable a reconstruction of the mapped areas on the martian surface.

The entire OMEGA team has direct, full and protected access to the data server at IAS, on which a variety of auxiliary files (such as calibration files) are available. In accordance with ESA policy, the data processing is restricted to the team during the proprietary period.

For the distribution and archiving strategy after this period, OMEGA will comply with the overall ESA scientific data policy. The goal is to prepare a final level of data set, constituting: the raw compressed data, the decompression procedures, the decalibrated data for each pixel at the surface of Mars, referred to a (latitude, longitude) frame, and the complete spectrum from 0.38 μm to 5.1 μm , in physical units. This geometric reconstruction will include the instrumental and spacecraft corrections, thus allowing image-cubes to be generated. These calibrated image-cubes will be formatted according to the Planetary Data System (PDS) standard for distribution and archiving, through the ESA Planetary Science Archive. The actual storage medium will depend on availability at the time of operations; at present, erasable/rewritable CD-ROMs and DVDs are being considered.

MARSIS: Mars Advanced Radar for Subsurface and Ionosphere Sounding

G. Picardi¹, D. Biccari¹, R. Seu¹, J. Plaut², W.T.K. Johnson², R.L. Jordan², A. Safaeinili², D.A. Gurnett³, R. Huff³, R. Orosei⁴, O. Bombaci⁵, D. Calabrese⁵ & E. Zampolini⁵

¹*Infocom Department, 'La Sapienza' University of Rome, Via Eudossiana 18, I-00184 Rome, Italy
Email: aclr@aerov.jussieu.fr*

²*Jet Propulsion Laboratory, 4800 Oak Grove Drive, Pasadena, CA 91109, USA*

³*Department of Physics and Astronomy, University of Iowa, Iowa City, IW 52242-1447, USA*

⁴*CNR/IAS, Planetology Department, Via del Fosso di Cavaliere, I-00133 Rome, Italy*

⁵*Alenia Spazio S.p.A., Via Saccomuro 24, I-00131 Rome, Italy*

This paper describes the science background, design principles and the expected performance of the Mars Advanced Radar for Subsurface and Ionosphere Sounding (MARSIS), developed by a team of Italian and US researchers and industrial partners to fly on the ESA Mars Express orbiter. The unique capability of sounding the martian environment with coherent trains of long-wavelength wide-band pulses, together with extensive onboard processing, will allow the collection of a large amount of significant data about the subsurface, surface and ionosphere. Analysis of these data will allow the detection and 3-D mapping of subsurface structures down to several kilometres below the surface, the estimation of large-scale topography, roughness and reflectivity of the surface at wavelengths never used before, and the production of global and high-resolution profiles of the ionospheric electron density (day and night). Finally, the MARSIS frequency-agile design allow the sounding parameters to be tuned in response to changes in solar illumination conditions, the latitude and other factors, allowing global coverage to be achieved within the Mars Express baseline orbit and mission duration.

The set of scientific objectives for MARSIS was defined in the context of the objectives of the Mars Express mission and within the more general frame of the open issues in Mars studies. The primary objective is to map the distribution of liquid and solid water in the upper portions of the crust of Mars (Carr, 1996). Detection of such water reservoirs will address key issues in the hydrologic, geologic, climatic and possible biologic evolution of Mars, including the current and past global inventory of water, mechanisms of transport and storage of water, the role of liquid water and ice in shaping the landscape of Mars, the stability of liquid water and ice at the surface as an indication of climatic conditions, and the implications of the hydrologic history for the evolution of possible martian ecosystems.

Three secondary objectives are also defined for MARSIS: subsurface geologic probing, surface characterisation and ionosphere sounding. The first is to probe the subsurface of Mars, to characterise and map geologic units and structures in the third dimension. The second is to acquire information about the surface: to characterise the surface roughness at scales of tens of metres to kilometres, to measure the radar reflection coefficient of the upper surface layer, and to generate a topographic map of the surface at approximately 10 km lateral resolution. The final secondary objective is to use MARSIS as an ionosphere sounder to characterise the interactions of the

1. Introduction

solar wind with the ionosphere and upper atmosphere of Mars. Radar studies of the ionosphere will allow global measurements of the ionosphere electron density and investigation of the influence of the Sun and the solar wind on the ionosphere.

2. Composition Models of the Upper Layers

In this section, models of the composition of the upper layers of Mars are described, based on the recent literature and classical Mars studies.

The state and the distribution of H₂O in the martian megaregolith are a function of crustal thermal conductivity, geothermal heat flow, ground-ice melting temperature and the mean temperature at the surface (this last is the only quantity varying systematically with latitude). These factors determine the thickness of the cryosphere, which is the layer where the temperature remains continuously below the freezing point of H₂O. Although the mean annual surface temperatures vary from about 220K at the equator to about 155K at the poles, the annual and secular surface temperature variations determine periodic freezing and melting of any H₂O present down to a depth of about 100 m. The cryosphere extends below this 'active layer' to the depth where the heat flux from the interior of the planet raises the temperature above the melting point of ground-water ice. Below the cryosphere, H₂O in the pore space can only be in liquid form.

Estimates of the depth of the melting isotherm range from 0 km to 11.0 km at the equator, and from 1.2 km to 24 km at the poles, according to different values of the parameters found in the literature. Liquid water may persist only below such depths; moreover, liquid water would diffuse towards the bottom of the regolith layer and thus could lay further below, although local conditions may still offset the above considerations. A nominal depth in the range 0-5000 m is assumed.

Estimates of the desiccation of the martian megaregolith, via ice sublimation in the cryosphere, yield values of the depth at which ice is still present ranging from zero to several hundred metres. A nominal depth in the range 0-1000 m is assumed.

The interfaces most likely to be detected by MARSIS, being closer to the surface, are the contact between the desiccated regolith and the permafrost, and the interface between a subterranean reservoir of liquid water and the cryosphere. These are the basic scenarios for the detection and identification of water-related interfaces in the martian subsurface.

The structure of the martian crust is the result of many different processes, given the complex geological history of the planet. However, it appears that the most significant on a global scale are impact processes, which have played a major role in the structural evolution of the crust by producing and dispersing large quantities of ejecta, and by fracturing the surrounding and underlying basement. It is estimated that, over the course of martian geologic history, the volume of ejecta produced by impacts was sufficient to have created a global blanket of debris up to 2 km thick. It is likely that this ejecta layer is discontinuously interbedded with volcanic flows, weathering products and sedimentary deposits, all overlying a heavily fractured basement.

A 50% surface porosity of the regolith is consistent with estimates of the bulk porosity of martian soil as analysed by the Viking Landers. A value this high requires that the regolith has undergone a significant degree of weathering. A lower bound for the surface porosity can be taken at 20%, derived from the measured porosity of lunar breccias. An equation of the decline of porosity with depth owing to the lithostatic pressure can be obtained by adapting a similar equation devised for the Moon, based on seismic data unavailable for Mars. The equation is of the form:

$$\Phi(z) = \Phi(0) e^{-\frac{z}{K}} \quad (1)$$

where $\Phi(z)$ is the porosity at depth z , and K is a decay constant that, for Mars, can be computed by scaling the measured lunar decay constant for the ratio between the lunar and martian surface gravitational acceleration, under the assumption of comparable crust densities. The resulting value for Mars is $K = 2.8$ km.

Table 1. Dielectric properties of the subsurface material.

	<i>Crust Material</i>		<i>Pore-Filling Material</i>	
	<i>Andesite</i>	<i>Basalt</i>	<i>Water Ice</i>	<i>Liquid Water</i>
ϵ_r	3.5	7.1	3.15	88
$\tan \delta$	0.005	0.014	0.00022	0.0001

Table 2. Value ranges of the surface geometric parameters.

<i>Large-Scale Model</i>		<i>Small-Scale Model</i>	
<i>rms slope</i>	<i>correlation length</i>	<i>rms slope</i>	<i>rms height</i>
0.01-0.1 rad (0.57-5.7°)	200-3000 m	0.1-0.6 rad (5.7-34.3°)	0.1-1 m

It appears almost certain from morphologic and chemical evidence, as well as from SNC meteorites, that the martian surface is primarily basaltic. However, it could have a thin veneer of younger volcanics overlying a primitive crust. Whether this primitive crust is basaltic, anorthositic like the Moon, granodioritic like the Earth's continents or some other kind of composition, is unknown. The NASA Pathfinder APXS analyses of rocks and soils confirm the basaltic nature of Mars' surface. Chemical classifications of lavas show that the Barnacle Bill and Yogi rocks are distinct from basaltic martian meteorites. These rocks plot in or near the field of andesites, a type of lava common at continental margins on Earth. Although a multitude of different chemical compositions is present at the surface of Mars, it is necessary to select a few representative materials as most meaningful for electromagnetic studies. Given the above considerations about the nature of the martian crust, andesite and basalt were chosen because their dielectric constants are end-members of the range within which the martian surface materials may vary.

The dielectric properties of the crust end-member materials, together with those of the water and ice filling the pores, are listed in Table 1.

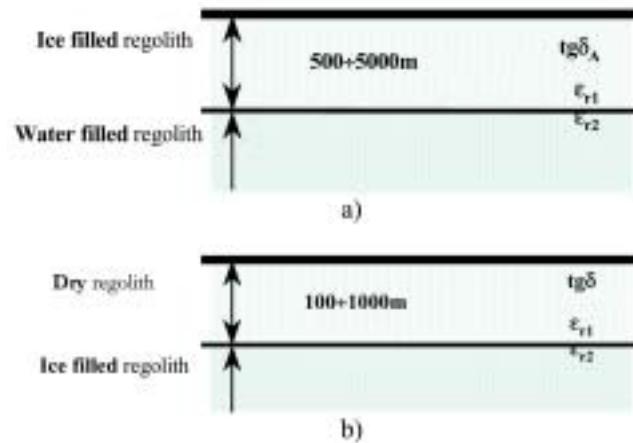
To summarise, the reference models representing the two most likely detection scenarios for a Mars orbital sounder at km depths are (Fig. 1):

Ice/water interface detection. According to the model, the porosity of the martian megaregolith is maximum at the surface and its decay with increasing depth is given by the exponential law in Eq. (1). The pores are filled with ice from the surface down to a depth below which liquid water is stable and becomes the pore-filling material. The change causes a discontinuity of the overall dielectric constant, which can be detected by the radar sounder. The ice/water interface is believed to be at a depth of between 0 m and 5000 m.

Dry/ice interface detection. This model is based on the same assumptions as the ice/water model with respect to the megaregolith properties. However, the pore-filling material here is considered to be gas or some other vacuum-equivalent material up to a certain depth below which ice fills the pores. Hence the interface to be detected is between dry regolith and ice-filled regolith, expected to be at a depth of between 0 m and 1000 m.

These models will be used to estimate the penetration performance under typical MARSIS operating conditions.

Fig. 1. Martian crust stratification models. Simple 2-layer structures are proposed. The discontinuity is created by a change in the pore-filling material. a: ice/water interface detection; b: dry/ice interface detection.



3. Surface Characterisation

Images of the surface from the Viking Landers and Mars Pathfinder depict a gently undulating surface strewn with rocks ranging in size from a few centimetres to metres. Although these images cover only a minute portion of the planet, Mars' thermal and radar properties have prompted extensive modelling of a rock population scattered over the entire surface. The surface geometric structure is thus characterised in terms of a *large-scale* morphology on which a *small-scale* geometric structure, of rocks, is superimposed. It is assumed that the surface can be described as a random distribution of heights, characterised by a variance σ_h , a correlation length L and a local surface rms slope m_s . By assuming that the height distribution is Gaussian, then $m_s = \sqrt{2} \sigma_h / L$, so that the distribution is completely determined once the values of two of these parameters are known. The terms large-scale and small-scale refer to different approximations in the modelling of the radar backscattering coefficient; the divide between large-scale and small-scale is essentially the radar wavelength.

Topographic data can be used to derive the large-scale geometry of the surface. The global topographic maps of Mars currently available were compiled from several types of measurements with different resolutions and sources of uncertainties. These data do not provide a complete, global picture of Mars' topography, but allow the inference that elevation changes, although relevant in magnitude, do not involve average slopes greater than 5° (0.1 rad), and often much less. Also, the correlation lengths for the topography appear to be rather large, perhaps of the order of tens of kilometres.

To characterise the surface geometry at scales smaller than the radar resolutions, it is necessary to use proper data sets: measured values for Mars are in the range 0.7 - 13° , averaging 2° , with a remarkable diversity from place to place over the surface. Such values refer to scales that, according to model interpretations, range from a few tens to a few hundred metres.

To summarise, plausible ranges for the parameters describing the surface geometry are listed in Table 2.

Recent attempts to describe the structure of planetary surfaces by means of fractals have also been taken into account. Tests on MGS/MOLA data have shown that the Hurst exponent (H) with very high probability lies in the range 0.7 - 1 and the rms slope ($s(\Delta x)$) extrapolated with a lag $\Delta x = 166$ m is lower than 0.05 .

4. Characterisation of the Ionosphere

The study of the martian ionosphere is important not only as a topic in its own right, but also because the ionosphere has a strong influence on the subsurface and surface soundings. Electromagnetic radiation cannot propagate through an ionised gas at frequencies below the electron plasma frequency, given by $f_p = 8980 \sqrt{N_e}$ Hz, where

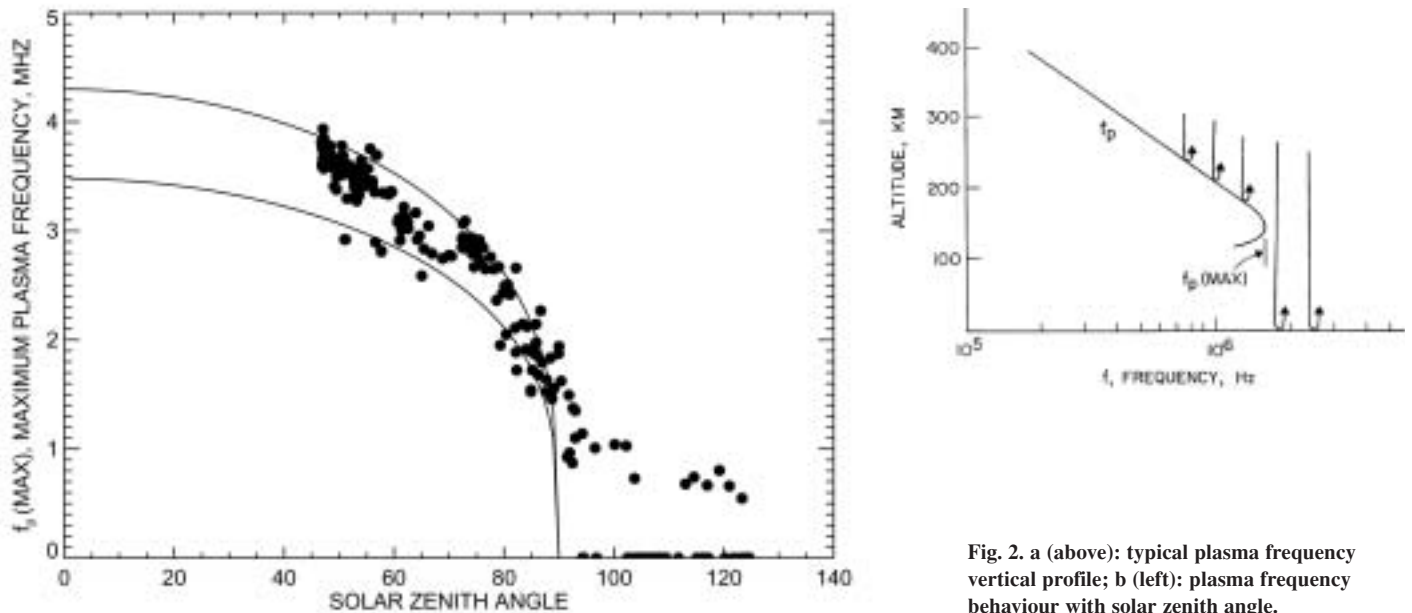


Fig. 2. a (above): typical plasma frequency vertical profile; b (left): plasma frequency behaviour with solar zenith angle.

N_e is the electron number density in cm^{-3} . A typical profile of the electron plasma frequency in the dayside martian ionosphere is shown in Fig. 2a, based on plasma density measurements from the Viking Landers (Hanson, 1977). Usually the electron plasma frequency on the dayside of Mars has a single, well-defined maximum, at an altitude of 125-150 km. Radio waves incident vertically on the ionosphere are reflected at the point where the wave frequency is equal to the electron plasma frequency. Transmission through the ionosphere is possible only at frequencies above the maximum electron plasma frequency in the ionosphere, $f_p(\text{max})$. Figure 2b shows a plot of $f_p(\text{max})$ versus solar zenith angle. The solid dots give the plasma frequency obtained from radio occultation measurements (Zhang et al., 1990a; 1990b), and the solid lines give extrapolations using the Chapman theory of planetary ionospheres.

Subsurface soundings are possible only at frequencies greater than $f_p(\text{max})$. Since they require frequencies as low as possible, the global distribution of the ionospheric electron density (hence plasma frequency) becomes an important factor in selecting the operating frequency of the sounder and the optimal orbital strategy for data collection. The lowest frequency that can penetrate the martian ionosphere varies from about 4 MHz on the dayside to somewhat below 1 MHz on the nightside. Clearly, the best region for carrying out subsurface soundings is on the nightside, at solar zenith angles greater than 90° . Unfortunately, very little is known about the ionosphere on the nightside. A typical nightside maximum plasma frequency appears to be about 800 kHz. From our knowledge of the ionosphere of Venus, for which better nightside electron density measurements are available, it is likely that there are isolated regions on the nightside of Mars where the plasma frequency extends well below 800 kHz.

Even when the sounding frequency is above $f_p(\text{max})$, the ionosphere still has an effect on the radar signal. As is well known (Stix, 1964), the index of refraction for an electromagnetic wave propagating through an unmagnetised plasma is given by $n = [1 - (f_p/f)^2]^{1/2}$. Even at frequencies several times the plasma frequency, the index of refraction has a noticeable deviation from the free-space value of $n = 1$. This deviation causes a frequency-dependent time delay, called dispersion, that distorts the shape of the radar pulse. It is easily demonstrated that the phase shift induced by the ionosphere over the $\Delta f = 1$ MHz bandwidth of the radar chirp signal is substantial, approximately 200 rad for a centre frequency at $f = 2f_p(\text{max})$, and 5 rad at

$f = 10f_p(\text{max})$. Since the sounder must almost certainly operate at frequencies below $10f_p(\text{max})$, it follows that we must be prepared to remove the dispersive effects of the ionosphere, otherwise the signal-to-noise ratio and range resolution of the radar signal would be severely degraded in the chirp compression process.

5. MARSIS Orbital Requirements

The baseline orbit for Mars Express has a periapsis distance of 250 km, apoapsis distance of 10 142 km, inclination 86.35° and period of 6.75 h. Figure 3 shows the tangential and radial components of the satellite's orbital velocity as a function of altitude above the equatorial radius. MARSIS is designed to perform subsurface sounding during each orbit when the altitude is lower than about 800 km; for the baseline orbit that means a period of about 26 min. This allows mapping of about 100° on the surface on each orbit, allowing extensive coverage at all latitudes within the nominal mission duration. To achieve this global coverage, MARSIS is designed to support both dayside and nightside operations, although performances are maximised during the night (solar zenith angle $> 80^\circ$), when the ionosphere plasma frequency drops off significantly and the lower frequency bands, which have greater penetration capability, can be used. Ionospheric soundings will be also carried out by MARSIS on certain passes when the orbiter is at an altitude up to 1200 km, both during day and night time.

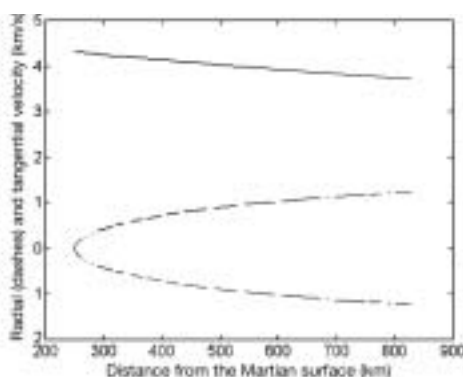
6. Measurement Concept and Experiment Description

6.1 Subsurface and surface sounding

The sounder's principle of operation is explained in Fig. 4. The electromagnetic wave transmitted by the antenna impinges on the surface, producing a first reflection that propagates back to the radar, generating a strong return signal received at time $t_0 = 2H/c$, H being the spacecraft height and c the speed of light in vacuum. However, thanks to the long wavelengths employed, a significant fraction of the energy impinging on the surface is transmitted into the crust and propagates down with a decreased velocity $v = c/n$ (n is the refractive index of ice related to the real dielectric constant ϵ_r by $n = \sqrt{\epsilon_r}$) and an attenuation proportional to the penetration depth (z), to the wavelength (λ) and to the material loss tangent ($\tan \delta$, defined as the ratio of the imaginary part to the real part of the complex dielectric constant, $\tan \delta = \epsilon_i/\epsilon_r$). Should subsurface dielectric discontinuities be present at depth z_0 below the surface, additional reflections would occur and the echoes would propagate back through the first layer medium and then to the radar, generating further echo signals, much weaker than the front surface signal, with time delay $t_0 + 2z_0/v$. As a consequence, time-domain analysis of the strong surface return, eventually after multi-look non-coherent integration, allows estimation of surface roughness, reflectivity and mean distance, just as in classical pulse-limited surface radar altimeters. Moreover, the weaker signals after the first strong surface return will enable the detection of subsurface interfaces, while their time delays will allow measurement of the depths of those interfaces.

Detection performance will be limited by two main factors: the strength of the surface clutter echoes and the noise floor entering the receiver. The surface clutter echoes originate by reflections from those surface areas (marked C in Fig. 4) that have 2-way propagation path delays identical to that of the useful subsurface signal (point B in Fig. 4). While this is not a problem for perfectly flat surfaces (the angular backscattering law imposes a very high attenuation on such lateral reflections), most natural surfaces are not at all flat and surface clutter echoes can be very strong in practical situations. As a direct consequence, when the competing subsurface echoes are highly attenuated by the propagation into the crust, the surface clutter echoes may mask the useful signal and limit the detection. Furthermore, even when the surface clutter power is lower than the competing subsurface echo, the detection performance can be limited by the noise floor of the receiver. Such noise can be very high at the low frequencies commonly used for radar sounding owing to the contribution of the cosmic noise temperature entering the receiver, which is many order of magnitudes

Fig. 3. Radial and tangential spacecraft velocity.



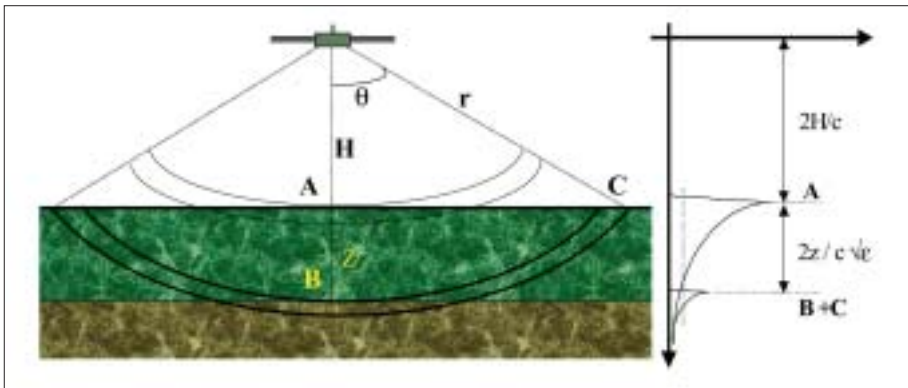


Fig. 4. MARSIS observation geometry and principle of operation.

higher than receiver internal noise for typical noise figures of 3-4 dB and frequencies of 1-10 MHz (Picardi et al., 1998a; 1999a).

In the standard subsurface sounding mode, MARSIS can transmit and receive any of the following bands: 1.3-2.3 MHz (centred at 1.8 MHz), 2.5-3.5 MHz (centred at 3 MHz), 3.5-4.5 MHz (centred at 4 MHz) and 4.5-5.5 MHz (centred at 5 MHz). The instantaneous bandwidth is 1 MHz for all the bands, and the transmitted waveform is a pseudo-linear frequency modulated pulse (chirp). Since, on the dayside of Mars, the ionosphere will not allow the use of frequencies below ~ 3 MHz, only the two higher bands (4 MHz and 5 MHz) can be used for surface/subsurface sounding during the day. However, the best penetration is during nightside observations, when the longest wavelengths can also be used.

Transmitted pulses are radiated through a 40 m tip-to-tip dipole mounted normally to the orbiter's direction of motion, fed by a matching network that flattens the antenna frequency response over the full 1.3-5.5 MHz range. The reflected echoes are received both from the primary dipole antenna and from a secondary receiving antenna. This short monopole is mounted vertically, aligned with the nadir axis, and features a null in the nadir direction and thus records off-nadir surface echoes alone (Picardi et al., 1999b). Received echoes on both channels are converted to a small offset frequency and digitised for onboard processing and later downlink. The receiving window accommodates echoes from a maximum depth of 5-8 km, depending on the crust dielectric constant. Since the data rate of the digitised samples is on the order of a few Mbit/s, substantial data reduction is performed onboard to comply with the orbiter's data rate and volume constraints. Data reduction is performed by the onboard processor, which features adaptive range compression, azimuth compression and multi-look non-coherent integration, depending on the operating modes. The range compression allows a range resolution equivalent to 150 m in vacuum and waveform sidelobes controlled to provide a system dynamic range in excess of 50 dB. Azimuth compression is performed by coherent unfocused Doppler processing, to reduce along-track surface clutter and noise power; the along-track resolution after azimuth compression is sharpened to 5-9 km, depending on the altitude. Cross-track surface clutter reduction by dipole/monopole signal combination is performed during ground processing. Non-coherent averaging with multiple Doppler filters (looks) can also be performed before downlink to reduce statistical fluctuations of the final profiles. Finally, echo profiles collected at different frequencies can be processed to enhance the discrimination of subsurface reflections, which are strongly dependent on the frequency, from the surface reflections, which are mostly frequency-independent.

During ground processing, downlinked data will be analysed for time delay to subsurface reflector(s), intensity of subsurface reflection(s), and a measure of 'confidence' that a subsurface interface was detected. These parameters will be incorporated into a global map database, to allow interpretation of local and regional behaviour. Detailed analysis will be conducted for regions of interest. This will include modelling of the electrical properties of the layers and interfaces. The modelling will

result in estimates of thickness of layers, depth to interfaces, dielectric properties of the materials, and an interpretation of the properties of the materials, including composition. It is expected that the abrupt dielectric contrasts that should exist at a martian water table would allow an unambiguous identification of liquid water. If small (tens of km in lateral extent) aquifers are present, the resolution and processing scheme of MARSIS should allow their detection, unlike other systems that may require extensive, uniform layer and interface conditions. Boundaries involving the presence and absence of ground-ice will be more difficult to distinguish, but regional trends (with latitude and elevation) should allow discrimination of ground-ice boundaries.

The first surface reflection echoes of MARSIS operating as a sounder will be processed to give estimates of the average height, roughness and reflection coefficient of the surface layer, according to the classical altimetric approach. By measuring the time delay of the echo, it will be possible to estimate the average distance of the radar from a reference flat surface level, while the duration of the waveform leading edge will be proportional to the large-scale surface roughness averaged over the pulse-limited spatial resolution cell. Finally, the peak value of the average echo waveform will be used to estimate the backscattering coefficient and, in conjunction with the roughness value, to estimate the Fresnel reflection coefficient of the surface. A further improvement of the altimeter mode performance, in terms of resolution and accuracy, can be achieved by processing the return echoes collected over the same region during different orbits. During ground processing, surface reflection profiles will be analysed for surface reflectivity at each frequency, echo dispersion at the surface (an indication of surface roughness) and surface elevation. These parameters will be further incorporated into the global map database, to allow interpretation of local and regional behaviour, and for comparisons with other data sets.

6.2 Ionospheric sounding

MARSIS ionospheric measurements employ both passive and active techniques. The passive technique uses the thermal emission line at the local electron plasma frequency to make highly accurate measurements of the local electron density. The active technique uses radar signals (soundings) to measure the vertical range to the ionospheric reflection point as a function of frequency. For active soundings, a simple ionospheric mode of operation is used in which sinusoidal pulses with a nominal duration of 91.4 ms are transmitted in 160 frequency steps from 0.1 MHz to 5.4 MHz. The time required to step through a complete frequency sweep is 1.23 s. Using these measurements, the vertical profile of the plasma electron frequency (hence, electron density) can be determined, as in Fig. 2a. There are two modes of operation: continuous and interleaved. The continuous mode of operation provides a contiguous series of ionospheric sounding sweeps, thereby providing the highest possible horizontal resolution. Since such a contiguous series of sweeps leaves no time for subsurface soundings, this mode is used relatively infrequently. The more common mode interleaves the subsurface soundings with the ionospheric soundings in a regular pattern. These will be particularly useful if ionospheric electron density information is needed to interpret or optimise the subsurface soundings.

7. Instrument Description

A functional block diagram of MARSIS is shown in Fig. 5; the principal characteristics are given in Table 3. There are three main subsystems:

- the Antenna Subsystem (AS), including the primary dipole antenna for transmission and reception of the sounder pulses, and the secondary monopole antenna for surface-clutter echo reception only;
- the Radio Frequency Subsystem (RFS), including both the transmit channel and the two receive channels for the dipole and monopole antennas, respectively;
- the Digital Electronics Subsystem (DES), including the signal generator, timing and control unit and the processing unit.

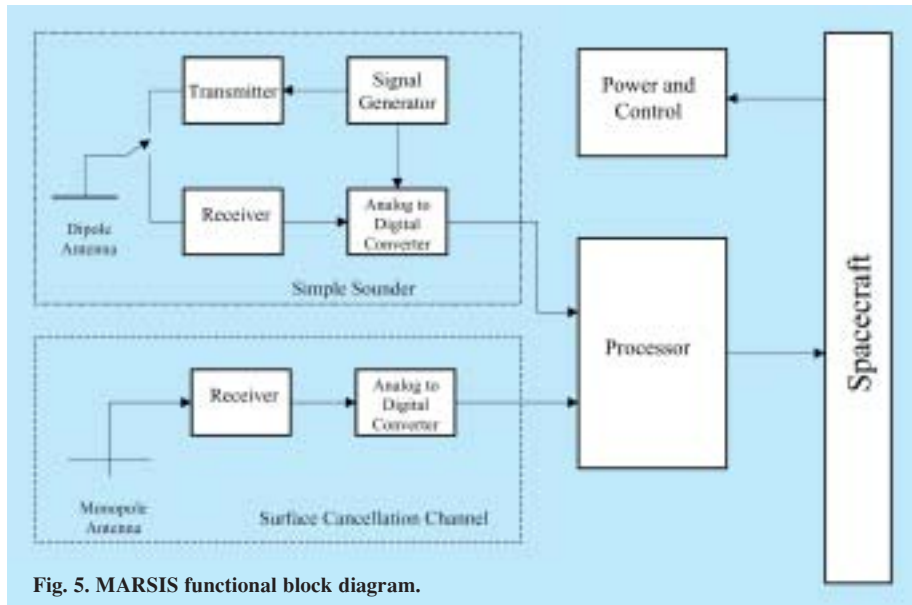


Fig. 5. MARSIS functional block diagram.

In nominal surface/subsurface sounding operations, MARSIS transmits in rapid sequence up to four quasi-simultaneous pulses at one or two different frequencies, selected from the four available bands, and receives the corresponding echoes on both the dipole and monopole antennas. The whole transmit/receive cycle is repeated at a rate fixed by the system Pulse Repetition Frequency (PRF). The selection of the PRF is an important issue in the definition of the MARSIS timing scheme, since the antenna pattern is practically isotropic in the along-track direction. With this system, spectral aliasing of surface clutter echoes could occur if the Doppler bandwidth is under-sampled. Considering that a folding localised into far-range cells can be accepted at the highest frequency bands (because penetration to the corresponding depths is unlikely) a fixed PRF of 130 Hz was selected as the baseline for surface/subsurface sounding. In fact, the risk of folding in useful range cells seems to be very small, while the implementation burden is significantly reduced. With such a PRF, the basic transmit/receive repetition interval is 7.69 ms. Within this time frame, the MARSIS transmitter radiates through the main dipole antenna up to four chirps of nominal duration 250 μ s, waiting for about 100 μ s between any two consecutive chirps. Two different frequency bands can be assigned to the four pulses, selectable from the four operating bands. After transmission is completed, MARSIS turns to the receive mode and records the signals received from both dipole and monopole channels for each transmitted pulse. The duration of the receiving window 350 μ s, accommodating an echo dispersion of about 100 μ s, which corresponds to about 5–8 km of penetration, depending on the propagation velocity in the crust. Upon reception, echoes are down-converted and digitised to a format suitable for the onboard processor. Four processing channels allow the processing of two frequency bands received from the dipole and monopole at each PRF. The digitised echo stream is processed by the digital electronics subsystem in order to reduce the data rate and data volume, and allow global mapping of the observed scene within the allocated amount of orbiter mass memory.

Starting from the desired along-track sampling rate of the surface, the basic azimuth repetition interval is identified and all the pulses received within such an interval (frame) are processed to yield a single echo profile referring to one azimuth location. Range compression is performed on each pulse by classical matched filtering, although adaptive techniques are used to update the matched filter reference

Table 3. Principal parameters for the MARSIS subsurface sounding mode.

Centre frequencies	
Band 1	1.8 MHz
Band 2	3.0 MHz
Band 3	4.0 MHz
Band 4	5.0 MHz
Bandwidth	1.0 MHz
Irradiated power	
Band 1	1.5 W
Band 2	5.0 W
Band 3	5.0 W
Band 4	5.0 W
Transmit pulse width	250 μ s
	(30 μ s in mode SS5)
PRF	130/s
Minimum altitude	250 km
Max. altitude subsurface sounding	800 km
Max. altitude ionosphere sounding	1200 km
Receive window size per channel (baseline)	350 μ s
Analog to digital conversion rate	2.8 MHz
Analog to digital conversion	8 Bit
No. processed channels	4 (max)
Max. no. simultaneous frequencies	2
Radiation gain	2.1 dB
Dipole antenna element length	20 m
Monopole antenna length	7 m
Data rate output (min/max)	18/75 kbit/s
Data volume daily (max)	285 Mbit
Mass	17 kg
Power (max. incl. margins)	64.5 W

function at each frame in order to correct for the time-variant phase distortions introduced by the ionosphere propagation (Picardi et al., 1998a; 1999a; Picardi & Sorge, 1999). The information needed for this adaptive filtering is estimated by a dedicated processing of the initial pulses of each frame, and is then used for all the remaining pulses of the same frame, thus assuming the fluctuation rate of the distortion is slower than the frame duration. Alternative techniques for such adaptive filtering are based either on using the front surface reflection for direct extraction of the propagation medium's impulse response (Safaenili & Jordan, 2000), on the estimation of some parametric model of the propagation medium using a contrast maximisation technique (Picardi & Sorge, 1999; Biccari et al., 2001c).

By correctly sampling the surface and subsurface Doppler spectra, coherent integration of the range-compressed echoes within each frame is possible, enhancing the spatial resolution in the along-track direction and linearly reducing the cosmic noise level (Picardi et al., 1998a; 1999a). For simplicity, unfocused Doppler processing has been implemented, entailing an azimuth resolution of 5000 m at altitudes below 300 km, increasing to 9000 m at higher altitudes. Coherent integration is performed using a fixed number of phase-correction functions, thus synthesising a bank of parallel Doppler filters around the zero Doppler point (or the Doppler centroid). However, since the small amount of computational and memory resources available in the processor limits the number of Doppler filters that can be synthesised to about five, the position and usage of these filters are optimised taking into account the behaviour of the observed surface. Specifically, if specular scattering from a flat surface is dominant, the greatest portion of the echo power falls into the single Doppler filter that contains the point of specular reflection (the central Doppler filter for a non-tilted surface), leaving mostly noise to the lateral Doppler filters. Under such conditions, it is clear that the best choice is to use that single Doppler filter, eventually located by a Doppler-tracking algorithm, and discard the others. For the contrary case of a rough layer, non-coherent scattering is dominant and the signal power is distributed over several Doppler filters, so it is worth averaging echoes from the same zone processed by different Doppler filters to improve the signal-to-noise (S/N) ratio and reduce statistical fluctuations (speckle).

A primary indication of MARSIS' capability for subsurface sounding is given by the S/N at the processor's output (Picardi et al., 1999a). Under normal MARSIS operating conditions, the contribution of the receiver internal noise to the system noise temperature can be neglected, compared to the contribution of the external cosmic noise. This assumption is easily verified at low frequencies, where the cosmic noise temperature is millions of K, which corresponds to receiver noise figures higher than 40 dB.

The maximum dynamic range of the sounder can be computed by evaluating the S/N in the case of a rough surface, where the surface echo can be evaluated according to the geometric optics approximation, and in the case of a perfectly specular surface return, where the geometric optics approximation cannot be applied and we get a higher echo from the surface.

Evaluating the radar equation in the two cases shows that, during nominal sounding operations, an S/N always better than 14 dB is available on the front surface echo. This allows precise positioning of the receiving window using a tracking algorithm, and allows precise estimation of surface parameters with the surface altimetry mode, provided that sufficient averaging is performed to reduce statistical fluctuations of the signal (speckle noise).

8. Model Performance

To assess the interface-detection performance of the radar sounder, the backscattering cross-sections of concurrent echoes from the surface and subsurface layers (Fig. 4) as operating conditions change need to be evaluated. These can be expressed as $\sigma_s = \Gamma_s f_s (\sigma_{h,s}, L_s, \lambda)$ and $\sigma_{ss} = \Gamma_{ss} f_{ss} (\sigma_{h,ss}, L_{ss}, \lambda)$, with Γ_s and Γ_{ss} being the Fresnel reflectivity terms, which deal with the surface and subsurface dielectric properties, and f_s and f_{ss} the geometric scattering terms, which deal with the geometric structure

of the surface and subsurface; L_s and L_{ss} are the correlation lengths; λ is the wavelength. In the following sections, the Fresnel terms and the geometric scattering terms are evaluated using the simplified reference crust models introduced in Sections 2 and 3.

8.1 Modelling of Fresnel reflectivity terms

According to electromagnetic theory, the Fresnel reflectivity for nadir incidence on a surface can be expressed as:

$$\Gamma_s = \left| \frac{1 - \sqrt{\epsilon_{r1}(0)}}{1 + \sqrt{\epsilon_{r1}(0)}} \right|^2 = R_{01}^2 \quad (2)$$

with $\epsilon_{r1}(0)$ the real dielectric constant of the crust evaluated at the surface ($z = 0$). The Fresnel reflectivity for the subsurface layer at depth z can be expressed as:

$$\Gamma_{ss,z} = R_{12,z}^2 (1 - R_{01}^2)^2 10^{-0.1 \int_0^z \alpha(\zeta) d\zeta} \quad (3)$$

with $R_{12,z}^2$ the reflection coefficient of an interface located at depth z :

$$R_{12,z}^2 = \left| \frac{\sqrt{\epsilon_{r1}(z)} - \sqrt{\epsilon_{r2}(z)}}{\sqrt{\epsilon_{r1}(z)} + \sqrt{\epsilon_{r2}(z)}} \right|^2 \quad (4)$$

and $\alpha(\zeta)$ the 2-way unit depth attenuation due to dielectric dissipation in the crust, expressed in dB/m:

$$\alpha(\zeta) = 1.8 \times 10^{-7} f_0 \sqrt{\epsilon} \tan \delta \quad (5)$$

The evaluation of the Fresnel reflectivity terms requires knowledge of the complex dielectric constants of the crust as a function of depth. This can be modelled starting from the dielectric constants of the basic elements contained in the martian crust (Table 1) and using the exponential law (Eq. 1) for the porosity decay against the depth into well-known Host-Inclusion mixing formulae (Picardi et al., 1999a). Since porosity depends on depth, then so do the effective dielectric constants of the mixtures. The Maxwell-Garnett model for spherical inclusions was adopted for this analysis. As a result, the real dielectric constant at the surface (a water-filled regolith is not considered to be possible at the surface) ranges between 4 and 6 for a basalt-like regolith, and between 2 and 4 for andesite-like regolith; the lower values correspond to higher surface porosity and dry regolith. As the depth increases, the first layer's dielectric constant increases because of the lower porosity and approaches the dielectric constant of the pure host material (basalt or andesite in our models). If an interface among ice-filled and water-filled regolith or dry-regolith and ice-filled regolith occurs at a certain depth, there will be an abrupt change in the real part of the dielectric constant. The dielectric contrast will be higher for ice/water interfaces, for higher surface porosity and, of course, for greater depths. This dielectric contrast is the origin for the subsurface reflection process, and the subsurface reflection coefficient will be proportional to its intensity through Eq. 4. Moreover, the absorption in the crust can be modelled using Eq. 5 and the obtained loss tangent profiles and the total subsurface reflectivity can be computed by performing integration over the depth according to Eq. 3. Figure 6 shows the resulting reflectivity of the surface and subsurface echoes for both ice/water and dry/ice interface scenarios, assuming the different materials and surface porosity values listed in Table 1. It is clear from the figures that the surface reflectivity ranges between -7 dB

and -15 dB, depending on the surface composition and porosity, and has a typical value of -10 dB for most scenarios.

8.2 Backscattering model

As mentioned in Section 3, backscattering from the martian surface can be modelled by considering two main terms: the large-scale scattering contribution results from gentle geometrical undulations of the surface on a scale of many hundreds to thousands of metres, whereas the small-scale scattering contribution arises from the rapid, slight variations of surface height over a horizontal scale of some tenths of metres. Both surface scales are modelled as Gaussian random processes with a circular symmetric correlation function, and are described by the rms height σ_h and correlation length L . A third non-independent parameter is introduced, called rms slope, which for a Gaussian correlation function is given by $m_s = \sqrt{2}\sigma_h/L$ and represents the average geometric slope of the surface.

Simple approximate methods can be applied for surfaces that present a unique roughness scale, with either a large correlation length (gently undulating surface) or a very small rms height (slightly rough surface) compared to the incident wavelength. Specifically, the Kirchhoff method can be applied for gently undulating surfaces, which respect the tangent plane conditions, and the Small Perturbation Method can be applied to slightly rough surfaces. The classical studies on the validity conditions of these two models have recently been updated, and regions of validity currently defined show that the Kirchhoff approximation can be used to evaluate the large-scale backscattering contribution, whereas the Small Perturbation Method can be used for the small-scale contribution. The approach here for modelling the total surface backscattering is to consider the two roughness scales independently and to sum the respective backscattering cross-sections obtained with the Kirchhoff and Small Perturbation Method approximations.

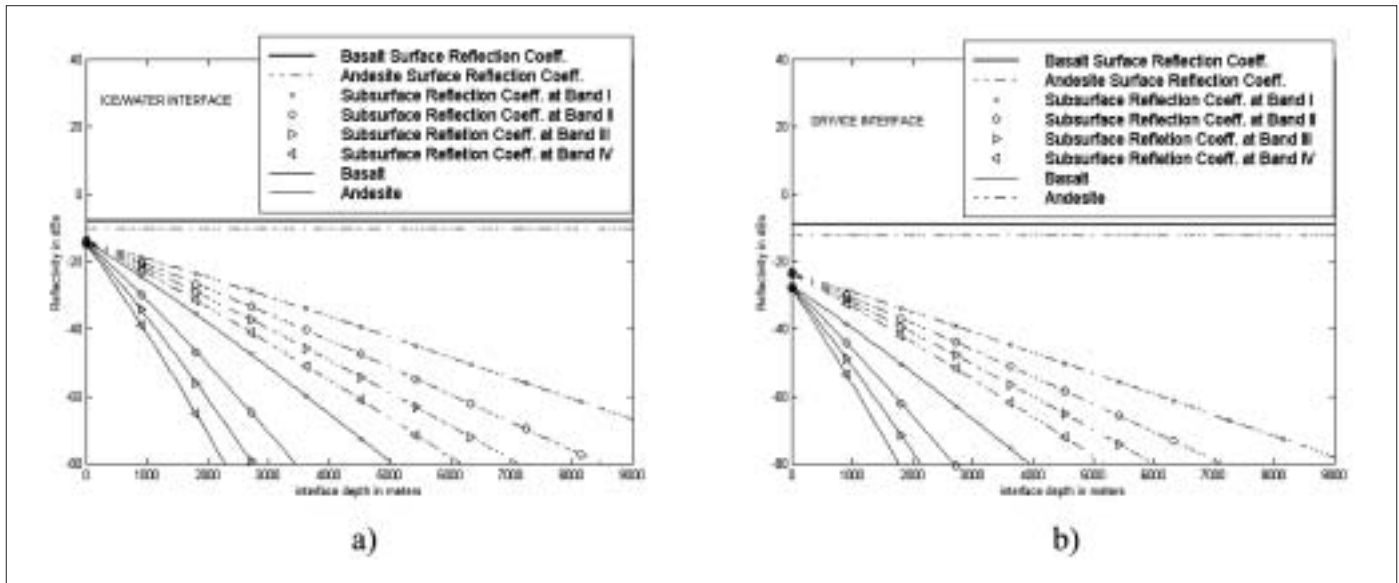
For the Kirchhoff term, an analytic model of the backscattering cross-section was obtained by extending the electric field method followed by Fung & Eom (1983) to the case of a generic Kirchhoff surface and pulsed radar. The expression found allows prediction of the backscattering cross-section without restriction to the geometrical optics approximation (pure diffuse scattering), but properly taking into account both the coherent (specular) and non-coherent (diffuse) component of the scattering process. Under the simplifying assumptions of a Gaussian surface correlation function and Gaussian (compressed) pulse shape, the expression of the Kirchhoff backscattering cross-section is:

$$P_K(\tau) = \Gamma\pi H^2 (P_c + P_{nc1} - P_{nc2}) \quad (6)$$

where H is the altitude, $P_c(\tau)$ is the coherent (specular) scattering component, while $P_{nc}(\tau) = P_{nc1}(\tau) - P_{nc2}(\tau)$ is the non-coherent (diffuse) scattering component.

The maximum power is received when full coherent reflection occurs, i.e. when the surface is perfectly flat. In such a condition, it is easy to verify that $P_{nc1} = P_{nc2}$ and the non-coherent term P_{nc} reduces to zero, while the coherent term P_c approaches the shape of the transmitted pulse, which is maximum in the origin; the maximum cross-section of the large-scale contribution of the surface is then $\sigma_{K,max} = \Gamma\pi H^2$, which is a value consistent with that predicted by the image theorem for the reflection coefficient of perfectly flat surfaces. As the surface becomes rougher, the coherent component goes towards zero and non-coherent scattering becomes dominant (geometrical optics model). By considering the fractal surface model (Section 3), the geometric optics model ($H = 1$ in the fractal model) can be considered as the end model. Moreover, the Hagfors model ($H = 1/2$ in the fractal model) will be the other end-model: the geometric optics model is considered as the worst case (Biccari et al., 2001a).

Turning to the small-scale contribution, the Small Perturbation Method approximation allows the backscattering coefficient to be expressed as:



$$\sigma_{pp}^0(\theta) = 8k^4 \sigma_{h2}^2 |\alpha_{pp}(\theta)|^2 \cos^4 q W(K_B) \quad (7)$$

Fig. 6. Surface and subsurface Fresnel reflectivity with medium surface porosity (35%) and (a) ice/water interface, (b) dry/ice interface.

where $k = 2\pi/\lambda$ is the wave number, θ is the incidence angle, $\alpha_{pp}(\theta)$ is the Fresnel Reflection Coefficient for the pp polarisation, $W(K)$ is the surface roughness small-scale spectrum and K_B is the Bragg Frequency, given by $K_B = 2k \sin\theta$.

Summarising, the surface backscattered power, $\sigma_T(\tau)$, can be obtained by summing the large-scale and small-scale contributions:

$$\sigma_T(\tau) = \sigma_K(\tau) + \sigma_{SP}(\tau) \quad (8)$$

where $\sigma_{SP}(\tau)$ is the Small Perturbation term. Figure 7 shows the surface cross-section given by Eq. 8, assuming the worst-case small-scale contribution and a large-scale correlation length of about 2000 m, as a function of the depth of the competing subsurface return (assuming a reference average $\epsilon_r = 4$). The plots are normalised so that the 0 dB axis indicates the maximum possible cross-section, which is given again by $\sigma_{K,max} = \Gamma\pi H^2$. As seen in the figure, the scattering cross-section is maximum at nadir and rapidly falls as the ‘equivalent depth’ increases, up to a level at which it becomes practically a constant. This behaviour can be easily understood by considering the superposition of the two scale contributions. In fact, according to classical random scattering theory, the large-scale Kirchhoff component dominates the backscattering around the nadir and determines the cross-section fall-off rate (owing to the small value of m_s), while the small-perturbation component dominates at high off-nadir locations and is responsible for the flat behaviour of the cross-section when the Kirchhoff contribution has vanished.

8.3 Surface clutter reduction techniques

As apparent from Fig. 7, when sounding over rough areas of the martian crust (rms slope $> 2-3^\circ$) the detection depth will be severely limited by the surface clutter, rather than by the cosmic noise. In order to improve the sounding performance in these regions, different methods of reducing the surface clutter contributions were included in MARSIS: Doppler filtering of surface clutter; dual-antenna clutter cancellation; and dual-frequency clutter cancellation. Detailed descriptions and performance assessment of the three methods can be found in Picardi et al. (1999a). Below is a short review of the techniques and their cancellation performances.

Doppler filtering of the surface clutter is a direct consequence of the azimuthal synthetic aperture processing performed by the MARSIS onboard processor to

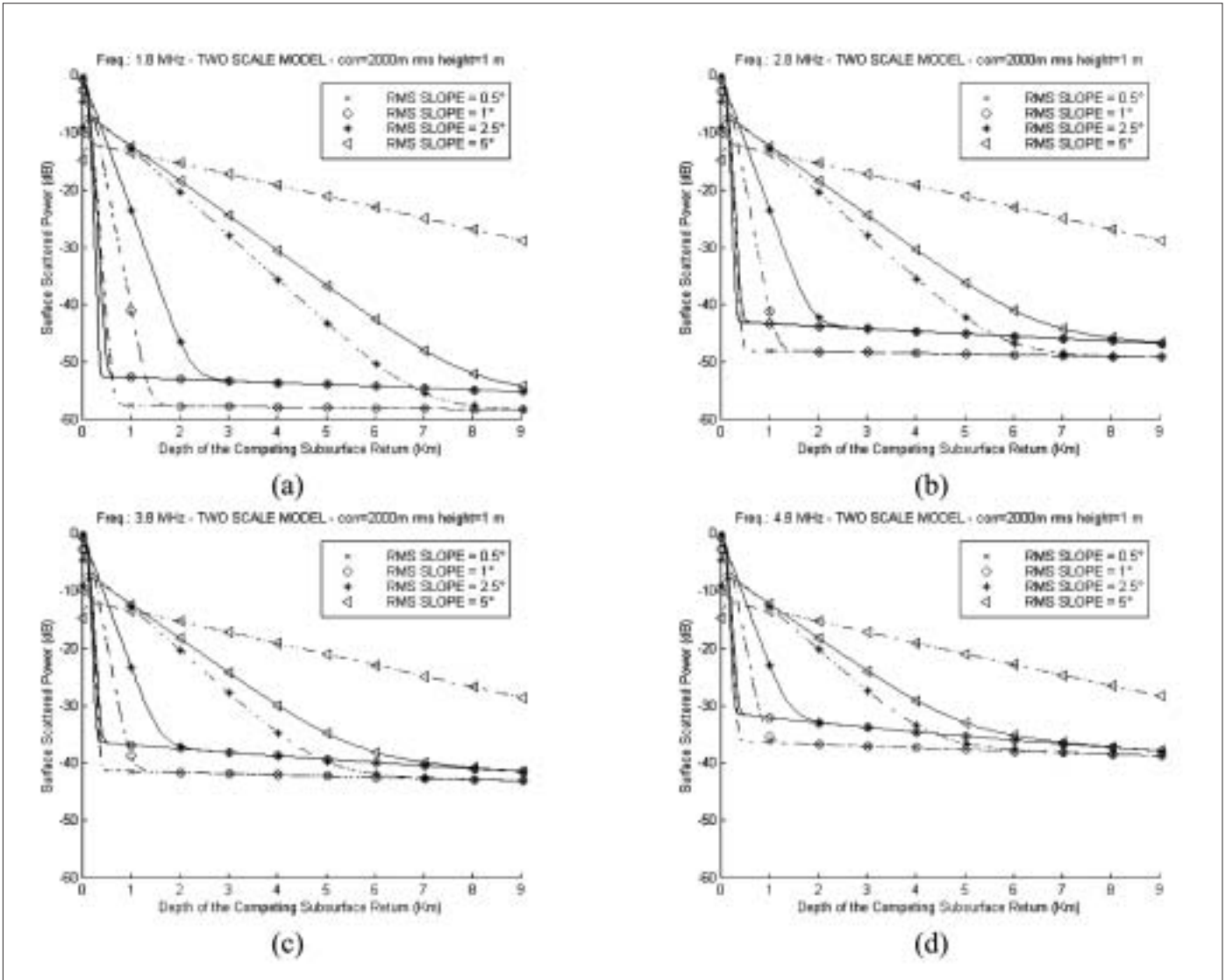


Fig. 7. Surface scattered power according to the two-scale model. A Gaussian spectrum at large-scale and a 1.5-power law spectrum at small-scale are assumed. Large-scale correlation length is 2000 m, small-scale rms height is 1 m. $H = 250$ m (-) and 800 km (-.-). a: 1.8 MHz; b: 2.8 MHz; c: 3.8 MHz; d: 4.8 MHz.

sharpen the along-track resolution and enhance noise suppression. In fact, if the Doppler spectrum at each specific range location is sampled using a proper PRF, the surface clutter contribution from along-track off-nadir angles is mapped to the high end of the Doppler spectrum, while subsurface echoes from nadir are mapped to the lowest portion of the Doppler spectrum.

The amount of clutter reduction from this technique can be evaluated by simple geometric considerations, taking into account the reduction of the scattering areas for the nadir subsurface return and the off-nadir surface return, after Doppler filtering. An improvement factor (IF) can be defined as the ratio of signal-to-clutter ratios before and after the cancellation technique. The Doppler filtering IF can be expressed approximately by:

$$IF = \sqrt{\frac{z}{\Delta}} \left(1 - \sqrt{1 - \frac{\Delta}{z}} \right) \quad (9)$$

where z is the depth of the subsurface return and Δ is the radar range resolution, and the condition $z > \Delta$ is assumed to be verified. As clearly seen in Fig. 8a, an IF of about 12 dB can be obtained by this technique at large depths.

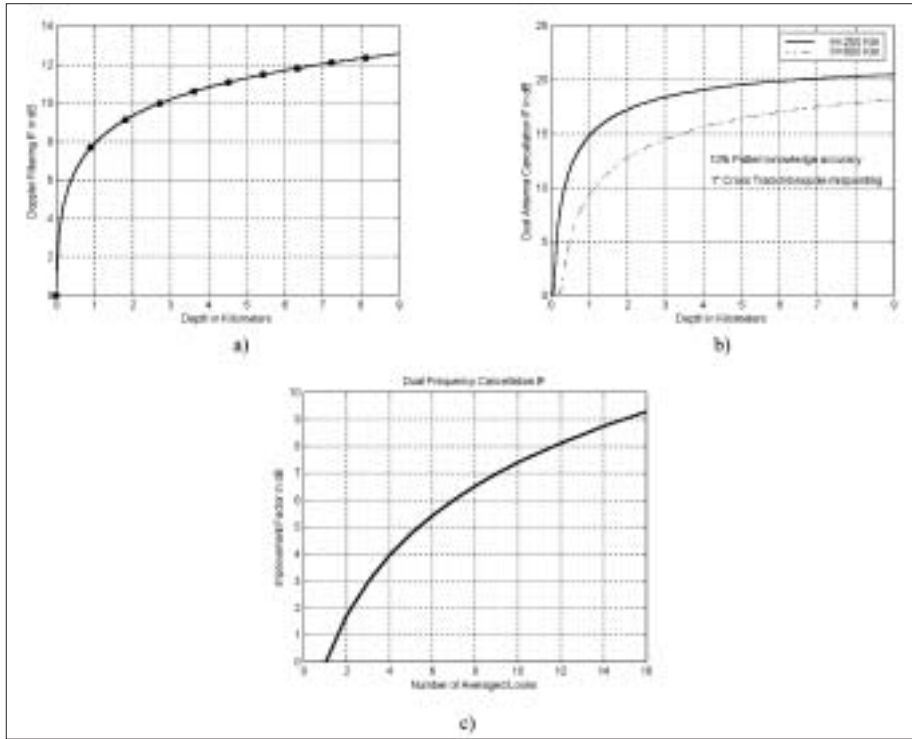


Fig. 8. Improvement Factor (IF) of the surface clutter cancellation techniques. a: Doppler filtering; b: dual-antenna cancellation (1° roll angle and 10% antenna pattern knowledge accuracy); c: dual-frequency cancellation as a function of number of averaged looks.

Since surface clutter echoes from off-nadir in the cross-track direction are not affected by any Doppler modulation and cannot be eliminated by the previous technique, additional clutter suppression techniques were studied for MARSIS, based on a dual-antenna or dual-frequency processing concept.

The dual-antenna cancellation technique (Picardi et al., 1998a; 1999a) uses a primary antenna to transmit and receive the composite subsurface/surface signal, with a pattern maximum in the nadir direction (for MARSIS, a dipole mounted parallel to the surface and normal to the motion direction) and a secondary antenna to receive surface clutter only, with a pattern null in the nadir direction (for MARSIS, a short monopole oriented vertically under the spacecraft). The cancellation scheme is a coherent subtraction after correction for the antenna gain imbalance between the two channels:

$$V_{\text{tot}} = V_1 - V_2 \sqrt{\frac{G_1(\theta)}{G_2(\theta)}} \quad (10)$$

with V_1 and V_2 the complex signals at the dipole and monopole channels, and $G_1(\theta)$ and $G_2(\theta)$ the antenna gain patterns for the dipole and monopole, respectively. It is simple to show (Picardi et al., 1999a) that the surface clutter echoes are completely removed by the subtraction, leading to infinite IF, if we assume that:

- returns from the two antennas are totally correlated;
- surface and subsurface return contributions to V_1 and V_2 are totally uncorrelated;
- the antenna patterns $G_1(\theta)$ and $G_2(\theta)$ are perfectly known;
- the monopole pattern null points exactly towards the nadir direction in both along-track and cross-track directions;
- the primary and secondary antenna channels have the same phase/amplitude transfer function (perfectly amplitude-balanced and phase-matched channels).

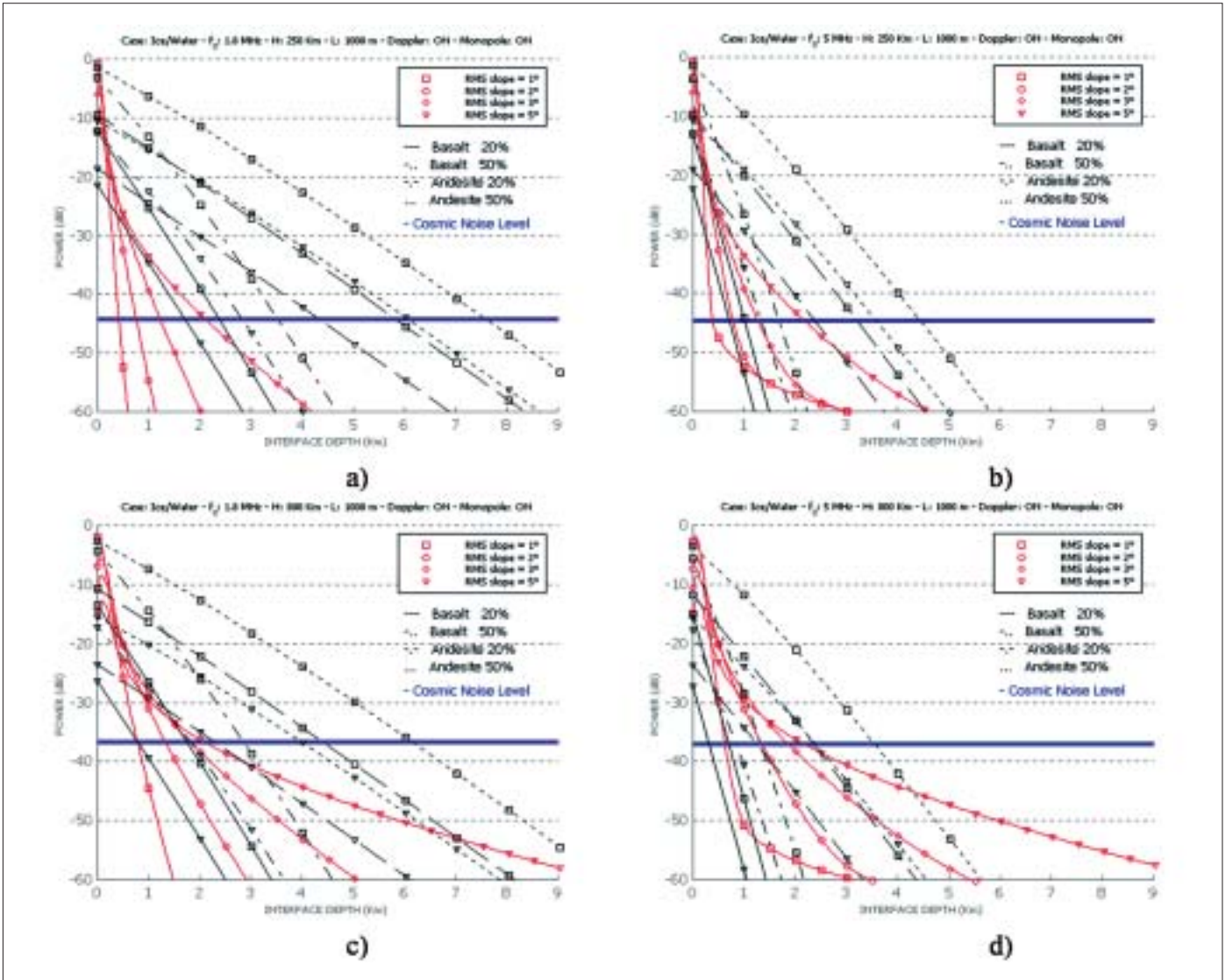
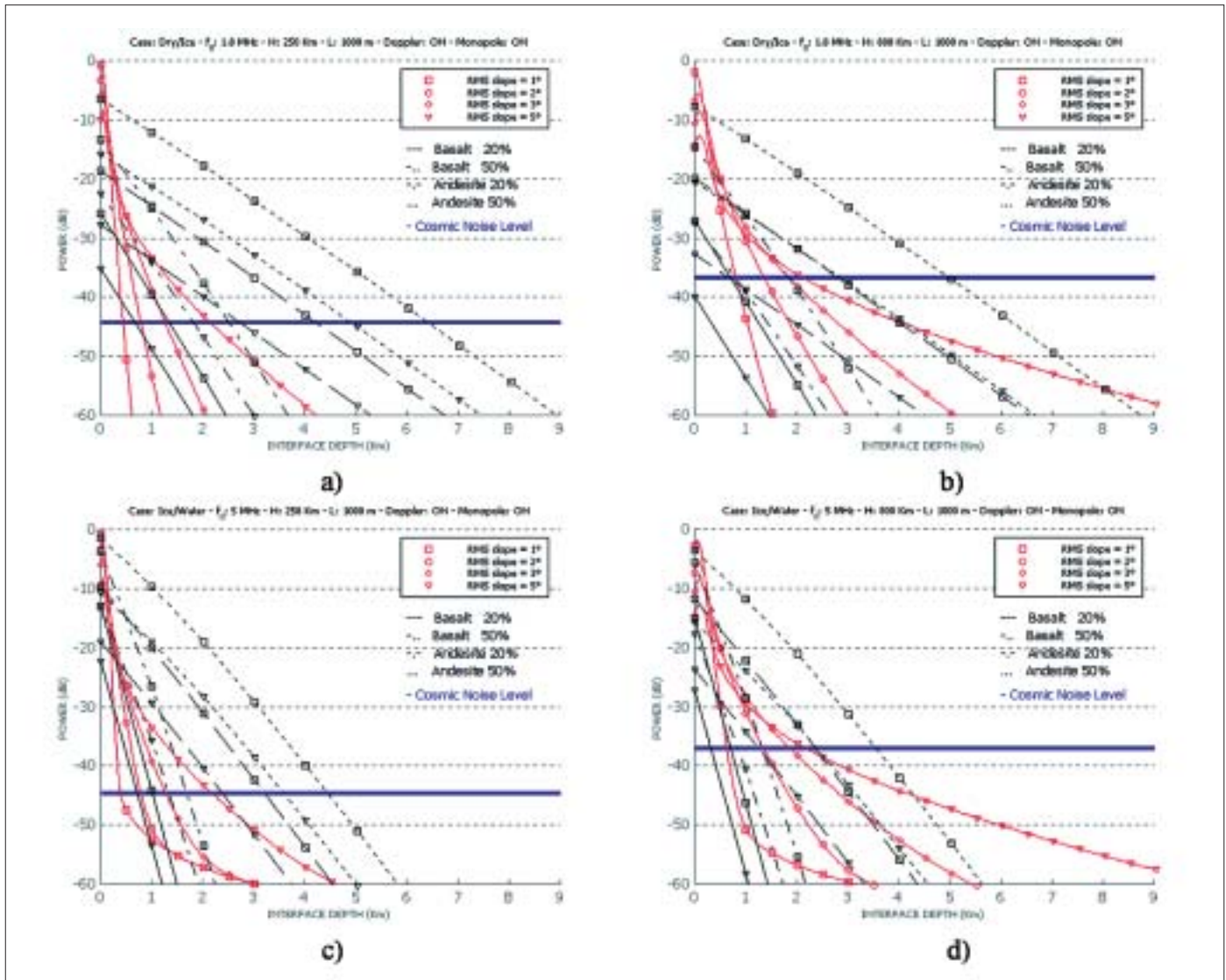


Fig. 9. Ice/Water interface detection charts. Subsurface attenuation (including absorption and scattering loss) appears in black; surface clutter after coherent cancellation in red; noise floor in blue. Altitudes are $H = 250$ km and 800 km; frequencies are 1.8 MHz and 5 MHz. Surface correlation length is 1000 m.

In practice, the dual-antenna cancellation IF is limited by imperfect knowledge of the antenna pattern, unknown antenna pointing errors (roll and pitch angles) and amplitude/phase mismatching between the two channels. In Picardi et al. (1999a), these effects were considered and it was concluded that the main limitation to the IF comes from the antenna pattern knowledge and the cross-track pointing error of the monopole (roll angle).

Typical IF behaviour as a function of the antenna gain variance σ_g^2 and the spacecraft roll angle α is shown in Fig. 8b. Values of 10% accuracy in the knowledge of the antenna patterns and $\pm 1^\circ$ roll angle result in a maximum IF of about 20 dB. Note that this clutter cancellation technique could also be performed on the square-law detected signals on the two dipole and monopole channels, but with reduced performance.

Another technique for clutter suppression, based on non-coherent processing of echoes acquired simultaneously at different frequencies, has been proposed (Picardi et al., 1999a), in order to provide surface clutter cancellation if the dual-antenna technique proves insufficient (for example, owing to problems in positioning the monopole null) or cannot be applied because monopole channel data are not available on the ground. The dual-frequency technique uses the fact that the surface clutter



power at two frequencies remains almost constant (or the changes can be easily predicted by modelling), while the subsurface power is a strong function of frequency. As consequence, if the detected signals at both frequencies are subtracted, the surface contribution is significantly reduced while the subsurface contribution remains unchanged. The main limitation of this technique arises from the speckle which decorrelates at the two frequencies, and represents a clutter residual after cancellation. If the mean powers of surface clutter at the two frequencies are assumed to be equal, IF can be shown to be linearly related to the number of averaged looks before subtraction of the signal (Picardi et al., 1999a). As clearly seen in Fig. 8c, an IF of about 5 dB can be obtained using five averaged looks.

8.4 Subsurface return signal-to-noise performance

Figures 9-10 summarise the predicted performance of the radar sounder in detecting the ice/water and dry/ice subsurface interfaces, according to the simple models described above and using the nominal MARSIS design parameters discussed in Section 6.1. Figure 9 refers to ice/water interface detection, and Fig. 10 to dry/ice. The four graphs in each figure present the detection at the two boundary frequency

Fig. 10. Dry/Ice interface detection charts. Subsurface attenuation (including absorption and scattering loss) appears in black; surface clutter after coherent cancellation in red; noise floor in blue. Altitudes are $H = 250$ km and 800 km; frequencies are 1.8 MHz and 5 MHz. Surface correlation length is 1000 m.

bands (1.8 MHz and 5 MHz) from two altitudes (250 km and 800 km), which represent the minimum and maximum heights of Mars Express during the portion of the orbit when MARSIS is active. Each detection chart contains the following normalised power levels as a function of the interface depth:

- subsurface return power, including effects of absorption and scattering. Absorption is taken into account as in Section 8.1, assuming the two end-member host materials (basalt and andesite) and porosities (20-50%). The backscattering is computed assuming a subsurface correlation length equal to 2000 m and two extreme values of the subsurface layer rms slope (1° and 5°);
- surface clutter power after coherent clutter cancellation, including Doppler filtering and dual-antenna cancellation (dual-frequency cancellation is not considered because we want to evaluate single-look performance). Two values of rms slope are used, between 1° and 5°, while the surface correlation length is also assumed to be 2000 m;
- noise floor level, computed to match the S/N values reported in Section 8.2, plus a little increment from the receiver internal noise amplification after the dual-antenna cancellation.

Based on a 0 dB detection threshold criterion, it is easily seen from the figure that, thanks to the surface clutter cancellation techniques and to the strong noise suppression, penetration depths to several kilometres can be achieved under the most likely scenarios for the martian crust.

9. Ionospheric Sounding Performance

Since the ionosphere is a very good specular reflector, the S/N for active ionospheric sounding is expected to be good. The main difficulty is that, at frequencies below the half-wavelength resonance of the antenna (~3 MHz), the radiated power decreases rapidly with decreasing frequency (approximately as frequency to the fourth power). This is compensated for to some extent by the fact that the range to the ionospheric reflection point decreases with decreasing frequency (Fig. 2a), which tends to improve the S/N at low frequencies. Also, at frequencies below ~1 MHz, the cosmic noise background falls with decreasing frequency, which also improves the S/N at low frequencies. At a spacecraft altitude of 500 km, the resulting S/N for the daytime ionospheric model shown in Fig. 2a is expected to be 5.4 dB at 0.1 MHz, increasing to 8.6 dB at 0.3 MHz, 18.4 dB at 1.0 MHz and 21.3 dB at 3.0 MHz. These S/Ns are adequate to perform ionospheric sounding on the dayside of Mars under almost all conditions. On the night side, where the electron densities are expected to be much lower, the S/N is likely to become marginal, since the plasma frequencies are much lower, which increases the range to the reflection point for any given spacecraft altitude. It is also possible that the ionosphere may be more disturbed on the nightside of Mars, which could cause scattering from small-scale irregularities, thereby causing a further reduction in the S/N. Although the ionospheric sounding performance is somewhat marginal on the nightside, it is almost certain that useful information will be obtained, particularly at low altitudes where the range to the reflection point is very small. Also, a very strong return signal is expected when the sounding frequency passes through the local plasma frequency, which will give the local electron plasma density under almost all conditions.

References

- Biccari, D., Picardi, G., Seu, R. & Melacci, P.T. (2001a). Mars Surface Models and Subsurface Detection Performance in MARSIS. In *Proc. IEEE International Symp. on Geoscience and Remote Sensing, IGARSS 2001*, Sydney, Australia, 9-13 July 2001.
- Biccari, D., Ciabattoni, F., Picardi, G., Seu, R., Johnson, W.K.T. Jordan, R., Plaut, J., Safaeinili, A., Gurnett, D.A., Orosei, R., Bombaci, O., Provvedi, F., Zampolini, E. & Zelli, C. (2001b). Mars Advanced Radar for Subsurface and Ionosphere Sounding (MARSIS). In *Proc. 2001 International Conference on Radar*, October 2001, Beijing, China.
- Biccari, D., Cartacci, M., Lanza, P., Quattrociochi, M., Picardi, G., Seu, R., Spanò, G. & Melacci, P.T. (2001c). *Ionosphere Phase Dispersion Compensation*, Infocom Technical Report N.002/005/01-23/12/2001.
- Carr, M.H. (1996). *Water on Mars*, Oxford University Press, Oxford, UK.
- Fung, A.K. & Eom, H.J. (1983). Coherent Scattering of a Spherical Wave from an Irregular Surface. *IEEE Trans. on Antennas and Propagation*, **AP-31**(1), 68-72.
- Hanson, W.B., Sanatani, S. & Zuccaro, D.R. (1977). The Martian Ionosphere as Observed by the Viking Retarding Potential Analyzers. *J. Geophys. Res.* **82**, 4351-4363.
- Picardi, G. & Sorge, S. (1999). *Adaptive Compensation of Mars Ionosphere Dispersion: A Low Computational Cost Solution for MARSIS*, Infocom Technical Report MRS-002/005/99, October 1999.
- Picardi, G., Plaut, J., Johnson, W., Borgarelli, L., Jordan, R., Gurnett, D., Sorge, S., Seu, R. & Orosei, R. (1998a). *The Subsurface Sounding Radar Altimeter in the Mars Express Mission, Proposal to ESA*, Infocom document N188-23/2/1998, February 1998.
- Picardi, G., Sorge, S., Seu, R., Fedele, G., Federico, C. & Orosei, R. (1999a). *Mars Advanced Radar for Subsurface and Ionosphere Sounding (MARSIS): Models and System Analysis*, Infocom Technical Rep. MRS-001/005/99, March 1999.
- Picardi, G., Sorge, S., Seu, R., Fedele, G. & Jordan, R.L. (1999b). Coherent Cancellation of Surface Clutter Returns for Radar Sounding. In *Proc. IEEE International Symp. on Geoscience and Remote Sensing, IGARSS'99*, Hamburg, Germany, 28 June - 2 July 1999, pp2678-2681.
- Safaeinili, A. & Jordan, R.L. (2000). Low Frequency Radar Sounding through Martian Ionosphere. In *Proc. IGARSS 2000*, 24-28 July 2000, Honolulu, Hawaii, IEEE, pp987-990.
- Stix, T.H. (1964). *The Theory of Plasma Waves*, McGraw-Hill, New York.
- Zhang, M.H.G., Luhmann, J.G., Kliore, A.J. & Kim, J. (1990a). A Post-Pioneer Venus Reassessment of the Martian Dayside Ionosphere as Observed by Radio Occultation Methods. *J. Geophys. Res.* **95**, 14,829-14,839.
- Zhang, M.H.G., Luhmann, J.G., Kliore, A.J. & Kim, J. (1990b). An Observational Study of the Nightside Ionospheres of Mars and Venus with Radio Occultation Methods. *J. Geophys. Res.* **95**, 17,095-17,102.

PFS: the Planetary Fourier Spectrometer for Mars Express

V. Formisano¹, D. Grassi¹, R. Orfei¹, D. Biondi¹, E. Mencarelli¹, A. Mattana¹, F. Nespoli¹, A. Maturilli¹, M. Giuranna¹, M. Rossi¹, M. Maggi¹, P. Baldetti¹, G. Chionchio¹, B. Saggin², F. Angrilli², G. Bianchini², G. Piccioni³, A. Di Lellis³, P. Cerroni³, F. Capaccioni³, M.T. Capria³, A. Coradini³, S. Fonti⁴, V. Orofino⁴, A. Blanco⁴, L. Colangeli⁵, E. Palomba⁵, F. Esposito⁵, D. Patsaev⁶, V. Moroz⁶, L. Zasova⁶, N. Ignatiev⁶, I. Khatuntsev⁶, B. Moshkin⁶, A. Ekonomov⁶, A. Grigoriev⁶, V. Nechaev⁶, A. Kiselev⁶, Y. Nikolsky⁶, V. Gnedych⁶, D. Titov⁶, P. Orleanski⁷, M. Rataj⁷, M. Malgoska⁷, A. Jurewicz⁷, M.I. Blecka⁷, H. Hirsh⁸, G. Arnold⁸, E. Lellouch⁹, A. Marten⁹, T. Encrenaz⁹, J. Lopez Moreno¹⁰, S. Atreya¹¹ & P. Gobbi¹²

¹*Istituto di Fisica dello Spazio Interplanetario CNR (IFSI), Via del Fosso del Cavaliere 100, I-00133 Roma, Italy*

Email: formisan@nike.ifs.rm.cnr.it

²*Universita di Padova, Dipartimento Ingegneria Meccanica (DIUNP), Via Venezia 1, I-35131 Padova, Italy*

³*Istituto Astrofisica Spaziale CNR (IAS), Reparto di Planetologia, Viale dell'Universita 11, I-00185 Roma, Italy*

⁴*Universita degli Studi di Lecce, Dipartimento di Fisica Via Arnesano, I-73100 Lecce, Italy*

⁵*Osservatorio Astronomico di Capodimonte (OAC), Via Moiariello 16, I-80131 Napoli, Italy*

⁶*Space Research Institute of Russian Academy of Sciences (IKI), Profsojuznaja 84/32, 117810 Moscow, Russia*

⁷*Space Research Center of Polish Academy of Sciences (SRC PAS), Bartycka 18A, 00716 Warsaw, Poland*

⁸*Deutsche Forschungsanstalt fur Luft und Raumfahrt (DLR), Institut fur Planetenerforschung, Rudower Chausse 5, D-12489 Berlin Adlershoft, Germany*

⁹*Observatoire de Paris Meudon, Department de Recherch Spatiale (DESPA), Place J. Janssen 5, F-922195 Meudon, France*

¹⁰*Istituto de Astrofisica de Andalusia CSIC, p.o.b. 3004, E-18080 Granada, Spain*

¹¹*The University of Michigan, Planetary Science Laboratory, 2455 Hayward Ave., Ann Arbor, MI 48109-2143, USA*

¹²*Istituto di Fisica dell'Atmosfera CNR (IFA), Via del Fosso del Cavaliere 100, I-00133 Roma, Italy*

The Planetary Fourier Spectrometer (PFS) for the Mars Express mission is optimised for atmospheric studies, covering the IR range of 1.2-45 μm in two channels. The apodised spectral resolution is 2 cm^{-1} , while the sampling is 1 cm^{-1} . The FOV is about 2° for the short wavelength (SW) channel and 4° for the long wavelength (LW) channel, corresponding to spatial resolutions of 10 km and 20 km, respectively, from an altitude of 300 km. PFS will also provide unique data on the surface-atmosphere interaction and the mineralogical composition of the surface. It will be the first Fourier spectrometer covering 1-5 μm to orbit the Earth or Mars.

The experiment has real-time onboard Fast Fourier Transform (FFT) in order to select the spectral range of interest for data transmission to ground. Measurement of the 15- μm CO₂ band is very important. Its profile gives, via a complex temperature-profile retrieval technique, the vertical pressure temperature relation, which is the basis of the global atmospheric study. The SW channel uses a PbSe detector cooled to 200-220K, while the LW channel is based on a pyroelectric (LiTaO₃) device working at room temperature. The interferogram is measured at every 150 nm displacement step of the corner cube retroreflectors (corresponding to 600 nm optical path difference) via a laser

diode monochromatic interferogram (a sine wave), with the zero crossings controlling the double pendulum motion.

PFS will operate for about 1.5 h around the pericentre of the orbit. With a measurement every 10 s, 600 measurements per orbit will be acquired, corresponding to 224 Mbit. Onboard compression will reduce it to 125 Mbit or less, depending on the allocated data volume per day. An important requirement is to observe at all local times in order to include night-side vertical temperature profiles. Total instrument mass is 31.2 kg.

1. Scientific Objectives

1.1 Introduction

In the past 30 years, ground-based observations and space missions have built an impressive body of information about Mars. Nevertheless, a large number of questions remain open. One of the most interesting problems is the evolution of the climate and atmosphere in relation to water. It is widely believed that the younger Mars possessed a dense atmosphere and liquid water on the surface. However, careful investigation of the recent atmosphere and surface is required for clarification.

The widespread use of IR spectroscopy in recent years for systematically studying planetary surfaces and atmospheres has detected molecular species in both major and minor quantities. Strong vibration-rotation bands in the 1-20 μm wavelength range are the fingerprints for unambiguous identification of chemical species. Many spectral bands of CO_2 , H_2O and CO come within the range of sensitivity of PFS. Their detection will help to solve a wide set of scientific problems concerning atmospheric composition, solid-phase surface components and atmospheric dust.

In the near-IR range, where the incident solar radiation is either absorbed or scattered by molecules and dust grains, molecular bands usually appear in absorption. In the far-IR, molecular bands appear in both emission and absorption because the observed flux strongly depends on the thermal profile of the atmosphere.

However, even when the absolute intensities of the molecular bands are known from laboratory studies, it can be far from simple to derive the abundance of atmospheric constituents from a planetary spectrum. In the near-IR, a rough estimate of the absorber abundance can be obtained using the 'reflecting layer model'. This model assumes no scattering above a purely reflecting layer (cloud or surface). It is reasonable to apply it to the case of a tenuous atmosphere, such as that on Mars. Various methods can be used to determine the temperature-pressure T(P) relationship. In the cases of Mars, Venus and Jupiter, thermal profiles have been derived from strong absorption bands in the thermal-IR and also from radio occultation measurements by probes such as Mariner and Pioneer (Kliore et al., 1972; 1976). *In situ* measurements have been made on Mars and Venus.

Near-IR spectroscopy has greatly increased our knowledge of the surface composition and structure of planetary bodies, moons and asteroids. For planets with atmospheres, the identification of surface spectral signatures is strongly related to the simultaneous knowledge of the atmospheric structure. Electronic and molecular transitions occur at definite energies associated with near-IR wavelengths and result in the absorption of incident solar radiation by surface materials. In the visible and near-IR range (up to approximately 2.5 μm), transition of d-shell electrons and electron exchange between ions dominate. Particularly evident are the signatures from iron ions (e.g. McCord & Cruikshank, 1981). At longer wavelengths, the crystal structure and the nature of different rocks and minerals can be discriminated on the basis of the strength and position of absorption bands (e.g. Bartholomew et al., 1990).

A number of mineralogically significant bands of silicates, carbonates, sulphates, nitrates, phosphates, oxides and hydroxile-bearing materials occur in the thermal-IR. A great amount of laboratory work has been devoted to the systematic study of the relative strengths and positions of diagnostic spectral signatures (e.g. Hunt et al., 1974). Experimental results are supported by theoretical models in which the relations

Table 1. PFS scientific objectives.

Atmospheric studies: global long-term monitoring of the 3-D temperature field in the lower atmosphere (from the surface up to 40-60 km); measuring the variations of minor constituents (water vapour and carbon monoxide); searching for other minor components of the atmosphere; a new determination of the D/H ratio; studying the optical properties of atmospheric aerosols (dust clouds, ice clouds, hazes) and determining their size distributions and chemical compositions; investigating the radiance balance of the atmosphere and the influence of aerosols on atmospheric energetics; studying global circulation, mesoscale dynamics and wave phenomena.

Surface studies: monitoring the surface temperature; determining the thermal inertia obtained from the daily surface temperature variations; determining the restrictions on the mineralogical composition of the surface layer; determining the nature of the surface condensate and seasonal variations of its composition; measuring the scattering phase function for selected surface locations; determining local pressure and height (CO₂ altimetry) for selected regions; surface-atmosphere exchange processes.

between IR spectral signatures and ion mass band strength and crystal structure were investigated (e.g. Carr, 1974).

1.2 The atmosphere of Mars

Mars resembles the Earth much more than any other planet in the Solar System, and studying its atmosphere provides a better understanding of our own. There is evidence of an earlier denser martian atmosphere, warmer climate and free water on the surface. However, explaining how warming was supported on the young Mars is not easy. The history of water on Mars is one of the most interesting problems in Solar System studies, and it directly connects with the possible presence of life on ancient Mars.

The investigations of Mars' atmosphere have determined an average composition of mainly carbon dioxide (95%), nitrogen (2.7%) and argon (1.6%) (Owen, 1992). About ten minor constituents have been identified. Of them, water vapour plays an important role in atmospheric processes and surface/atmosphere interactions. Water vapour bands will be observed by both PFS channels; monitoring water vapour variations (time, latitude, location) is an important task for PFS, and simultaneous observations in the two channels will provide estimates of H₂O vertical distribution.

The global annual average surface temperature of Mars is 210K (Arnold et al., 1993); the atmosphere is colder than Earth's at all heights. In general, the vertical structure of both can be divided into three main regions: low, middle (mesosphere) and upper (thermosphere). The middle atmosphere of Mars is its coldest region. Here is the sink for the energy flux coming from the surface and troposphere (heated by solar visible and near-IR) and the thermosphere. There are several important qualitative differences with the terrestrial atmosphere:

- there is no temperature maximum in the mesosphere;
- the lapse rate in the low atmosphere is less than on Earth;
- there are strong daily variations near the surface because of the much lower thermal capacity;
- the strong influence of aerosols on atmospheric heating.

The computation of realistic General Circulation Models (GCMs) is a very difficult task because it has to accommodate so many different effects. Horizontal differences in temperatures lead to differences in pressure, but they are smoothed by winds. Winds transfer heat together with air masses, influencing local temperature profiles. Temperatures are also affected by dust being lifted from the surface. Condensation is another route to aerosol formation, and it also feeds back to

temperatures. Winds vary with topography. However, a few groups of theoreticians have made significant large progress in GCM modelling. They work mainly with data from Mariner-9/IRIS for Ls 290-350° and much less for Ls 45-55° (full profiles; Ls is the angle between the Sun-Mars line and the northern spring equinox) and the much less informative Viking/IRTM atmospheric temperatures. PFS LW observations of the 15 µm band will help to fill the gaps. Such measurements will strengthen the empirical base for checking the martian GCMs.

Aerosols play a major role in the formation and variations of 3-D temperature and wind patterns in the atmosphere. There are two aerosol types: dust lifted from the surface, and condensates. A Global Dust Storm is the most pronounced manifestation of the influence of dust on martian meteorology, but aerosols are always present in the atmosphere and both kinds participate in heating/cooling processes. The chemical nature (minerals/ices), size distribution and optical depth of the aerosol medium will be estimated from PFS observations. Simultaneous observations by the two channels should be very helpful.

Previous data exhibited both seasonal and daily variations, and occasional climatic events. During northern winter, two different regimes have been observed in different years. In the first case, one or more dust storms cover nearly all the planet; in the second, there is no global storm but high winds raise dust in confined regions. By contrast, summer weather appears to be more repetitive: winds are generally low and evolve on a diurnal timescale. Storms are very peculiar events and require more detailed investigation. Pressure profiles, wind patterns and atmospheric dust-evolution must be carefully analysed to determine the effects on surface morphology. Surface changes produced by atmospheric activity have been revealed by observations of albedo patterns, and suggest close coupling of surface morphology with ambient evolution. In particular, chemical and physical processes at the lithosphere-atmosphere boundary must be better described and understood.

Temperature changes control the polar cap condensation rate and influence the formation and the evolution of clouds. Until now, white condensation (mainly water-ice) clouds have been observed; however, their evolution and detailed composition are still uncertain.

Atmospheric data can also be helpful, in combination with surface composition analyses, in determining the:

- distribution, abundance and physical status of water on the planet;
- volatile distribution and abundance in the atmosphere, on the crust, and at depth;
- outgassing processes.

The spectrum of Mars (as for any planet) consist of two elements: short wavelengths dominated by bireflected solar radiation, and long wavelengths dominated by the planet's thermal radiation. For Mars, the boundary between these two regimes is near 4 µm. The PFS SW and LW ranges almost match these regimes of the martian spectrum. Bands of atmospheric gases in the SW range appear only as absorption features; in the LW they can appear as absorption (if atmospheric temperature falls with height) or emission (if it rises), and occasionally the band may have a complicate shape.

1.3 Thermal sounding of the martian atmosphere

1.3.1 Physical background

In a strong absorption band, the thermal radiation emitted from the surface and lower atmospheric levels is absorbed by the higher regions and cannot escape to space. However, the strength of absorption bands usually varies by several orders of magnitude within a given spectral interval. If the outgoing radiation is measured across the entire band then different parts will bear information about the temperature at different altitudes.

The thermal sounding needs several conditions to be satisfied. First, the gas must

have spectral bands in the thermal-IR region. Second, the gas must be abundant enough to give strong absorption in the centre of the band in order to maximise the altitude range of sounding. Third, it is desirable that the gas is uniformly mixed within the bulk of the atmosphere and its abundance must not vary significantly with space, local time or season. Carbon dioxide meets these requirements rather well for the terrestrial planets. That is why CO₂ fundamental bands are usually chosen for thermally sounding the atmospheres of Venus, Earth and Mars.

The solution of radiative transfer equation for the outgoing radiation takes the form:

$$I(\nu) = \varepsilon(\nu) B(\nu, T_s) t(\eta_s, -\infty) + \int_{\eta_s}^{-\infty} B[\nu, T(\eta)] K(\nu, \eta) d\eta \quad (1)$$

where ν is the wavenumber, $\eta = \log(p)$ (p is pressure) is the vertical coordinate, ε and T_s are the emissivity and temperature of the surface, respectively, B is the Planck function describing the blackbody radiation, $T(\eta)$ is the vertical temperature profile, and

$$K(\nu, \eta) = - \frac{\partial t(\eta, -\infty)}{\partial \eta} \quad (2)$$

is the weighting function, where $t(\eta, -\infty)$ is the transmittance between the atmospheric level η and space along the line-of-sight. The first term in Eq. (1) corresponds to the radiation from the surface attenuated by the atmosphere. The second one describes the emission of the atmosphere. The weighting functions $K(\nu, \eta)$ define the weight with which the atmospheric layer at pressure η contributes to the radiation measured at wavenumber ν . Eq. (1) is written under the following assumptions:

- the atmosphere is plane parallel. This is valid until the emission angle is smaller than $\sim 80^\circ$;
- the scattering is neglected. This assumption is valid for almost all seasons on Mars because the dust loading is small. Only during dust storms should the scattering by dust be taken into account and Eq. (1) modified;
- it is assumed that the local thermodynamic equilibrium (LTE) requirement is met. This assumption means that the scattering in spectral lines is negligible and the energy of each absorbed photon is converted to the thermal energy of the gas via molecular collisions. This provides the necessary coupling between the radiation and kinetic temperature of the emitting gas. Detailed studies showed that the LTE conditions are fulfilled in the martian atmosphere at least in the altitude region 0-60 km, which will be covered by PFS.

1.3.2 PFS temperature sounding capabilities

The positions of the absorption bands of CO₂ gas in the PFS spectral region are shown in Fig. 1. The central wavenumbers and line intensities were taken from the HITRAN database (Rothman et al., 1992). Two very strong fundamental bands of CO₂ are in the thermal-IR region (200-2500 cm⁻¹) and they can be used for thermal sounding. The first at 15 μm is in the region of maximum radiation from Mars and is optimal for thermal sounding. The band at 4.3 μm falls in the spectral interval where the thermal radiation is already low and the contribution from reflected solar light is not negligible. However, this band can be used at least at the night side to improve the quality of thermal sounding provided by the 15 μm band. PFS will be the first instrument to measure the outgoing radiation in these two bands simultaneously.

The altitude coverage and vertical resolution of the remote sensing are defined by

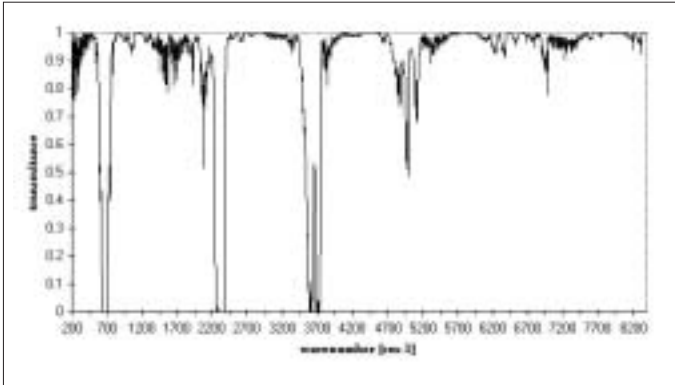


Fig. 1. Transmittance of gases in the atmosphere of Mars.

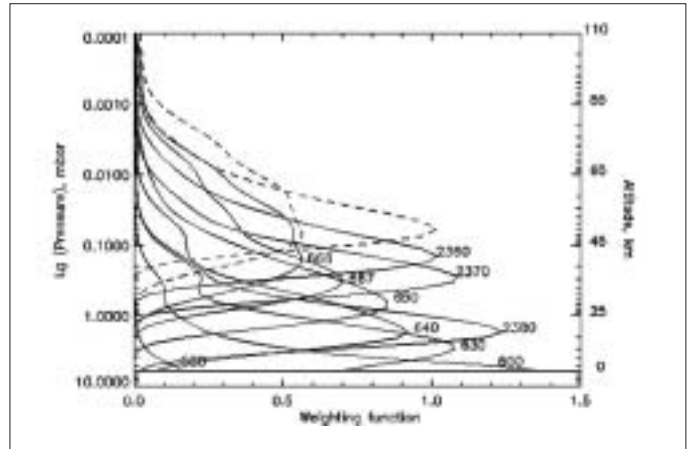


Fig. 2. Carbon dioxide weighting functions for the 4.3 μm and 15 μm absorption bands.

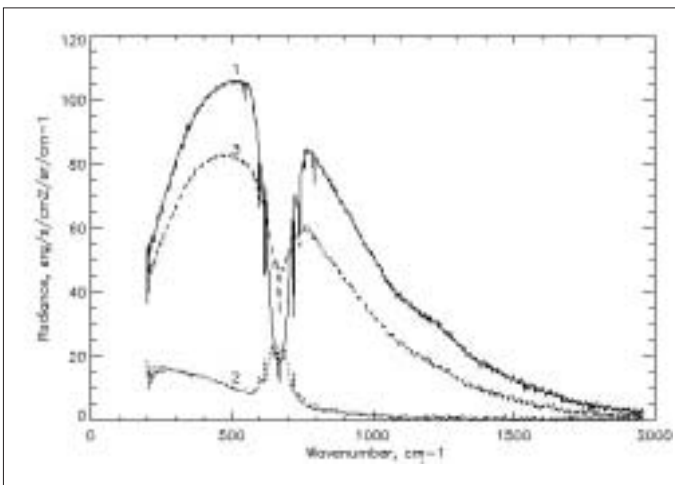


Fig. 3. Synthetic spectra in the LW channel of PFS.

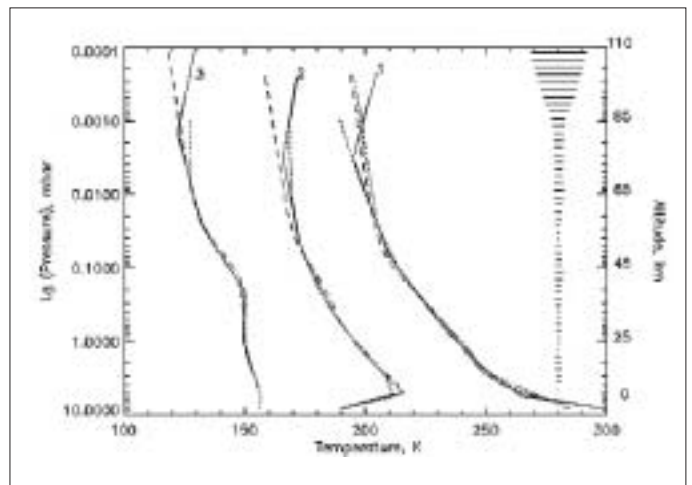


Fig. 4. Test temperature retrievals from PFS spectra.

the behaviour of weighting functions (Eq. 2). Examples of the weighting functions for PFS are shown in Fig. 2. The numbers on the curves designate the wavenumber: 550-668 cm^{-1} corresponds to 15 μm and 2360-2380 cm^{-1} to 4.3 μm . PFS weighting functions cover the pressure range from the surface up to $\sim 10^{-3}$ mbar, corresponding to altitudes 0-70 km. However, the effectiveness of thermal sounding drops as the weighting functions decrease with altitude. The width of weighting functions is defined by the scale height of the atmosphere (~ 10 km) and the band structure. From Eq. 1 it is clear that broad weighting functions smooth small-scale features of the temperature profile. Nevertheless, practise shows that the features much smaller than the width of the weighting function can be retrieved from the emission spectrum because many spectral channels are used. The vertical resolution is estimated to be 3-5 km.

Additional use of the measurements in the 4.3 μm CO_2 band can improve the quality of the sounding, especially above 30 km. At these altitudes, the weighting functions for 15 μm (667 cm^{-1} and 668 cm^{-1}) are very broad. Those for the 4.3 μm band (2360 cm^{-1} and 2370 cm^{-1}) have smaller widths. These channels can provide better determination of the temperature profile above 30 km. The sounded region can

be extended upward by ~ 10 km in the off-nadir observations allowed by the PFS scanning capability. Fig. 2 (dashed lines) shows examples of weighting functions for slant geometry with emission angle of 80° for the 668 cm^{-1} and 2360 cm^{-1} channels.

1.3.3 Test temperature retrievals from PFS radiance spectra

The vertical temperature profile $T(\eta)$ is the solution of the non-linear integral Eq. 1 using the radiance measurements $I(\nu)$ in the CO_2 band. The solutions of this problem are unstable with respect to small perturbations of the right hand side of the equation. The experimental errors in the measured radiance spectrum can result in a non-physical temperature profile. The procedures that can provide a stable solution of the ill-posed problems are *regularisation* algorithms. They use various kinds of *a priori* information about the solution in order to select physically meaningful functions among mathematically possible solutions.

Several methods were developed to solve the thermal-sounding Eq. 1. The Smith iterative (Smith, 1970) and Tikhonov regularisation (Tikhonov et al., 1990) methods were used for testing temperature retrievals from PFS radiance spectra. First, using the MARSGRAM software (Justus et al., 1995), three ‘true’ temperature profiles were selected, representing the variety of conditions on Mars: 1 equatorial day model; 2 equatorial night model; 3 polar summer model. The synthetic spectra of the outgoing radiation calculated for each temperature model and dust-free atmosphere are shown in Fig. 3.

Each retrieval algorithm organises its own process of iterative correction of the initial profile. It is done in different ways but all the methods tend to reduce the deviation of the synthetic profile from the ‘measured’ one.

The surface pressure is usually a free parameter in the retrieval procedures. However, the measurements in the $2.0\text{ }\mu\text{m}$ CO_2 band simultaneously carried out in the PFS short wavelength channel will provide the necessary data on the surface pressure, at least for daytime observations. So it was assumed that the surface pressure was known in this set of test retrievals.

Temperature profiles retrieved by the Smith iterative and Tikhonov regularisation methods are compared in Fig. 4 with the ‘true’ profiles. The retrieval error bars for dust-free tests are also presented in the right side of the figure. The following conclusions about the PFS temperature-sounding capabilities can be drawn from the test retrievals:

- in the dust-free atmosphere, the temperature profile can be retrieved from the measurements in the $15\text{ }\mu\text{m}$ CO_2 band with an accuracy of $\sim 3\text{K}$ in the altitude region 0-65 km. This value can be considered as the noise of the retrieval procedures. The accuracy of the retrievals from the actual measurements will depend on the signal-to-noise ratio (S/N) achieved in the PFS measurements;
- the retrieval errors increase above 65 km because the weighting functions decrease with altitude (Fig. 2) and the radiance measurements are no longer sensitive to atmospheric temperature;
- the retrieval accuracy at the surface is 2-3K by deriving the surface pressure from the $2.0\text{ }\mu\text{m}$ CO_2 measurements. This was proved by several test retrievals with the wrong surface pressure;
- test temperature retrievals from the dusty spectrum without taking aerosols into account resulted in $\sim 10\text{K}$ errors in the lower 10 km of the atmosphere.

1.3.4 The influence of aerosols

Dust is always present in the martian atmosphere. Its abundance varies significantly with season and from year to year. Its optical depth changes from 0.2 to more than unit in the visual range. The absorption features of palagonite dust were discovered in Mariner-9 spectra. In the short wavelength wing of the $15\text{ }\mu\text{m}$ CO_2 band, the water ice features have been found in Mars Global Surveyor/TES spectra. They were observed at high zenith angle, together with palagonite bands.

The influence of aerosols on martian spectra were modelled, assuming the presence of palagonite aerosols (optical parameters were taken from Roush et al., 1993) with modified gamma particle size distribution (Pollack & Toon, 1982):

$$n(r) \propto r^\alpha \exp\left[\frac{-\alpha}{\gamma (r/r_m)^\gamma}\right] \quad (3)$$

The modal radius $r_m = 0.4$, effective radius $r_{eff} = 1.6 \mu\text{m}$ and constants $\alpha = 1$ and $\gamma = 1$ were used. In the spectral range favourable for temperature and aerosol retrieval, the single scattering albedo is less than 0.4; aerosol particles are black and non-scattering. In order to model the aerosol influence in the spectral range of temperature retrieval, spectra were calculated for optical depth $\tau = 0.3, 1, 10$, and scale height $H_a = 10 \text{ km}$ at zenith angles of observations 0° and 70° . The results are shown in Fig. 5.

The aerosol influence on the spectra can be summarised as:

- aerosol absorption increases the altitude of the effective emission level. So a temperature profile retrieved with pure gaseous transmission functions relates to the shifted levels;
- aerosol absorption can be asymmetrical in the wings of the $15 \mu\text{m}$ band. The absorption coefficient is doubled in the long wavelength wing. The measured brightness temperature in the short wavelength wing agrees with calculations, although in the long wavelength wing it is systematically lower.

1.4 The 3-D global atmospheric circulation

Direct observations of winds in the martian atmosphere are very rare, available for only a few landing sites. Wind direction and speed derived from cloud tracking and aeolian streaks correspond to the boundary layer and are often ambiguous (see Zurek et al., 1992, and references therein). Remote sounding from orbit remains the most valuable source of information about the large-scale dynamics of the atmosphere. Long-term global monitoring by PFS of such atmospheric parameters as vertical temperature profiles, aerosol optical depth, surface pressure and water vapour column density will provide an important insight into the following aspects of the atmospheric dynamics:

Global circulation. The fundamentals of atmospheric dynamics on rapidly rotating planets like Earth and Mars show that geostrophic winds derived from the remotely determined 3-D temperature field are a good approximation of the true large-scale atmospheric motions in a non-equatorial zone (Pedlosky, 1979). So far, thermal winds have been retrieved only from the Mariner-9/IRIS observations taken during the northern winter (Zurek et al., 1992). Long-term global temperature sounding of the martian atmosphere by PFS will have complete latitude, longitude and seasonal coverage in the altitude range from the surface up to about 60 km. This will allow us to determine systematically the wind pattern and to follow seasonal changes in global circulation. Simultaneous monitoring of the atmosphere's dust content will provide further insight into the role of dust in the atmospheric dynamics. PFS observations will also help us to understand the mechanisms of polar warming, which is supposed to be of a dynamical nature.

Wave phenomena. The experience gained from the analysis of Mariner-9/IRIS and Viking/IRTM data shows that similar observations of the atmospheric temperature field by PFS will allow us to study some important wave phenomena: thermal tides and their interaction with large-scale topography, quasi-stationary waves probably generated by instabilities in the mid-latitude zonal jet, and large-amplitude waves at high latitudes during the polar warming.

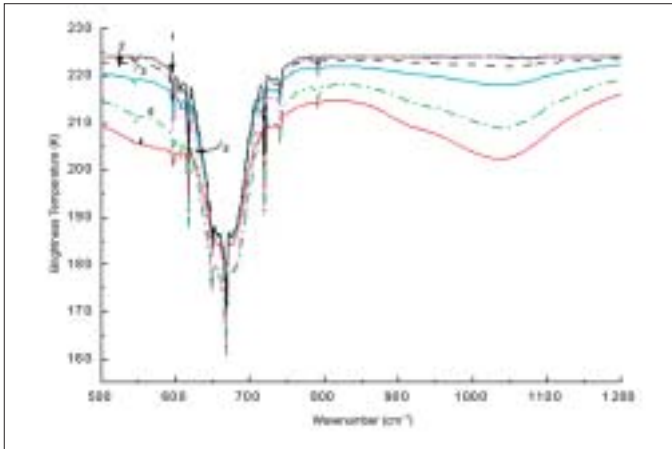


Fig. 5. Synthetic spectra of Mars' atmosphere, including the 9 μm palagonite absorption band.

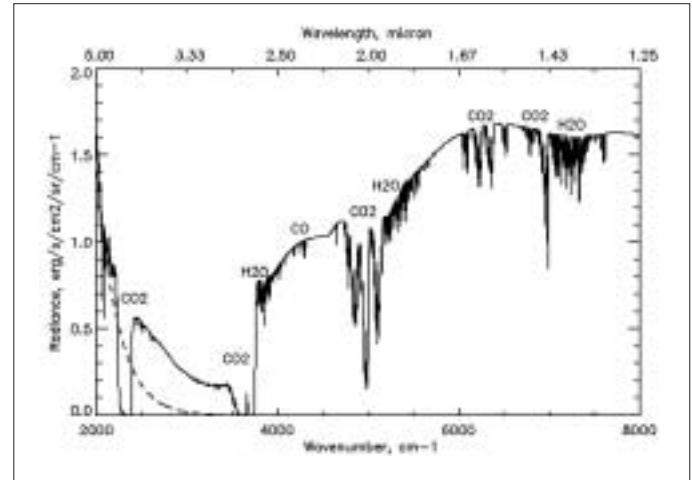


Fig. 6. Synthetic spectrum for the PFS SW channel.

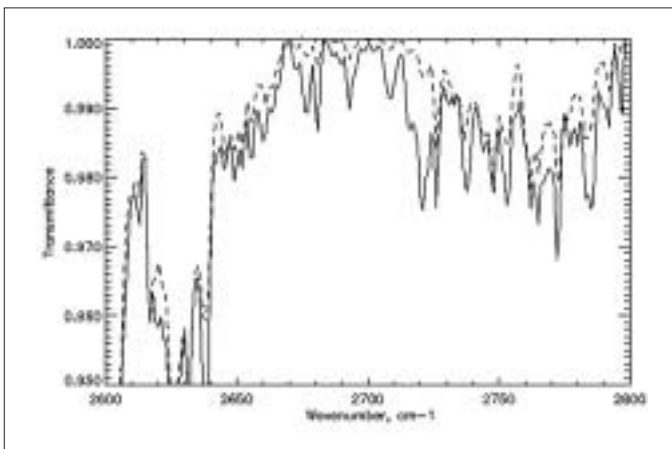


Fig. 7. Synthetic transmittance spectrum in the 3.7 μm HDO band.

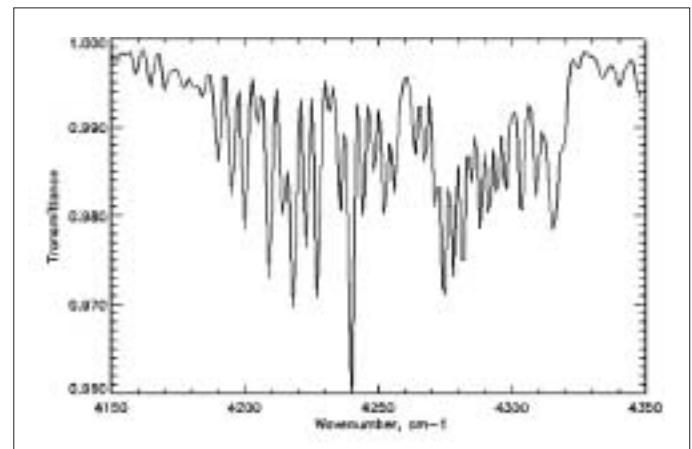


Fig. 8. Synthetic transmittance spectrum in the 2.35 μm CO band.

Transport of atmospheric species. Mars is a unique planet, where the main atmospheric component (carbon dioxide) is deposited on the polar caps in winter. This produces seasonal variations of up to 25% in surface pressure. Systematic measurements of this parameter by PFS will give an estimate of the mean meridional flow from summer to winter hemisphere. Furthermore, the water vapour that sublimates from the polar cap in summer and is then transported to the lower latitudes can be used as a tracer of the large-scale atmospheric motions (Haberle & Jakosky, 1990). PFS observations of atmospheric water will impose additional constraints on the transporting winds.

1.5 The minor constituents

Minor constituents identified in the atmosphere of Mars are H_2O , CO , O_2 , O_3 , He , Ne , Ar , Kr and Xe . Their mixing ratios are less than 10^{-3} . Four of these gases have bands in the PFS spectral range: H_2O , CO , O_3 , O_2 (Fig. 1). The bands of isotopes such as HDO , ^{13}C , $^{16}\text{O}_2$, ^{12}C , ^{16}O and ^{18}O are well separated from the bands corresponding to the main isotopes and may be used to re-estimate the isotopic ratios.

Synthetic spectra of Mars in the wide spectral range of 1.2–45 μm were computed

in order to analyse the PFS capabilities in the investigation of minor constituents. The general view of the martian spectrum in the near-IR range is shown in Fig. 6.

The spectrum demonstrates sharp absorption features of the atmospheric CO₂, H₂O and CO, and a broad spectral signature of surface minerals at ~3 μm. It also shows the contribution from thermal emission at λ > 4 μm (dashed line). The computations were performed for the nominal temperature model (mid-latitudes, northern summer) elaborated on the basis of Viking landing data (Seiff, 1982). PFS measurements will provide the H₂O detection limit of ~1 μm. The transmittance spectrum of HDO is shown in Fig. 7. Fig. 8 presents the CO transmittance spectrum for the mixing ratio of 6x10⁻⁴.

The martian volcanoes are the highest in the Solar System. They cover more than 2 atmospheric scale heights (~27 km in the case of Olympus Mons). Such topographical features offer the possibility of obtaining vertical profiles for trace gases and dust. PFS observations along the slopes will sound increasingly high altitudes as the field of view moves towards the top. However, the analysis of such observations is not straightforward because the vertical profiles of the species in the vicinity of the slopes can be affected by the surface-atmospheric interactions and can differ from those in the free atmosphere.

1.6 Water distribution and cycle in the martian atmosphere

The first detection of H₂O on Mars was made by Earth-based spectral observations at high resolution (about 0.1 Å) using the Doppler shift of weak lines with respect to much stronger telluric features in the band at 8200 Å (Spinrad & Richardson, 1963; Kaplan et al., 1964). If a telluric absorption line is not oversaturated, then a much weaker planetary feature belonging to the same gas can be visible on its wing because of Doppler shift. Water vapour in the martian atmosphere have been studied systematically using this method, including average abundance and latitude, daily and seasonal variations. Average water abundance of about 10 μm ppw (precipitable microns water equivalent) is a typical value. However, the ground-based observations had intrinsic limitations in spatial resolution and coverage.

Measurements of water bands in the atmosphere of Mars were also performed by several experiments onboard the orbiters Mars-3 (Moroz & Nadzhip, 1975), Mariner-9 (Hanel et al., 1972) and Viking-1 & -2 (Jakosky & Farmer, 1982). These experiments provided much better spatial resolution (≤ 20 km) and detection threshold (1-3 μm ppw).

Mariner-9/IRIS detected atmospheric water vapour in the region from the South Pole to the Equator, using rotational lines in the spectra between 250 cm⁻¹ and 500 cm⁻¹. These features were not observed over the North Pole. The total amount of water vapour in the atmosphere was estimated from a quantitative comparison of observed and synthetic spectra in the range 10-20 μm ppw. It has been proposed (e.g. Pollack et al., 1979) that water vapour abundance in the atmosphere may be greatly affected by the adsorption of water vapour on dust particles. Suspended dust particles would supply a large surface, producing rather efficient adsorption. Much of the water vapour would settle with dust and it would be released again into the atmosphere as the temperature increases. There is a strong coupling between the temperature and the water abundance fields, but there is still no clear understanding of all the possible sources and sinks of atmospheric water.

Sublimation of water from the north polar cap certainly occurs, but the best model is still uncertain on the quantity. Similarly the regolith is certainly capable of adsorbing and desorbing water, thereby modulating to some degree the amount of water within the atmosphere. The efficiency of this process depends, however, on the composition of the regolith and on the ability of water molecules to diffuse through the uppermost centimetres of regolith, and both of these are very uncertain (Jakosky & Haberle, 1992). A set of experiments on future Orbiters and Landers is necessary for a real understanding of the seasonal cycle. First of all, long-term studies (many martian years) of water vapour are necessary. Several missions are required and PFS will make a crucial contribution.

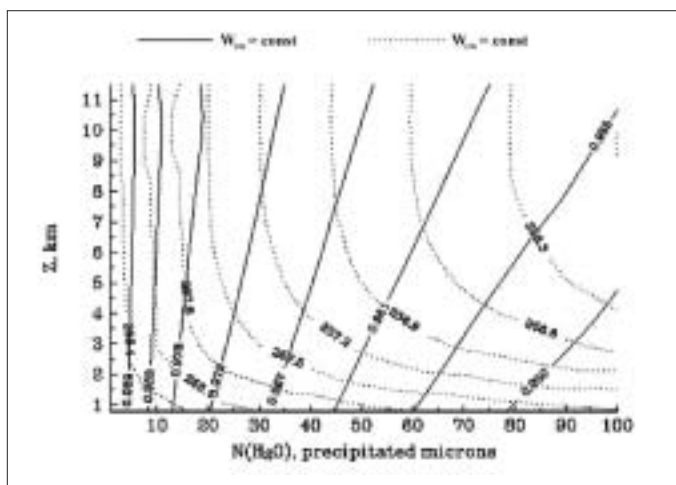


Fig. 9. Simultaneous measurements of the equivalent width of two H_2O bands gives information about the vertical distribution of water vapour.

The water vapour mixing ratio profile seems to indicate the existence of two regions in the atmosphere: below 20-25 km there is relatively high water abundance; above this boundary, it is about 10 times lower (Rodin et al., 1997).

Three different spectral ranges could be used for remote measurements of atmospheric water from orbit:

- near-IR: bands at 1.38, 1.87, 2.7 μm ;
- thermal-IR details of the pure rotational H_2O band in the range 20-50 μm ;
- microwave lines of the pure rotational bands (1.63 μm , for instance).

The sensitivity curve of PFS is such that the 1.87 μm and 2.7 μm bands are more favorable. The detection threshold of 1 μm ppw could be achieved in measurements with an S/N of 100.

The 1.87 μm band appears to be the most convenient for H_2O detection, as it is almost free of overlap with the CO_2 bands. However, the 2.7 μm band will be used to make the H_2O abundance determination more accurate.

The disadvantage of the thermal-IR range is the strong dependence of the water spectral features on the temperature profile in the lowest 1-3 km of the atmosphere, which cannot be resolved directly by any remote-sounding experiment. In principle, we can observe H_2O features in the thermal-IR range not only in absorption but even in emission (in the case of the temperature inversion just above the surface). However, the joint analysis of the H_2O spectral details observed simultaneously in the near-IR and in the pure rotational bands can impose constraints on the vertical distribution of water vapour. Fig. 9 shows the isolines of equivalent widths of the 1.87 μm band (solid lines) and 50 μm band (dots). This diagram is based on a set of calculations of synthetic spectra for various H_2O vertical profiles. The abscissa shows the H_2O column density and Z is the effective altitude of water location. Fig. 9 demonstrates that simultaneous measurements in several water vapour bands will be able to give an estimate of vertical distribution.

PFS also provides an additional opportunity for detection of the 3.7 μm HDO band. It was observed in the martian spectrum by Owen et al. (1988) and the D/H ratio was found to be considerably higher than on Earth (about 6 times). PFS could provide a new, independent determination of this ratio.

In summary, PFS will perform long-term observations of atmospheric water vapour on Mars. This will provide further understanding of the behaviour of water on the planet, its seasonal and diurnal cycles, and distribution of sources and sinks. In comparison with other experiments that have measured martian H_2O , PFS has several advantages:

- the uncertainties in temperature profile, which are usual for near-IR observations of water vapour bands, will be minimised by simultaneous temperature-sounding in the 15 μm CO_2 band;
- high spectral resolution in the near-IR range will result in clear discrimination between the atmospheric and surface spectral features, making the quantitative analysis more reliable;
- simultaneous observations of the water vapour bands in thermal-IR and near-IR will help the vertical distribution of H_2O to be estimated.

1.7 The aerosol investigation

1.7.1 Introduction

The scientific objectives of PFS include:

- the determination of the optical properties, size distribution and chemical composition of the atmospheric aerosols: dust clouds, ice clouds and hazes;
- the investigation of the influence of aerosols on energy exchanges in the atmosphere.

The surface-atmosphere interaction plays a role in the surface's morphology and chemical composition and the atmosphere's temperature, pressure and composition. It is well known that the CO_2 , water and dust cycles are strongly interconnected and with the seasonal variations. Winds, erosion processes and global dust storms are the principal mechanisms for material exchange between aerosols and the surface and between different regions of the planet. Studying the atmosphere's solid components is therefore an important task. Furthermore, the composition of the atmospheric dust provides clues on the chemical composition of the surface, because the identification of dust materials implies characterisation of the soil properties. Last but not least, correctly interpreting the atmosphere's pressure and temperature behaviour must include the role played by the aerosols.

1.7.2 The dust cycle

Atmospheric dust has a role in determining the martian climate and it is clear that it is key for surface geology over a long time scale.

Suspended dust affects the thermal structure and atmospheric circulation with a typical seasonal evolution (Haberle, 1986). The increase of opacity in the northern hemisphere autumn and winter is consistent with global dust storms. This effect is linked to the planet's perihelion, when heating and atmospheric circulation reach maximum. Atmospheric opacity also depends on the form, dimension and composition of the dust grains.

During local dust storms, the lifted materials are redistributed over contiguous areas, while global dust storms transfer dust from the southern hemisphere to the north and the polar cap. Beside the storm effects, dust can be transferred through the atmosphere by baroclinic and planetary waves (Kahn et al., 1992). The dust is probably placed in suspension by strong winds and/or water and CO_2 degassing from the regolith.

The continuous monitoring of the martian atmosphere by PFS in the IR will reveal the evolution of the aerosol composition and amount. Moreover, the dust cycle is strongly linked to the water and CO_2 atmospheric cycles. In fact, the presence of dust at the poles can significantly affect the energetic balance and, then, influence the water vapour and CO_2 fluxes. Dust grains in the atmosphere may become condensation nuclei for CO_2 and H_2O accretion on their surfaces. In particular, the CO_2 condensed on the grain surface may act as a cold trap for atmospheric water. In addition, the transfer of dust from the surface to the atmosphere depends on the pressure and, therefore, on the CO_2 abundance. These elements are further evidence that dust and gas composition of the atmosphere are connected and cannot be treated separately.

1.7.3 Aerosol dust particles

Although spectral signatures of dust particles were clearly evident in Mariner-9/IRIS spectra, it was difficult to define the bulk composition of solid grains with a high degree of confidence. The content of SiO_2 in the dust has been inferred from the comparison of observations with laboratory data; it appears to be $60 \pm 10\%$. Phobos-2 observations of the martian atmosphere using solar occultations in the UV and visible revealed absorption features, probably owing to aerosols (dust particles interpreted as haematite-type) and ozone. A correlation seems to exist between the amount of particulate material in the atmosphere and ozone abundance. This evidence suggests the possibility of heterogeneous chemistry in martian aeronomy (Atreya, 1989) and confirms that aerosols and dust particles play an important role in atmospheric evolution. However, the nature of the particles and their size distribution is not well determined. Atreya (1989) suggests that they could be ices covered by different types of dust (haematite, magnetite and limonite). The PFS data will be helpful in identifying the aerosol nature: the spectrum of light scattered by the atmospheric particles and their thermal emission are sensitive to the chemical composition and size distribution. Additional restrictions could be imposed by the phase function measured by PFS. The problem of separating contributions from the surface and atmospheric radiation should be solved when the aerosol optical depth is not very large. PFS will provide the opportunity for simultaneous measurements of the spectra of the scattered light and the thermal emission of clouds and hazes in the wide range 1.25–45 μm .

1.7.4 The composition of dust

The wavelength range of PFS over 5 μm can be diagnostic for the composition of dust. Much observational evidence indicates the presence of silicate materials, but attribution to a specific class has not yet been achieved. The Mariner-9 data suggested that montmorillonite might be a major component (Hunt et al., 1973). While the observed 10 μm silicate band is easily reproduced by laboratory spectra of crystalline clays, problems occur in simulating the 20 μm band: it does not exhibit any double peak, as is typical of many terrestrial silicate materials. Further observations by PFS at 10 μm and 20 μm could reveal spectroscopic details helpful for identifying the silicate minerals in martian dust. Thermal emission spectra of Mars in the 5–10 μm range have been obtained by a grating array spectrometer aboard the Kuiper Airborne Observatory (Pollack et al., 1989). The observations confirmed that the spectrum of Mars at $> 5 \mu\text{m}$ has more features than previously believed (Roush et al., 1989). Features at 6.1, 7.8 and 9.8 μm are attributed to water and silicate minerals on the surface. Weaker features appear atmospheric in origin: the CO_3^{2-} anionic group can contribute with bands at 6.7 μm and 7.05 μm , when included in distorted sites of complicated crystalline structures; and SO_4^{2-} and HSO_4^- in sulphates and bisulphates produce resonances at 8.7 μm and 9.78 μm . Again, there are doubts about the relative amount of carbonates and sulphates in the form of dust. PFS observations could provide details on cation composition in complex crystalline materials.

1.8 The soil of Mars

1.8.1 Introduction

The spectral studies of the martian surface indicate there to be different types of soil and rocks. They include drift soil, which is similar to the global dust and already analysed by remote spectral measurements from Mariner-9/IRIS, Viking and Phobos-2/ISM and directly at the Viking and Pathfinder landing sites by X-ray fluorescence (Toulmin et al., 1977). There is also sand – attributed to local weathering processes – and more crystalline soil that could be a mixture of dust and local material. The Pathfinder landing site is dominated by three rock types. Dark rocks such as Barnacle Bill and Bambam seem to be fresh basalt or basaltic andesite (Rieder et al., 1997). Bright rocks like Broken Wall and Wedge are attributed to weathered basalts or basaltic andesite. Pink rocks are thought to be chemically cemented drift formations. There is clearly a wide variety of chemical, mineralogical and

morphological characteristics in the surface material at the site. Global spectral studies by PFS will add information on how representative these features are for the whole surface, by comparing the PFS observations of the Pathfinder site with other martian targets. Mapping the distribution of hydrated minerals and salts in the soil is important for understanding the weathering processes and the former role of water on Mars.

1.8.2 The role of PFS

To study the surface of Mars, PFS observations will address the following objectives:

- thermal measurements and determination of the soil's thermal inertia;
- evaluate the local atmospheric pressure and the relative altitude of various regions;
- overview of generic areas of the surface in order to trace the overall distribution of various materials (iron oxides, clays, palagonites, hydrates, sulphates, nitrates, igneous minerals, ices);
- study specific areas chosen to search for answers to fundamental questions on the evolution of the planet and the ancient paleoclimate, e.g. the past existence of abundant liquid water on the surface (by searching for carbonates and other evaporites);
- study the surface-atmosphere exchange processes.

IR spectroscopy in the range covered by PFS is a powerful tool for exploring the surface composition. Different families of resonance fall within the IR spectral range:

- charge transition bands of electrons in the lattices of transition metal ions;
- charge transfer bands due to electron exchange between ions in the material;
- vibrational bands of radicals/molecules present in minerals.

In general, discriminating between atmospheric and surface contributions to the spectrum is rather difficult, requiring a combined study of surface and aerosol/dust constituents. Correctly interpreting the gaseous atmospheric composition requires the subtraction of the solid material's contribution from the recorded spectra.

Finally, a quantitative identification of materials must be based on a comparative analysis of the collected spectra with laboratory measurements on analogue compounds representing martian materials.

1.8.3 Determination of the thermal inertia of the soil

Thermal inertia, which depends on thermal conductivity, mass density and specific heat, is a measure of the responsiveness of a medium to changes in its temperature. The dominant reason for variations in thermal inertia is generally grain-size differences in the superficial material. Thus data on thermal inertia have the potential for telling us if the superficial material is relatively coarse- or fine-grained.

Using PFS measurements of the thermal spectrum from the martian surface in the wide spectral range 5-45 μm , it is possible to determine the pre-dawn temperature of the soil and, from this, its thermal inertia. This can be done by comparing the actual pre-dawn temperatures with those predicted by an idealised thermal model of the surface layer (Kieffer et al., 1977).

1.8.4 Evaluation of the local atmospheric pressure and elevation

The depth of the carbon dioxide unsaturated absorption band measured at a specific site depends on the local atmospheric pressure and, consequently, on the altitude. The PFS SW channel (1.2-5.0 μm) could be used to acquire pressure and relative elevation data and, finally, to map the surface relief. Such an approach was applied to the Mars-3 and -5 and Phobos data.

1.8.5 The chemical and mineral composition of the surface

Among the prime unresolved and oft-debated questions of Mars is the structure and composition of its surface materials. Reflectance and emittance spectroscopy in the near-IR and mid-IR is diagnostic of mineralogy, and hence provides useful information on the surface composition. The spectra of minerals in terrestrial conditions show remarkable dependence on varying experimental situations, including the form of the material (which may be bulk or particulate with different granularity and packing), background temperature, uniformity of sample heating, pressure and insolation angle.

1.8.6 Iron oxides

Crystalline ferric oxides, such as haematite, have long been proposed as one of the major components of the martian surface, in view of the planet's colour and the substantial amount of Fe_2O_3 measured in the soil by the Viking Landers. The broad absorption bands around $10\ \mu\text{m}$ and $20\ \mu\text{m}$, observed in the spectra from Mariner-9/IRIS, appear inconsistent with crystalline ferric oxides. On the other hand, there is no evidence for such compounds at the Pathfinder site.

The comparisons performed so far with the spectra of Mars suggest that either only a few percent of coarsely crystalline haematite or abundant but nanocrystalline haematite are present in the studied areas (Morris & Lauer, 1990). However, a more systematic research of spectral features typical of Fe^{3+} resonances on the martian surface can be useful to clarify this point. Spectroscopic observations by PFS in both SW and LW channels (where haematite shows narrow bands at 2.9 , 6.1 and $7.8\ \mu\text{m}$ and broad bands around $18.5\ \mu\text{m}$ and $21.5\ \mu\text{m}$) can be a great help in determining the main allotropic form of haematite on Mars. The spectral resolution of PFS in this case should have a strong diagnostic power, since the spectral bands of samples with a high degree of crystallinity are, in general, more structured than those of nanocrystalline or amorphous samples (which tend, instead, to be structureless).

1.8.7 Water in the martian soil

PFS will also trace the distribution of hydrates on the surface, by analysing the H_2O bands around $3\ \mu\text{m}$ (due to O-H stretching) and around $6\ \mu\text{m}$ (H-O-H bending). Although it is clear that hydration water is widespread on the surface, there is not much of it. Surface materials should, in fact, be dehydrated in comparison with terrestrial soils, with a water content of up to a few percent (Soderblom, 1992). PFS can improve, on a statistical basis, these evaluations by searching for regions with a higher content of hydration water.

1.8.8 Ices

Mars has a dynamical seasonal cycle of CO_2 and H_2O exchange between the surface and atmosphere. The interplay between vaporisation and condensation of both CO_2 and H_2O produces clouds and mists in the atmosphere and frost and ices on the surface. We expect – apart from polar summers – that PFS observations of ice and frost deposits may be hindered by clouds and mists.

As the role of H_2O in the polar cycles remains to be clarified, searching for CO_2 and H_2O ice and frost features in the spectra of the north polar region will be very useful. Unlike H_2O ice, which strongly absorbs throughout the thermal-IR, CO_2 ice absorbs strongly in the bands at $2.7\ \mu\text{m}$, $4.3\ \mu\text{m}$ in the SW channel of PFS and at $15\ \mu\text{m}$ in the LW channel. This difference could be a basis for distinguishing between the two substances while observing the surface ice deposits. If, however, there are abundant particles of solid CO_2 more than a few μm in size, as there probably are at the polar caps, the reflectivity and emissivity of the surface deposits are also strongly influenced by the weak absorption between the strong bands (Hansen, 1997). In such conditions, a thorough examination of these spectral regions is important.

2. Instrument Description

2.1 Introduction

PFS is a double pendulum interferometer working in two wavelength ranges (1.2-5 μm and 5-45 μm ; Table 2). Martian radiation is divided into two beams by a dichroic mirror. The two ranges correspond to two planes (one on top of the other) containing the two interferometers, so that the same motor can simultaneously move the two pendulums and the two channels are sampled simultaneously and independently. The pendulum motion is accurately controlled via a laser diode reference channel using the same optics as the martian radiation. The same laser diode also generates the sampling signal for the analogue-digital converter (ADC), measuring the 600 nm displacements of the double pendulum mirror. The measurements are double-sided interferograms, so that the onboard FFT can be computed without needing the zero optical path difference location.

2.2 Instrument organisation

PFS is a Fourier spectrometer produced by the combined efforts of several groups from Italy, Russia, Poland, Germany, France and Spain. The flight hardware was built in Italy (the Interferometer Block with its controlling electronics, the digital electronics controlling the experiment, and the Ground Support Equipment with the spacecraft simulator) and Poland (power supply and pointing system). Special flight parts and subassemblies were built in Russia and Germany.

2.3 Technical description

The flight hardware, totalling 31.2 kg, is divided into four modules (Fig. 10), with connecting cables (0.8 kg):

- Module-O (PFS-O): the interferometer, with its optics and proximity electronics, is the core of PFS. 21.5 kg;
- Module-S (PFS-S): the pointing device, which allows PFS to receive radiation from Mars or from the inflight calibration sources, 3.7 kg;
- Module-E (PFS-E): the digital electronics, including a 32-Mbit mass memory and a realtime FFT. 3.0 kg;
- Module-P (PFS-P): the power supply, with the DC/DC converter, redundancies and the separate power supplies for the 16-bit ADCs. 2.2 kg.

Power requirements are: 5 W thermal control, 10 W in sleep mode, 35 W full operational mode and 44 W peak.

2.4 Module-O (PFS-O)

PFS-O is divided into the Interferometer Block (IB) and Electronics Block (EB). They are mechanically separated but electrically connected through six cables. The highly compact IB is a gas-tight box filled by dry nitrogen in order to preserve the hygroscopic optical elements.

2.4.1 Optical scheme of PFS-O

The optical scheme of PFS is shown in Fig. 11. The incident IR beam falls onto the entrance filter that separates the radiation of the SW channel from that of the LW channel and directs each into the appropriate interferometer channel. The PFS-S in front of the interferometer allows the FOV to be pointed along and across the projection of the flight path onto the martian surface. It also directs the FOV at the internal blackbody sources diffusers and to open space for inflight calibration. Each PFS channel is equipped with a pair of retroreflectors attached by brackets to an axle rotated by a torque motor. The axle and drive mechanism are used for both channels, which are vertically separated. The optical path difference is generated by the rotation of the retroreflectors (Hirsch & Arnold, 1993). The motor controller uses the outputs of two reference channels, which are equipped with laser diodes. This interferometer design is very robust against misalignment in a harsh environment, in comparison

Table 2. PFS characteristics.

	SW	LW
Spectral range, μm	1.2 – 5.0	5 – 50
Spectral range, cm^{-1}	2000 – 8200	250 – 1750
Spectral resolution, cm^{-1}	1.5	1.5
FOV, deg	1.7	2.8
NEB, $\text{W cm}^{-2} \text{sr}^{-1}$	5×10^{-9}	4×10^{-8}
Detector type	photoconductor	pyroelectric
Material	PbSe	LiTaO ₃
Temperature, K	220	290
Interferometer type	double pendulum	
Reflecting elements	cubic corner reflectors	
Beamsplitter	CaF ₂	CsI
Max. optical path difference, mm	5	5
Time for motion, s	5	5
Reference source	laser diode	
SW/LW separation	KRS-5 with a multi-layer coating reflecting SW radiation	
Interferogram	two-sided	
Sampling number	16384	4096
Sampling step, nm	600	600 (over-sampled)
Dynamical range	2^{15}	
Spectra (from onboard FFT), number of points	8192	2048

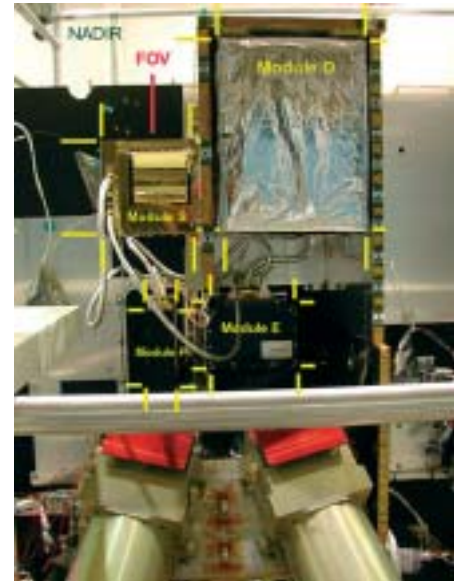


Fig. 10. PFS Flight Model integrated on Mars Express at prime contractor Alenia Spazio in Turin.

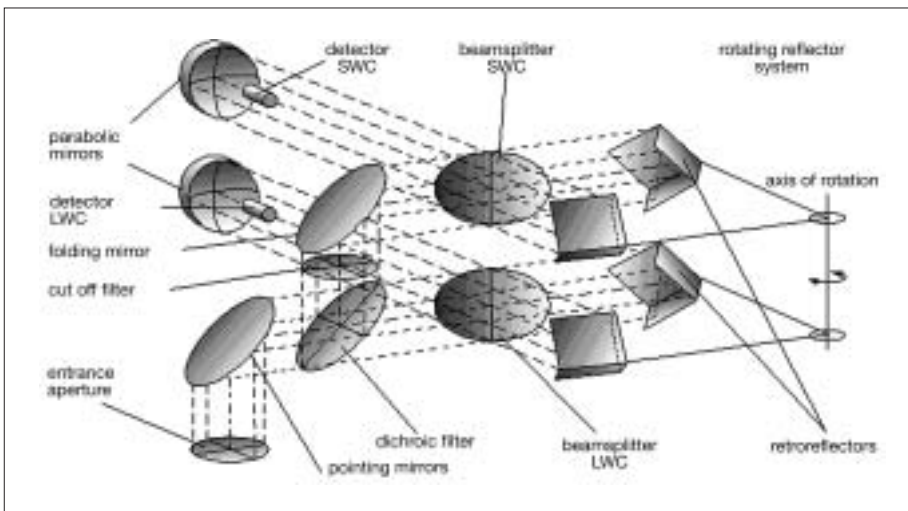


Fig. 11. PFS optical scheme.

with the classical Michelson-type interferometer (Hirsch, 1997). The detectors are in the centre of the parabolic mirrors. The optical path is changed by rotating the shaft of the double pendulum along its axis. In this way, the optical path is four times that provided by a single cube-corner displacement because two mirrors move at the same time. The dichroic mirror acts as a fork that divides the two spectral ranges. Indeed, it reflects all the wavelengths below $5 \mu\text{m}$ and remains more or less transparent for longer wavelengths. The band stop for wavelengths below $1.2 \mu\text{m}$ is provided by the silicon window, with its cutoff at $1.24 \mu\text{m}$ and placed in the optical inlet of the SW

channel. This filter is tilted by 1.5° so that the radiation returning to the source is not partially reflected on the detector.

The double-pendulum axis is rotated by a brushless, frictionless motor (two for redundancy). The shaft of the double pendulum is held only by two preloaded ball bearings so additional mechanical friction is required for stabilising the pendulum speed.

Double-sided interferograms are acquired by placing the zero optical path difference in the centre of the mirror displacement. A double-sided interferogram has several advantages, including a relative insensitivity to phase errors. Bilateral operation is adopted in order to reduce the time-cycle of each measurement, but separate calibration for each direction is recommended in order to maintain the radiometric accuracy.

The spectral reference beam is a diode laser (InGaAsP at $1.2\ \mu\text{m}$); its detector is an IR photodiode with maximum response at about $1.2\ \mu\text{m}$. The beam of the reference channel is processed like the input signal so that its optical path coincides with that of the signal being studied. Each channel has its own reference beam and the different lengths of the double-pendulum arms are fully compensated for. Because the LW beam splitter is not transparent at the wavelength of the corresponding reference diode laser, a special small window was added in order to keep the attenuation of the laser beams negligible through the beam splitter itself. The unused output beams of the two reference channels terminate into optical traps.

2.4.2 Electronics of PFS-O

Most of the electronics inside PFS-O are analogue but the microprocessor-based On-Board Data Management (OBDM) board controls all the complex procedures during acquisition of the interferogram, including communication with PFS-E. It includes 32 kword of EPROM for software storage and 96 kword for data. The most important electronics block is the speed controller. The zero crossing of an interferogram of a monochromatic source that is very stable in wavelength can be used for sampling the interferogram of the source under study. Ideally, the interferogram of the monochromatic source should be a pure sine wave but it is not simply because its interferogram is limited in time. The shorter the wavelength of the reference source means better sampling accuracy.

For PFS, $1.2\ \mu\text{m}$ is the reference source because of the limited variety of diode lasers and it simplifies the optical design. The wavelength of a diode laser depends on its temperature and power, so great care has to be taken in their control.

The speed of the double pendulum is such that a frequency of 2 kHz is generated for the SW channel, so a train of 4 kHz pulses is produced from the electronics of the SW reference channel. Thermal control is also very important for an IR interferometer; heaters and thermometers are positioned at eight locations.

A 'locking system' blocks the double pendulum during launch and manoeuvring for orbital insertion and correction. The procedure of locking and unlocking takes a minimum of 3 min but using a paraffin actuator means it can be repeated hundreds of times. The launch acceleration vector will be along the axis of the double pendulum for maximum robustness.

The photoconductor SW channel detector can work at temperatures down to 200K. It is passively cooled through a radiator and its holder is partially insulated from the rest of the IB. For the LW channel, the pyroelectric detector can operate without performance degradation even at ambient temperatures.

2.5 Module-E (PFS-E)

PFS-E controls all the PFS modules: the communications to and from the spacecraft, memorising and executing the command words, and operating PFS and sending back the data words to the spacecraft. Moreover, it synchronises all the procedures according to the time schedule and to the clock time from the spacecraft.

2.6 Module-P (PFS-P)

PFS combines many kinds of electrical energy consumers: standard digital and analogue electronics, sensitive preamplifiers and ADCs, light sources and electromechanical devices (motors and relays). All of them have different supply requirements and some need to be electrically isolated (to ensure extremely high stability) and/or individually controlled by Module E's processor. This is why PFS-P is more complicated than a simple DC/DC converter: there are three independent converters, six different power outputs (totalling 13 independent voltages), one common input interface to satellite and one interface to DAM. All converters have cold redundancy. Switching between main/reserve +5 V is controlled by the spacecraft, while the other main/reserve converters are controlled by PFS itself.

2.7 Module-S (PFS-S)

The previous version of the pointing system, for the Mars-96 mission, had two degrees-of-freedom in pointing (two rotation axes), but was rather heavy (8.5 kg for the system and 2.3 kg for the controlling electronics). The pointing system is certainly necessary for generating a complete set of measurements, since we need to measure not only the martian radiation but also the calibration blackbody and empty space. Mars Express provides nadir pointing so PFS itself needs only one degree of rotation, simplifying the PFS-S design and reducing mass considerably (to 3.7 kg).

2.8 Modes of operation, data-acquisition cycle

PFS-S and PFS-O work in parallel during an observation session, while PFS-E coordinates operations of the other modules by sending commands and receiving messages. During measurements, PFS-S must be motionless while PFS-O acquires data. This is the only synchronisation point in the data-acquisition cycle. Upon completion of acquisition, all the modules work asynchronously while PFS-E coordinates their operations:

- starts rotation of PFS-S;
- receives LW and SW interferograms from PFS-O;
- if spectra are required, PFS uploads previously acquired LW and SW interferograms into the Fast Fourier Transform processor and downloads computed spectra;
- prepares the telemetry data pack i.e. splits information into frames and stores them in the mass memory;
- upon completion of the PFS-S rotation gives a command to PFS-O to start new acquisition.

After each data-acquisition cycle, PFS checks whether new telecommands have been received and, if any, executes them. Telemetry can be sent at any time on request from the spacecraft.

2.9 Inflight calibration

During observation sessions, PFS periodically performs calibrations by sending commands to PFS-S to point sequentially at the calibration sources: deep space, internal blackbody and calibration lamp. The housekeeping information obtained from PFS-O after each calibration measurement contains, in particular, the temperatures of the sensors and the blackbody. These data are used for the computation of the absolute spectra for the LW channel.

3.1 What is measured

The two detectors of the LW and SW channels measure the light intensity of the two interferograms. The repetition of the measurement while the double pendulum moves at constant speed gives the interferogram. In order to compute the spectrum from the

3. Test and Calibration

interferogram, the measurements must be taken at constant optical path difference, information given by the zero crossings of the sine signal from the interferogram of a monochromatic light (the laser diode).

3.2 Responsivity and signal-to-noise ratios

Three PFS models passed through the laboratory ‘calibration’ process: PFS-06 (Qualification), PFS-07 (Flight) and PFS-08 (spare FM, the refurbished PFS-06). ‘Calibration’ in this context means laboratory studies of the instrument properties that are necessary (although perhaps not sufficient) to extract spectra in absolute units from the observations of Mars by PFS. Ideally, calibrations should result in the algorithm of transfer from telemetric information to spectra of Mars in absolute units. However, instrument properties are not constant with time and the problem is complicated by the differences between laboratory and space conditions. Additional information, including inflight calibration and even models of martian spectra, is necessary for processing actual data.

Having a set of n independently found $B_{\nu^0}(i)$ spectra, we can compute the average spectrum B_{ν^0} and noise equivalent brightness (NEB)

$$NEB_{\nu}^2 = \sum \frac{B_{\nu^0}(i) - B_{\nu^0}}{n - 1} \quad (4)$$

A more detailed discussion of the processing procedure for IR spectrometer data is given in Hanel et al. (1992). Two blackbody-imitator sources (cooled by liquid nitrogen) were used to study the PFS LW channel properties; one blackbody at 1400K was used to study the SW channel. Sensitivity D_{ν} and noise equivalent brightness NEB_{ν} were then computed from these measurements. The spectral resolution was measured with a mercury lamp and taking spectra with known features.

Fig. 12 shows the measured spectrum of the lamp used for calibrating both channels. The S/N is also computed from the measurements. Fig. 13 shows a CH_4 feature as measured in the LW and at maximum spectral resolution, to indicate that 2 cm^{-1} was achieved.

Rough computations show that an S/N at Mars of about 100 or larger will be achieved in the vicinity of $15 \mu\text{m}$ bands with the detector at 220K. This is good enough for retrieving the vertical temperature profiles of the atmosphere. Further studies of the instrument’s thermal behaviour will be performed.

The responsivity for wavenumbers $\nu > 5000 \text{ cm}^{-1}$ is rather poor, because the reflectivity of the semi-transparent mirror separating LW and SW radiation is too low in this part of spectra. It is also this part of the spectrum where errors in optical alignment have greater impact. The situation is improved by optimising the transfer function of the SW channel filter.

3.3 Sample of performed measurements

Laboratory measurements were made on gases such as CO_2 by using a gas cell, and studying the transmission of radiation from a source. Fig. 14 shows the LW spectra around $15 \mu\text{m}$, obtained for different CO_2 pressures inside the cell. Measurements were made at room temperature. Figs. 15 & 16 show the SW CO_2 band at $4.3 \mu\text{m}$ and $2.7 \mu\text{m}$. It is evident that the spectral resolution allows the observation of rotovibrational features of the gas.

4. Data-taking Along the Orbit

4.1 Data-transmission modes

The data-transmission mode (DTM) defines the kind of scientific data that PFS must select and store in the mass memory to be sent to Earth. PFS has 15 DTMs, numbered for historical reasons, 0, 2, 4, 5, 6, 7, 8, 17, 18, 27, 28, 9, 10, 15, 16. DTM 0 is for PFS operating in the autonomous test mode; the others are obtained in the science

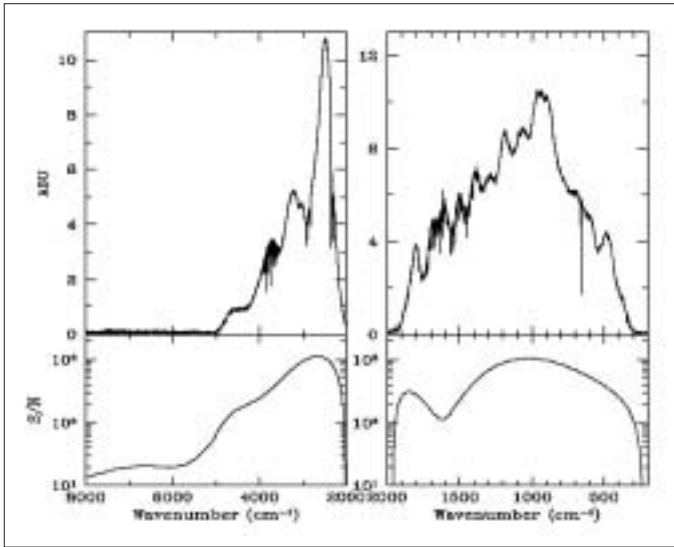


Fig. 12. Computed S/N for SW and LW using a single globar lamp spectrum.

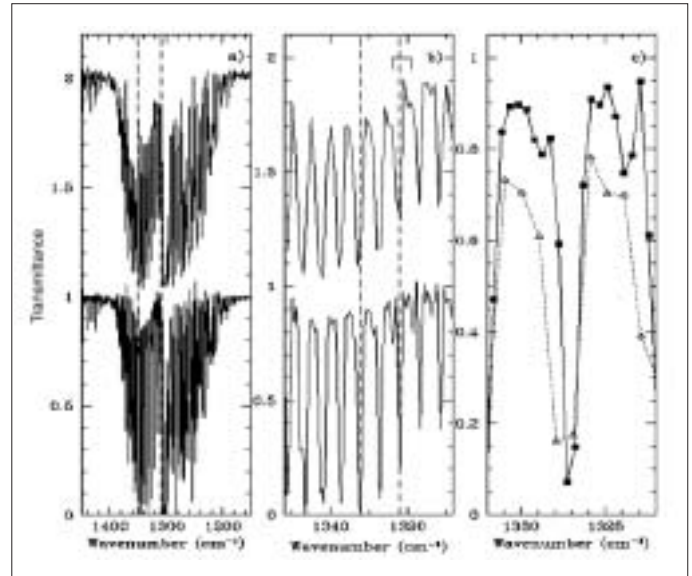


Fig 13. CH₄ bands in the LW channel at different resolution (PFS measurements: triangles; laboratory spectrometer: squares).

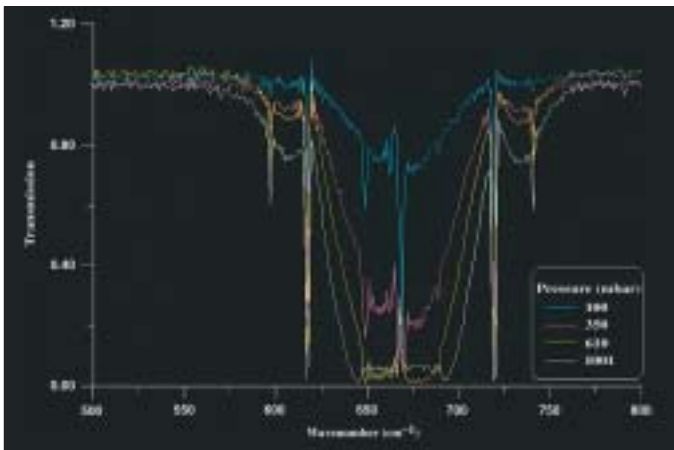


Fig. 14. CO₂ 15 μm transmission band measured in the laboratory with PFS at different gas pressures.

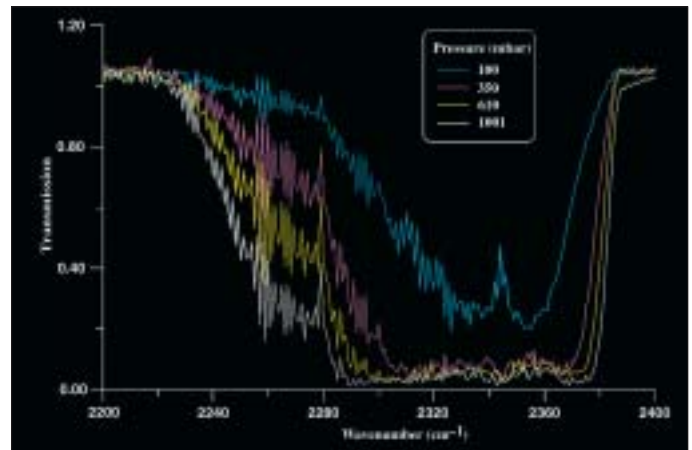


Fig. 15. CO₂ 4.3 μm band measured with PFS in the laboratory at different gas pressures.

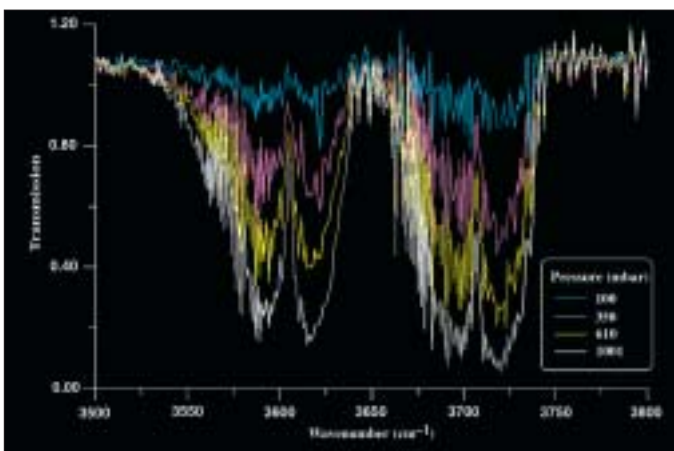


Fig. 16. CO₂ 2.7 μm band measured with PFS in the laboratory at different gas pressures.

mode, where PFS acquires both LW and SW interferograms. If spectra are required (DTM 9, 10, 15, 16), PFS makes Fast Fourier Transforms of the interferograms. Then, depending on the DTM, PFS selects the required data. Interferograms can be selected completely or partially.

Of the 15 DTMs, 10 provide interferograms and four spectra:

- MODE 0: autotest of the interferometer (4096 points in the LW channel and 16384 points in the SW channel provide the sine wave shape and the monitoring of the speed during the double pendulum motion);
- MODE 2: full LW interferograms;
- MODE 4: half-resolution interferograms, SW and LW;
- MODE 5: half-resolution LW interferograms;
- MODE 6: half-resolution SW interferograms;
- MODE 7: full LW interferogram + one-sided SW interferogram (including the zero optical path difference and right side);
- MODE 8: one-sided LW and SW interferograms (right side);
- MODE 17: full LW and SW interferograms;
- MODE 18: full SW interferograms;
- MODE 27: full LW interferogram + one-sided SW interferogram (including the zero optical path difference and left side);
- MODE 28: one-sided LW and SW interferograms (left side);
- MODE 9: modules of LW and SW spectra;
- MODE 10: modules of LW spectra;
- MODE 15: full modules of LW spectra and SW spectra with reduced range (2000 points in the SW channel between 2000 and 4000 cm^{-1});
- MODE 16: modules of SW spectra (6144 points).

4.2 Data-taking along the orbit.

PFS will perform measurement when the spacecraft is below 4000 km. PFS will wake up from its sleep mode about 1 h before and follow the scheme:

- apocentre: PFS is in sleep mode, telecommands can be received;
- pericentre minus 60 min: wake-up, wait for warm-up, start autonomous test, calibration LW, calibration SW, calibration deep space. PFS-S in nadir direction. Give data to the spacecraft;
- pericentre minus 40 min: start martian observations. Give data to the spacecraft;
- pericentre plus 48 min: stop martian observations. Give data to the spacecraft;
- pericentre plus 53 min: calibration LW, calibration SW, calibration deep space, autonomous test. Give data to the spacecraft. Go into sleep mode;
- up to apocentre in sleep mode.

In total, 600 measurements per orbit are taken, of which 60 are calibrations. This corresponds to 1200 measurements per day (the third orbit per day being for downlink) and 823 440 spectra in a martian year. The footprint from 4000 km is of the order of 109 km for the SW channel and 188 km for the LW channel; at pericentre (250 km) they become respectively 6.8 km and 11.8 km (perpendicular to the ground track, but 20 km along it) .

References

- Arnold, G., Hirsch, H., Formisano, V. & Moroz, V. (1993). Studies of Martian Atmosphere and Surface by the Planetary Fourier Spectrometer on Board of the Mars-94 Mission. *Proc. SPIE 2089*, 284.
- Atreya, S.K. (1989). The Martian Upper Atmosphere. In *Colloque International, Premiere Resultats de la Mission Phobos et Future Missions d'exploration de Mars*, CNES, Paris, France, p42.
- Bartholomew, M.J., Cruikshank, D.P. & Roush, T. (1990). Asteroid and Meteorite Spectral Analogs for Phobos. *Bull. Amer. Astro.Soc.* **22**, 1115.
- Carr, M.H. (1974). The Geology of Mars. In *A Primer in Lunar Geology*, NASA Ames Research Center, pp459-460.
- Haberle, R.M. (1986). The Climate of Mars. *Sci. Am.* **254**, 54-62.
- Haberle, R.M. & Jakowsky, B.M. (1990). Sublimation and Transport of Water from the North Residual Polar Cap on Mars. *J. Geophys. Res.* **95**, 1423.
- Hanel, R.A., Conrath, B.J., Jennings, D.E. & Samuelson, R.E. (1992). *Exploration of the Solar System by Infrared Remote Sensing*, Cambridge University Press, UK.
- Hanel, R., Conrath, B., Howis, W., Kunde, V., Lowman, P., Maguire, W., Pearl, J., Pirraglia, J., Prabhakara, C. & Schlachman, B. (1972). Investigation of the Martian Environment by Infrared Spectroscopy on Mariner-9. *Icarus* **17**, 423-442.
- Hansen, G.B. (1997). The Infrared Absorption Spectrum of Carbon Dioxide Ice from 1.8 to 333 μm . *J. Geophys. Res.* **102**, E9, 21569-21588.
- Hirsch, H. & Arnold, G. (1993). Fourier Transform Spectroscopy in Remote Sensing of Solid Planetary Surfaces. *Vib. Spectrosc.* **5**, 119-123.
- Hirsch, H. (1997). Optical Design and Performance of the Planetary Fourier Spectrometer (PFS). *Microchimica Acta [Suppl.]* **14**, 571-574.
- Hunt, G.R., Logan, L.M. & Salisbury, J.W. (1973). Mars: Components of Infrared Spectra and Composition of the Dust Clouds. *Icarus* **18**, 459.
- Hunt, G.R., Salisbury, J.W. & Lenhoff, C.J. (1974). Visible and Near Infrared Spectra of Minerals and Rocks: IX. Basic and Ultrabasic Igneous Rocks. *Modern Geology* **5**, 15-22.
- Jakosky, B.M. & Haberle, R.M. (1992). The Seasonal Behavior of Water on Mars. In *Mars* (Eds. H.H. Kieffer, B.M. Jakosky, C.W. Snyder & M.S. Matthews), The University of Arizona Press, Tucson, USA, pp969-1016.
- Jakosky, B.M. & Farmer, C.B. (1982). The Seasonal and Global Behavior of Water Vapor in the Mars Atmosphere – Complete Global Results of the Viking Atmospheric Water Detector Experiment. *J. Geoph. Res.* **87**, 2999-3019.
- Justus, C.G., James, O. & Johnson, A. (1995). *Mars Global Reference Atmospheric Model (Mars-GRAM 3.34): Programmer's Guide*. Computer Sciences Corp., USA.
- Kahn, R.A., Martin, T.Z., Zurek, R.W. & Lee, S.W. (1992). The Martian Dust Cycle. In *Mars* (Eds. H.H. Kieffer, B.M. Jakosky, C.W. Snyder & M.S. Matthews), The University of Arizona Press, Tucson, USA, pp1017-1053.
- Kaplan, L.D., Munch, G. & Spinrad, H. (1964). An Analysis of the Spectrum of Mars. *Astrophys. J.* **139**, 1.
- Kieffer, H.H., Martin, T.Z., Peterfreund, A.R., Jakosky, B.M., Miner, E.D. & Palluconi, F.D. (1977). Thermal and Albedo Mapping of Mars during the Viking Primary Mission. *J. Geoph. Res.* **82**, 4249-4291.
- Kliore, A.J., Cain, D.L., Fjeldbo, G., Seidel, B.L., Sykes, M.J. & Rasool, S.I. (1972). The Atmosphere of Mars from Mariner 9 Radio Occultation Measurements. *Icarus* **17**, 484-516.
- Kliore, A.J., Woiceshyn, P.M. & Hubbard, W.B. (1977). Pioneer 10 and 11 Radio Occultations by Jupiter. In *Symposium on Minor Constituents and Excited Species*, Philadelphia, Pa., USA, 9-10 June 1976 (A78-18101 05-42), p703-710.
- McCord, T.B. & Cruikshank, D.P. (1981). Spectrophotometric Remote Sensing of Planets and Satellites. In *Infrared Astronomy; Proceedings of the Symposium*, Kona, HI, USA, 23-27 June 1980 (A82-33729 16-90), p57-87.
- Morris, R.V. & Lauer, H.V. (1990). Matrix Effects for Reflectivity Spectra of

- Dispersed Nanophase (Usuperparamagnetic) Hematite with Application to Martian Spectral Data. *J. Geophys. Res.* **95**, 5101.
- Moroz, V. & Nadzhip, A.E. (1975). Measurements of Water Vapour Densities on Mars 5 Orbiter: Preliminary Results. *Cosmic Res.* **13**, 28.
- Owen, T. (1992). The Composition and Early History of the Atmosphere of Mars. In *Mars* (Eds. H.H. Kieffer, B.M. Jakosky, C.W. Snyder & M.S. Matthews), The University of Arizona Press, Tucson, USA, pp818-834.
- Owen, T., Maillard, J.P., de Bergh, C. & Lutz, B.L. (1988). Deuterium on Mars: The Abundance of HDO and the Value of D/H. *Science* **240**, 1767.
- Pedlosky, J. (1979). *Geophysical Fluid Dynamics*, Springer-Verlag, Germany.
- Pollack, J.B. & Toon, O.B. (1982). Quasi Periodic Climate Changes on Mars: A Review. *Icarus* **50**, 259.
- Pollack, J., Roush, T., Witteborn, F., Bregman, J., Wooden, D., Stoker, C., Toon, O., Rank, D., Dalton, B. & Freedman, R. (1989). Thermal Emission Spectra of Mars (5.4-10.5 mm): Evidence for Sulfates, Carbonates and Hydrates. In *Colloque International, Premiere Resultats de la Mission Phobos et Future Missions d'exploration de Mars*, CNES, Paris, France, p93.
- Pollack, J.B., Colburn, D.S., Flasar, F.M., Kahn, R., Carlston, C.E. & Pidek, D.G. (1979). Properties and Effects of Dust Particles Suspended in the Martian Atmosphere. *J. Geoph. Res.* **84**, 2929-2945.
- Rieder, R., Wänke, H., Economou, T. & Turkevich, A. (1997). Determination of the Chemical Composition of Martian Soil and Rocks: The Alpha Proton X-ray Spectrometer. *J. Geoph. Res.* **102**, E2, 4027-4044.
- Rodin, A.V., Korablev, O.I. & Moroz, V.I. (1997). Vertical Distribution of Water in the Near-Equatorial Troposphere of Mars: Water Vapor and Clouds. *Icarus* **125**, N1, 212-229.
- Rothman, L.S., Gamache, R.R., Tipping, R.H., Rinsland, C.P., Smith, M.A.H., Benner, D.C., Devi, V.M., Flaud, J.-M., Camy-Peyret, C. & Perrin, A. (1992). The HITRAN Molecular Data Base – Editions of 1991 and 1992. *J. Quan. Spect. & Rad. Transfer* **48**, N5-6, 469-507.
- Roush, T.L., Blaney, D.L. & Singer, R.B. (1993). The Surface Composition of Mars as Inferred from Spectroscopic Observations. In *Remote Geochemical Analysis: Elemental and Mineralogical Composition*, (Eds. C.M. Pieters & P.A.J. Englert), Cambridge Univ. Press, UK, pp367-393.
- Roush, T.L., Pollack, J.B., Stoker, C., Witteborn, F., Bregman, J., Wooden, D. & Rank, D. (1989). CO³² and SO⁴²⁻-bearing Anionic Complexes Detected in Martian Atmospheric Dust. *Lunar Planet. Sci. Conf. XX*, p928.
- Seiff, A. (1982). Post-Viking Models for the Structure of the Summer Atmosphere of Mars. *Adv. Space Res.*, **2**, N2, 3-17.
- Smith, W.L. (1970). Iterative Solution of the Radiative Transfer Equation for the Temperature and Absorbing Gas Profile. *Appl. Optics* **9**, N9, 1993-1999.
- Soderblom, L.A. (1992). The Composition and Mineralogy of the Martian Surface from Spectroscopic Observations: 0.3 mm to 50 mm. In *Mars* (Eds. H.H. Kieffer, B.M. Jakosky, C.W. Snyder & M.S. Matthews), The University of Arizona Press, Tucson, USA, pp557-593.
- Spinrad, H. & Richardson, E.H. (1963). High Dispersion Spectra of the Outer Planets. II. A New Upper Limit for the Water Vapor Content of the Martian Atmosphere. *Icarus* **2**, 49.
- Tikhonov, A.N., Goncharskij, A.V., Stepanov, V.V. & Jagola, A.G. (1990). *Numerical Methods of Solving the Ill-posed Problems*. Nauka, Moscow (in Russian).
- Toulmin, P., Baird, A.K., Clark, B.C., Keil, K., Rose, H.J., Christian, R.P., Evans, P.H. & Kelliher, W.C. (1977). Geochemical and Mineralogical Interpretation of the Viking Inorganic Chemical Results. *J. Geophys. Res.* **82**.
- Zurek, W.R., Barnes, J.R., Haberle, R.M., Pollack, J.B., Tillman, J.E. & Leovy, C.V. (1992). Dynamics of the Atmosphere of Mars. In *Mars* (Eds. H.H. Kieffer, B.M. Jakosky, C.W. Snyder & M.S. Matthews), The University of Arizona Press, Tucson, USA, pp799-817.

SPICAM: Studying the Global Structure and Composition of the Martian Atmosphere

J.-L. Bertaux¹, D. Fonteyn², O. Korablev³, E. Chassefière⁴, E. Dimarellis¹, J.P. Dubois¹, A. Hauchecorne¹, F. Lefèvre¹, M. Cabane¹, P. Rannou¹, A.C. Levasseur-Regourd¹, G. Cernogora¹, E. Quemerais¹, C. Hermans², G. Kockarts², C. Lippens², M. De Maziere², D. Moreau², C. Muller², E. Neefs², P.C. Simon², F. Forget⁴, F. Hourdin⁴, O. Talagrand⁴, V.I. Moroz³, A. Rodin³, B. Sandel⁵ & A. Stern⁶

¹*Service d'Aéronomie du CNRS, F-91371, Verrières-le-Buisson, France*

Email: jean-loup.bertaux@aerov.jussieu.fr

²*Belgian Institute for Space Aeronomy, 3 av. Circulaire, B-1180 Brussels, Belgium*

³*Space Research Institute (IKI), 84/32 Profsoyuznaya, 117810 Moscow, Russia*

⁴*Laboratoire de Météorologie Dynamique, 4 place Jussieu, F-75252 Paris Cedex 05, Paris, France*

⁵*Lunar and Planetary Laboratory, 901 Gould Simpson Building, Univ. of Arizona, Tucson, AZ 85721, USA*

⁶*SouthWest Research Institute, Geophysics, Astrophysics and Planetary Science, 1050 Walnut Ave., Suite 400, Boulder, CO 80302-5143, USA*

The SPICAM (SPectroscopy for the Investigation of the Characteristics of the Atmosphere of Mars) instrument consists of two spectrometers. The UV spectrometer addresses key issues about ozone and its H₂O coupling, aerosols, the atmospheric vertical temperature structure and the ionosphere. The IR spectrometer is aimed primarily at H₂O abundances and vertical profiling of H₂O and aerosols. SPICAM's density/temperature profiles will aid the development of meteorological and dynamical atmospheric models from the surface up to 160 km altitude. UV observations of the upper atmosphere will study the ionosphere and its direct interaction with the solar wind. They will also allow a better understanding of escape mechanisms, crucial for insight into the long-term evolution of the atmosphere.

1.1 SPICAM goals

SPICAM (Fig. 1), a lightweight (4.7 kg) UV-IR spectrometer on the Mars Express orbiter, is dedicated to recovering most of the atmospheric science that was lost with Mars-96 and its set of SPICAM sensors. The new configuration of SPICAM includes a 2-channel optical sensor (3.8 kg) and an electronics block (0.9 kg). The UV spectrometer (118-320 nm, resolution 0.8 nm) is dedicated to nadir viewing, limb viewing and vertical profiling by stellar and solar occultation. It addresses key issues about ozone and the H₂O coupling, aerosols, atmospheric vertical temperature structure and the ionosphere. The near-IR spectrometer (1.0-1.7 μ m, resolution 0.5-1.2 nm) is aimed primarily at nadir measurements of H₂O abundances, and at vertical profiling of H₂O and aerosols by solar occultation. A simple data processing unit (0.9 kg) provides the interface with the spacecraft.

For nadir observations, SPICAM UV is essentially an ozone detector, measuring the strongest O₃ absorption band at 250 nm in the solar light scattered from the ground. In its stellar occultation mode, the UV sensor will measure the vertical profiles of CO₂, temperature, O₃, clouds and aerosols. The density/temperature profiles will constrain and aid in developing the meteorological and dynamical atmospheric models from the surface and up to 160 km in the atmosphere. This is

1. Introduction

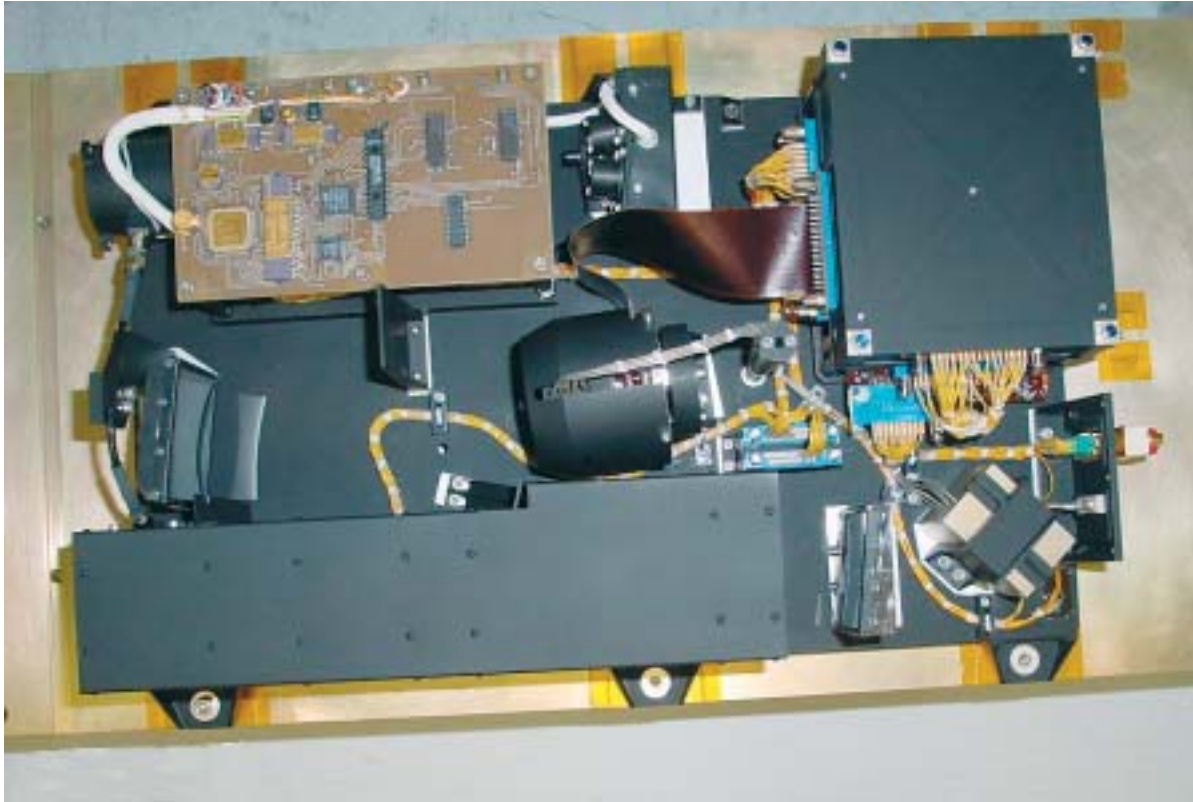


Fig. 1. Flight Model Sensor Unit of SPICAM viewed from above. The IR AOTF spectrometer is at top; the UV spectrometer is at bottom. The common optical axis points to the left. For the UV spectrometer, the light enters the mechanical baffle (black), is focused by a parabolic mirror (bottom right) through a slit, then dispersed by the grating (middle left), to be refocused on the intensified CCD Detector (at centre).

essential for future missions that rely on aerocapture and aerobraking. UV observations of the upper atmosphere will allow studies of the ionosphere through the emissions of CO , CO^+ and CO_2^+ , and its direct interaction with the solar wind. Also, it will allow a better understanding of escape mechanisms and estimates of their magnitude, crucial for insight into the long-term evolution of the atmosphere.

SPICAM's near-IR sensor, employing the pioneering technology of an acousto-optical tunable filter (AOTF), is dedicated to the measurement of water vapour column abundance in the IR simultaneously with ozone measured in the UV. It will be achieved with a much lower telemetry budget than the mission's Planetary Fourier Spectrometer. In solar occultation mode, this channel will study the vertical structures of H_2O , CO_2 and aerosols.

1.2 Background

Observations during the 18th century showed that light from the star Spica decreased abruptly during occultations by the Moon. It was concluded that the Moon has no atmosphere because, otherwise, refraction would have produced a progressive dimming of the star. The SPICAM acronym is a tribute to this early use of stellar occultation.

In the Earth's atmosphere, the occultation technique has been used to measure O_3 since the 1970s. Only one or two wavelengths were observed at a time in the early attempts, making identification of the absorber species uncertain. With the advent of multi-pixel detectors, the absorbing species can be safely identified by their spectral signatures. It also offers the potential to discover new, unexpected species in the atmosphere. The method of absorptive occultation spectroscopy is reviewed in Roscoe et al. (1994) and Smith & Hunten (1990). For terrestrial stratospheric research, it has become the most advanced method for long-term monitoring of ozone. In the IR, the most remarkable results are those of the ATMOS/Atlas Space Shuttle experiment, which provided a set of high-resolution IR spectra of the terrestrial

atmosphere. In the UV-visible, NASA's SAGE-3 is using full-wavelength coverage of the Sun. Onboard Envisat, SCIAMACHY (Scanning Imaging Absorption Spectrometer for Atmospheric Chartography) is performing solar occultation and nadir observations, and the GOMOS (Global Ozone Monitoring by Occultations of Stars) instrument is dedicated to the monitoring of ozone and other species by stellar occultations. SPICAM's methodology is clearly in line with the most advanced instrumentation for studying Earth's atmosphere.

The only solar occultation measurements so far of Mars from spacecraft were performed during the Phobos mission using the Auguste instrument (Blamont et al., 1989; Krasnopolsky et al., 1989). Though the Phobos mission was not fully successful, the solar occultation observations lasted more than a month, resulting in an important improvement of our knowledge of the martian water vapour profile (Krasnopolsky et al., 1991; Rodin et al., 1997), aerosol vertical distribution (Chassefière et al., 1992; Korablev et al., 1993) and ozone distribution (Blamont & Chassefière, 1993).

The promising results from the Phobos mission were not fully developed because of the failure of the Mars-96 mission, where the SPICAM set of sensors (total 46 kg) was dedicated to studying the martian atmosphere. The 4.7 kg SPICAM 'Light' of Mars Express will recover most of the science of SPICAM/Mars-96. The considerable mass saving was achieved by sacrificing all the visible part of the spectrum and by suppressing all redundancy between the two sensors. Also, using the spacecraft for pointing removes the need for pointing platforms and devices. The proposal for this SPICAM included a separate solar occultation IR sensor (SOIR), inherited from the solar package of SPICAM/Mars-96. This 3.8 kg sensor consisted of a grating spectrometer (1.2-4.8 μm , resolution 0.4-1 nm) for vertical profiling during solar occultations of H_2O , CO_2 , CO and aerosols and exploration of carbon compounds (Bertaux et al., 2001). Owing to the severe mass constraints of Mars Explorer, this sensor was deleted at the development stage, and replaced by the extremely lightweight near-IR spectrometer based on AOTF technology. The consequences for the scientific return are discussed below.

The tenuity of the CO_2 martian atmosphere and the partial transparency to solar UV results in intense photochemical activity, possibly including photocatalytic processes at the surface or on aerosols. Although the global mechanism of atmospheric chemical stability proposed at the beginning of the 1970s (Parkinson & Hunten, 1972) is generally accepted, no substantial progress in modelling has been made in the last 20 years. Understanding martian atmospheric chemistry is of fundamental importance for characterising the history of Mars (escape of species to space, atmosphere/surface interactions such as oxidation) as well as for comparison with terrestrial processes (chemistry/dynamics coupling, possible role of heterogeneous chemistry). Besides chemical processes, addressing the key problems of the martian climate includes understanding the transport of radiatively active aerosols, microphysics of clouds, regolith/atmosphere water exchange and wave activity in the atmosphere. So far, most of the data on the composition and structure of the martian atmosphere relate to the total content of the species, with very little information on the vertical profiles of aerosols, ozone, water vapour and other trace gases. SPICAM focuses on the determination of atmospheric characteristics from the surface up to 160 km altitude. SPICAM's main objectives are defined in the following five subsections.

2. Scientific Objectives

2.1 Three-dimensional studies related to atmospheric chemical stability

An important step in improving our knowledge of martian photochemistry is the validation of the currently accepted scheme of chemical atmospheric stability, originally proposed by Parkinson & Hunten (1972). To explain the CO_2 stability, this scheme invokes odd-hydrogen photochemical species that catalyse the recombination of CO and O. These catalytic reactions are so efficient that O_2 and CO appear in the

atmosphere only in very small amounts – the observed quantities are around 0.1%. The photochemistry scheme is complicated by the amount of water, which is highly variable. The ozone density is directly connected to HO_x radicals, which are the product of water vapour dissociation. Early photochemical theories (McElroy & Donahue, 1972; Parkinson & Hunten, 1972) are confirmed by more recent photochemistry models (Nair et al., 1994; Krasnopolsky, 1993). SPICAM provides the opportunity to validate the stability scheme through simultaneous measurements of water vapour, ozone and temperature with a good vertical resolution, as well as of their diurnal, seasonal and latitudinal variations.

Since the water vapour cycle is one of the three important atmospheric cycles (the others being the dust and CO₂ cycles), the present distribution and annual variability of water reflect both current and past climate processes. In the 1970s, the Mars Atmosphere Water Detector (MAWD) on the Viking orbiters mapped for the first time the column abundance of water, for 1.5 martian years. Maximum water content is observed above the North Pole in summer as a consequence of the sublimation of the polar cap. In addition, the exchange of water between the atmosphere and the regolith is likely on both diurnal and seasonal bases. The pore volume of the martian regolith is substantial and implies that a large part of it can act as a water reservoir. Using solar occultations, the IR channel will accurately measure the vertical structure of water vapour in the atmosphere, allowing these important water-exchange processes to be assessed.

The key processes controlling the vertical distribution of water vapour on Mars are likely to be large-scale transport, turbulent mixing, the microphysics of nucleation, growth and sedimentation of ice crystals, and photochemical reactions. Moreover, the water vapour profile is closely connected to the temperature structure (both dynamic and radiative) through saturation water pressure. However, the available data do not allow an adequate determination of the detailed spatial and seasonal variations in the vertical distribution of water.

Observations of other trace species will also be important in understanding the behaviour of atmospheric water. One of these trace gases is ozone. The ozone vertical profile is governed mainly by the abundance of water vapour and it is widely acknowledged that there is a strong anti-correlation between water vapour and atmospheric ozone (Barth et al., 1973). Even if the atmospheric ozone content is low, this constituent is important for characterising the physico-chemical structure of the atmosphere. Only marginal information is available about the vertical distribution of ozone: a layer has been tentatively detected in the middle atmosphere by solar occultation (Blamont & Chassefière, 1993). SPICAM will fill this gap by measuring ozone profiles using stellar occultations in the UV.

Finally, SPICAM's nadir-viewing capability will allow the mapping of ozone column density. In conjunction with the column density of water vapour, as measured by SPICAM's IR channel or other Mars Express instruments, this will permit detailed global scale correlation studies. It should be emphasised that, so far, there is no direct experimental correlation between H₂O and ozone distributions, owing to the lack of simultaneous measurements. Some correspondence of high ozone near the poles with H₂O derived from temperature-dependent water pressure was found from Mariner-9 ozone (Barth et al., 1973) and temperature measurements (Barth et al., 1992). SPICAM offers the first possibility of firmly establishing this correlation.

2.2 Atmospheric escape

The efficiency of atmospheric escape is strongly mass-dependent, and it is quite significant for hydrogen and deuterium. The geological evidence for running water on the martian surface in the distant past is well established, but the total amount of water and the periods of activity are still controversial (Carr, 1996). Observation of D/H is thus particularly important for reconstructing the history of water on Mars. For this, the fundamental 3.7 μm HDO band was to be studied with the SOIR solar occultation channel.

An important goal of atmospheric studies is the characterisation of escape processes, which are believed to have played an important role in climate evolution. The main processes of removing mass from the atmosphere are the sputtering of atmospheric species by oxygen pick-up ions at the exobase level, and photochemical escape (Kass & Yung, 1995; Jakosky et al., 1994). The close coupling of all the atmospheric layers makes it interesting to measure the profiles of hydrogen, carbon and oxygen species in the lower ionosphere, where strong vertical fluxes of these species are supposed to take place. SPICAM will observe resonant scattering emissions of H, C and O in the altitude range 100-200 km, as well as some fluorescence bands of CO and major ions (CO_2^+ , CO^+). This altitude range, an essential interface region between the low atmosphere and the upper ionosphere (where escape occurs through direct interaction with the solar wind), cannot be studied with *in situ* measurements because of the pericentre altitude of 300 km. UV glow measurements by SPICAM should provide information about thermospheric ion-neutral chemistry and related vertical fluxes of chemical species at the top of the atmosphere, as well as about their diurnal and seasonal variations.

2.3 Surface/atmosphere chemical interaction; mapping of the atmospheric and surface oxidant

The level of biologically lethal UV arriving at the surface of Mars is controlled by the vertical column of ozone, which is itself controlled by H_2O , according to present photochemistry models. These models also predict the presence of O, H_2O_2 , HO_2 , OH molecules and radicals, which are extremely reactive with the surface. Together with ozone, they are the main factors destroying any organic molecule that could be present on the surface (Stoker & Bullock, 1997). This radiative-chemical environment of exobiological significance will be evaluated at a variety of locations, latitudes and seasons, thanks to the polar orbit of Mars Express and its martian-year lifetime. A photochemistry model validated by the consistency of various measurements makes it possible to extrapolate back in time and to assess more safely the conditions constraining the development of life on Mars.

More than 25 years ago, the Viking life detection experiments proved that the martian soil is extraordinarily oxidising. The evolution of CO_2 from the labelled release experiment is consistent with the presence of a thermally labile oxidant. Detection and characterisation of the chemical and physical nature of this powerful oxidant is therefore of great interest not only from an exobiological point of view but also for studying exchanges between the atmosphere and the regolith on Mars. In the thin and cold atmosphere, photochemical reactions between traces of water and solar UV probably lead to the production of H_2O_2 which, in turn, can condense onto soil grains and airborne dust. Hydrogen peroxide has not yet been detected in the Martian atmosphere. A tentative detection/upper limit experiment in millimetric waves was carried out using the Interferomètre Radio Astronomique Millimétrique (IRAM) telescope (Moreau et al., 1998). Estimating the total abundance of this constituent might be feasible using SPICAM's UV channel.

2.4 Wave activity in the middle atmosphere and thermosphere

Theory predicts that the temperature structure of the thermosphere above 120 km is dominated by the balance between EUV heating, non-LTE cooling and molecular diffusion. In the middle atmosphere (40-120 km), the vertical structure is determined primarily by non-LTE solar heating and radiative cooling in the absorption bands of CO_2 , and by solar EUV heating at higher levels. The thermal structure is modified by the circulation driven by this force, and by tides and gravity waves that propagate from the lower atmosphere, break and deposit their energy in this region. Lower and upper circulation models (including General Circulation Models) have recently been extended into the middle atmosphere, and need adequate temperature/density data to be validated.

Until recently, there were few temperature profiles measured in the upper atmosphere: Viking lander entry profiles (Seif & Kirk, 1977) and an indirect deriva-

tion above 120 km from Mariner-9 airglow (Stewart et al., 1972). New profiles were derived from Mars Pathfinder (MPF) entry accelerometry (Magalhaes et al., 1999) and Mars Global Surveyor (MGS) aerobraking data (Keating, 1998). The Thermal Emission Spectrometer (TES) on MGS produces 3-D temperature fields up to 35 km in its nadir mode and up to 65 km in the limb-viewing mode (Conrath et al., 1998; 1999). Radio occultation studies from Mars probes result in profiles below 20 km (see Hinson et al., 1999 for recent MPF radio profiles). Ground-based microwave observations based on CO-line profiling (Clancy et al., 1990) constrain temperature profiles on large (planetary) scales up to ~50 km. The thermal structure and circulation of this part of the atmosphere is of primary importance on Mars: unlike on Earth, where the circulation in the troposphere is somewhat decoupled from that in the stratosphere, the vertical extension of meteorological phenomena appears to be considerable. In some cases, this extension probably reaches the top of the neutral atmosphere around 120 km (e.g. the Hadley cell during northern winter). The circulation there may even affect the meteorology at much lower altitude (Forget et al., 1996). For instance, the strong warming of the polar-night atmosphere during dust storms is thought to result from an enhancement of the meridional wind between 60 km and 100 km (Wilson, 1997). In fact, this behaviour of the martian atmosphere may limit the performance of the general circulation models and thus our understanding of martian meteorology. How can we account for these upper atmospheric processes? Is the lower thermosphere circulation of importance? Because of their limited vertical coverage (< 65 km), TES and similar instruments will not solve the problem, leaving SPICAM as the single optical spectrometer covering this altitude range.

Gravity waves have small vertical wavelengths relative to their horizontal scales, which makes them well adapted for detection by SPICAM. In addition, SPICAM will allow us to observe the propagation and the breaking of these waves up to high altitude for the first time.

2.5 Impact of aerosols on the martian climate

Dusty and volatile aerosols are important components of the martian atmosphere. The strong involvement of the aerosols in basic climate fields means that the lower atmosphere may be considered as a 'dusty climate' system. A permanent haze exists with a column optical depth from 0.1 to 1 depending on season, with sporadic increases up to several units during great dust storms. It is known to control temperatures in the troposphere and lower stratosphere. Heating and cooling by aerosols drive dynamical phenomena, varying on scale from general circulation to local waves that give rise to atmospheric turbulence. The contents and distribution of aerosols in the atmosphere are, in turn, controlled by atmospheric motion, being included in the complex feedback that makes the current climate of Mars extremely variable. Volatile aerosols also affect the thermal field by changing the optical properties and settling rates of particles, and therefore provide strongly non-linear thermal feedback determined by the saturation curve. This effect is expected to be most significant during aphelion (Clancy et al., 1996; Rodin et al., 1999).

Exploring the phenomena described above implies detailed studies of the vertical, lateral and size distribution of mineral and volatile aerosols, as well as water vapour, in the lower atmosphere. SPICAM's large wavelength range (0.12-1.7 μm) provides a unique opportunity to study micron-sized aerosols at high spatial resolution. Simultaneous high-resolution measurement of the water vapour profile yields data on microphysical condition of cloud formation, e.g. the degree of supersaturation in the stratosphere and water eddy transport rates in both gaseous and condensed phases. Comprehensive modelling of thermal balance, turbulent transport and microphysics of water vapour, ice and dust interaction with a self-consistent 1-D model (Rodin et al., 1999) will support these measurements.

The components of the martian atmosphere to be measured by SPICAM are given in Table 1.

Table 1. Components of the martian atmosphere measurable by SPICAM.

<i>Species</i>	<i>Scientific objective</i>	<i>Mode</i>	<i>Spectral range</i>	<i>Accuracy</i>	<i>Altitude range</i>
O ₃	concentration vertical profile	stellar/solar occultation	220-300 nm	2-10%	10-50 km, $\Delta z < 1$ km
O ₃	total abundance	nadir	220-300 nm	5% ($> 0.15 \mu\text{atm}$)	ground res 4x4 km
CO ₂	atmospheric density and temperature vertical profile	solar/stellar occultation	180 nm	2-10% 5K	20-160 km, $\Delta z < 1$ km
CO ₂	surface pressure, tides	nadir	200 nm 1.43 μm	0.2 mbar 0.1 mbar	n/a
H ₂ O	total abundance	nadir	1.38 μm	0.2. pr. μm (detectable)	ground res 5x5 km
H ₂ O	concentration/vertical profile	solar occultation	1.1, 1.38 μm	see text	5-30 km (clear atm.) 20-50 km (dusty atm.) $\Delta z = 2-3\text{km}$
D, H	isotope ratios	limb emission	121 nm	20%	
Aerosols	vertical profile of characteristics mapping of characteristics	solar/stellar occultation nadir spectropolarimetry	UV-IR 1.0-1.7 μm	10 ⁻³ (photometry) polarisation rejection 10 ⁻⁴	5-60 km, $\Delta z = 2-3$ km exploratory
O ₂	concentration vertical profile	stellar occultation	200 nm	20%	35-90 km never done before
O ₂	concentration	limb emission	1.27 μm		tentative
H ₂ O ₂	total abundance	nadir	210 nm		never done before
SO ₂	total abundance	nadir	220 nm		tentative
H, C, O, CO ₂ ⁺ ,CO	vertical profiling of aeronomic emissions	limb emission	118-320 nm	20%	80-400 km, $\Delta z \sim 2$ km
Soil	contribution to surface studies	nadir spectropolarimetry	1.0-1.7 μm	10 ⁻³ (photometry)	ground res 5x5 km

Table 2. SPICAM mass, power and telemetry budgets.

<i>Mass</i>	Electronics block (DPU)	0.9 kg	
	Sensor unit (SU)	3.8 kg	
	Total	4.7 kg	
<i>Power</i>	DPU+SUV	13 W	
	DPU+SUV+SIR	18 W	
<i>Data volume</i>			
	per measurement	SUV	3.1 kB
		SIR	1.05 kB
per orbit		~ 5 MB	

3.1 Overview

SPICAM (Figs. 2-5) consists of two blocks: a sensor unit (SU) that includes UV (SUV) and near-IR (SIR) spectrometers, and a simple data processing unit (DPU). The SOIR solar occultation package (Bertaux et al., 2001) was excluded because of mission mass constraints, but the UV and IR channels have solar occultation capability in their limited wavelength ranges. The instrument's mechanical layout is shown in Fig. 1. Mass, power and telemetry budgets are summarised in Table 2.

3. The Instrumentation

Fig. 2. Optical scheme of SPICAM's UV and IR channels. 1: aperture blend of the UV channel; 2: off-axis parabolic mirror; 3: slit (can be changed from wide to narrow, by a mechanical actuator, see text); 4: concave UV grating; 5: intensifier; 6: CCD; 7: IR channel objective; 8: IR FOV diaphragm; 9/11: collimating lens; 10: AOTF crystal; 12: light trap for undiffracted light; 13: detector proximity lenses; 14: 'extraordinary' beam detector; 15: 'ordinary' beam detector; 16: solar opening (closed by shutter when not looking at Sun); 17/21: flat mirror; 18: IR solar entry; 19: optical fibre; 20: fibre collimator.

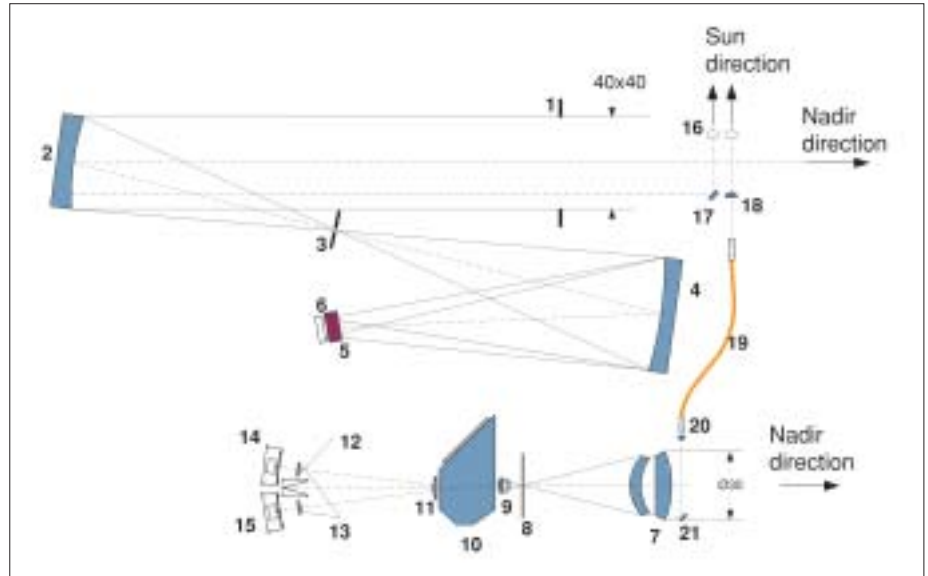
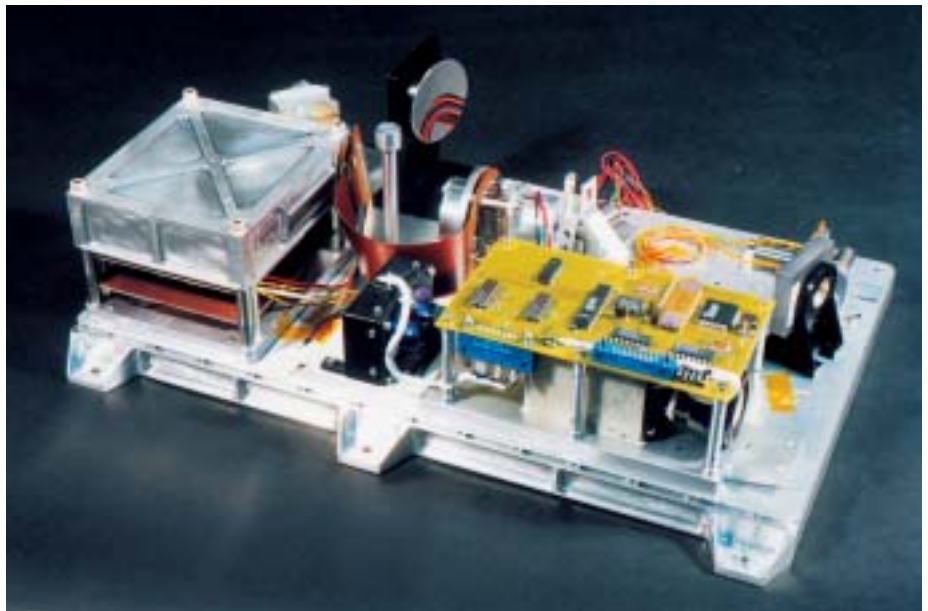


Fig. 3. Breadboard instrument (June 2000; SIR is the prototype), seen from the same vantage point as in Fig. 1. In the final configuration, the parabolic mirror is rectangular, and not circular.



3.2 UV spectrometer (SUV)

The characteristics of the UV spectrometer are summarised in Table 3. For better UV efficiency, SUV includes only two reflective surfaces (Fig. 2). The light flux is collected by an off-axis parabolic mirror, which reflects the light towards the entrance of the spectrometer. At the focal plane, a mechanical slit system provides two configurations: no slit for stellar occultations, and with a slit for extended sources. The slit is divided into two parts, with different widths allowing two spectral resolutions when observing an extended source. The first ($50\ \mu\text{m}$ width) gives good resolution with lower flux; the second ($500\ \mu\text{m}$) gives more sensitivity at the expense of a coarser spectral resolution. The slit can be completely retracted, creating a hole corresponding to the total useful field of view of $2 \times 3.16^\circ$. This configuration is used in the stellar occultation mode at dark limb when the spectrum of the star is recorded on a few lines of the CCD. The required pointing accuracy is 0.2° .

A holographic concave toroidal grating from Jobin-Yvon, ion-etched for higher

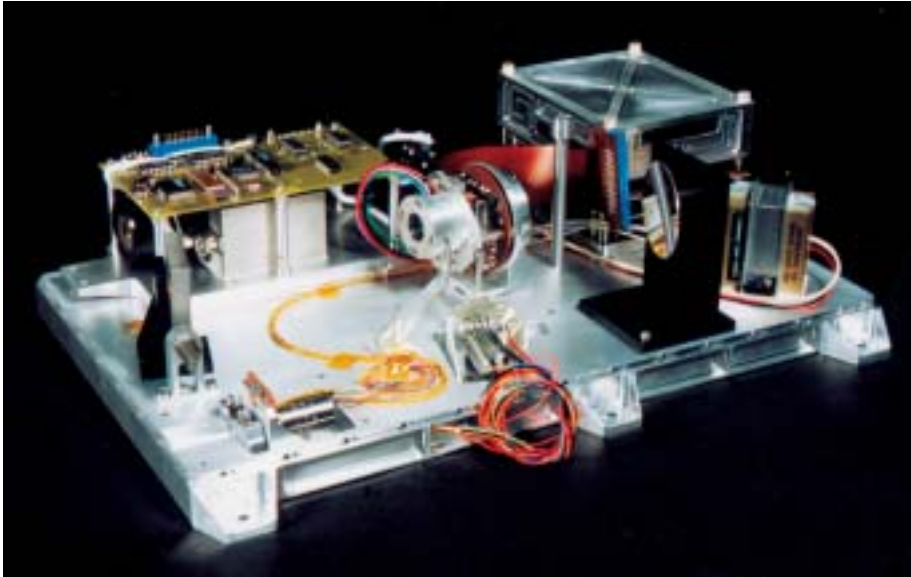


Fig. 4. SPICAM Qualification Model seen from the side of the UV spectrometer. The intensified CCD is placed at the centre. The mirror is at left, the grating is at right.

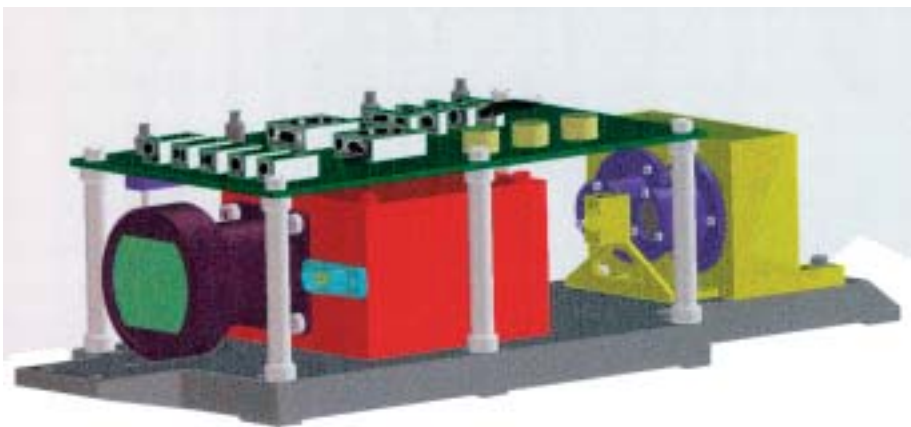
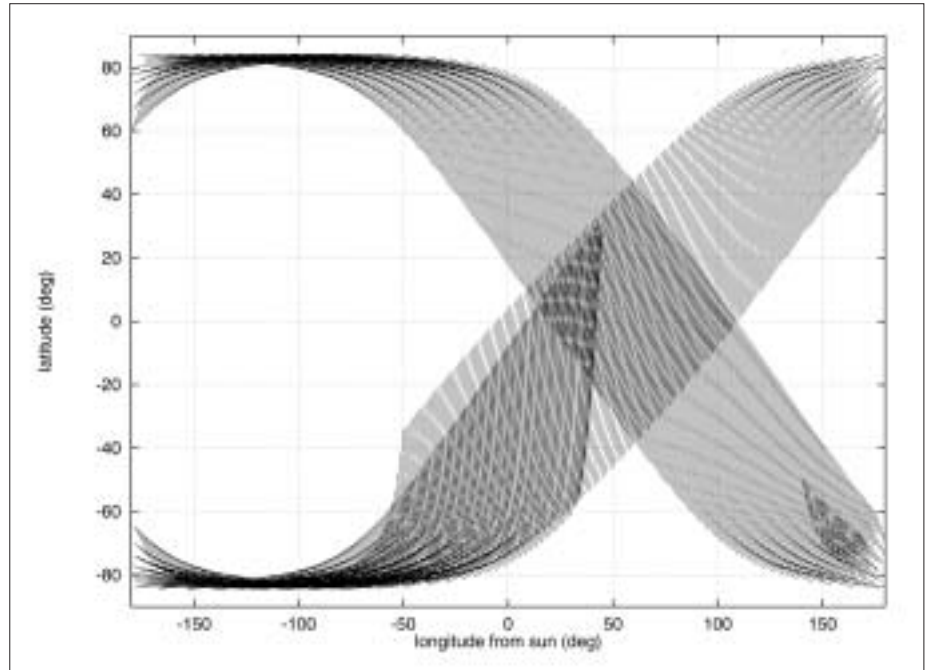


Fig. 5. The AOTF IR channel. From right: entrance lens, AOTF crystal and the two detectors, with the electronics board on top.

Table 3. Characteristics of the SPICAM UV channel (SUV).

Primary mirror	Off-axis parabola 40×40 mm, coated MgF ₂ , $f = 120$ mm
Slit	50 μm × 4.6 mm; 500 μm × 2.2 mm
FOV	of a pixel 0.7×0.7' 2×3.16° no slit (stellar occultation) 0.24×0.95° with double slit
Spectral range	118 - 320 nm
Grating	holographic, concave, toroidal coated MgF ₂ , 290 lines/mm, blazed 170 nm
Spectral resolution per pixel	0.51 nm
Resolving power (occultations)	120-300 stellar; small slit
Resolving power (extended source)	120-300 small slit, ~20 large slit
Pointing accuracy	< 0.2°
Detector	CCD Thomson TH7863 TE cooled at 270K, useful 288×384 pixels, 23×23 μm
Intensifier	Hamamatsu 200M, solar blind CsTe photocathode, input window MgF ₂ + sapphire
Vertical resolution	< 1 km (occultations), ~10 km (limb)

Fig. 6. Longitude from the Sun around pericentre (spacecraft altitude below 800 km) during the first martian year of the mission. (Figure adopted from Hechler & Yanes, 1999).



efficiency, feeds the detection block. The image ratio is ~ 1 , which means that a monochromatic image in the entrance of the spectrometer is conserved in the plane of the detector. The spectral resolution for a point source determined by aberrations is about 1 nm. The CCD detector is a Thomson TH7863 with 288×384 useful pixels and a masked zone of equivalent size. Pixel size is $23 \times 23 \mu\text{m}$. The detector is electrically cooled to $\sim 0^\circ\text{C}$, where the dark current equals 800 electrons per pixel per second, or a few ADU (Analogue to Digital Unit) only. By means of custom-made fibre optics, the CCD is coupled with the output window of the image intensifier (from Hamamatsu, type 200M). A solar blind CsTe photocathode has zero quantum efficiency beyond 320 nm. The input window is made of MgF_2 in order to reach down to Lyman- α (a target of SPICAM). An additional sapphire filter is glued above the window and covers it in part, preventing overlapping of diffraction orders and Lyman- α stray light.

3.2.1 Expected performances

Taking into account the optical characteristics of the UV spectrometer components, quantum efficiency of the photocathode, star spectrum and its reddening owing to interstellar dust absorption, the S/N ratio of SUV in stellar occultation mode can be estimated. Adopting the equation of Henry, it was found that there are nine stars emitting more than $10^4 \text{ phot. s}^{-1} \text{ cm}^{-2} \text{ nm}^{-1}$ at 220 nm, and 86 stars emitting 10^3 - $10^4 \text{ phot. s}^{-1} \text{ cm}^{-2} \text{ nm}^{-1}$. For these two thresholds, S/N is respectively > 91 and > 29 per pixel. There are ~ 100 pixels that may be used to determine the CO_2 or ozone absorption, and this gives an idea of the likely accuracy achieved on the retrieval of line density of CO_2 and O_3 . Simulation exercises show that the accuracy should be of the order of 2-10% for CO_2 (20-160 km) and ozone (below 50 km).

For an extended source observation, the whole slit is illuminated, and it is possible to integrate over several lines of the CCD. When looking at nadir (dayside), the expected number of photoevents that yield $S/N \sim 500$ for 1 s integration is $2.5 \times 10^5 \text{ nm}^{-1}$ at 270 nm.

For limb observations, a typical airglow emission of 8 kR nm^{-1} (as recorded at the bright limb by Mariner-9) results in ~ 4000 photoevents per pixel at 220 nm, yielding a S/N of 62. At wavelengths longer than 300 nm, the large slit would be used for better S/N if necessary. Along the large slit, where the spectral resolution is about

Table 4. Characteristics of the SPICAM near-IR channel (SIR).

Spectral range	1.0-1.7 μm
Spectral resolution	0.5 nm at 1.0 μm ; 1.2 nm at 1.7 μm or better than 4 cm^{-1}
FOV	1°
Telescope	Lens type, \varnothing 30 mm
AOTF	TeO ₂ , efficiency 70% (in polarised light), aperture 3.6×3.6 mm, $\pm 3.5^\circ$
Detector	2 InGaAs PIN diodes (Hamamatsu G5832), \varnothing 1 mm, 1 stage TE cooled to -15°C , $D \sim 3 \times 10^{13} \text{ W}^{-1} \text{ cm Hz}$
Transmission of optics	20%
S/N	~ 1000

5 nm, there is 10 times more flux on each pixel than along the narrow slit. It is possible again to integrate over several lines of the CCD. For 50 lines, it yields $\sim 10^4$ photoevents per nm at 270 nm, or a S/N of 100 for 1 s integration.

For solar occultations, a 0.2 cm^2 mirror looking 90° from the main optical axis is positioned at the entrance pupil, and the detector operates at the lowest gain and integration time of 10 ms.

3.3 Near-IR spectrometer (SIR)

A single-pixel detector of InGaAs, associated with an AOTF, will allow the measurement of the H₂O column at nadir for an instrument mass of only 0.7 kg. The new AOTF devices are based on Bragg diffraction of an entrance beam by the ultrasonic acoustic wave excited within a crystal. They offer the potential of reaching a resolving power, $\lambda/\Delta\lambda$, superior to 1000, amply sufficient to measure nadir H₂O by scanning the absorption lines at 1.38 μm in the solar reflected spectrum. There are no moving parts such as a chopper. This new concept for IR spectroscopy has not flown before on a civil spacecraft but it is now sufficiently mature for space research application.

The AOTF near-IR spectrometer (SIR) is included alongside the UV package; the optical scheme is shown in Fig. 2. The principal characteristics of SIR are summarised in Table 4. A lens telescope 30 mm in diameter has a focal ratio of 1:1.9. A circular diaphragm 1 mm in diameter placed in the focal plane of the telescope forms the FOV. A collimator with two small lenses forms a beam into a custom-made TeO₂ AOTF crystal with an active zone of 23 mm. The divergence of the beams inside the crystal is limited to $\pm 5.5^\circ$. The linear aperture has the minimal pupil of 3.12 mm in the centre of the crystal and is less than 3.5 mm at the edges. The output system separates the beams for different polarisations; it consists of two lenses, the first compensating for the divergence of the output beam, and the second focusing the light at the detector. There are two detectors and two short-focus proximity lenses, for the ordinary and extraordinary beams, to allow measurement of the polarisation of the incoming light.

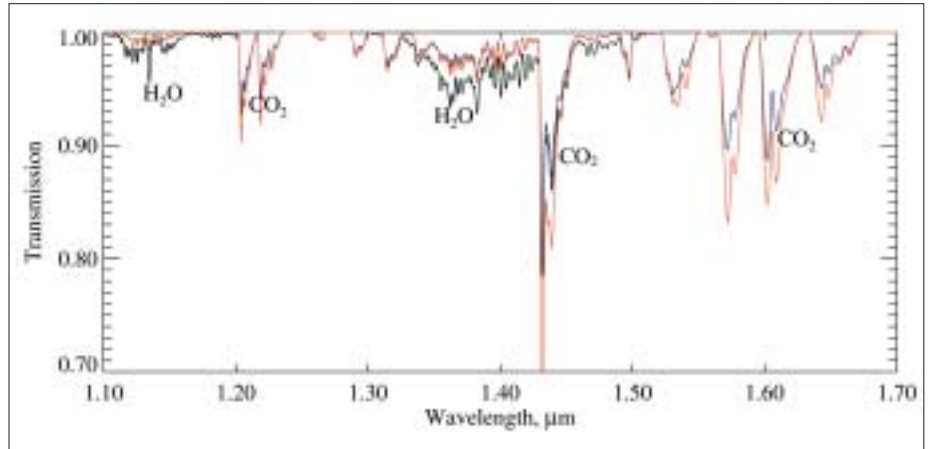
For simplicity, SIR uses the same solar entrance as SUV. An optical fibre delivers the light to the SIR objective. The entry optics of this fibre creates the angular FOV of about 4 arcsec. A collimator lens at the output of the fibre and a 45° flat mirror mounted at the baffle of the SIR objective complete the design of SIR's solar entrance.

4.1 Nadir viewing

SPICAM will obtain the first simultaneous measurements of water vapour and ozone for the martian atmosphere. The vertical column of H₂O and O₃ will be obtained

4. Measurements

Fig. 7. Line-by-line spectra of nadir atmospheric transmission. Spectra are computed for the water vapour abundance of 15 pr. μm and 50 pr. μm (offset in H_2O bands) and for surface pressures of 6 mbar and 7 mbar (offset in CO_2 bands).



systematically along track, on the dayside, when the spacecraft is nadir-oriented, with a ground resolution of ~ 4 km at pericentre. The latitude-season coverage for the first year of the mission is presented in Fig. 6. SPICAM will operate up to 15 min before and after pericentre (altitudes up to 1500 km), and its coverage may be denser than is shown in Fig. 6.

4.1.1. Mapping of H_2O total column abundance in the IR

The method of nadir sounding of water vapour in the near-IR bands continues the approach of Mars 3 and MAWD on the Viking orbiters (Farmer & LaPorte, 1972). For Mars Express, the OMEGA instrument will perform spectral mapping in the same spectral range, but H_2O retrievals from these data will be limited because of the much coarser spectral resolution. The principal contribution to water vapour mapping on Mars-Express is expected from the Planetary Fourier Spectrometer (PFS). PFS offers a near-IR range similar to that of MAWD and a thermal-IR range similar to that of Mariner-9's Fourier spectrometer (IRIS). The thermal-IR sounding of H_2O requires a precise knowledge of the temperature profile but it provides redundancy and can be used at night.

SPICAM's observational principle in its nadir mode is the same as that of PFS. SIR's optical axis is parallel to those of all the nadir-looking instruments on Mars Express. SIR's spectral range (1000-1700 nm) requires ~ 1900 points to be measured. Practically, the amount of data produced by the instrument (polarimetry measurements double the quantity) will be limited by the telemetry budget. The frequency of the AOTF ultrasonic excitation is selected by software, so only the most interesting parts of the spectrum will normally be measured with the desired sampling. The H_2O band could be characterised using only 20 well-chosen points per nadir viewing ($\text{FOV } 1^\circ$), instead of the several thousand for a complete PFS spectrum. The normal exposure time is expected to be within 4 s, allowing the measurement of two spectra (one for each polarisation) of ~ 300 points each.

Simulated spectra of the atmospheric transmittance in the nadir configuration are shown in Fig. 7. They were computed using the HITRAN-96 database, for a multilayered atmospheric model. The water vapour band at $1.38 \mu\text{m}$ is apparent. This band is highly suited to H_2O detection because it is strong and almost free from CO_2 influence. For those reasons, it was used by MAWD/Viking (Farmer & LaPorte, 1972). The spectral signatures of H_2O are well resolved at the expected spectral resolution of 4 cm^{-1} . Owing to this relatively high spectral resolution, the gaseous absorption signatures are easy to distinguish from surface spectral features. The estimated nadir S/N will be better than 500, so the minimal detectable amount of H_2O column abundance is well below 1 pr. μm .

SIR is capable of measuring the column abundance of CO_2 in the $1.43 \mu\text{m}$ band

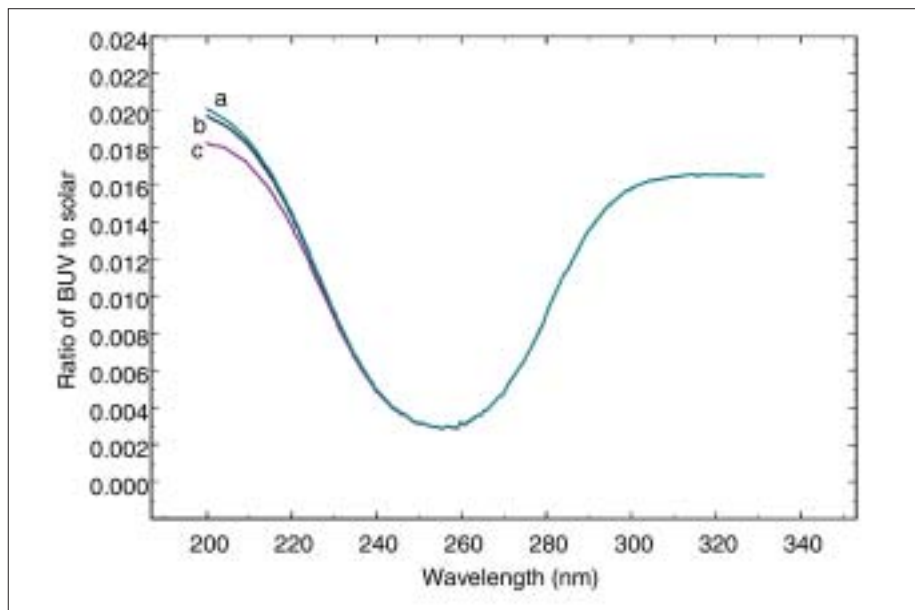


Fig. 8. Modtran computations for nadir geometry. Solar zenith angle 60° , ozone total abundance $5 \mu\text{-atm}$. A possible effect of H_2O_2 is considered: no H_2O_2 (curve a); H_2O_2 column of $2 \times 10^{16} \text{ cm}^{-2}$ (curve b) and $2 \times 10^{17} \text{ cm}^{-2}$ (curve c).

and, therefore, the surface pressure. The pressure change from 6 mbar to 7 mbar results in a very large modification of the spectrum (Fig. 7). Combined with the S/N of 1000, it produces an accuracy of better than 0.02 mbar (at least on a relative scale) in the ground pressure. Owing to the AOTF wavelength selection capability, the surface pressure will be measured simultaneously with H_2O , at a very low telemetry budget.

The ordinary and extraordinary beams at the output of an AOTF crystal can be analysed simultaneously using two identical detectors, and the polarisation of the incident light can be measured with high accuracy (Glenar et al., 1994). The second single-element detector does not significantly complicate the instrument. Polarimetry measurements enable a characterisation of grain size for the surface of Mars and of the properties of atmospheric aerosol components (Santer et al., 1985). In particular, it is possible to detect cirrus-like crystal clouds (Lee et al., 1990). With such measurements at a very limited number (2-3) of wavelengths of atmospheric absorption features (e.g. at $1.25 \mu\text{m}$ and $1.7 \mu\text{m}$, see Fig. 7), important additional information about the reflectivity of the surface and the aerosol extinction will be obtained. AOTF's wavelength control means that these measurements will be performed simultaneously with H_2O detection.

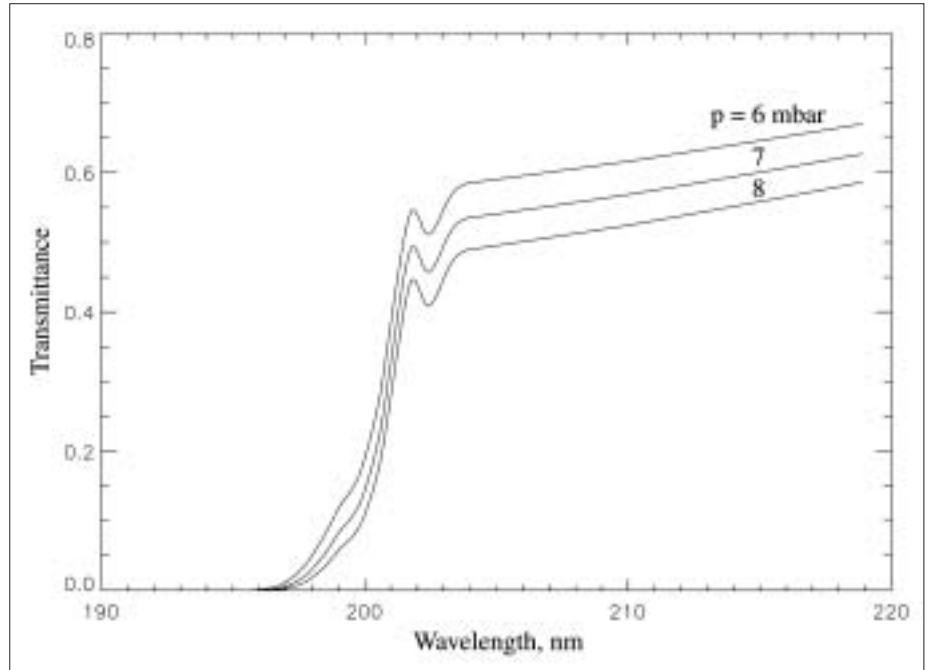
Also, the spectral measurements by SIR could be used for cross-validation of OMEGA and PFS data.

4.1.2 Mapping of ozone in the UV

For nadir measurements of ozone, the most sensitive method will be used: the strong Hartley band around 255 nm imprinted on the solar light scattered by the ground and lower atmosphere. This is the technique that discovered ozone on Mars, and it is extensively used on Earth, showing the Antarctic ozone hole. The reflectance UV spectrum results from several sources:

- light reflected by the surface, defined by an albedo A , and modified twice by extinction of dust and CO_2 Rayleigh scattering (at $\lambda > 200 \text{ nm}$);
- light produced by Rayleigh scattering of CO_2 ;
- solar light reflected by aerosols, distributed vertically;
- absorption by ozone, distributed vertically.

Fig. 9. Variation of the UV nadir transmission spectrum with surface pressure.



Wehrbein et al. (1979) were able to fit the Mariner-9 data with a simple single scattering model, defined by four parameters: ozone optical depth (τ_0), surface albedo (A , assumed to be constant in the UV range), optical depth of dust and Rayleigh (τ_c) and the scale height H_0 of ozone, different from the fixed atmospheric scale height H_S . Indeed, they found a better fit of the bottom of the spectral reflectance trough (Fig. 8) with a ratio $H_0/H_S = 0.6$ than with a fixed value $H_0 = H_S$, showing that ozone was found mostly near the cold surface where the air is dry in high-latitude regions.

A refined analysis scheme requires a more sophisticated algorithm than the one used for the early interpretation of Mariner-7 and -9 data (Barth & Hord, 1971; Barth et al., 1973; Wehrbein et al., 1979) but such algorithms are already working for the Earth (the solar backscatter UV method, used by the Global Ozone Monitoring Experiment on ERS-2).

With SPICAM UV, which registers all wavelengths simultaneously, the S/N will be much greater than for Mariner-9's UV spectrometer (larger than 100 for each nanometer of spectrum in 1 s integration time). This allows the aerosol distribution to be disconnected from the air scale height and Rayleigh scattering. Either a discrete ordinate method or codes similar to those used for interpreting solar backscatter UV spectra in the Earth's atmosphere will be used.

Figure 8, computed for an ozone quantity of $5 \mu\text{atm}$ ($1 \mu\text{atm} = 2.689 \times 10^{15} \text{ mol cm}^{-2} = 0.1 \text{ Dobson units}$), shows the trough of ozone centred at 255 nm. It is estimated that a trough of $\sim 1\%$ is detectable, corresponding to a vertical optical thickness at 255 nm of 0.5%, or a column density of $N = \tau_0/\sigma = 4 \times 10^{14} \text{ mol cm}^{-2}$, or $0.15 \mu\text{atm}$. This allows measurements of ozone in all seasons and latitudes. Above this threshold (say, $N > 2 \mu\text{atm}$), the statistical noise will be a negligible source of error, while systematic errors give an uncertainty of 5%.

SUV will be regularly calibrated in flight by observing standard stars and the Sun. The absolute solar spectrum outside the atmosphere is well known. The reflectance spectrum of Mars will therefore be obtained with a good absolute accuracy and at a spectral resolution of 1 nm. Then, in addition to the main features of the reflection spectrum such as Rayleigh and aerosol scattering overlaid with ozone and CO_2 absorption, other unknowns can be retrieved:

- for surface pressures of 6 mbar and 8 mbar (the total CO₂ vertical column is directly connected to the surface pressure), the absorption edge varies in wavelength position at 210 nm (Fig. 9). Therefore, there is the promising possibility of measuring the surface pressure from the position of the absorption edge in the reflected spectrum. An accuracy of half-a-pixel (easily achievable with such a high S/N) or 0.25 nm on the wavelength would translate into an accuracy of ~0.2 mbar. These data will be used for cross-validation of more precise nadir SIR surface pressure measurements and, combined with the known altimetry, will provide a valuable source for meteorological studies.
- H₂O₂ presents continuous absorption in the UV around 200-220 nm (Yung & Demore, 1999). A simulation of the reflectance (Fig. 8) shows that even for case b, which is not for maximum H₂O₂ conditions, there is a small difference. Though it is difficult to disentangle the continuous absorption by H₂O₂ from dust, it is hoped that a careful analysis with assimilation of aerosol data obtained at other wavelengths will allow the first measurement of this important molecule.

4.2 Vertical profiling by stellar occultation in the UV

SPICAM will measure the vertical distribution of CO₂, temperature, O₃, aerosols, O₂ and possibly H₂O₂ by using stellar occultation, as planned for SPICAM/Mars-96.

The principle is simple. Along the spacecraft's orbit, stars are occulted one after the other by the planetary limb opposite the velocity vector. At a predetermined time, the spacecraft is oriented in such a way that the line of sight of SUV points towards a given star. The stellar spectrum recorded above the atmosphere (say, at 200 km), unaltered by atmospheric absorption, serves as a reference spectrum. Then, while the spacecraft is maintained in a 3-axis, inertial attitude, the line of sight intersects increasingly deeper parts of the atmosphere, down to total occultation.

The stellar occultation technique offers three decisive features:

- an absolute concentration derived from a relative measurement (self-calibration means there is no need for instrument calibration);
- excellent vertical resolution, whatever the distance to the planet (because the star is a point source);
- the accuracy of altitude knowledge, in contrast with limb emission methods, is independent of the spacecraft attitude. The line of sight is determined entirely by the direction of the star in the sky (known) and the position of the spacecraft on its orbit.

Stellar occultations will be performed preferably on the night side of the orbit, and will not affect the operation of dayside mapping instruments. The spacecraft is commanded to direct the SUV line of sight towards a bright UV star and this fixed orientation is maintained within 0.5° (nominal spacecraft capability is better than 0.05°, ensuring that the star remains within the 1° FOV of the instrument during the occultation, which lasts typically 1-4 min). Several (3-5) occultations per orbit are foreseen, the limiting factor being the spacecraft orientation, which is a resource to be shared among the various investigations. Hot stars are preferred, because they are brighter in the UV. Their spectra are flatter than the solar spectrum in the UV. This occultation method offers other features:

- whatever the orbit, there will be numerous opportunities for stellar occultations;
- when a star is occulted during one orbit, it will be occulted again during the following orbits at about the same latitude, but at different longitudes;
- the vertical profiling is not restricted to be along the ground track, in comparison with other instrumental methods;
- de-occultation (star rise) is also possible, since there is no closed-loop tracking system.

Fig. 10. Absorption cross-sections of CO₂ and ozone in SPICAM's UV spectral range.

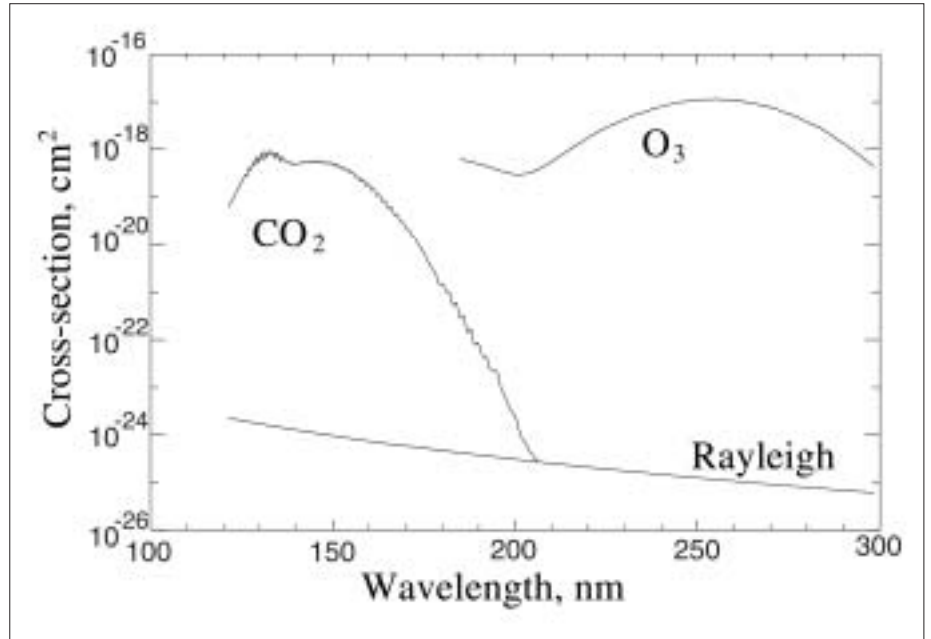


Figure 10 shows the absorption cross-sections of CO₂ and ozone in the UV as a function of wavelength. O₂ is absorbing (Schumann-Runge bands) between the peaks of CO₂ and O₃, offering the possibility of actually measuring O₂. Other absorbers are dust (Mie scattering generalised to non-spherical particles) and possibly H₂O₂ and SO₂. The atmospheric transmission simulations are presented in Fig. 11 for various tangential heights. Besides CO₂ and ozone, a dust profile was assumed, with a vertical optical thickness $\tau_d = 0.2$ at 300 nm. Rayleigh extinction by CO₂ was also included in the simulations.

Because the CO₂ cross-section presents an enormous dynamic range in the UV, CO₂ absorption may begin to be detected at an altitude of 150 km. For decreasing tangential heights, the CO₂ manifests itself by a sharp cut-off that increases in wavelength, up to ~200 nm at $z = 10$ km. Longward of 200 nm, the transmission spectrum is dominated by dust and CO₂ Rayleigh extinction, with the additional trough at 255 nm due to ozone. The depth of this trough is a direct measure of ozone line density. From the given S/N in stellar occultation mode (see above), the O₃ line density N_h accuracy will depend on the UV magnitude of the star. It can be estimated that the accuracy on the O₃ line density will be about 2% for about 20 stars in the sky and the measuring threshold corresponding to an absorption of ~1% corresponds to $N_h = 10^{15}$ mol cm⁻² (horizontal) and local density of 3.5×10^7 cm⁻³ at all altitudes $z > 15$ km (Korablev, Bertaux & Dubois, 2001).

The Rayleigh extinction above 200 nm can be computed from the CO₂ line density determined below 200 nm. The remaining continuous absorption above 200 nm may be attributed to dust/aerosols for a determination of its vertical distribution and spectral characteristics in the UV.

4.2.1 CO₂ density and temperature profile

Once the line density of CO₂ is determined from the transmission spectra, the local density $n(z)$ is determined from an Abel inversion. Then, the hydrostatic equation allows temperature to be determined. As for O₃, the accuracy on the CO₂ line density will be about 2% for 20 stars. The accuracy of the retrieved temperature is estimated to be ± 5 K in the whole range of altitude, starting at 130-160 km at the top level, while the lowest altitude achieved will depend on the absorption by aerosols or clouds, and will most likely be 5-20 km.

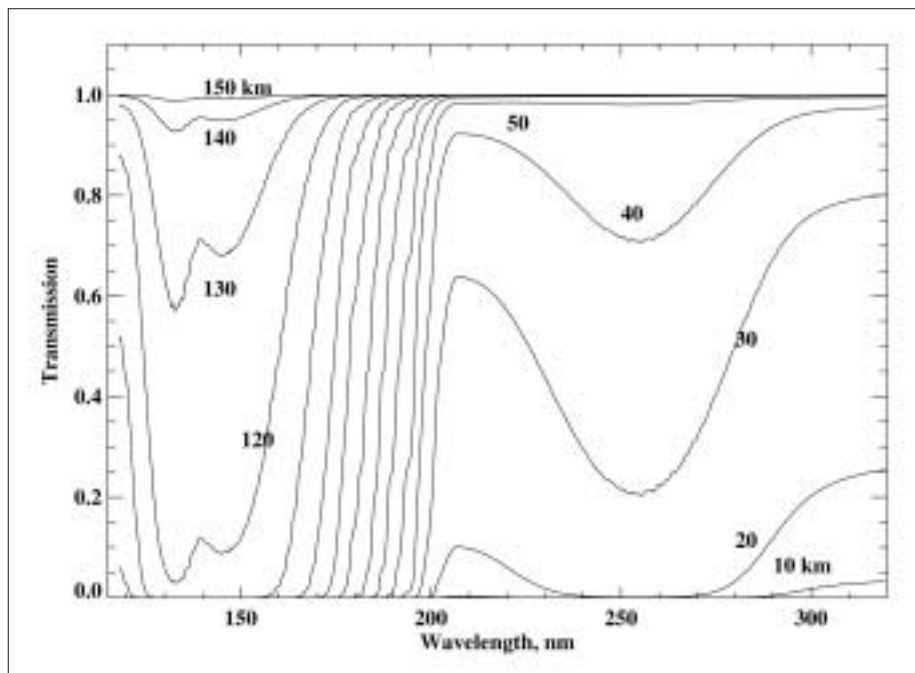


Fig. 11. Simulated stellar occultation transmission spectra for tangential altitudes from 150 km to 10 km in steps of 10 km.

There is a known dependence of the CO_2 absorption cross-section on the temperature T . The retrieval process begins by a first iteration with an *a priori* profile $T(z)$ and corresponding choice of CO_2 cross-section. Then, N and n are retrieved, and the scale height is derived, independently of a wrong choice of the cross-section, providing a new guess for $T(z)$. A few iterations allow convergence of the process. A similar retrieval procedure was developed and tested for the GOMOS/Envisat stellar occultation experiment.

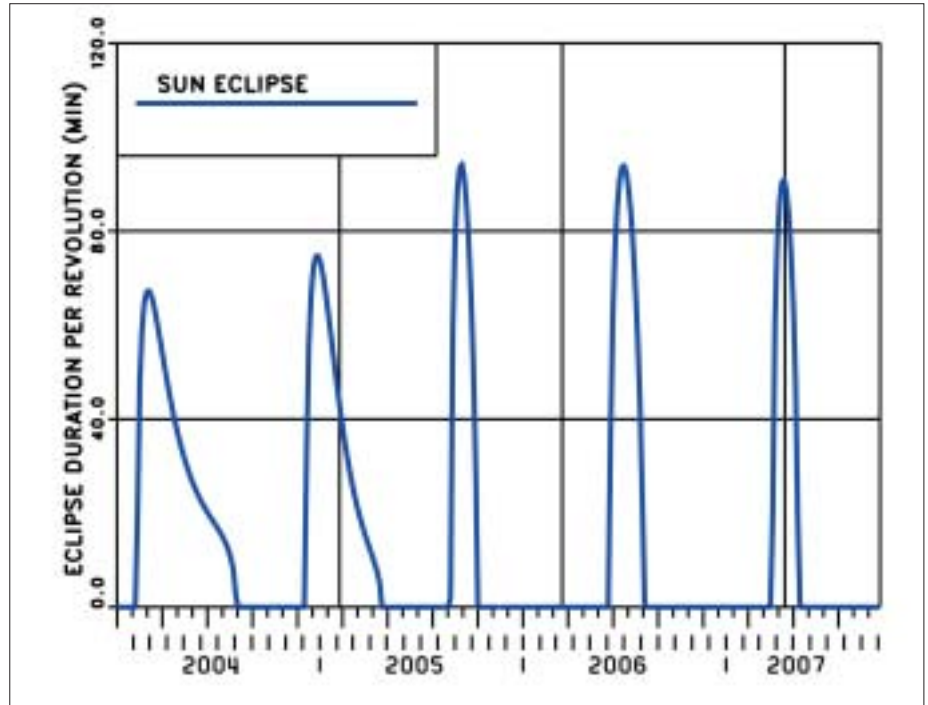
Though nighttime stellar occultations are preferred, it is important to keep in mind that some daytime occultations should be performed on particularly bright stars on the bright limb. They could be combined with UV airglow limb observations to get a better understanding of thermal structure, and to solve unambiguously the discrepancy between Viking and Mariner-9 temperature profiles at $z > 120$ km. In addition, the day-night amplitude variation of the exospheric temperature (at the top of the thermosphere) is a crucial test for the validity of sophisticated Thermospheric General Circulation Models (TGCMs), such as that developed by Bougher et al. (1990). The model predicts a dayside temperature of 270K at 170 km, and a night side $T = 160\text{K}$ at the same altitude, but it was impossible to validate this model owing to the lack of measurements. SPICAM offers a wide coverage of density/temperature profiles (local time, season, latitude, geography and solar activity) with which the TGCM could be validated (or invalidated, and modified accordingly). Then, such a model could be used as a predictive tool for managing aerocapture/aerobraking operations in future.

Finally, SUV has a unique ability to detect condensation clouds during the night. The Pathfinder camera detected fog, but was not able to determine the layer's altitude. SUV will do this accurately.

4.2.2 The case for molecular oxygen

Molecular oxygen is the result of CO_2 photodissociation. Its mixing ratio was measured to be of the order of 10^{-3} , and is assumed to be constant. O_2 provides in the Schumann-Runge bands (170-210 nm) an additional absorption that should be measurable. Calculations show that the difference of transmission between an atmosphere with O_2 ($\text{O}_2/\text{CO}_2 = 10^{-3}$) and an atmosphere without O_2 amounts to 2%

Fig. 12. Periods of solar eclipse for Mars Express orbit G3A. (Figure adopted from Hechler & Yanes, 1999.)



between 80 km and 50 km, in a bandwidth of about 20 nm centred on 190 nm. The absorption decreases somewhat below, but is detectable down to 35 km. In principle, one expects a constant mixing ratio of O_2 , in altitude and over the planet, inasmuch as we understand the chemical reactions that control this molecule. There is, however, the special case of the polar winter, when the CO_2 condenses on the martian surface while the O_2 remains, enriching the airmass. The O_2 mixing ratio may be used as a tracer of polar airmass circulation. Its exact value depends on how fast the non-polar airmasses flow to the pole to replenish the locally condensing CO_2 atmosphere. The UV occultation technique is the only way of accessing to this important molecule.

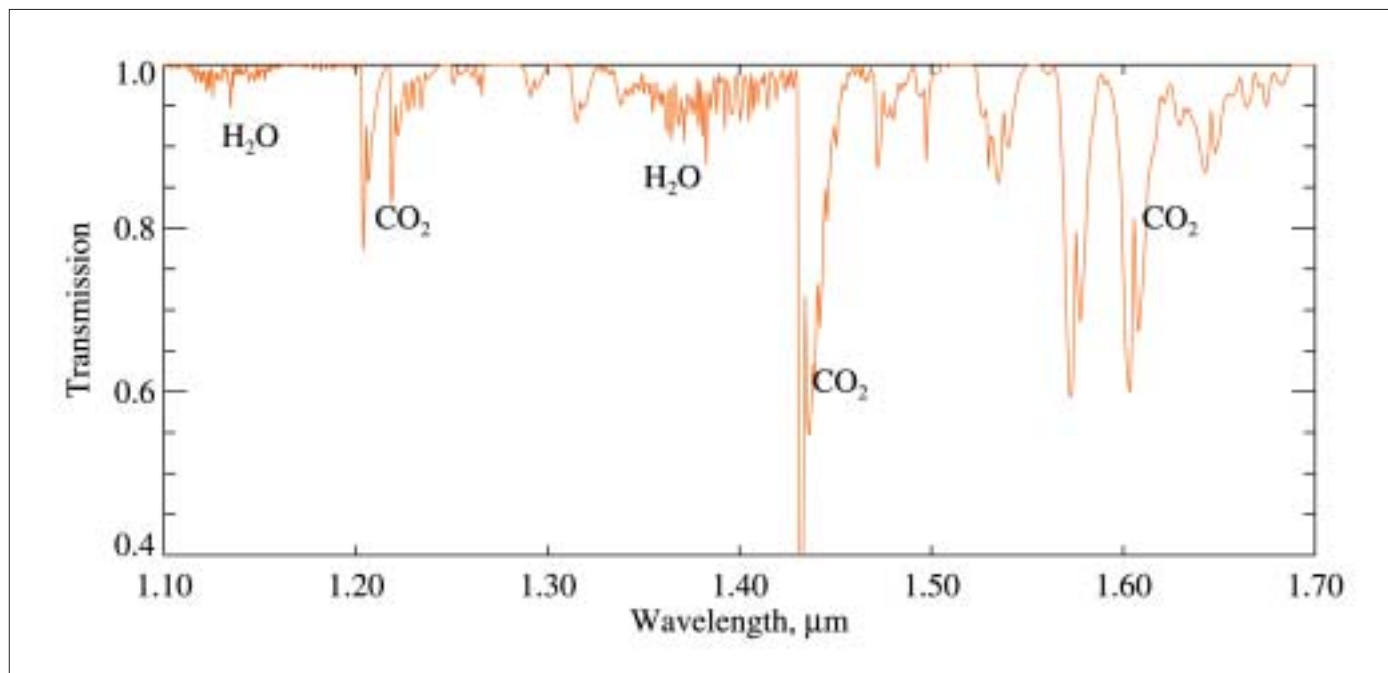
4.3 Solar occultation measurements

As well as the SUV working in the stellar occultation mode, both SUV and SIR will benefit from the advanced pointing capabilities of Mars Express for solar occultations. A solar aperture below the sensor will be pointed towards the Sun by orienting the spacecraft. The angular diameter of the Sun as seen from Mars is 0.35° , but the variability in the brightness of the solar disc requires an attitude control accuracy of 0.1° , well within the spacecraft specifications.

In the case of a polar orbit, there is no precession of the orbital plane. Then, during one martian year, there are two periods of solar occultations, centred on the two dates when the Sun is in the orbital plane (the angle between the solar vector and the orbit plane is zero). Therefore, the possibilities of solar occultation measurements are independent of the other orbital elements.

For the nominal orbit during the mission lifetime, some 700 sunset-sunrise occultation sequences are expected. The occultations occur within about 60 min of pericentre. The two hemispheres are covered twice during spring and autumn (Fig. 12). The spacecraft-limb distance during these periods varies between 4000 km and 11 500 km. The duration of each occultation sequence for the altitude range of 0-150 km is 2-3 min. During the second martian year, there will be fewer occultations closer to apocentre (spacecraft-limb distance above 8000 km).

Solar occultation spectroscopic sounding of a planetary atmosphere offers several advantages. The radiation of the Sun is an incomparably powerful source and it



traverses the largest possible atmospheric path (the airmass factor reaches 40-45 for Mars). As for stellar occultations, the measured spectra are compared with the unattenuated signal above the atmosphere, which is measured in the same sequence before occultation to provide self-calibration. A disadvantage is that the atmosphere can be observed only when and where there is a sunset/sunrise.

Vertical resolution of the UV channel is determined by the slit width in one direction and by the pixel height in the other. Assuming that the spectra will be integrated over two lines of the CCD, the FOV will be 1.5×1.5 arcmin, leading to a linear resolution of 1.7-5 km. Using a single CCD line doubles the linear resolution in one direction. The FOV of the IR channel will be better than 4 arcmin because of the fibre optics that deliver the solar light to SIR, limiting the vertical resolution at the limb to 5 km under the best conditions.

The solar-mode SUV will target the same scientific objectives at the terminator as the stellar occultation mode but with a better S/N. The Sun's brightness allows deeper sounding for dusty conditions. The solar mode SIR can measure water vapour vertical profiles – extremely important measurements that cannot be done by any other instrument aboard Mars Express or any planned US mission.

4.3.1 Water vapour profiling by SIR

The efficiency of the solar occultation method for studying the vertical distribution of water vapour was proved during the Phobos mission, when measurements at $1.87 \mu\text{m}$ determined H_2O vertical profiles in the altitude range 10-50 km (Rodin et al., 1997).

The simulated absorption spectrum of the martian atmosphere at the limb is shown in Fig. 13. It is similar to the nadir spectra, but the absorptions are much more profound. The same near-IR absorption band at $1.38 \mu\text{m}$ will be used for both. The absorption features of H_2O in this band are deeper than 10%. The accuracy of water-vapour limb sounding depends on atmospheric conditions. Based on available observations (one of which comes from the solar occultation experiment on Phobos, Rodin et al., 1997) and modelling results (Rodin et al., 1999), two types of H_2O profiles can be considered: 'dry and cold' and 'warm and wet'. The dry vertical profile of H_2O constrained by a relatively cold temperature profile in a clean atmosphere (Clancy et al., 1990; Rodin et al., 1997) can be described as 100 ppm below

Fig. 13. Simulated near-IR spectrum of the martian atmosphere at the limb (tangential altitude 10 km).

10 km, ~30 ppm at 15-20 km and 10 ppm above 25 km. In these conditions, the highest sounding altitude is around 30-35 km, and the lowest, constrained by the aerosol absorption, is within 5-10 km. For 'warm and wet' conditions, the highest altitude is 45-50 km (though the absorption at these altitudes is ~0.5%) but the lowest may be 10-15 km because of the larger amount of dust in the atmosphere, which levitates to higher altitudes.

4.3.2 Profiling and characterisation of atmospheric aerosols

The main component of martian aerosols is micron-sized dust, a product of soil weathering, and water ice. According to MGS data (Pearl et al., 1999; Smith et al., 1999), clouds composed of 2 μm particles with visible optical depths of up to 0.1 are formed at the water vapour condensation level, which, in equatorial regions, varies from lower than 10 km at aphelion to almost 50 km in the perihelion season. Occultation spectroscopy is probably the most sensitive remote-sensing technique for directly sounding the vertical structure of clouds and aerosols. In solar occultation, the information about the spectral continuum at distant spectral wavelengths is a byproduct of gaseous absorption retrievals. As soon as the slant atmospheric opacities at different wavelengths are obtained from occultation data, the aerosol extinction can be retrieved by Abel inversion. Then, using the Mie theory (possibly adapted for non-spherical particles), a number of unknown parameters characterising the aerosol component can be extracted, such as the size distribution, and the real and imaginary parts of the refractive index. Also, the vertical variation of key parameters such as the effective size and the number density can be retrieved.

SPICAM measurements are expected to be able to separate the mineral and volatile aerosol fractions. However, when both fractions are present, it will be difficult to determine whether mineral dust particles are cloud condensation nuclei or two kinds of aerosols mixed along the optical path. To help the interpretation, these data will be compared with or assimilated into the 1-D cloud microphysics model mentioned above. It is especially interesting that the vertical profiles of icy aerosols will be obtained in parallel with water vapour profiles. If the observed water vapour is far from saturation, we expect mostly mineral dust aerosols that can be verified by spectroscopic analysis. It is a general assumption that the mineral-dust profile is controlled by the vertical component of large-scale atmospheric circulation and eddy mixing. Therefore, these phenomena can be constrained by the retrieved dust profiles (Korablev et al., 1993).

4.3.3 The consequences of deleting the dedicated solar occultation sensor (SOIR)

The classical IR grating spectrometer for solar occultations (Bertaux et al., 2000) covers a broad spectral range (1.3-4.8 μm) at a relatively high spectral resolution (2-4 cm^{-1}), almost the same as the spectral resolution and FOV of PFS. The AOTF spectrometer has the spectral range of 1.0-1.7 μm and the spectral resolution of ~3.5 cm^{-1} . The FOV in occultation mode is larger (4-5 arcmin) because of the simplified entrance system.

Unfortunately, the mass constraints of Mars Explorer dictated the deletion of SOIR. Apart from the vertical resolution, there is no significant degradation of accuracy for H₂O profiling in solar occultation. No redundancy is lost; only the 1.38 μm H₂O band of the three main short-IR absorption bands (1.38, 1.87, 2.56 μm) will be measured, but the grating spectrometer could measure only one at a time anyway. Reduced spectral resolution does not affect the accuracy drastically. The narrower spectral range makes the aerosol profiling less effective, losing the capacity to measure some interesting components:

- the HDO band at 3.7 μm , so the IR measurements of D/H in the lower atmosphere cannot be compared with the UV measurements in the thermosphere;
- exploratory studies of the carbonic compounds at 3.3-3.7 μm ;
- CO measurements in the fundamental CO band at 4.7 μm and in the 2.3 μm

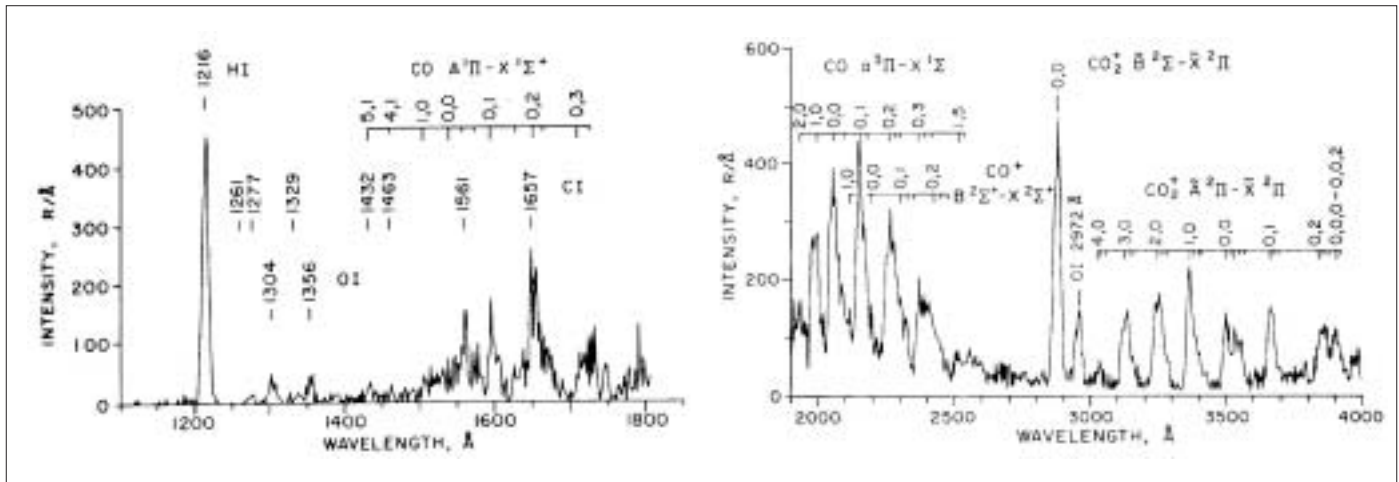


Fig. 14. Mariner-6 and -7 UV spectrum of the upper atmosphere of Mars at a resolution of 20 Å. Limb spectrum at altitudes between 140 km and 180 km, including four individual observations (figure adapted from Barth et al., 1971).

overtone band. Photochemical models predict that CO with its long lifetime would not show any significant altitude stratification, but geographical variability of CO in the lower atmosphere is worth monitoring;

- strong saturated CO₂ bands (at 4.0 μm and 2.7 μm) fall outside of the AOTF spectral range. It was planned to use these bands for atmospheric density studies at 80-120 km; the same sounding will be done in the UV. This redundancy, and the possibility of independently measuring the rotational temperature in the CO₂ bands, is lost.

Conversely, an important advantage of the AOTF spectrometer over the grating spectrometer is that all the interesting regions of the spectral range can be acquired with the desired sampling during the same occultation session using spectral micro-windows (for gaseous components) and distant points (for aerosol characterisation in the spectral continuum). Thus full advantage will be taken of each occultation, which are relatively infrequent events.

4.4 Airglow observations at the limb

4.4.1 Study of the ionosphere in UV

Most of the ionosphere lies below the planned pericentre altitude of Mars Express (300 km) so *in situ* measurements will be impossible. However, the natural UV airglow of the atmosphere allows remote studies of the ionosphere and its temporal behaviour as a function of solar-wind parameters. Figure 14 shows the dayglow spectrum recorded by the Mariner-6 and -7 UV spectrometers (Barth et al., 1971).

The main ionisable neutral constituent is CO₂. The CO₂⁺ transition (B²Σ^{u+} - X²π_g) at 289 nm is produced by photoionisation of CO₂ from solar UV at λ < 69 nm. The other band CO₂⁺ (A²Σ_u - X²π_g), between 300 nm and 400 nm, is produced by a combination of photoionisation and fluorescence scattering on CO₂⁺ ions. The SPICAM UV long-wavelength cut-off is at 320 nm, which is sufficient to measure the (4,0) and (3,0) transitions of the A-X band.

The intense Cameron band of CO a³π - X¹Σ⁺ observed at 190-270 nm is produced by a combination of photodissociation of CO₂ by solar UV (λ < 108 nm), electron impact dissociation of CO₂ and dissociative recombination of CO₂⁺. The variation of this band intensity with altitude was used to determine the vertical profile of CO₂ above 120 km, and from the scale height the temperature of the thermosphere was derived (Stewart et al., 1972). This indirect method of determining CO₂ could be validated with SUV, when a stellar occultation is performed on the dayside. The large slit of the FOV will be used to ease the pointing requirement; the bright stellar spectrum would show up, superimposed on the general airglow only on a few lines of the CCD, and the

analysis of the spectro-image would provide information on CO₂: direct measurement by absorptive occultation, and indirect CO Cameron band emission. Neutral O and neutral H vertical density profiles may be derived from the vertical variations of their resonance lines at 130.4 nm and 121.6 nm (Lyman- α), respectively.

4.4.2 Hot oxygen corona, atmospheric escape and D/H ratio

While $\text{CO}_2 + h\nu \rightarrow \text{CO}_2^+$ is the main photoionisation source, it is the O₂⁺ ion that is the most abundant. As a result, a hot atomic oxygen corona around Mars (Ip, 1988), similar to that detected by Venera-11 (Bertaux et al., 1981) around Venus from the emission at 130.4 nm, can be easily detected with SPICAM's better sensitivity. This may be an important source of O escape from the martian atmosphere, somewhat equilibrating the escape of H atoms responsible for the measured enrichment of D/H ratio (a factor of 6) detected in the IR in the lower atmosphere (Owen et al., 1988).

D atoms and H atoms both produce a Lyman- α resonant emission in the upper atmosphere, excited by the H solar Lyman- α line. Since the wavelength separation (H, 121.566 nm; D, 121.533 nm) is larger than the thermal width of each line, the radiative transfer of both types of Lyman- α are totally decoupled. Though SUV has insufficient spectral resolution, these two emissions could be tentatively separated from the vertical distribution of the sum intensities. While the H emission should present a smooth variation around the CO₂ absorption limb (around 120 km), because it is optically thick, the D Lyman- α emission is optically thin, and the intensity doubles just above the limb. Any spike at the CO₂ limb in the vertical distribution of Lyman- α total intensity limb (estimated to be ~300 R) would be due to D atoms. Therefore, both D abundance and H abundance could be determined in the upper atmosphere, and compared with HDO/H₂O measurements in the lower atmosphere in the IR. With Lyman- α measurements from the Hubble Space Telescope, Krasnopolsky et al. (1998) reported that the D/H ratio in the upper atmosphere was lower by a factor of 10 than the D/H ratio in the lower atmosphere. One possible explanation (Cheng et al., 1999) is that HDO is less photo-dissociated than H₂O, because of a smaller cross-section. This effect is probably insufficient to explain the discrepancy, and another explanation is known to be important (Bertaux & Montmessin, 2001): fractionation through condensation. HDO is more prone to condense in ice crystals than is H₂O from the vapour phase, decreasing the D/H ratio with altitude in regions where the photo-dissociation rate is important. This effect is known to play an important role in the Earth's upper troposphere-stratosphere, where HDO is severely depleted just above the tropopause.

4.4.3 O₂ limb airglow in the IR

A dayglow 1.27 μm O₂ (¹ Δ_g) emission was observed from the ground at high resolution by Noxon et al. (1976). This emission was predicted just after the discovery of ozone on Mars by Mariner-9 (Barth & Hord, 1971). The martian situation is similar to Earth's, where a strong airglow arises from O₂ (¹ Δ_g) production from ozone photolysis. Latitude correlation of this emission with Mariner-9 O₃ was reported by Traub et al. (1979). Mapping of this emission was reported by Krasnopolsky & Bjoracker (2000). Krasnopolsky (1997) argues that the O₂ emission provides even better insight to photochemistry than ozone, since it is more sensitive to the variations of the water vapour saturation level (10-35 km) than total ozone, which remains almost constant.

The band intensity observed by different authors from the ground varies from 1.5 MR to 26 MR; the limb intensity should be greater by a factor of 25 if the dayglow layer is above dust. If, however, the dayglow and dust are uniformly mixed, this factor is approximately 3. A reasonable compromise of these factors is a mean value of ~10. Therefore, if pointed to a sunlit limb together with SUV, SIR could observe the O₂ (¹ Δ_g) band intensity of 15-260 MR in a 30 km-thick layer at the limb. This height corresponds roughly to the FOV of the IR spectrometer, and the predicted S/N will be better than 20 in a single spectral bin, or 200-300 for the entire band.

Several measurements provided by SPICAM are unique, including:

- ozone measurements are not included on any flying or planned mission. The vertical distribution of ozone will be measured during stellar occultations. H_2O_2 will possibly be detected.
- the density/temperature profiles will provide important constraints for building meteorological and dynamical atmospheric models, from the surface to the exosphere. TES/MGS overlaps up to 80 km altitude, but SPICAM will be the only way to access up to 160 km, the region used for aerocapture and aerobraking. Stellar occultations provide a unique opportunity for detecting clouds on the night side and for measuring O_2 .
- the remote sensing of the ionosphere from natural emissions is not included in any other planned mission. The measurements of D/H from UV limb emissions will verify if this ratio is constant or if it varies according to condensation/evaporation processes (as around the terrestrial tropopause).
- after the loss of the Pressure Modulation IR Radiometer on the Mars Climate Orbiter, the only instrument to provide water-vapour vertical profiling will be SPICAM (via solar occultations).

It is already clear that, as on Earth, the atmosphere of Mars has a strong interannual variability. Atmospheric studies must be pursued at every opportunity. It is also essential that a variety of techniques be employed: SPICAM applies the most successful methods from terrestrial studies: backscatter UV spectroscopy and solar/stellar occultation limb sounding.

Acknowledgements

The authors wish to thank M. Richardson, T. Schofield and V. Krasnopolsky for useful discussions. CNES and the Belgian government are financing SPICAM.

- Atreya, S.K. & Z.G. Gu (1994). Stability of the Martian Atmosphere: Is Heterogeneous Catalysis Essential? *J. Geophys. Res.* **99**, E6, 13,133-13,145
- Barth, C.A. & C.W. Hord (1971). Mariner Ultraviolet Spectrometer: Topography and Polar Cap. *Science* **173**, 197-201.
- Barth, C.A., C.W. Hord, A.I. Stewart, A.L. Lane, M.L. Duck & G.P. Anderson (1973). Mariner 9 Ultraviolet Spectrometer Experiment: Seasonal Variation of Ozone on Mars. *Science* **179**, 795-796.
- Barth, C.A., C.W. Hord, J.B. Pearce, K.K. Kelly, G.P. Anderson & A.I. Stewart (1971). Mariner 6 and 7 Ultraviolet Spectrometer Experiment: Upper Atmosphere Data. *J. Geophys. Res.* **76**, 2213-2227.
- Barth, C.A., A.I.F. Stewart, S.W. Bougher, D.M. Hunten, S.J. Bauer & A.F. Nagy (1992). Aeronomy of the Current Martian Atmosphere. In *Mars* (Eds. Kieffer et al.), Univ. of Arizona Press, Arizona, USA, pp1054-1089.
- Bertaux, J.L., J.E. Blamont, V.M. Lépine, V.G. Kurt, N.N. Romanova & A.S. Smirnov (1981). Venera 11 and Venera 12 Observations of EUV Emissions from the Upper Atmosphere of Venus. *Planet. Space Sci.* **29**, 149-166.
- Bertaux, J.L., D. Fonteyn, O. Korablev, E. Chassefière, E. Dimarellis, J.P. Dubois, A. Hauchecorne, M. Cabane, P. Ranou, A.C. Lévassieur-Regourd, G. Cernogora, E. Quemerais, C. Hermans, G. Kockarts, C. Lippens, M. De Maziere, D. Moreau, C. Muller, E. Neefs, P.C. Simon, F. Forget, F. Hourdin, O. Talagrand, V.I. Moroz, A. Rodin, B. Sandel & A. Stern (2000). The Study of the Martian Atmosphere from Top to Bottom with SPICAM Light on Mars Express. *Planet. Space Sci.* **48**, 1303-1320.
- Bertaux, J.L. & F. Montmessin (2001). Isotopic Fractionation through Water Vapor

5. Conclusion

References

- Condensation: the Deuteropause, a Cold Trap for Deuterium in the Atmosphere of Mars. *J. Geophys. Res. Planets* **106**, E 12, 32879-32884.
- Blamont, J.E. & E. Chassefière (1993). First Detection of Ozone in the Middle Atmosphere of Mars from Solar Occultation Measurements. *Icarus* **104**, 324-336.
- Blamont, J.E., E. Chassefière, J.P. Goutail, B. Mege, M. Nunes-Pinharanda, G. Soushon, V.A. Krasnopolsky, A.A. Krysko & V.I. Moroz (1989). Vertical Structure of Dust and Ozone in the Martian Atmosphere Deduced from Solar Occultation Measurements. *Nature* **341**, 600-603.
- Bougher, S.W., C.G. Fesen, E.C. Ridley & R.W. Zurek (1993). Mars Mesosphere and Thermosphere Coupling – Semidiurnal Tides. *J. Geophys. Res.* **98**, 3281-3295.
- Bougher, S.W., R.G. Roble, E.C. Ridley & R.E. Dickinson (1990). The Mars Thermosphere. II. General Circulation with Coupled Dynamics and Composition. *J. Geophys. Res.* **95**, 14811-14827.
- Carr, M. (1996). *Water on Mars*, Oxford Univ. Press, Oxford, UK.
- Chassefière, E., J.E. Blamont, V.A. Krasnopolsky, O.I. Korablev, S.K. Atreya & R.A. West (1992). Vertical Structure and Size Distributions of Martian Aerosols from Solar Occultation Measurements. *Icarus* **97**, 46-69.
- Cheng, B.M., E.P. Chew, Ching-Ping Liu, M. Bahou, Yuan-Pern Lee, Yuk L. Yung & M.F. Gerstell (1999). Photo-Induced Fractionation of Water Isotopomers in the Martian Atmosphere. *Geophys. Res. Lett.* **26**, 3657-3660.
- Clancy, R.T., D.O. Muhleman & G.L. Berge (1990). Global Changes in the 0-70 km Thermal Structure of the Mars Atmosphere derived from 1975 to 1989 Microwave CO Spectra. *J. Geophys. Res.* **95**, 14543-14554.
- Clancy, R.T., A.W. Grossman, M.J. Wolff, P.B. James, D.J. Rudy, Y.N. Billawala, B.J. Sandor, S.W. Lee & D.O. Muhleman (1996). Water Vapor Saturation at Low Altitudes around Mars Aphelion: A Key to Mars Climate? *Icarus* **122**, 36-62.
- Conrath, B.J., J.C. Pearl, M.D. Smith & P.R. Christensen (1998). MGS TES Results: Characterization of the Martian Atmospheric Thermal Structure. DPS meeting #30, #11.P06
- Conrath, B.J., J.C. Pearl, M.D. Smith & P.R. Christensen (1999). Mars Global Surveyor TES Results: Atmospheric Thermal Structure Retrieved from Limb Measurements. DPS meeting #31, #49.08.
- Farmer, C.B. & D.D. LaPorte (1972). The Detection and Mapping of Water Vapor in the Martian Atmosphere. *Icarus* **16**, 34-46.
- Forget, F., F. Hourdin & O. Talagrand (1996). Simulation of the Martian Atmospheric Polar Warming with the LMD General Circulation Model. *Ann. Geophys.* **14**, C797.
- Fox, G.K., A.D. Code, C.M. Anderson, B.L. Babler, K.S. Bjorkman (1997). Solar System Observations by the Wisconsin Ultraviolet Photopolarimeter Experiment. I. The First Ultraviolet Linear Spectroscopy of Mars. *Astron. J.* **113**, 1152-1157.
- Glenar, D.A., J.J. Hillman, B. Saiff & J. Bergstralh (1994). Acousto-optic Imaging Spectropolarimetry for Remote Sensing. *Appl. Opt.* **33**, 31, 7412-7424.
- Hapke, B. (1981). Bidirectional Reflectance Spectroscopy. I. Theory. *J. Geophys. Res.* **86**, 3039-3054.
- Hechler, M & A. Yanes (1999). Mars Express Mission Analysis: the Orbits around G3-A and G3-B. MAS working paper #413. ESOC, Darmstadt.
- Hinson, D.P., R.A. Simpson, J.D. Twicken, G.L. Tyler & F.M. Flasar (1999). Initial Results from Radio Occultation Measurements from Mars Global Surveyor. *J. Geophys. Res.* **104**, E11, 26997-27012.
- Ip, W.H. (1988). On a Hot Oxygen Corona of Mars. *Icarus* **76**, 135-145.
- Jakosky, B.M., R.O. Pepin, R.E. Johnson & J.L. Fox (1994). Mars Atmospheric Loss and Isotopic Fractionation by Solar-wind-induced Sputtering and Photochemical Escape. *Icarus* **111**, 271-288.
- Kass, D.M. & Y.L. Yung (1995). Loss of Atmosphere from Mars due to Solar Wind-induced Sputtering. *Science* **268**, 697-699.
- Keating, G.M., S.W. Bougher, R.W. Zurek, R.H. Tolson, G.J. Cancro, S.N. Noll,

- J.S. Parker, T.J. Schellenberg, R.W. Shane, B.L. Wilkerson, J.R. Murphy, J.L. Hollingsworth, R.M. Haberle, M. Joshi, J.C. Pearl, B.J. Conrath, M.D. Smith, R.T. Clancy, R.C. Blanchard, R.G. Wilmoth, D.F. Rault, T.Z. Martin, D.T. Lyons, P.B. Esposito, M.D. Johnston, C.W. Whetzel, C.G. Justus & J.M. Babicke (1998). The Structure of the Upper Atmosphere of Mars: In situ Accelerometer Measurements from Mars Global Surveyor. *Science* **279**, 1672.
- Korablev, O.I., J.L. Bertaux & J.P. Dubois (2001). Occultation of Stars in the UV: Study of the Atmosphere of Mars. *J. Geophys. Res.* **106**, 7597-7610.
- Korablev, O.I., V.A. Krasnopolsky, A.V. Rodin & E. Chassefière (1993). Vertical Structure of Martian Dust Measured by the Solar Occultation from Phobos Spacecraft. *Icarus* **102**, 76-87.
- Krasnopolsky, V.A. (1993). Photochemistry of the Martian Atmosphere (Mean Conditions). *Icarus* **101**, 313-332.
- Krasnopolsky, V.A. (1997). Photochemical Mapping of Mars. *J. Geophys. Res. (Planets)* **102**, 13,313-13,320.
- Krasnopolsky, V.A. & G.L. Bjoracker (2000). Mapping of Mars O₂(¹Δ) Emission. AGU 2000 Spring meeting, Washington DC, USA.
- Krasnopolsky, V.A., O.I. Korablev, V.I. Moroz, A.A. Krysko, J.E. Blamont & E. Chassefière (1991). Infrared Solar Occultation Sounding of the Martian Atmosphere by the Phobos Spacecraft. *Icarus* **94**, 32-44.
- Krasnopolsky, V.A., V.I. Moroz, A.A. Krysko, O.I. Korablev, V.S. Zhegulev, A.V. Grigoriev, A.Yu. Tkachuk, V.A. Parshev, J.E. Blamont & J.-P. Goutail (1989). Phobos-2: Solar Occultation Spectroscopic Measurements of the Martian Atmosphere at 1.9 and 3.7 μm. *Nature* **341**, 603-604.
- Krasnopolsky, V.A., M.J. Mumma & G.R. Gladstone (1998). Detection of Atomic Deuterium in the Upper Atmosphere of Mars. *Science* **280**, 1576-1580.
- Lee, P., S. Ebisawa & A. Dollfus (1990). Crystal Clouds in the Martian Atmosphere. *Astron. Astroph.* **240**, 2, 520-532.
- Lellouch, E., G. Paubert & T. Encrenaz (1991). Mapping of CO Millimeter Wave Lines in Mars' Atmosphere: The Spatial Variability of Carbon Monoxide on Mars. *Planet. Space Sci.* **39**, 219-224.
- Luhmann, J.G., R.E. Johnson & M.H.G. Zhang (1992). Evolutionary Impact of Sputtering of the Martian Atmosphere by O⁺ Pickup Ions. *Geophys. Res. Lett.* **19**, 2151-2154.
- Magalhaes, J.A., J.T. Schofield & A. Seiff (1999). Results of the Mars Pathfinder Atmospheric Structure Investigation. *J. Geophys. Res.* **104**, 8943-8955.
- Maguire, W.C. (1977). Martian Isotopic Ratios and Upper Limits for Possible Minor Constituents as Derived from Mariner 9 Infrared Spectrometer Data. *Icarus* **32**, 85-97.
- McElroy, M.B. (1972). Mars: An Evolving Atmosphere. *Science* **175**, 443-445.
- McElroy, M.B. & T.M. Donahue (1972). Stability of the Martian Atmosphere. *Science* **177**, 986.
- Moreau, D., A. Marten & Y. Biraud (1998). Meridional and Seasonal Distributions of Trace Gases in the Lower and Middle Atmosphere of Mars. Lunar and Planetary Science Conference, 1998, Houston, TX, USA, Abstract #1369.
- Nair, H., M. Allen, A.D. Anbar & Y.L. Yung (1994). A Photochemical Model of the Martian Atmosphere. *Icarus* **111**, 124-150.
- Noxon, J.F., W.A. Traub, N.P. Carleton & P. Connes (1976). Detection of O₂ Airglow Emission from Mars and the Martian Ozone Abundance. *Astrophys. J.* **207**, 1025-1035.
- Owen, T., J.P. Maillard, C. de Bergh & B.L. Lutz (1988). Deuterium on Mars: The Abundance of HDO and the Value of H/D. *Science* **240**, 1767-1170.
- Parkinson, T.D. & D.M. Hunten (1972). Spectroscopy and Aeronomy of O₂ on Mars. *J. Atm. Sci.* **29**, 1390.
- Pearl, J.C., M.D. Smith, B.J. Conrath, J.L. Bandfield & P.R. Christensen (1999). Mars Global Surveyor TES Results: Observations of Water Ice Clouds. DPS meeting #31, #76.08.

- Rodin, A.V., R.T. Clancy, R.J. Wilson (1999). Dynamical Properties of Mars Water Ice Clouds and their Interactions with Atmospheric Dust and Radiation. *Adv. Space Res.* **23**, 1577-1585.
- Rodin, A.V., O.I. Korablev & V.I. Moroz (1997). Vertical Distribution of Water in Near-equatorial Troposphere of Mars: Water Vapor and Clouds. *Icarus* **125**, 21-29.
- Roscoe, H.K., R.A. Freshwater, R. Wolfenden, R.L. Jones, D.J. Fish, J.E. Harries & D.J. Oldham (1994). Using Stars for Remote Sensing of the Earth's Stratosphere. *Appl. Optics.* **33**, 7126-7131.
- Rosenqvist, J., P. Drossart, M. Combes, T. Encrenaz, E. Lellouch, J.P. Bibring, S. Erard, Y. Langevin & E. Chassefière (1992). Minor Constituents in the Martian Atmosphere from the ISM/Phobos Experiment. *Icarus* **98**, 254-270.
- Santer, R., M. Deschamps, L.V. Ksanfomaliti & A. Dollfus (1985). Photopolarimetric Analysis of the Martian Atmosphere by the Soviet MARS-5 Orbiter. I: White Clouds and Dust Veils. *Astron. Astroph.* **150**, 2, 217-228.
- Seif, A. & D.B. Kirk (1977). Structure of the Atmosphere of Mars in Summer at Mid-latitudes. *J. Geophys. Res.* **82**, 4364-4378.
- Smith, G.R. & D.M. Hunten (1990). Study of Planetary Atmospheres by Absorptive Occultations. *Rev. Geophys.* **28**, 117.
- Smith, M.D., J.C. Pearl, B.J. Conrath & P.R. Christensen (1999). Mars Global Surveyor TES Results: Observations of Atmospheric Dust during Mapping. DPS meeting #31, #48.06.
- Stewart, A.I. (1972). Mariner 6 and 7 Ultraviolet Spectrometer Experiment: Implication of CO₂⁺, CO and O Airglow. *J. Geophys. Res.* **77**, 54-68.
- Stewart, A.I., C.A. Barth & C.W. Hord (1972). Mariner 9 Ultraviolet Spectrometer Experiment: Structure of Mars' Upper Atmosphere. *Icarus* **17**, 469-474.
- Stoker, C.R. & M.A. Bullock (1997). Organic Degradation under Simulated Martian Conditions. *J. Geophys. Res.* **102**, 10881-10888.
- Traub, W.A., N.P. Carleton, P. Connes & J.F. Noxon (1979). The Latitude Variation of O₂ Airglow and O₃ Abundance on Mars. *Astrophys. J.* **229**, 846-850.
- Wehrbein, W.M., C.W. Hord & C.A. Barth (1979). Mariner 9 UV Spectrometer Experiment: Vertical Distribution of Ozone on Mars. *Icarus* **38**, 288-299.
- Wilson, R.J. (1997). A General Circulation Model Simulation of the Mars Polar Warming. *Geophys. Res. Lett.* **24**, 123-126.
- Yung, Y.L. & W.D. DeMore (1999). *Photochemistry of Planetary Atmospheres*, Oxford Univ. Press., UK, p.34.

ASPERA-3: Analyser of Space Plasmas and Energetic Ions for Mars Express

S. Barabash¹, R. Lundin¹, H. Andersson¹, J. Gimholt^{1,a}, M. Holmström¹, O. Norberg^{1,b}, M. Yamauchi¹, K. Asamura², A.J. Coates³, D.R. Linder³, D.O. Kataria³, C.C. Curtis⁴, K.C. Hsieh⁴, B.R. Sandel⁴, A. Fedorov^{5,c}, A. Grigoriev^{5,d}, E. Budnik^{5,c}, M. Grande⁶, M. Carter⁶, D.H. Reading⁶, H. Koskinen⁷, E. Kallio⁷, P. Riihela⁷, T. Säles⁷, J. Kozyra⁸, N. Krupp⁹, S. Livi^{9,e}, J. Woch⁹, J. Luhmann¹⁰, S. McKenna-Lawlor¹¹, S. Orsini¹², R. Cerulli-Irelli¹², M. Maggi¹², A. Morbidini¹², A. Mura¹², A. Milillo¹², E. Roelof¹³, D. Williams¹³, J.-A. Sauvaud¹⁴, J.-J. Thocaven¹⁴, T. Moreau¹⁴, D. Winningham¹⁵, R. Frahm¹⁵, J. Scherrer¹⁵, J. Sharber¹⁵, P. Wurz¹⁶ & P. Bochsler¹⁶

¹*Swedish Institute of Space Physics, Box 812, S-98 128, Kiruna, Sweden*

Email: stas@irf.se

²*Institute of Space and Astronautical Science, 3-1-1 Yoshinodai, Sagamichara, Japan*

³*Mullard Space Science Laboratory, University College London, Surrey RH5 6NT, UK*

⁴*University of Arizona, Tucson, AZ 85721, USA*

⁵*Space Research Institute, 117810 Moscow, Russia*

⁶*Rutherford Appleton Laboratory, Chilton, Didcot, Oxfordshire OX11 0QX, UK*

⁷*Finnish Meteorological Institute, Box 503 FIN-00101 Helsinki, Finland*

⁸*Space Physics Research Laboratory, University of Michigan, Ann Arbor, MI 48109-2143, USA*

⁹*Max-Planck-Institut für Aeronomie, D-37191 Katlenburg-Lindau, Germany*

¹⁰*Space Science Laboratory, University of California in Berkeley, Berkeley, CA 94720-7450, USA*

¹¹*Space Technology Ltd., National University of Ireland, Maynooth, Co. Kildare, Ireland*

¹²*Instituto di Fisica dello Spazio Interplanetari, I-00133 Rome, Italy*

¹³*Applied Physics Laboratory, Johns Hopkins University, Laurel, MD 20723-6099, USA*

¹⁴*Centre d'Etude Spatiale des Rayonnements, BP-4346, F-31028 Toulouse, France*

¹⁵*Southwest Research Institute, San Antonio, TX 7228-0510, USA*

¹⁶*University of Bern, Physikalisches Institut, CH-3012 Bern Switzerland*

^a*now at Scania, Volvo Corporation, Södertälje, Sweden*

^b*now at ESRANGE, Swedish Space Corporation, Kiruna, Sweden*

^c*now at Centre d'Etude Spatiale des Rayonnements, Toulouse, France*

^d*now at Swedish Institute of Space Physics, Box 812, S-981 28 Kiruna, Sweden*

^e*now at Applied Physics Laboratory, Johns Hopkins University, Laurel, MD 20723, USA*

The ASPERA-3 (Analyser of Space Plasma and Energetic Atoms) instrument of Mars Express is designed to study the solar wind-Mars atmosphere interaction and to characterise the plasma and neutral gas environment in near-Mars space through energetic neutral atom (ENA) imaging and local charged-particle measurements. The studies address the fundamental question: how strongly do the interplanetary plasma and electromagnetic fields affect the martian atmosphere? This question is directly related to the problem of martian dehydration. The instrument comprises four sensors; two ENA sensors, and electron and ion spectrometers. The Neutral Particle Imager (NPI) measures the integral ENA flux (0.1-60 keV) with no mass and energy resolution but with high angular resolution. The Neutral Particle Detector (NPD) measures the ENA flux, resolving energy (0.1-10 keV) and mass (H and O) with a coarse angular resolution. The electron spectrometer (ELS) is a standard top-hat electrostatic analyser of a very compact design. These three sensors are mounted on a scanning platform providing 4π coverage. The instrument includes an ion mass composition sensor, IMA (Ion Mass Analyser). Mechanically, IMA is a separate unit connected by a cable to the ASPERA-3 main unit. IMA provides ion measurements in the energy range 0.01-40 keV/ q for the main ion components H^+ , He^{2+} , He^+ , O^+ , with 20-80 amu/ q .

1. The Science

1.1 Scientific task

The scientific objectives of the Mars Express Orbiter mission are to study the subsurface, surface and atmosphere of Mars, as well as the interaction of the atmosphere with the interplanetary medium. ASPERA-3 will fulfil the last objective by:

- remote measurements of energetic neutral atoms (ENAs) in order to (a) investigate the interaction between the solar wind and the martian atmosphere, (b) characterise quantitatively the impact of plasma processes on atmospheric evolution, and (c) obtain the global plasma and neutral gas distributions in the near-Mars environment;
- *in situ* measurements of ions and electrons to (a) complement the ENA images (electrons and multi-charged ions cannot be imaged), (b) study local characteristics of the plasma (dynamics and fine structure of boundaries), (c) provide the undisturbed solar wind parameters required for interpreting ENA images.

As established by earlier missions, and confirmed recently by Mars Global Surveyor, Mars does not possess an intrinsic dipole magnetic field but only local crustal magnetisations (Acuna et al., 1998). The local field plays a role in the solar wind interaction only over limited regions. For the overall interaction picture, the solar wind interacts directly with the martian ionosphere, exosphere and upper atmosphere. As a result of the low gravity on Mars, the neutral density can reach 10^4 - 10^6 cm $^{-3}$ in the interaction region where the main plasma boundaries, bow shock and magnetopause, are located. The co-existence of these two components, the solar wind plasma and the planetary neutral gas, produces a strong interaction. One of the fundamental collisional interactions is the charge-exchange process between the energetic ion, A^+ , and the cold atmospheric gas, M :



which produces energetic neutral atoms, A , and an ionised gas particle. Directional detection of the ENA thereby yields a global image of the interaction, if the observer is at a remote location with respect to the plasma population (Wurz, 2000). ASPERA-3 will concentrate on studying the effects of the plasma-neutral coupling at Mars via ENA imaging, complemented by the electron and ion observations.

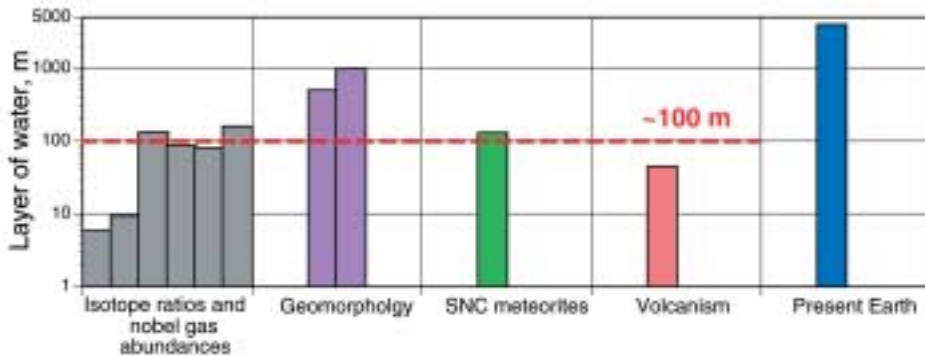


Fig. 1. Martian water inventory derived from different approaches. The present Earth is also shown for reference (adapted from McKay & Stoker, 1989).

1.2 The solar wind-atmosphere coupling

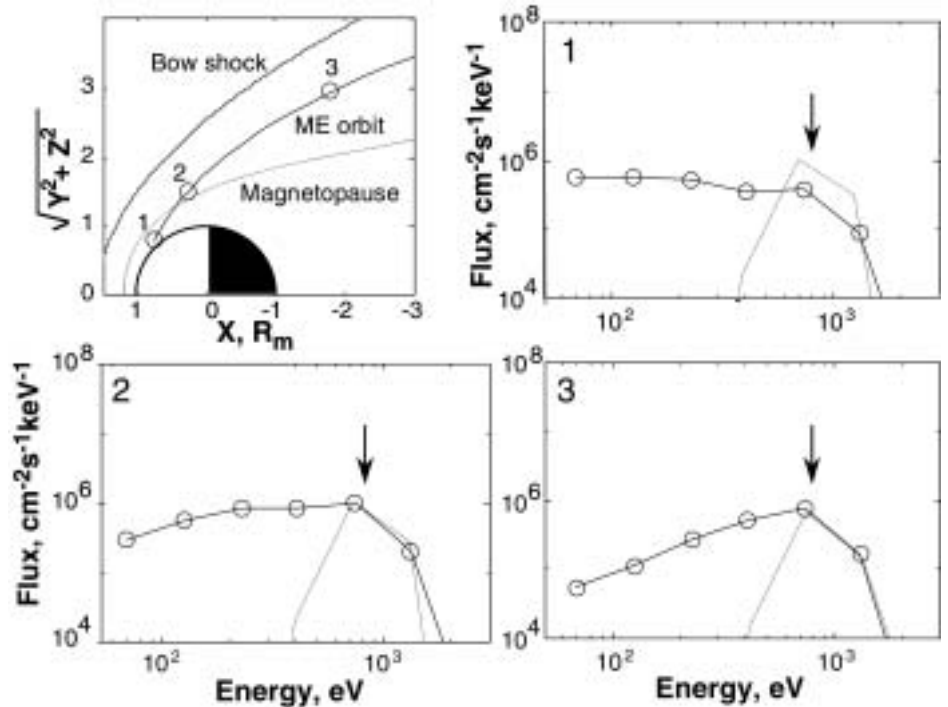
Near-Mars space is strikingly different from Earth-space because of the absence of a substantial intrinsic martian magnetic field. Without the magnetic cavity of a magnetosphere to shield the upper atmosphere from the solar wind, Mars is subject to comet-like atmosphere erosion processes and solar wind-induced current systems that have no terrestrial counterparts. From previous missions to Mars (especially Phobos-2) and from Pioneer Venus Orbiter circling the similarly weakly magnetised Venus, ideas on how the martian upper atmosphere and solar wind interact and the consequences for the planet have been developed. In particular, the scavenging of planetary ions may have resulted in the removal of ~1 m of surface water over 4.5 Gyr (Lundin et al., 1991). More detailed studies (Perez-de-Tejada, 1992), taking into account the variability of the ionosphere throughout the planet's history, give a much higher (~30 m) equivalent depth of water that has escaped owing to the solar wind interaction process.

The current atmospheric conditions on Mars indicate that water does not exist on the surface in any significant amount: 15 mm equivalent water layer (Farmer et al., 1977). On the other hand, independent analyses of several features of the planet unambiguously indicate that water did exist in the past on the martian surface. Fig. 1 shows the water inventory based on different approaches: geomorphologic features, analysis of the SNC meteorites, isotopic abundance and volcanic activity. The total amount of past surface water results in an equivalent water layer of at least 100 m. This leads to the problem of martian dehydration. Where is the water? Is it lost or frozen and buried? If the former, what could produce such an effective escape mechanism? If the latter, where is this tremendous amount of water stored? As indicated above, the processes associated with the solar-wind interaction could account for the escape of up to 30% of past surface water.

Another problem of the solar wind-atmosphere coupling that has not been explored experimentally is the energetic consequences for the atmosphere of the lack of a significant dipole field. Kinetic and test-particle models of the Mars-solar wind interaction (Brecht, 1997; Kallio et al., 1997) suggest that solar wind absorption by the atmosphere may be an important energy source for the upper atmosphere. The ENAs generated as a product of the solar wind interaction increase the deposition of solar wind energy (Kallio & Barabash, 2001) and, at the same time, provide a means of 'imaging' the solar wind interaction. The atmosphere, although thin, alters the incoming energetic solar wind by:

- generation of ionospheric currents that partially deflect the ion flow around the ionosphere;
- 'mass loading' the solar wind with planetary ions produced mainly by photoionisation, and solar wind electron impact ionisation of the atmospheric gases;
- undergoing charge-transfer or charge-exchange interactions with the solar wind ions.

Fig. 2. ENA spectra along the Mars Express orbit. The ENAs originate in the shocked solar wind. The arrows mark ENA flux produced in the upstream solar wind. The energy resolution corresponds to that of ASPERA-3.



According to the models, some of the solar wind ions (mainly protons and alpha particles) directly impact Mars' upper atmosphere near its exobase (~ 180 km altitude) because their gyroradii are too large to behave as a deflected 'fluid' in the subsolar magnetosheath (Brecht, 1997; Kallio & Janhunen, 2001) or because they are partially thermalised by the bow shock (Kallio et al., 1997). Others undergo charge-exchange reactions with ambient exospheric and thermospheric neutrals, particularly hydrogen, and then impact the exobase as ENAs (Kallio et al., 1997). In both cases, solar wind energy is 'directly' deposited into the upper atmosphere, increasing ionisation rates and UV emissions. Kallio & Barabash (2000, 2001) have studied the effects of such ENA precipitation using Monte Carlo simulations and estimated that, under typical solar wind conditions, the precipitating hydrogen atoms increase the ionisation rate by about 1% in comparison with ionisation rates owing to extreme UV radiation. This effect is comparable to, or even stronger than, similar effects caused by the O^+ and H^+ precipitation (Luhmann & Kozyra, 1991; Brecht, 1997; Kallio & Janhunen, 2001). The results also indicate that a substantial part of the incoming particles is scattered back from the atmosphere, resulting in an ENA hydrogen albedo. Imaging these particles would visualise the spots or regions of the most intense ENA precipitation.

While the energy transfer associated with the proton or ENA precipitation exceeds that from the O^+ precipitation, it is the oxygen ions that cause massive sputtering of the atmosphere (Luhmann & Kozyra, 1991; Luhmann et al., 1992). Luhmann & Bauer (1992) estimated that the O^+ sputtering results in the escape of 0.1 - 0.5 $kg s^{-1}$ of oxygen atoms. This is on the same level as the non-thermal escape of the hot oxygen atmospheric component. For comparison, the direct solar wind pick-up, excluding the bulk ionospheric scavenging, removes 0.01 $kg s^{-1}$ at most.

1.3 Sources of energetic neutral atoms at Mars

Barabash et al. (1995), Kallio et al. (1997), Holmström et al. (2002), Mura et al. (2002), Lichtenegger et al. (2002) and Barabash et al. (2002) considered the ENA production at Mars. ENAs are produced by charge-exchange between the exosphere containing H, H_2 , He and O, and the different plasma populations such as:

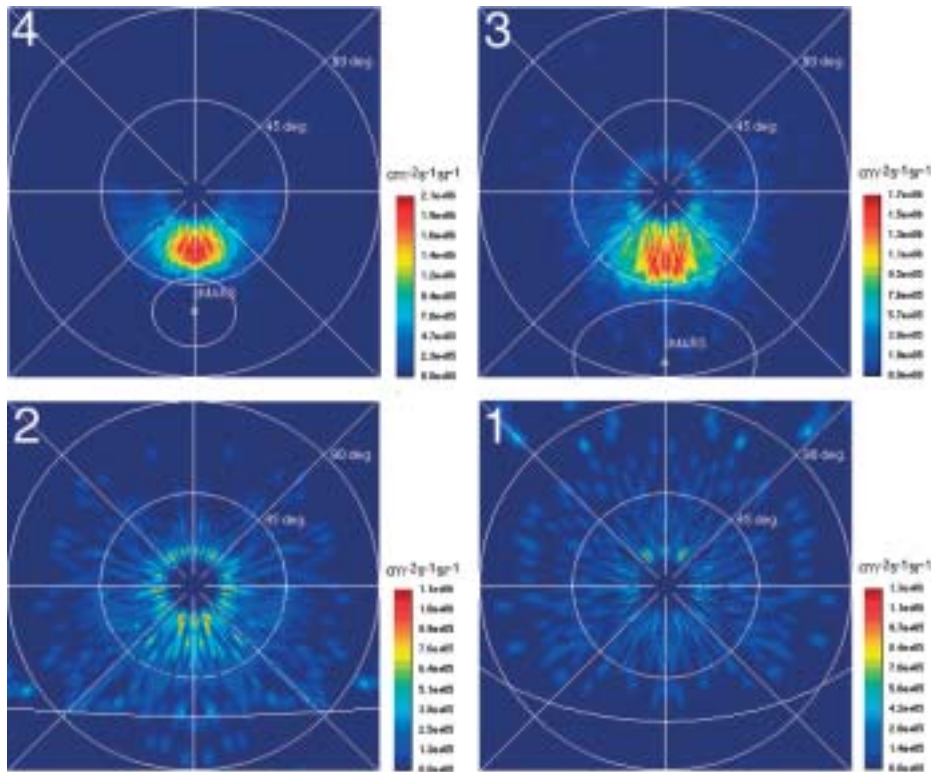


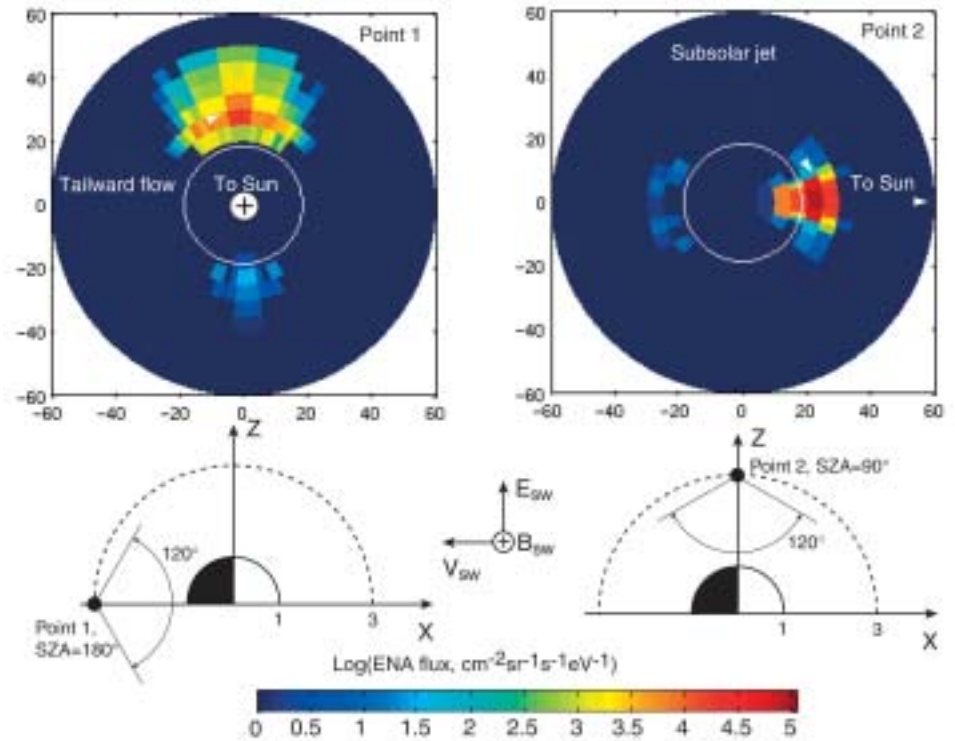
Fig. 3. Model ENA images for four locations along the Mars Express orbit (three marked in the inset of Fig. 2); position 4 (not shown in Fig. 2) corresponds to the orbit apocentre. The polar axis looks towards the Sun. The polar angle is the azimuth at the vantage point and the radius is the polar angle to the Sun direction. The solar wind ENAs are blocked.

- the supersonic solar wind (Holmström et al., 2002);
- the shocked solar wind (Holmström et al., 2002);
- accelerated planetary ions (Barabash et al., 2002; Lichtenegger et al., 2002);
- the tiny Phobos atmosphere can also interact with both the supersonic and the shocked solar wind, resulting in ENA generation (Mura et al., 2002);
- the energetic O^+ ions picked up by the plasma flow incident on the atmosphere are backscattered and sputter oxygen, CO_2 and its fragments (Luhmann & Kozyra, 1991; Luhmann et al., 1992). The backscattered and sputtered atoms have energies up to few hundred eV and form an oxygen ENA albedo. The intensity of these emissions directly determines the efficiency of the atmospheric erosion;
- the precipitating protons and hydrogen ENAs can also be scattered back, forming a hydrogen ENA albedo (Kallio & Barabash, 2001; Holmström et al., 2002).

The supersonic solar wind upstream of the bow shock can experience charge-exchange with the hydrogen exosphere over very long distances, producing a narrow ($\approx 10^\circ$) anti-Sunward beam of ENAs with the energy of the bulk flow of the solar wind (the spectrum marked by arrows in Fig. 2). These ENAs can be detected only at the beam edges because they are superimposed on the intense flux of the solar radiation.

The shocked solar wind is the strongest source of ENAs because the protons flowing around Mars can interact with dense neutral gas. The detailed modelling of the ENA production from this source was performed by Kallio et al. (1997), Holmström et al. (2002) and Mura et al. (2002). Using these models, ENA images that would be observed from the Mars Express orbit were simulated for solar maximum conditions. The spacecraft will reach Mars during the moderate solar activity characteristic of the decline of the solar cycle. The ENA emissions are weaker during solar maximum so the calculations give lower limits for the ENA fluxes. Fig. 2 shows the ENA spectra integrated over the unit sphere for several locations along the Mars

Fig. 4. Model ENA images of the pick-up oxygen ions for two vantage points in the tail and at the pole. The vantage points are in the plane perpendicular to the ecliptic. The polar axis is towards the planetary centre. The image projection is similar to that of Fig. 3. The energy range is 0.1-1.65 keV. The electric and magnetic field vectors in the solar wind are shown for reference.



Express orbit. The estimated ENA fluxes are well above $10^4 \text{ cm}^{-2} \text{ s}^{-1} \text{ keV}^{-1}$ and, therefore, easily detectable. The directional fluxes to be measured well exceed $10^5 \text{ cm}^{-2} \text{ s}^{-1} \text{ sr}^{-1}$.

Fig. 3 shows the directional ENA flux integrated over energy as a function of two spherical angles (ENA images) for several positions along the Mars Express orbit marked in Fig. 2. Position 4 corresponds to the apocentre. In this fish-eye projection, the polar axis is looking towards the Sun. The polar angle is the azimuth at the vantage point and the radius is the polar angle to the Sun direction. The images display the entire interaction region and can be converted into global distributions of the proton flow and neutral gas using extracting diagnostic methods similar to that developed for the Earth's conditions (Roelof & Skinner, 2000). Holmström et al. (2002) showed that the ENA fluxes generated from the shocked solar wind are most sensitive to the neutral hydrogen distribution controlled by the exobase temperature and the position of the boundary separating the solar wind and planetary plasmas.

Some of the ENAs produced by the shocked solar wind and ENAs originating in the solar wind can precipitate onto the ionosphere. Fig. 2 (position 1 inside the magnetosphere) gives a typical spectrum of precipitating ENAs at the 45° solar zenith angle. The spectrum is rather flat at the level $7 \times 10^5 \text{ cm}^{-2} \text{ s}^{-1} \text{ keV}^{-1}$. The peak corresponds to the solar wind energy. The planetary protons originating from ionisation of the hydrogen corona can charge-exchange with the exospheric gas as well, resulting in planetary hydrogen ENA emissions. These emissions, investigated in detail by Lichtenegger et al. (2002), differ from the shocked solar wind ENAs in energy because the pick-up protons can gain an energy up to four times that of the solar wind.

The ASPERA/Phobos observations of the plasma energisation inside the martian magnetosphere (Lundin et al., 1993) showed the existence of two basic ion populations: the tail beams of H^+ and O^+ of energy 1-3 keV, and outflowing ionospheric ions of energy 10-100 eV near the tail flanks. Barabash et al. (1995) estimated the related ENA flux to be $10^3 \text{ cm}^{-2} \text{ s}^{-1} \text{ keV}^{-1}$ for the energy range 1-10 keV, and up to $10^5 \text{ cm}^{-2} \text{ s}^{-1} \text{ keV}^{-1}$ for 10-100 eV. The ENA signal associated with the pick-up oxygen was investigated in detail by Barabash et al. (2002). Using the

empirical model of the solar wind plasma flow near Mars developed by Kallio & Koskinen (1999), Barabash et al. (2002) numerically solved the kinetic equation and obtained the global distribution of oxygen ions. This distribution was then converted to the corresponding ENA flux. It was found that the fluxes of the oxygen ENAs could reach $10^4 \text{ cm}^{-2} \text{ s}^{-1} \text{ keV}^{-1}$ and fully reflect the morphology of the oxygen population. This provides a way to determine the instantaneous oxygen escape rate. One of the simulated images for the energy range 0.1-1.65 keV is reproduced in Fig. 4. The projection is similar to that used for hydrogen ENA images but the polar axis in the vantage point points towards the centre of the planet. The image shows a strong ENA jet from the subsolar point, where the electric and magnetic field configuration effectively accelerates newborn planetary ions. The tailward flow is also clearly reproduced. The corresponding vantage points are shown below the images.

Several experiments on the Phobos mission observed brief plasma disturbances when the spacecraft crossed that moon's orbit (Barabash, 1995). They could be related to a hypothetical neutral gas torus resulting from the moon outgassing. The solar wind plasma can experience charge-exchange with the Phobos 'atmosphere' and the neutral torus, resulting in ENA emissions. Assuming an outgassing rate of 10^{23} s^{-1} , Mura et al. (2002) calculated the associated ENA flux to be of the order of 10^3 - $10^4 \text{ cm}^{-2} \text{ s}^{-1} \text{ keV}^{-1}$ for the shocked solar wind plasma, and up to $10^6 \text{ cm}^{-2} \text{ s}^{-1} \text{ keV}^{-1}$ for the solar wind beam. Because of solar radiation, the Phobos ENAs and the Phobos torus ENAs can be observed only when the moon is in the magnetosheath and the plasma flow deviates strongly from the anti-solar direction.

1.4 ENA imaging of the martian environment

ASPERA-3 will image all of the above ENA sources. The images provide two-fold information. Firstly, they reveal morphological features of the ENA sources, such as the location of boundaries and their relative sizes. ENA images are useful, in particular, for investigating different types of asymmetries expected for the plasma flow near Mars (Dubinin et al., 1996). The ENA images of the escaping plasma display globally and instantaneously the size and geometry of the outflowing plasma region. These characteristics are particularly important for calculations of the total non-thermal plasma outflow. For instance, the local ion measurements made using the ASPERA and TAUS instruments during the Phobos mission gave comparable ion fluxes. However, different assumptions made regarding the outflow region geometry (mass-loading boundary, plasma sheet) resulted in significant differences in the total outflow rate estimations, 0.5 - 1.0 kg s^{-1} (Lundin et al., 1989) and 0.15 kg s^{-1} (Verigin et al., 1991). One of the reasons for this was ambiguity in separating spatial and temporal variations, which is typical for local plasma measurements. Global and instantaneous observations of the outflowing plasma region morphology to be made via ENA imaging would help to resolve this issue, which is important for understanding the planetary atmosphere evolution.

Secondly, ENA images carry ample quantitative information about both the planetary plasma and neutral environments. By applying extraction techniques to the images of the shocked solar wind, quantitative models will be obtained giving the neutral gas profiles (exobase densities and temperatures) and global proton plasma distributions (flow geometry, bulk velocity, density and temperature).

Aerobraking measurements from Mars Global Surveyor (Dornheim, 1997) indicate that the atmospheric density at 150 km altitude varies by 30% in one out of three passes. Estimated scale heights of $\sim 8 \text{ km}$ implies that the densities in the interaction region higher up will also be much more variable with time than had been expected. Global ENA imaging of the interaction offers the greatest promise of separating the spatial and temporal variations of the atmosphere-solar wind interaction. Apart from imaging, the measurements of ENA flux from certain directions provide a diagnostic tool for plasma-atmosphere coupling studies. Precipitating ENAs and ENA albedo (backscattered oxygen) are direct manifestations of such an interaction.

Table 1. ASPERA-3 scientific objectives.

<i>Scientific objective</i>	<i>Associated Measurements</i>	<i>Measurement Requirements</i>
Determine the instantaneous global distributions of plasma and neutral gas near the planet	ENAs originating from the shocked solar wind	Measure the ENA flux in the energy range tens eV - few keV with 4π coverage. ENA flux $>10^4 \text{ cm}^{-2} \text{ s}^{-1} \text{ keV}^{-1}$. Measure the upstream solar wind parameters
Study plasma-induced atmospheric escape	ENAs originating from inside the magnetosphere	Mass-resolving (H/O) ENA measurements in the energy range up to tens keV. ENA flux $>10^3 \text{ cm}^{-2} \text{ s}^{-1} \text{ keV}^{-1}$
Investigate the modification of the atmosphere through ion bombardment	ENA albedo	Mass-resolving (H/O) ENA measurements in the energy range down to tens eV from the nadir direction. ENA flux $>10^6 \text{ cm}^{-2} \text{ s}^{-1} \text{ keV}^{-1}$ (100 eV)
Investigate the energy deposition from the solar wind to the ionosphere	Precipitating ENAs	ENA measurements in the energy range tens eV - few keV. ENA flux $>10^4 \text{ cm}^{-2} \text{ s}^{-1} \text{ keV}^{-1}$
Search for the solar wind-Phobos interactions	ENA originating from Phobos	ENA measurements in the energy range tens eV - few keV with 4π coverage. ENA flux $10^4 \text{ cm}^{-2} \text{ s}^{-1} \text{ keV}^{-1}$
Define the local characteristics of the main plasma regions	Ion and electron measurements of hot plasma	Ion and electron measurements in the energy range few eV - tens keV with 4π coverage

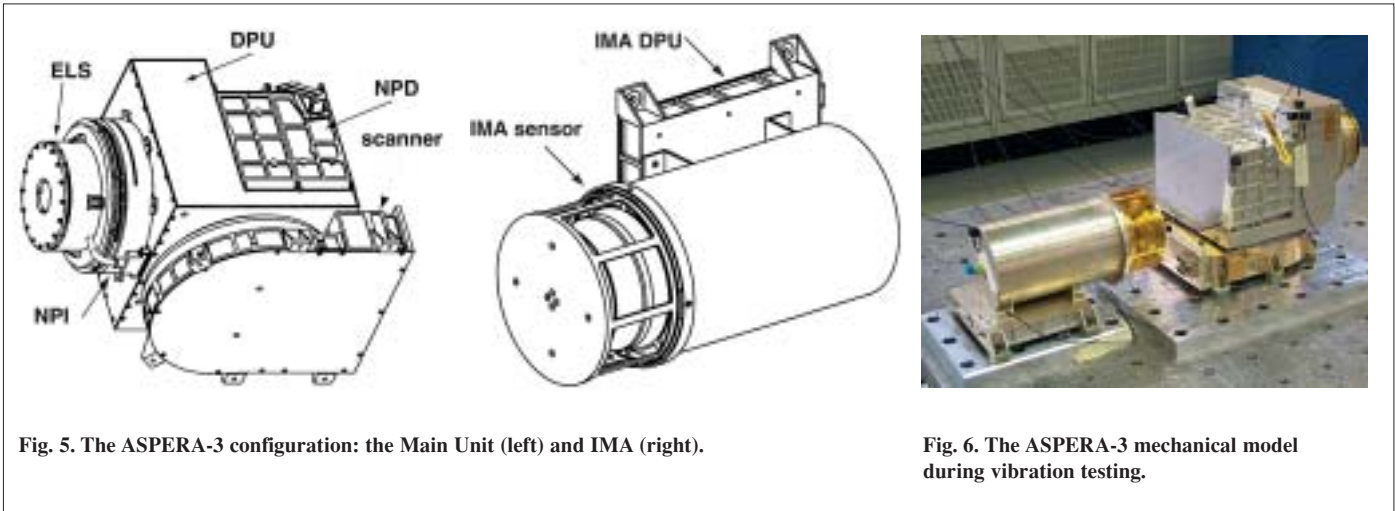


Fig. 5. The ASPERA-3 configuration: the Main Unit (left) and IMA (right).

Fig. 6. The ASPERA-3 mechanical model during vibration testing.

1.5 Scientific objectives and measurements requirements

The studies of martian ENAs resulting from the solar wind-atmosphere interaction address the fundamental question: how strongly do the interplanetary plasma and electromagnetic fields affect the atmosphere? This question is directly related to the problem of martian dehydration as described in Section 1.2. What happened to the martian water that once flowed in numerous channels? As we know from terrestrial experience, together with an inventory of organic compounds and external energy sources, liquid water is a fundamental requirement for life as we know it. Therefore, a clear understanding of the fate of the martian water is crucial for resolving whether life has ever existed on Mars.

The general scientific task of studying the solar wind-atmosphere interaction through ENA imaging can be subdivided into specific scientific objectives. These are listed in Table 1, together with the corresponding instrument requirements.

1.6 Relation to other missions

ASPERA-3 will perform the first ENA imaging of another planet in the low energy

range. No instruments with similar scientific objectives and capabilities are foreseen to fly to other planets. The only similar experiment, ASPERA-C, was carried by the failed Mars-96 mission. However, it did not have the ENA energy-analysing Neutral Particle Detector.

2.1 Overview

ASPERA-3 is designed for the analysis of ENAs, electrons and ions, with complete spherical coverage. Mechanically, ASPERA-3 (Figs. 5 and 6) consists of two units, the Main Unit (MU) and the Ion Mass Analyser (IMA). The MU comprises three sensors: NPI, NPD and ELS, with a digital processing unit, all located on a scan platform. All mechanical and electrical interfaces are made through the scan platform. The instrument's total mass is 8.2 kg and its power consumption 13.5 W. The MU envelope is 359x393x234 mm, and for IMA 255x150x150 mm.

2.2 Measurement principles and capabilities

To fulfil its scientific objectives, ASPERA-3 comprises four sensors; two ENA sensors (NPI, NPD), an electron spectrometer (ELS) and an ion mass analyser (IMA). The two ENA sensors are optimised for some of the scientific objectives, while being complementary. This approach offers the necessary redundancy as well as the independent cross-checking necessary for such ground-breaking measurements at another planet. The charged particle sensors not only characterise the local plasma environment but also support ENA measurements in terms of charged particles background and inter-calibrations.

The Neutral Particle Imager measures the integral ENA flux with no mass and energy resolution but with $5 \times 11^\circ$ angular resolution. The intrinsic field of view is $9 \times 344^\circ$. The sensor uses a graphite surface to suppress the UV background. ENAs incident on the surface at a grazing angle of 20° are reflected and/or cause ion sputtering. A micro-channel plate (MCP) stack detects the reflected particles and sputtered fragments with a discrete anode. The NPI head is a replica of the NPI-MCP sensor developed for ASPERA-C on Mars-96 (launch failure) and successfully flown on the Swedish Astrid microsatellite, launched in 1995 (C:son Brandt et al., 2000).

The Neutral Particle Detector measures the ENA differential flux over the energy range 100 eV to 10 keV, resolving H and O with a coarse $5 \times 30^\circ$ angular resolution. The sensor consists of two identical detectors, each with a $9 \times 90^\circ$ intrinsic field of view. The measurement technique is based on a principle similar to that of NPI. ENAs incident on a surface at a grazing angle of 15° are reflected and generate secondary electron emission. The secondary electrons are transported to an MCP assembly, which gives the START signal. The reflected ENAs hit the second surface and again produce the secondary electrons used to generate the STOP signal. The time-of-flight (TOF) electronics give the ENA velocity. The pulse-height distribution analysis of the STOP signals provides a rough determination of the ENA mass.

The Electron Spectrometer measures electrons in the energy range 0.01-20 keV. The intrinsic field of view is $10 \times 360^\circ$. The 360° aperture is divided into 16 sectors. The sensor is a standard top-hat electrostatic analyser in a very compact design. ELS is a reduced version of the MEDUSA experiment for the Astrid-2 and Munin missions launched in 1998 and 2000 (Norberg et al., 2001).

The Ion Mass Analyser is an improved version of the ion mass spectrographs TICS/Freja, IMIS/Mars-96 and IMI/Nozomi (Norberg et al., 1998) and a copy of Rosetta's ICA instrument. The IMA sensor is a separate unit connected by a cable to ASPERA-3. It measures ions in the energy range 0.01-30 keV/ q for the main ion components H^+ , H^+ , He^+ , O^+ and for the group of molecular ions $20 < M/q < \sim 80$. Mechanically, IMA is a separate unit with a $4.6 \times 360^\circ$ field of view. Electrostatic sweeping performs elevation ($\pm 45^\circ$) coverage. The IMA sensor is a spherical electrostatic analyser followed by a circular magnetic separating section. A large-diameter MCP with a discrete anode images the matrix azimuth x mass.

NPI, NPD and ELS are mounted on a scanning platform. The combination of the

2. The Instrument

Table 2. Baseline performances of the NPI, NPD, ELS and IMA sensors.

<i>Parameter</i>	<i>NPI</i>	<i>NPD</i>	<i>ELS</i>	<i>IMA</i>
Particles to be measured	ENA	ENA	electrons	ions
Energy range, keV per charge	≈ 0.1 - 60	0.1 - 10	0.01 - 20	0.01 - 30
Energy resolution, $\Delta E/E$	No	0.8	0.08	0.07
Mass resolution	No	H, O	–	$m/q = 1, 2, 4, 8, 16, >20$
Intrinsic field of view	9 x 344°	9 x 180°	10 x 360°	90 x 360°
Angular resolution (FWHM)	4.6 x 11.5°	5 x 30°	10 x 22.5°	4.5 x 22.5°
G-factor*/ pixel, cm ² sr	2.5 x 10 ⁻³ (ϵ not incl.)	6.2 x 10 ⁻³ (ϵ not incl.)	5 x 10 ⁻⁴	3.5 x 10 ⁻⁴
Efficiency, ϵ , %	~ 1	0.1-20	inc. in G	inc. in G
Time resolution (full 3D), s	32	32	32	32
Mass, kg	0.7	1.3	0.3	2.2
Power, W	0.8	1.5	0.6	3.5

*G-factor is the instrument geometrical factor

360° field of view and the scans from 0° to 180° give the required 4π maximum coverage. The actual coverage depends on the instrument location on the spacecraft. Table 2 summarises the instrument performance.

2.3 Neutral Particle Imager (NPI)

The NPI head is a replica of the NPI-MCP sensor developed for ASPERA-C/Mars-96 and flown successfully on Astrid (Barabash, 1995). In NPI, the charged particles, electrons and ions are removed by the electrostatic deflection system, which consists of two discs separated by a 3 mm gap (Fig. 7). The 5 kV potential between the grounded and biased discs produces a strong electric field, which sweeps away all charged particles with energies up to 60 keV. Since the integral ENA flux substantially exceeds the charged particle flux for energies greater than 60 keV, this rejection energy provides satisfactory performance. The discs also collimate the incoming beam in the elevation angle. Apart from being ‘on’ or ‘off’, the deflection system can be operated in two other modes: ‘alternative’ and ‘sweeping’. In the alternative mode, the deflection system is turned on and off for one sampling time. This mode will be used for more accurate separation between charged and neutral particles entering the system. The deflection system is connected to the high-voltage supply via an optocoupler. Regulating the optocoupler reference voltage changes the deflection voltage performing the sweeping and alternating. In order to reduce the time for discharging the deflection system discs to 1 ms, a second parallel optocoupler is used.

The space between the deflection system discs is divided into 32 sectors by plastic spokes forming 32 azimuthal collimators with an aperture of $9 \times 18^\circ$ each. Neutrals passing through the deflection system hit a 32-sided conical target at a grazing angle of 20° . The interaction with the target generates secondary particles, both electrons and ions, and/or reflection of the primary neutrals. An MCP stack in a chevron configuration, followed by a 32-sector anode, detects the particles leaving the target. The signal from the MCP gives the direction of the primary incoming neutral. The MCP operates in ion mode with a negative bias of -2.6 kV applied to the front side and thus detects (a) sputtered positive ions of the target material, (b) positive ions resulting from ionisation of the primary neutrals, and (c) neutrals reflected from the target surface. In order to improve the angular resolution and collimate the particles leaving the interaction surface, 32 separating walls are attached to the target, forming

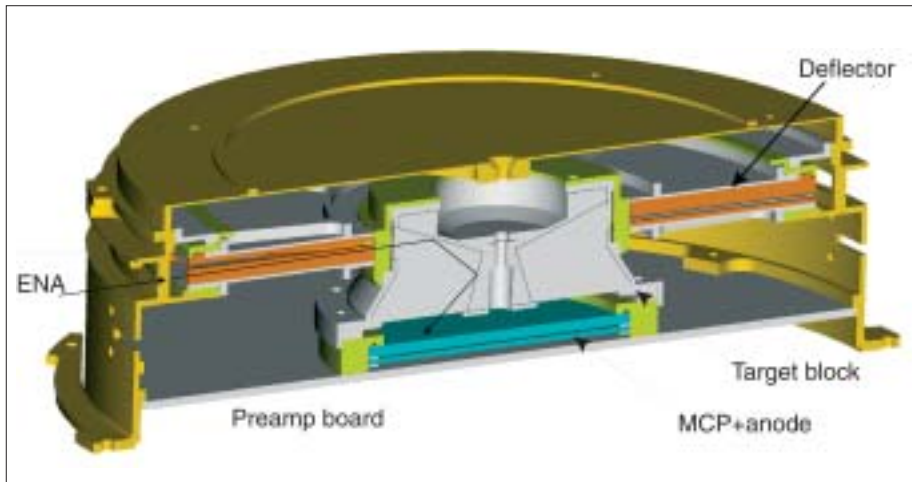


Fig. 7. Cutaway of the NPI sensor.

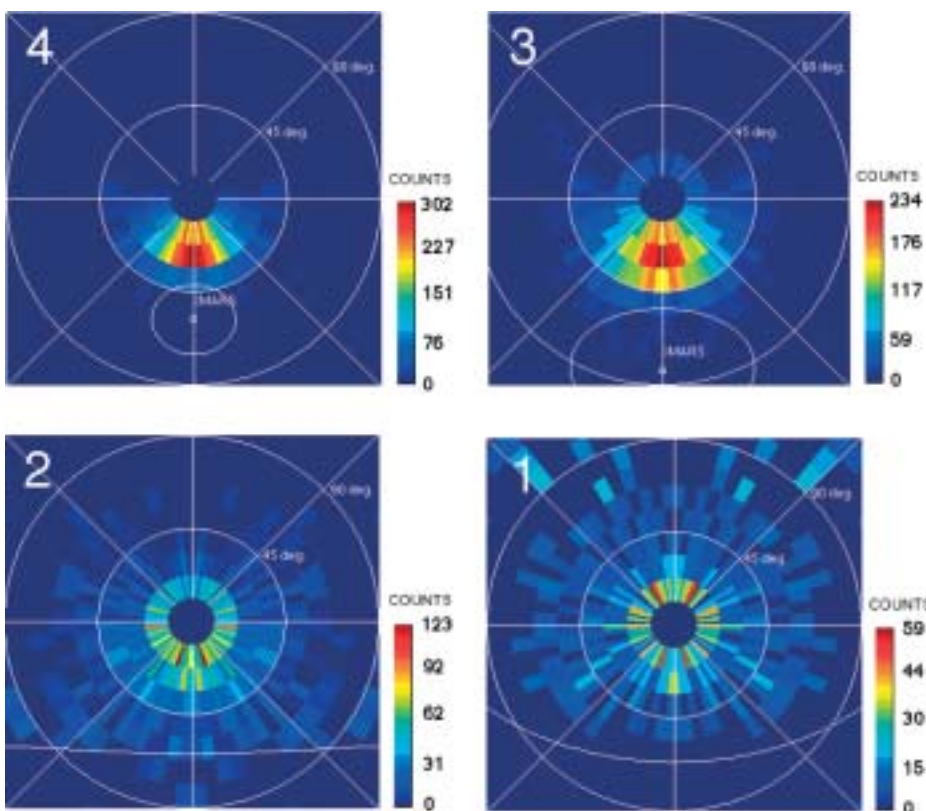
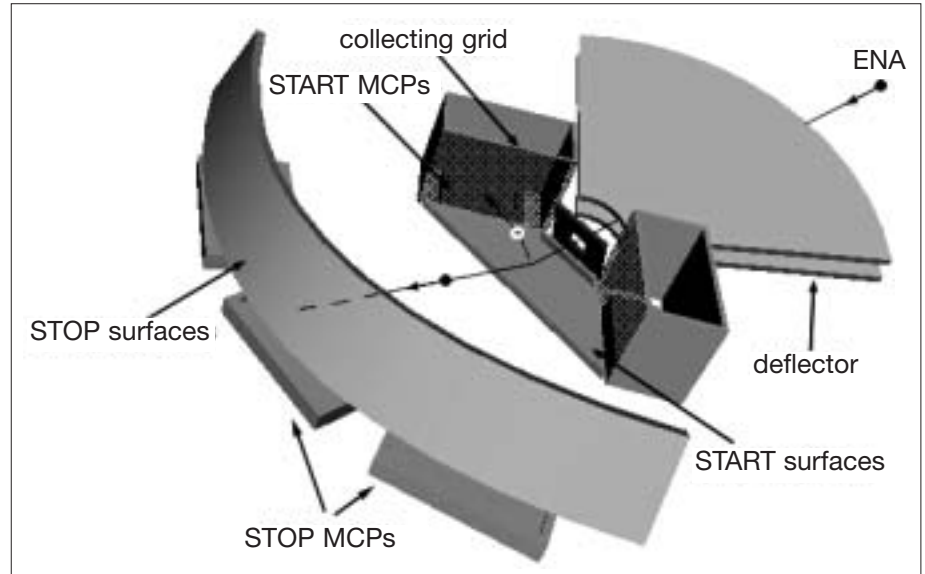


Fig. 8. ENA images expected from NPI for the locations along the Mars Express orbit specified in Fig. 2 (position 4 corresponds to the orbit apocentre). The images were generated assuming the instrument characteristics given in Table 2. The Sun is in the centre of the image. The solar wind ENAs coming from the Sun direction are not shown. The projection is similar to that in Fig. 3.

a star-like structure. This configuration allows the entering particles to experience multiple reflections and reach the MCP. NPI covers 4π in one instrument scan and produces an image of the ENA distribution in the form of an azimuth x elevation matrix. The direction vector of 32 elements can be read out once every $31.25 \mu\text{s}$. Two sectors centred around the spin axis and looking toward the spacecraft body are blocked to monitor the MCP assembly dark counts. This space is also used for the ELS sensor harness.

An important issue in designing the NPI was the target coating for suppressing UV photon fluxes, which produce the UV background in the measurements. NPI uses the same coating as in the PIPPI/Astrid and ASPERA-C experiments: DAG 213, a resin-based graphite dispersion. This is similar to Aquadag, which is a graphite dispersion in water. The coating demonstrated satisfactory performance in the PIPPI experiment

Fig. 9. NPD's principal components.



flown in the Earth's magnetosphere (C:son Brandt et al., 2000). Fig. 8 shows ENA images expected from NPI for the locations along the Mars Express orbit specified in Fig. 2.

2.4 Neutral Particle Detector (NPD)

The NPD contains two identical sensors, each a pinhole camera. Fig. 9 provides a conceptual view of one sensor. In each sensor, the charged particles, electrons and ions are removed by the deflection system, which consists of two 90° sectors separated by a 4.5 mm gap. In the normal operational mode, the 10 kV potential (± 5 kV) applied to the sectors results in a strong electric field that sweeps away all charged particles with energies up to 70 keV. The deflector also collimates the incoming beam in the elevation angle. The collimated ENA beam emerging from the 3.0×4.5 mm pinhole hits the START surface under the 15° grazing angle and causes secondary electron emission. By a system of collecting grids, the secondary electrons are transported to one of two MCP assemblies, giving the START signal for the TOF electronics. Depending on the azimuth angle, the collection efficiency varies from 80% to 95%. The incident ENAs are reflected from the START surface near-specularly. Since charge-state equilibrium is established during the interaction with the surface, the emerging beam contains both the neutral and ionised (positive and negative) components. To increase the total efficiency, no further separation by the charge is made. As proved by the ion tracing, there is very little disturbance to the reflected atomic ions leaving the START surface with energies above 80 eV, introduced by the START electron optics. Fig. 10 shows the results of electron ray-tracing in the START assembly electron optic.

Therefore, particles of all charge-states (negative, neutral and positive) will impact the second surface, the STOP surface, and again produce secondary electrons, which are detected by one of the three MCP assemblies giving the STOP signal. The TOF over a fixed distance of 8 cm defines the particle speed. The STOP MCPs also give the azimuthal direction. Since the secondary electron yield depends on mass for a given velocity, the pulse height distribution analysis of the STOP signals provides the estimation of ENA mass. Each event is stored in the array STOP MCP charge \times TOF \times direction. The content of the array is accumulated over the sampling time of $31.25 \mu\text{s}$. Fig. 11 shows one of the NPD Flight Model sensors.

The selection of the START and STOP surfaces was the most difficult part of NPD's development. Extensive studies were performed at the University of Bern

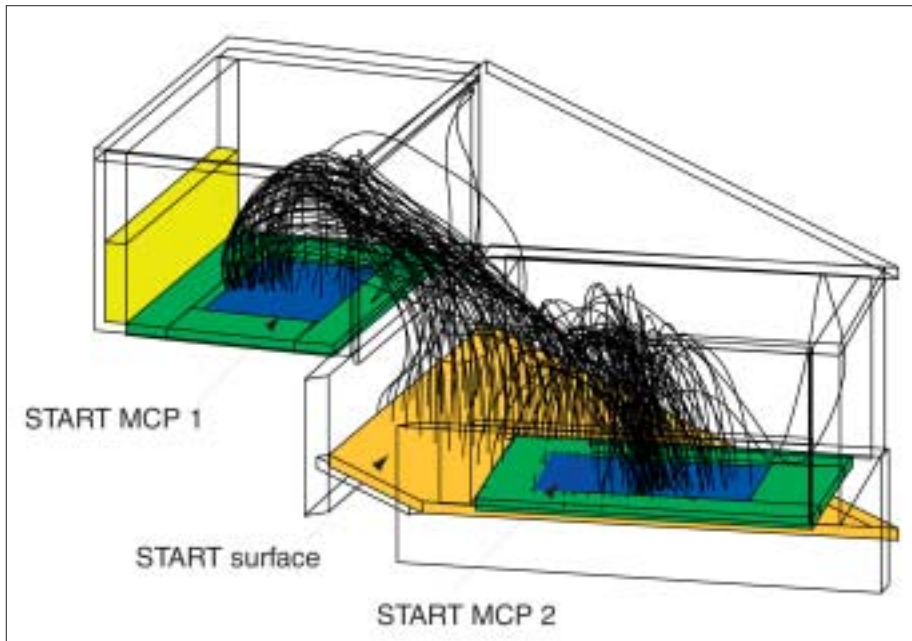


Fig. 10. The ray-tracing of the electron trajectories in the START assembly optics.

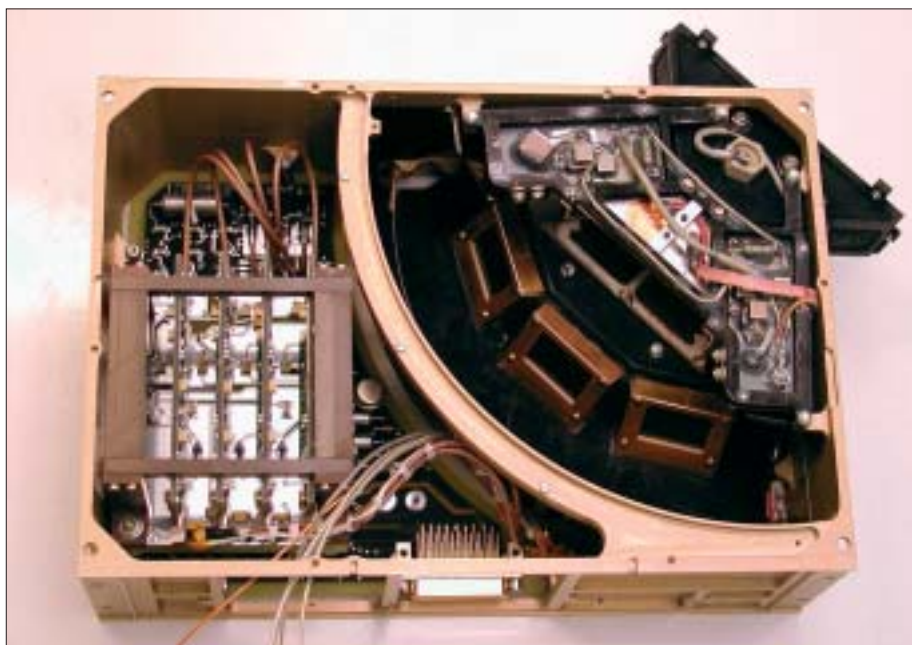


Fig. 11. Flight Model of the NPD sensor.

(Jans, 2000) and Brigham Young University (USA) to optimise the performance of the surfaces, which must satisfy a number of requirements: high secondary-electron yield, high UV absorption even at grazing angles, high particle reflection coefficient (START surface), low angular scattering of ions, and low photoelectron yield. For the START surface, a multi-layer coating composed of a thin layer of Cr_2O_3 covered by a thicker layer of MgF and topped with a thin layer of WO_2 was chosen. The coating is optimised for the absorption of the 121.4 nm line at the 15° incident angle. The reflection coefficient reached was about 30%, a factor of 2 lower than the uncoated surface. The coating is applied on a titanium substrate polished down to 100\AA roughness.

The STOP surface is graphite (roughness around 100 nm) covered by a MgO layer about 500 nm thick. This combination has a very high secondary electron yield, low

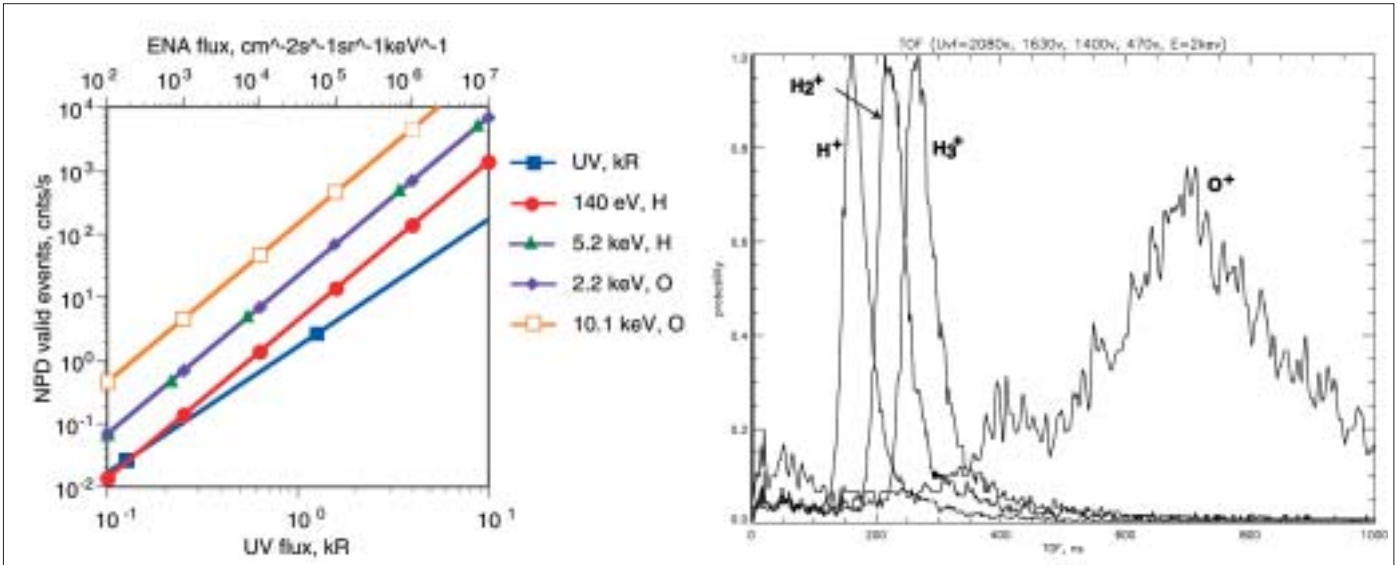


Fig. 12. The UV (Lyman-alpha) background and valid ENA count rates expected for different energies and species for a 1 keV energy window.

Fig. 13. NPD TOF spectra for 2 keV beams of different masses.

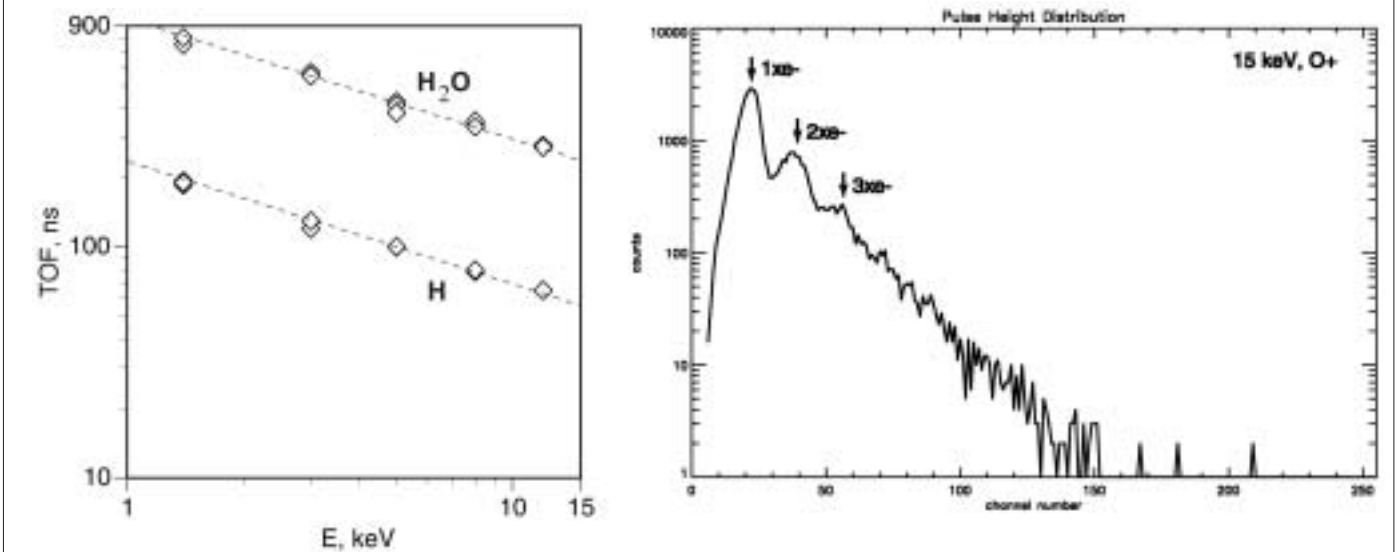


Fig. 14. The time-of-flight measurements for different masses as a function of energy. The dashed lines give the theoretical dependence corresponding to the 34% energy loss.

Fig. 15. Pulse-height distribution of the valid (START-STOP) signals obtained from the STOP MCP under a beam of 15 keV H_2O^+ ions.

photoelectron yield and high UV absorption. Considerable effort was made to increase the stability of the MgO coating against moisture. It was established that polishing the graphite substantially improves the stability, and that possible increases in air humidity during storage and pre-launch operations do not present any problems for the surface performance. Both surfaces are stable and do not require special maintenance. Fig. 12 presents the expected count rates for different ENA and UV fluxes (Lyman- α) and a TOF window of 1.56 ms defined by the slowest (300 eV) oxygen atoms travelling the TOF distance. The valid count rates are given for different species and energies because of the secondary electron yield and reflection coefficient variations. An energy window of 1 keV is taken and the coefficients

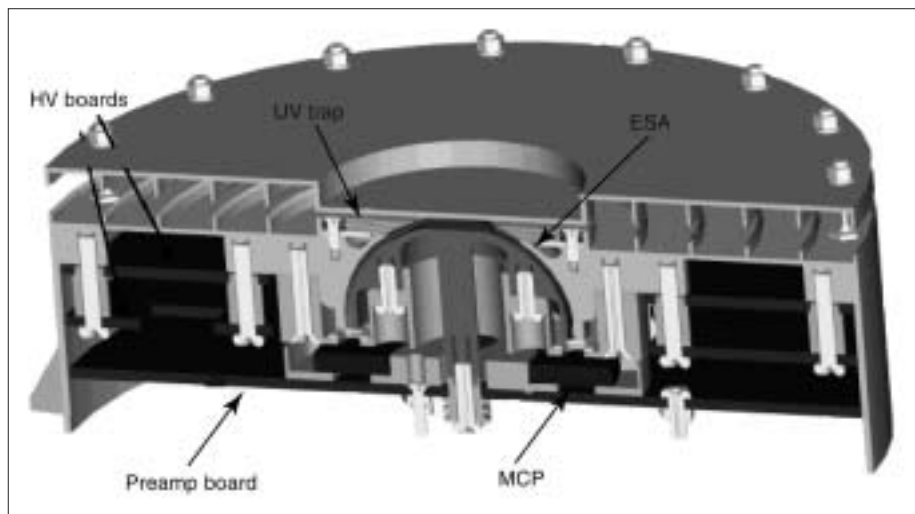


Fig. 16. The ELS sensor.

describing the interaction with the surface are assumed to be constant. In reality, of course, the instrument measures over the entire energy range 0.1-10 keV. Therefore, Fig. 12 gives count rates for a narrow (in energy terms) beam of oxygen and hydrogen atoms. The expected UV flux is about 4 kR close to the martian limb (Anderson, 1974); that gives fluxes, corresponding to a signal-to-noise ratio of 1, of $2 \times 10^5 \text{ cm}^{-2} \text{ s}^{-1} \text{ sr}^{-1} \text{ keV}^{-1}$ (H, 140 eV), $3 \times 10^4 \text{ cm}^{-2} \text{ s}^{-1} \text{ sr}^{-1} \text{ keV}^{-1}$ (H, O, few keV) and $4 \times 10^3 \text{ cm}^{-2} \text{ s}^{-1} \text{ sr}^{-1} \text{ keV}^{-1}$ (O, 10 keV).

The initial tests with the NPD technology model gave results fully corresponding to the specified performance. Fig. 13 shows TOF spectra for 2 keV beams of different masses. Fig. 14 summarises TOF measurements. The dashed lines show the theoretical dependence corresponding to the 34% energy loss in the START surface. The water molecules produced in the ion source break up during the impact but the residual components carry the same initial velocity corrected for the energy loss in the target. Fig. 14 shows that, within 1-10 keV, the TOF measurements give reliable mass identification. The other independent way of mass identification is based on the mass dependence of the number of electrons produced from the STOP surface. Fig. 15 shows a pulse-height distribution of the valid (START-STOP) signals obtained from the STOP MCP when a beam of 15 keV H_2O^+ ions was used. The different peaks correspond to different numbers of secondary electrons released from the STOP surface.

2.5 Electron Spectrometer (ELS)

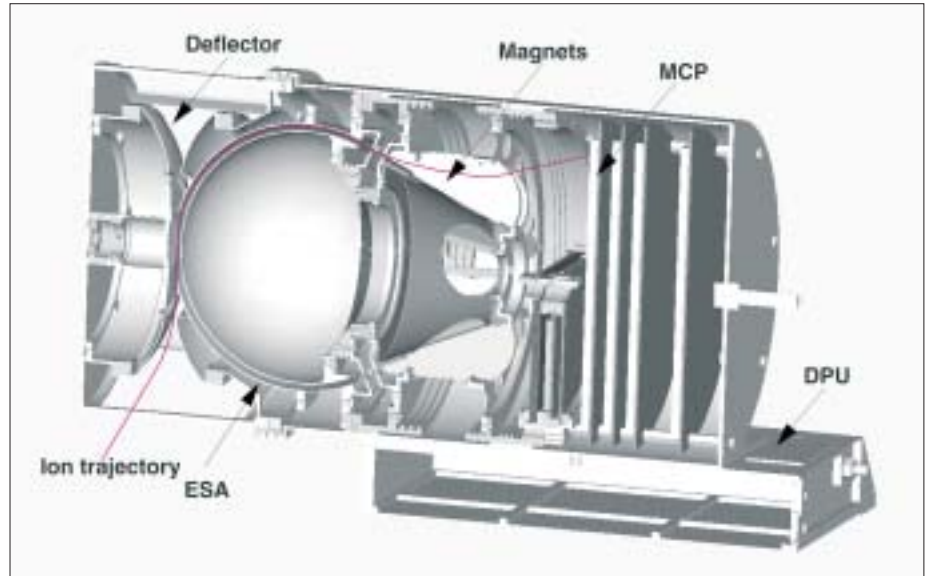
ELS represents a new generation of ultra-light, low-power, electron sensors (Fig. 16). It is formed by a spherical top-hat electrostatic analyser and a collimator system. Particles enter the aperture at any angle in the plane of incidence. Electrons are then deflected into the spectrometer by applying a positive voltage to the inner spherical electron deflection plate. The electrons hit an MCP after being filtered in energy by the analyser plates. The plates are stepped in voltage to achieve an energy spectrum.

Electrons with energies up to $20 \text{ keV}/q$ will be measured, with a maximum time resolution of one energy sweep per 4 s. There are 16 anodes behind the MCP, each anode defining a 22.5° sector and connected to a pre-amplifier. ELS is mounted on the ASPERA-3 scan platform, on top of the NPI sensor, so that the full 4π angular distribution of electrons is measured during each platform scan.

2.6 Ion Mass Analyser (IMA)

IMA (Fig. 17) is an improved version of the ion mass spectrographs TICS (Freja, 1992), IMIS (part of ASPERA-C/Mars-96, 1996) and IMI (Planet-B, 1998) (Norberg

Fig. 17. Cross-section view of the IMA sensor.



et al., 1998). It is a copy of the ICA instrument to be launched on Rosetta to Comet Wirtanen in 2003. Particles enter the analyser through an outer grid. Behind the grid is a deflection system to divert particles coming from between 45° and 135° with respect to the symmetry axis into the electrostatic analyser (ESA). Ions within a swept energy pass band pass the ESA. They are then deflected in a cylindrical magnetic field set up by permanent magnets. The field deflects lighter ions more than heavy ions away from the centre of the analyser. The ions finally hit an MCP and are detected by an anode system. Ions are simultaneously analysed for direction and mass per charge. The magnet assembly can be biased with respect to the ESA to post accelerate ions, enabling a selection of both mass range and mass resolution.

The electrons from the MCP are detected by an 'imaging' anode system. A system of 32 concentric rings behind the MCP measures the radial impact position (representing ion mass) and 16 sector anodes measure the azimuthal impact position (representing ion entrance angle). The read-out system is based on discrete pre-amplifiers. Six MOCAD (Monolithic Octal Charge Amplifier/Pulse Discriminator) chips provide 48 independent channels, 32 rings and 16 sectors. Each chip contains eight channels including a charge-sensitive pre-amplifier, shaper and discriminator. The transistor-transistor logic (TTL) outputs are fed to a field-programmable gate array FPGA device for decoding, addressing and coincidence analysis. Fig. 18 demonstrates the achieved mass resolution at 6 keV ion energy.

3. The Team

The ASPERA-3 experiment team is a large consortium that includes 15 groups from 10 countries in Europe, the USA and Japan. Table 3 shows the primary hardware responsibilities of the different groups.

References

- Acuna, M.H., Connerney, J.E.P., Wasilewski, P., Lin, R.P., Anderson, K.A., Carlson, C.W., McFadden, J., Curtis, D.W., Mitchell, D., Reme, H., Mazelle, C., Sauvaud, J.A., d'Uston, C., Cros, A., Medale, J.L., Bauer, S.J., Cloutier, P., Mayhew, M., Winterhalter, D. & Ness, N.F. (1998). Magnetic Field and Plasma Observations at Mars: Initial Results of the Mars Global Surveyor Mission. *Science* **279**, 1676.
- Anderson, D.E. (1974). Mariner 6, 7, and 9 Ultraviolet Spectrometer: Analysis of Hydrogen Lyman alpha Data. *J. Geophys. Res.* **79**, 1513-1518.

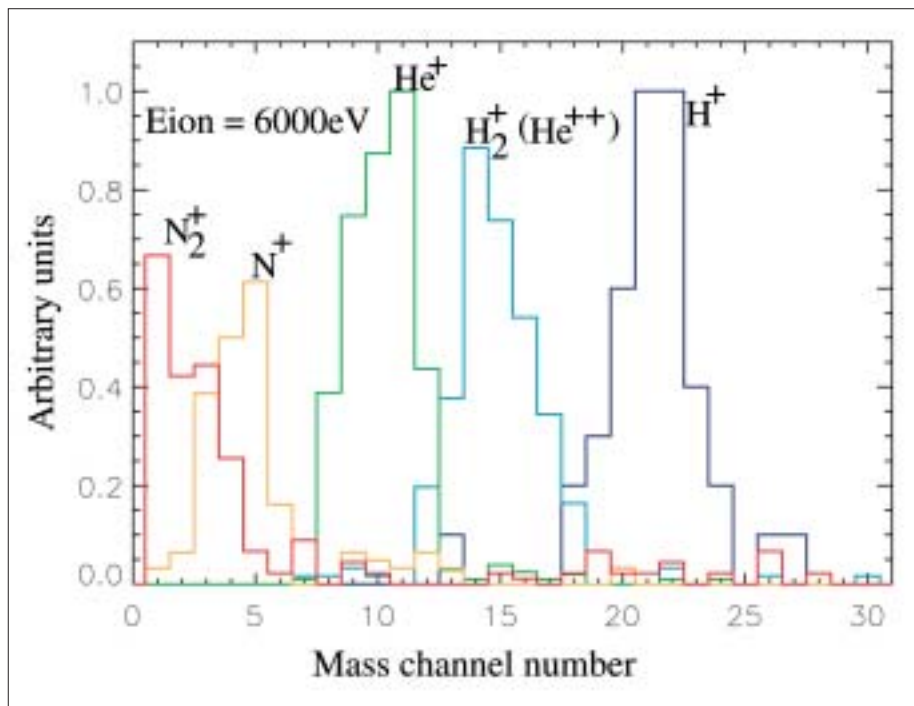


Fig. 18. IMA mass resolution at 6 keV.

Table 3. ASPERA-3 groups and primary hardware responsibilities.

<i>Species</i>	<i>Scientific objective</i>
Swedish Institute of Space Physics, Kiruna, S	PI-institute, NPI, NPD, IMA, scanner
Institute of Space and Astronautical Science, Sagamichara, JPN	Collaboration with Nozomi, NPI calibrations
University of Bern, Physikalisches Institut, CH	NPD surfaces, NPD mechanics
Instituto di Fisica dello Spazio Interplanetari, Rome, I	EGSE, NPI mechanics, NPD electronics
Mullard Space Science Laboratory, UCL, UK	ELS calibrations
University of Arizona, Tucson, Arizona, USA	START surface, NPD UV calibrations
Space Research Institute, Moscow, Russia	NPD design
Southwest Research Institute, San Antonio, USA	ELS, IMA imaging detector
Rutherford Appleton Laboratory, UK	NPD MCPs
Finnish Meteorological Institute, Helsinki, FIN	DPU, theory
Space Physics Research Lab/University of Michigan, Ann Arbor, Michigan, USA	Theory
Max-Planck-Institut für Aeronomie, Katlenburg-Lindau, D	NPD electronics
Space Science Lab/University of California in Berkeley, Berkeley, California USA	Theory
Space Technology Ltd., National University of Ireland, IRL	Hardware support
Applied Physics Lab/Johns Hopkins University, Laurel, Maryland, USA	Theory
Centre d'Etude Spatiale des Rayonnements, Toulouse, F	NPI MCPs, IMA calibrations, DC/DC board, scanner drivers

- Barabash, S., Lundin, R., Zarnowiecki, T. & Grzedzielski, S. (1995). Diagnostic of Energetic Neutral Particles at Mars by the ASPERA-C Instrument for the Mars-96 Mission. *Adv. Space Res.* **16**, (4)81.
- Barabash, S. (1995). Satellite Observations of the Plasma-Neutral Coupling near Mars and the Earth. *IRF Scientific Report* 228.
- Barabash, S., Holmström, M., Lukyanov, A. & Kallio, E. (2002). Energetic Neutral Atoms at Mars IV: Imaging of Planetary Oxygen. *J. Geophys. Res.* **107**(A10), doi: 10.1029/2001JA000326.
- Brecht, S.H. (1997). Solar Wind Proton Deposition into the Martian Atmosphere. *J. Geophys. Res.* **102**, 11,287.
- C:son Brandt, P., Barabash, S., Wilson, G.R., Roelof, E.C. & Chase, C.J. (2000). Energetic Neutral Atom Imaging at Low (< 10 keV) Energies from Astrid: Observations and Simulations. *J. Atmos. & Solar Terrestrial Phys* **62**, 901-910.
- Dornheim, M.A. (1997). Mars Atmosphere Thicker than Expected. *Av. Week & Space Tech.* (29 September), 36.
- Dubinin, E., Sauer, K., Lundin, R., Norberg, O., Trotignon, J.-G., Schwingschuh, K., Delva, M. & Riedler, W. (1996). Plasma Characteristics of the Boundary Layer in the Martian Magnetosphere. *J. Geophys. Res.* **101**, 27,061.
- Holmström, M., Barabash, S. & Kallio, E. (2002). Energetic Neutral Atoms at Mars I: Imaging of Solar Wind Protons. *J. Geophys. Res.* **107**(A10), doi: 10.1029/2001JA000325.
- Jans, S. (2000). *Ionization of Energetic Neutral Atoms for Application in Space Instrumentation*, Diplomarbeit der Philosophisch-naturwissenschaftlichen Fakultät der Universität Bern, CH.
- Farmer, C.B., Davies, D.W., Holland, A.L., LaPorte, D.D. & Downs, P.E. (1977). Mars: Water Vapour Observations from the Viking Orbiters. *J. Geophys. Res.* **82**, 4225.
- Kallio, E. & Barabash, S. (2000). On the Elastic and Inelastic Collisions between the Precipitating Energetic Hydrogen Atoms and the Martian Atmospheric Neutrals. *J. Geophys. Res.* **105**, 24973-24996.
- Kallio, E. & Barabash, S. (2001). Atmospheric Effects of Precipitating Energetic Hydrogen Atoms to the Martian Atmosphere. *J. Geophys. Res.* **106**, 165-177.
- Kallio, E. & Janhunen, P. (2001). Atmospheric Effects of Proton Precipitation in the Martian Atmosphere and its Connection to the Mars-Solar Wind Interaction. *J. Geophys. Res.* **106**, 5617.
- Kallio, E. & Koskinen, H. (1999). A Test Particle Simulation of the Motion of Oxygen Ions and Solar Wind Protons near Mars. *J. Geophys. Res.* **104**, 557-579.
- Kallio, E., Luhmann, J.G. & Barabash, S. (1997). Charge Exchange near Mars: The Solar Wind Absorption and Energetic Neutral Atom Production. *J. Geophys. Res.* **102**, 22,183.
- Lichtenegger, H., Lammer, H. & Stumptner, W. (2002). Energetic Neutral Atoms at Mars III: Flux and Energy Distribution of Planetary Energetic H Atoms. *J. Geophys. Res.* **107**(A10), doi: 10.1029/2001JA000326.
- Luhmann, J.G. & Bauer, S.J. (1992). Solar Wind Effects on Atmospheric Evolution at Venus and Mars. In *Venus and Mars: Atmospheres, Ionospheres, and Solar Wind Interactions*, AGU Monograph, **66**, 417-430
- Luhmann, J.G. & Kozyra, J.U. (1991). Dayside Pickup Oxygen Ion Precipitation at Venus and Mars: Spatial Distributions, Energy Deposition and Consequences. *J. Geophys. Res.* **96**, 5457.
- Luhmann, J.G., Johnson, R.E. & Zhang, M.H.G. (1992). Evolutionary Impact of Sputtering of the Martian Atmosphere by O⁺ Pickup Ions. *Geophys. Res. Lett.* **19**, 2151.
- Lundin, R., Zakharov, A., Pellinen, R., Borg, H., Hultqvist, B., Pissarenko, N., Dubinin, E.M., Barabash, S.W., Liede, I. & Koskinen, H. (1989). First Measurements of the Ionospheric Plasma Escape from Mars. *Nature* **341**, 609.
- Lundin, R., Dubinin, E., Koskinen, H., Norberg, O., Pissarenko, N. & Barabash, S.

- (1991). On the Momentum Transfer of the Solar Wind to the Martian Topside Ionosphere. *Geophys. Res. Lett.* **18**, 1059.
- Lundin, R., Dubinin, E., Barabash, S. & Norberg, O. (1993). ASPERA Observations of Martian Magnetospheric Boundaries. In *Plasma Environments of Non-magnetic Planets* (Ed. T.I. Gombosi), Pergamon Press, UK, p311.
- McKay, C.P. & Stoker, C.R. (1989). The Early Environment and its Evolution on Mars: Implications for Life. *Rev. of Geophys.* **27**, 189.
- Mura, A., Milillo, A., Orsini, S., Kallio, E. & Barabash, S. (2002). Energetic Neutral Atoms at Mars II: Energetic Neutral Atom Production near Phobos. *J. Geophys. Res.* **107**(A10), doi: 10.1029/2001JA000328.
- Norberg, O., Winningham, J.D., Lauche, H., Keith, W., Puccio, W., Olsen, J., Lundin, K. & Scherrer, J. (2001). The MEDUSA Electron and Ion Spectrometer and the PIA Ultraviolet Photometers on Astrid-2. *Ann. Geophys.* **19**, 593.
- Norberg, O., Yamauchi, M., Lundin, R., Olsen, S., Borg, H., Barabash, S., Hirahara, M., Mukai, T. & Hayakawa, H. (1998). The Ion Mass Imager on the Planet-B Spacecraft. *Earth, Planets and Space* **50**, 199-205.
- Perez-de-Tejada, H. (1992). Solar Wind Erosion of the Mars Early Atmosphere. *J. Geophys. Res.* **97**, 3159.
- Roelof, E.C. & Skinner, A.J. (2000). Extraction of Ion Distributions from Magnetospheric and EUV Images. *Space Sci. Rev.* **91**, 437-459.
- Verigin, M., Gringauz, K.I., Kotova, G.A., Shutte, N.M., Rosenbauer, H., Livi, S., Richter, A.K., Riedler, W., Schwingenschuh, K. & Szegö, K. (1991). On the Problem of the Martian Atmosphere Dissipation: PHOBOS 2 TAUS Spectrometer Results. *J. Geophys. Res.* **96**, 19,315-19,320.
- Wurz, P. (2000). Detection of Energetic Neutral Particles. In *The Outer Heliosphere: Beyond the Planets* (Eds. K. Scherer, H. Fichtner & E. Marsch), Copernicus Gesellschaft, Katlenburg-Lindau, Germany, pp251-288.

Acknowledgment

The authors are grateful to A. Balogh and C. Carr (both Imperial College, London, UK) for providing the IEEE-1355 link chip developed for the Rosetta mission.

MaRS: Mars Express Orbiter Radio Science

M. Pätzold¹, F.M. Neubauer¹, L. Carone¹, A. Hagermann¹, C. Stanzel¹, B. Häusler², S. Remus², J. Selle², D. Hagl², D.P. Hinson³, R.A. Simpson³, G.L. Tyler³, S.W. Asmar⁴, W.I. Axford⁵, T. Hagfors⁵, J.-P. Barriot⁶, J.-C. Cerisier⁷, T. Imamura⁸, K.-I. Oyama⁸, P. Janle⁹, G. Kirchengast¹⁰ & V. Dehant¹¹

¹*Institut für Geophysik und Meteorologie, Universität zu Köln, D-50923 Köln, Germany*
Email: paetzold@geo.uni-koeln.de

²*Institut für Raumfahrttechnik, Universität der Bundeswehr München, D-85577 Neubiberg, Germany*

³*Space, Telecommunication and Radio Science Laboratory, Dept. of Electrical Engineering, Stanford University, Stanford, CA 95305, USA*

⁴*Jet Propulsion Laboratory, 4800 Oak Grove Drive, Pasadena, CA 91009, USA*

⁵*Max-Planck-Institut für Aeronomie, D-37189 Katlenburg-Lindau, Germany*

⁶*Observatoire Midi Pyrenees, F-31401 Toulouse, France*

⁷*Centre d'etude des Environnements Terrestre et Planetaires (CETP), F-94107 Saint-Maur, France*

⁸*Institute of Space & Astronautical Science (ISAS), Sagamihara, Japan*

⁹*Institut für Geowissenschaften, Abteilung Geophysik, Universität zu Kiel, D-24118 Kiel, Germany*

¹⁰*Institut für Meteorologie und Geophysik, Karl-Franzens-Universität Graz, A-8010 Graz, Austria*

¹¹*Observatoire Royal de Belgique, B-1180 Bruxelles, Belgium*

The Mars Express Orbiter Radio Science (MaRS) experiment will employ radio occultation to (i) sound the neutral martian atmosphere to derive vertical density, pressure and temperature profiles as functions of height to resolutions better than 100 m, (ii) sound the ionosphere to derive vertical ionospheric electron density profiles and a description of the ionosphere through its diurnal and seasonal variations with solar wind conditions; MaRS will also (iii) determine the dielectric and scattering properties of the martian surface in target areas by a bistatic radar experiment, (iv) determine gravity anomalies for the investigation of the structure and evolution of the martian crust and lithosphere in conjunction with observations of the High Resolution Stereo Camera as a base for 3D topography, and (v) sound the solar corona during the superior conjunction of Mars with the Sun.

The radio carrier links of the spacecraft Telemetry, Tracking and Command subsystem between the Orbiter and Earth will be used for these investigations. Simultaneous and coherent dual-frequency downlinks at X-band (8.4 GHz) and S-band (2.3 GHz) via the High Gain Antenna will permit separation of contributions from the classical Doppler shift and the dispersive media effects caused by the motion of the spacecraft with respect to the Earth and the propagation of the signals through the dispersive media, respectively.

The investigation relies on the observation of the phase, amplitude, polarisation and propagation times of radio signals transmitted from the spacecraft and received with antennas on Earth. The radio signals are affected by the medium through which they propagate (atmospheres, ionospheres, interplanetary medium, solar corona), by the gravitational influence of the planet on the spacecraft and, finally, by the performances of the various systems aboard the spacecraft and on Earth.

1. Introduction

Initially conceived as an exploratory tool, radio-science techniques have provided considerable knowledge of the atmospheres and gravity of the planets – much of it unexpected. Previous experiments at Mars have demonstrated accuracies in measurements of martian atmospheric surface pressure and temperature that surpassed those of *in situ* measurements made with the Viking Landers (Hinson et al., 2001). This performance can be matched or possibly improved for occultation immersion measurements with Mars Express.

Radio-science techniques are applied to the study of planetary and cometary atmospheres, planetary rings and surfaces, gravity and the solar corona. Much of our current knowledge of these subjects is based on radio-science observations. Early investigations include the Mariner, Pioneer and Viking missions, as well as Soviet projects. Recent and current experiments involve Voyager (Eshleman et al., 1977; Tyler, 1987), Ulysses (Bird et al., 1994; Pätzold et al., 1995), Giotto (Pätzold et al., 1991a; 1991b; 1993), Galileo (Howard et al., 1992), Magellan (Tyler et al., 1991) and Mars Global Surveyor (Tyler et al., 2001). Planned experiments include Cassini (Kliore et al., 2002), Cassini-Huygens (Bird et al., 1995), Rosetta (Pätzold et al., 2000) and Mars Express.

Radio-science investigations fall into three broad categories: propagation, bistatic radar and gravity. First, when the trajectory of the spacecraft takes it behind the planet as seen from Earth, there is occultation by the planet's atmosphere. A radio signal propagating from the spacecraft to a ground station travels through the ionosphere and neutral atmosphere before being blocked by the planetary surface. This sequence is reversed upon emergence of the spacecraft. During an occultation event, the refractive index of the gases in the ionosphere and atmosphere alter the characteristics of the propagating radio wave. The method can be extended to any one of several separable 'atmospheres', including planetary rings and magnetospheres, as well as the relativistic gravitational effects of stars (Eshleman, 1973). In conducting such observations, the geometry and other experimental conditions must be controlled so that the only significant unknown factors are the properties of the medium along the radio path.

Second, oblique incidence scattering investigations using propagation paths between spacecraft, planetary surface and Earth station can be used to explore the surface properties through the microwave scattering function. The technique was first described by Fjeldbo (1964). It is referred to as 'bistatic radar' because the transmitter and receiver are separated by significant angular distances or ranges. The first such experiment in space was conducted with Luna-11 in August 1966 to study the Moon's surface (Yakaovlev & Efimov, 1966). The oblique scattering geometry afforded by Lunar Orbiter-1, in October 1966, provided the signal source for the first US experiment (Tyler et al., 1967). Signals from Explorer-35 also contained echos from the lunar surface (Tyler, 1968a). Fortuitously, the plane of the spacecraft spin axis and the antenna polarisation made it possible to measure the Brewster angle of the lunar crust, leading to an unambiguous value for the relative dielectric constant of lunar soil of between 2.9 and 3.1, confirming that landers would be on firm ground.

Third, when the radio path is well clear of occulting material, the spacecraft can be treated as a classical 'test particle' falling in the gravity field of the planetary system. This type of experiment is optimised when the component of its velocity is along the line-of-sight to the tracking station, thus allowing a measurement of the Doppler effect. The spacecraft motion causing the Doppler shift is in response to the variations in mass distribution within a planet or its satellites. This is a classical physics laboratory experiment carried out at planetary-scale. Our global knowledge of Earth's gravity field comes from such studies. The only information on the gravity field of Mercury is based on the two flybys of Mariner-10 (Anderson et al., 1987). Similarly, recent observational inferences on the internal structures of the Galilean satellites (for example, that there is an ocean on Europa) are based on the perturbations of Galileo's trajectory during close flybys (Anderson et al., 1992; 1997). A precise determination of the total mass of Uranus and Neptune from the Voyager-2 flybys (Tyler et al., 1986)

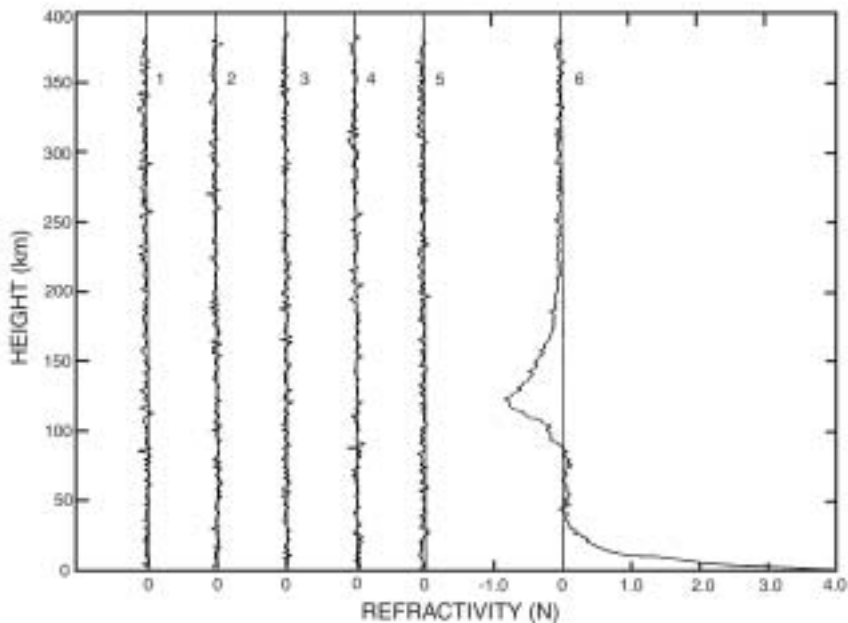


Fig. 1. Refractivity profiles at S-band obtained from the Mariner-4 occultation. Profiles 1-5 were taken prior to the occultation and represent the zero level after biases and trends owing to effects not connected with the martian atmosphere were removed. Profile 6 shows the refractivity of the martian atmosphere at S-band probed during occultation entry. Negative refractivity represents the ionosphere, positive the neutral atmosphere (from Fjeldbo & Eshleman, 1968).

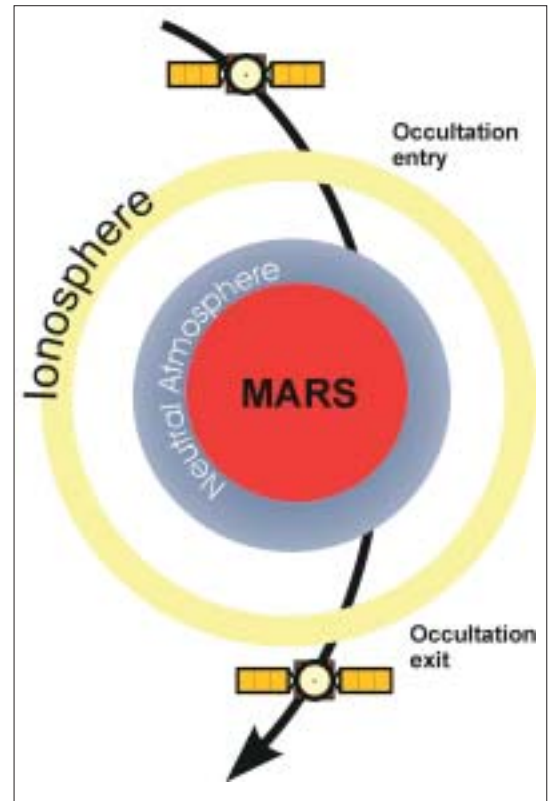


Fig. 2 (right). Operational sequence for the use of the two-way link for sounding the atmosphere/ionosphere as seen from the Earth. The sequence is seen projected on to the plane of the sky. The two-way radio ray slices through the atmosphere from the top to the surface during occultation entry and is then shadowed by the planet. After leaving occultation, the now one-way ray slices through the atmosphere from the surface to the upper levels of the ionosphere, where the two-way radio link may be reestablished.

has led to the conclusion that there is no need for a 'Planet X' to explain the orbits of these bodies (Standish, 1993). The method has been extended to small bodies, such as the mass determination of asteroid Mathilde (Yeomans et al., 1997) and the gravity field of asteroid Eros (Yeomans et al., 2000), and is planned for the Rosetta flyby at asteroid Siwa in 2008 (Pätzold et al., 2001). For Mars Express, these asteroid techniques can be applied to precise determinations of the masses of Phobos and Deimos during close encounters.

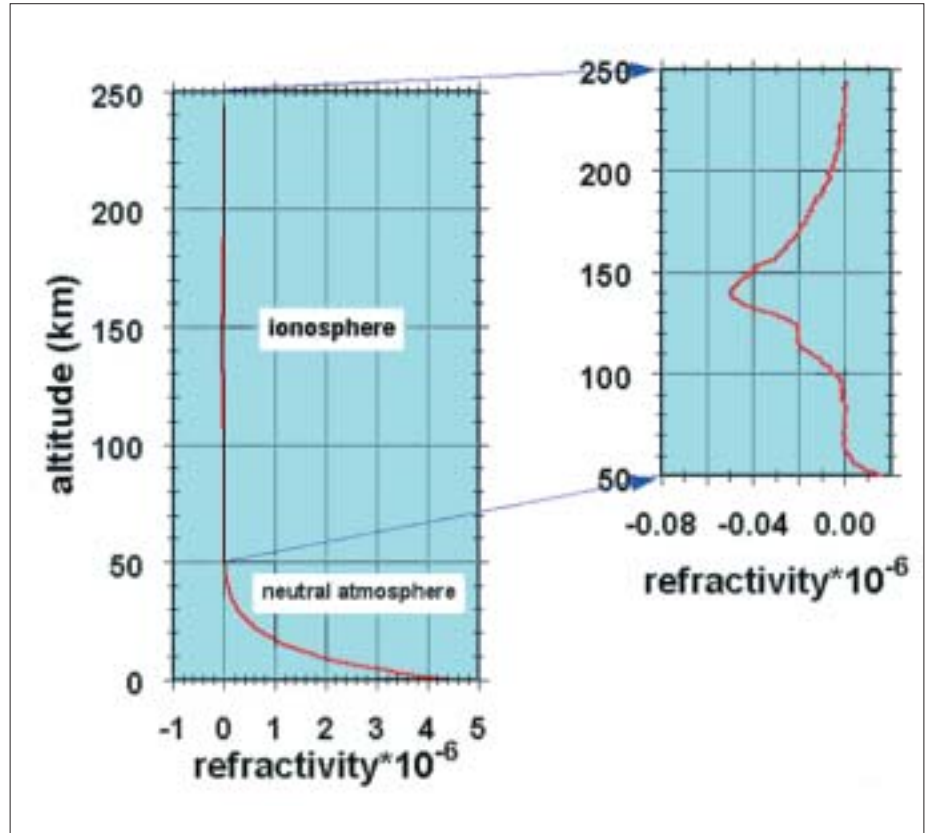
2.1 Radio sounding of the neutral atmosphere and ionosphere

The modern value for the surface pressure of Mars was first determined in 1965 by using the radio occultation method with Mariner-4 (Kliore et al., 1965). Prior to that, the literature indicated a consensus that the surface pressure was of the order 100 mbar (about 10% of Earth's), based on spectroscopic observations from the ground, with many believing that oxygen was a likely major constituent.

A more accurate value was needed in support of martian landers being studied by NASA teams lead by Wehrner von Braun. At the time of the Mariner-4 launch and cruise, new ground-based observations of the atmosphere had begun to cast doubt on the 100 mbar value, suggesting that the true value could be substantially lower. As a result, Mariner-4 was directed to fly behind Mars to perform radio occultation measurements. Initial results showed the surface pressure at the occultation point was approximately 4 mbar (Fig. 1). Further, since spectrographic studies indicated that the partial pressure of CO₂ on Mars was in this range, the atmosphere was almost entirely carbon dioxide with little, if any, oxygen. Radio occultation measurements have been included on almost all planetary missions flown since.

2. Science Objectives

Fig. 3. X-band refractivity profile obtained with Mars Global Surveyor on 11 March 1999. Note that the positive refractivity is comparable to that shown in Fig. 1 at S-band. The inset shows on a larger scale the negative refractivity of the ionosphere. The peak refractivity translates into a peak electron density of 8.7×10^{10} electrons m^{-3} . Ionospheric refractivity at X-band scales by a factor of $(3/11)^2$ relative to that at S-band in Fig. 1.



Sounding by radio occultation of Mars Express (Fig. 2) will contribute to the understanding of the structure of the martian atmosphere, its circulation and dynamics through the day and seasons. Vertical profiles of density, pressure and temperature with height resolutions better than 100 m can be derived. Observations of the vertical structure below 30 km altitude have been made by several spacecraft during occultations. *In situ* measurements of three atmospheric profiles during the descents of the two Viking landers and Pathfinder are available below 200 km altitude. Dust and haze in the atmosphere do not hinder the propagation of the radio carrier waves, but the local heating by entrained dust is observed in several occultation temperature profiles. The Mars Global Surveyor (MGS) radio occultation experiment (Tyler et al., 1992) retrieved vertical profiles of pressure and temperature extending from the surface to the 10 Pa level, with surface uncertainties of 2 Pa and 1K (Hinson et al., 1999).

Radio occultation also provides a measure of the ionosphere's vertical structure and an averaged large-scale electron density profile as a function of height and planetary latitude at each occultation point. One of the goals is to understand the global behaviour of the martian ionosphere with the effects of the magnetic field, solar activity and solar wind interaction through the day and seasons.

Photochemical processes control the behaviour of the main ionospheric layer in a manner similar to the terrestrial F layer (Barth et al., 1992). The electron density distribution of a weakly magnetised body like Mars is controlled by solar radiation and the solar wind interaction with the planet. A typical value of the daytime ionospheric peak density is of the order of 10^{11} electrons m^{-3} at altitudes of 110-135 km (Fig. 3).

Observations by MGS have revealed highly variable and localised magnetic fields (Acuna et al., 1998). Strong fields at the spacecraft orbit below the ionosphere were

observed locally. At other locations, much weaker magnetic fields were found. Therefore, the possibility of a sufficiently strong global magnetic field involved in the solar wind interaction might no longer be supported. However, only a narrow latitude range was covered by MGS observations owing to the low pericentre altitude during aerobraking.

On the other hand, the radio occultation data from Mariner-9 and Viking (Kliore, 1992) suggest the presence of a global magnetic field in the formation of the ionosphere. With its better resolution (about 100 electrons cm^{-3}), Mars Express may address the question of whether the Mariner/Viking profiles reflect only their low resolution or if a global magnetic field is indeed involved. The height of the ionopause is not well defined at Mars. At Venus, the ionopause has been defined as that altitude where the electron density falls below 500 electrons cm^{-3} (Kliore & Luhmann, 1991), while the density in the martian profiles never drops below that limit. Mars Express needs to solve the question of which physical processes define the ionopause altitude.

Either the entry or the exit of the Mars Express occultations will be at nighttime, providing the opportunity to investigate the nightside ionosphere. Viking resolved a nighttime ionosphere in only 40% of the measurements, which also showed a high variability in shape, peak density and height. The anticipated accuracy of Mars Express will help to solve the question of whether the nighttime ionosphere is maintained by horizontal transport from the dayside or by impact ionisation owing to electron precipitation from the tail, which should provide insights into the direction of the magnetic field on the nightside.

During occultation ingress, the Telemetry, Tracking and Command (TT&C) subsystem will operate in the two-way mode. The spacecraft downlink frequencies are derived from the uplink, stabilised by a hydrogen maser in the ground station. Changes in the received radio frequency (RF) to a fractional frequency stability of 10^{-14} over 3-100 s integration times correspond to a change in the angle of refraction of radio rays in occultation experiments of the order 10^{-8} rad (Tyler, 1987).

The signal-to-noise limitations of previous experiments limited the detectability of the atmosphere to below 30 km. Mars Express should improve this altitude to 50 km because of the high signal-to-noise ratio at X-band (transmitted RF power 65 W). The effective vertical resolution through use of the Abel transform is determined by the first Fresnel zone radius $(\lambda D)^{1/2}$, which is about 300 m for X-band and 600 m for S-band, respectively, (D is the distance of the spacecraft to the closest approach of the ray path to the planet). This resolution is far superior to what can be achieved by other passive sounding instruments, which are limited to typically one atmospheric scale height (order of km).

Marouf et al. (1986) developed a procedure to improve the resolution beyond the natural diffraction limit, applying it to the Voyager occultation by Saturn's rings. Gresh et al. (1989) applied the procedure to occultation data from the rings of Uranus. This resulted in a resolution of 100 m, about an order of magnitude improvement on the Fresnel diffraction limit, for flyby conditions at the outer planets. The technique was also applied in the first direct determination of Triton's surface pressure (Tyler et al., 1989). Karayel & Hinson (1997) applied a similar approach to atmospheres denser than Triton's and produced a resolution of about 40 m for simulated martian conditions. These results justify the expectation that it is feasible to derive vertical profiles in the martian atmosphere with a height resolution better than 100 m.

Separating the effects from the ionosphere and neutral atmosphere on the radio link is feasible by using (a) a dual-frequency downlink, (b) the opposite sign of the refractive index if the radio signal propagates in ionised or neutral media, and (c) the fact that the peak heights of the ionosphere and the detectable neutral atmosphere are well separated. This is demonstrated in Figs. 1 and 3 which show the refractivity profile derived from Mariner-4 occultation data (profile 6) at S-band and a refractivity profile from MGS at X-band, respectively, as a function of height. Negative refractivity results from the ionised plasma in the ionosphere and is proportional to the electron number density; positive refractivity is a property of the neutral

Fig. 4a. Duration of Mars Express occultations (in minutes) over the mission. There will be six occultation seasons (OCP1 to OCP6), with an Earth occultation in each orbit over the expected mission duration of two Martian years.

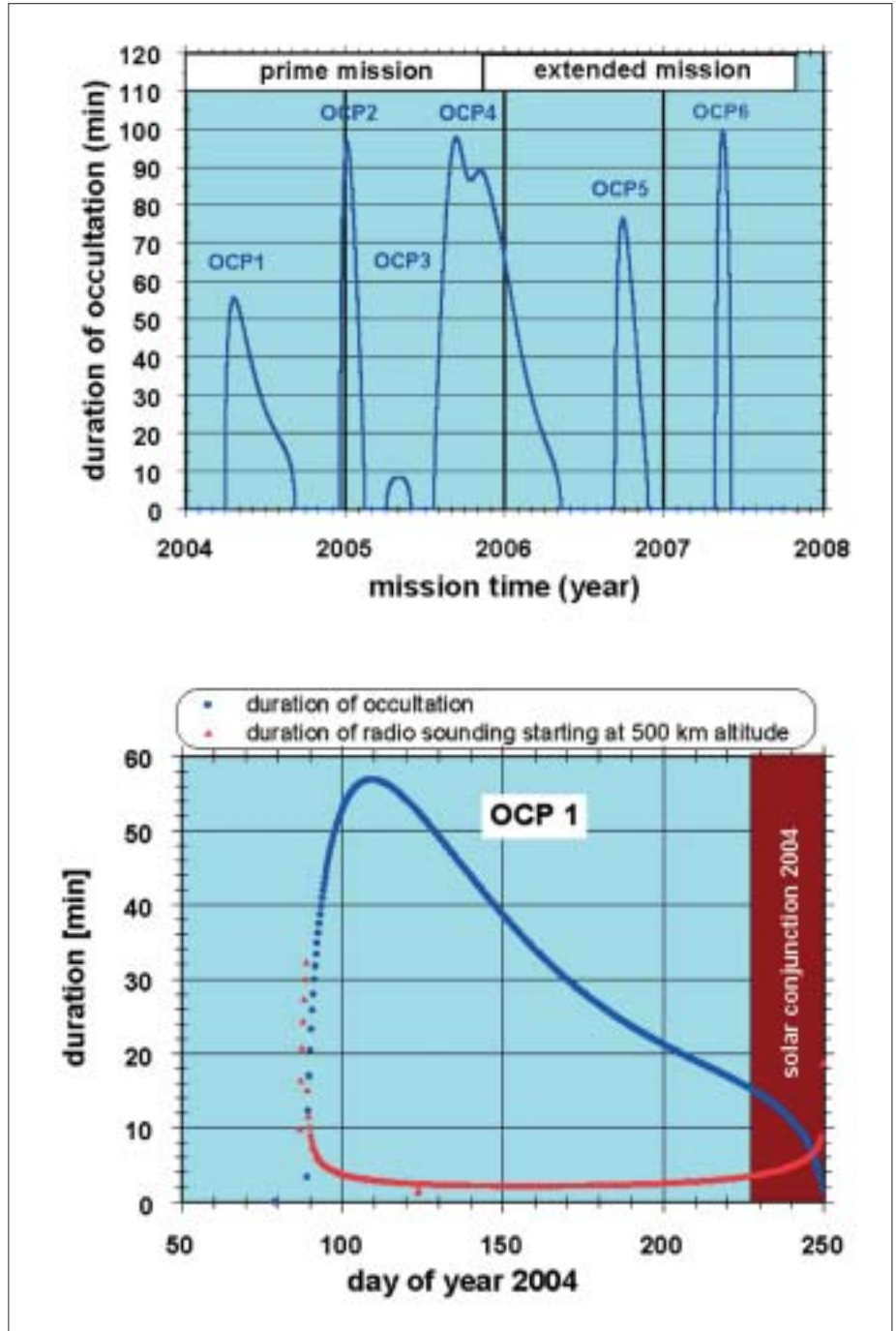


Fig. 4b. Duration of occultations by the planet body during the first season OCP1 (blue dots) and the duration of occultation by the atmosphere between 500 km altitude to the surface (red triangles). The end of the first occultation season is affected by the start of the superior solar conjunction of the planet at year day 238, 2004.

atmosphere which is linearly related to the mass density of the atmospheric constituents (Fjeldbo & Eshleman, 1968). The refractivity μ of free electrons is given by

$$\mu = - 40.31 \times 10^6 \frac{N_e}{f^2}$$

which allows conversion of refractivity into electron number densities (N_e in electrons m^{-3} is the electron density, f in Hz is the radio carrier frequency).

It is feasible to retrieve two refractivity profiles with Mars Express for each radio

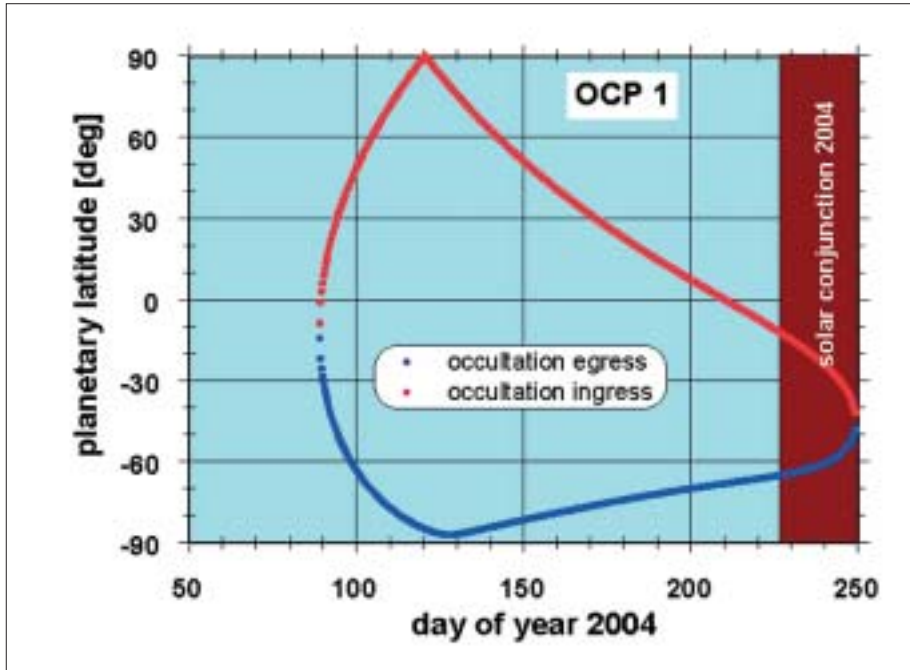


Fig. 5. Spacecraft position along the orbit at occultation entry (red) and occultation exit (blue) for OCP1 expressed as true anomaly. True anomaly of 0 deg is the pericentre position. The red area marks ± 60 deg true anomaly when the spacecraft is nominally in nadir pointing. Occultation can be observed only when ground coverage is available, typically every third occultation.

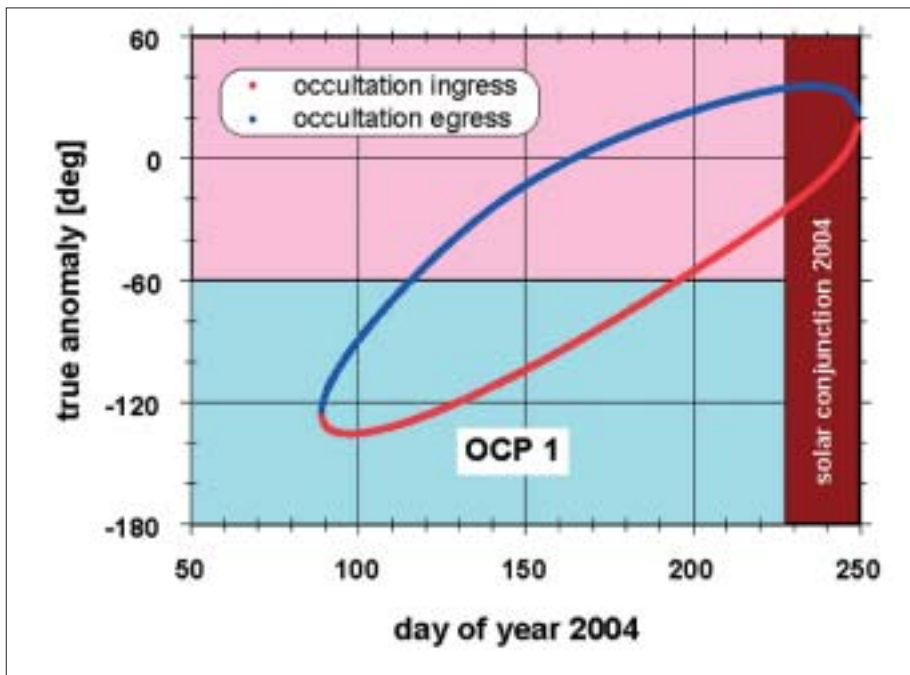


Fig. 6. Planetary latitude of occultation ingress and egress locations during OCP1. Effectively, all planetary latitudes are covered during all six occultation seasons.

carrier frequency at S-band and X-band. S-band is expected to be more sensitive to the negative refractivity (ionosphere) by a factor $(11/3)^2$ compared with X-band, while the positive refractivity (neutral atmosphere) is essentially independent of the frequency. Under favourable geometric conditions it will be possible to investigate the solar wind-magnetic anomalies-ionospheric interaction region.

Computing the differential Doppler from the received S-band and X-band residual Doppler shifts yields the dispersive media effects associated with free electrons in all ionised media (martian ionosphere, interplanetary medium, Earth ionosphere) along the downlink and can be used for calibration, inversion and correction of the classical Doppler shift. The spacecraft-Earth radio ray path will cross through the sensible

ionosphere quickly (in minutes) before entering occultation. The variation in the Earth ionosphere and the interplanetary medium is assumed to be slow for time scales shorter than a minute, so the observed changes in radio carrier properties are assumed to be dominated by the martian ionosphere.

Earth occultations will occur in six 'seasons' in the expected 4 years (two martian years) of operation, with one occultation in each orbit or three to four occultations per day. The mission baseline calls for one ground station tracking pass per day, which would cover typically one occultation (two under favourable operational conditions). The duration of the occultation and the entry and exit position of the spacecraft in its orbit expressed in true anomaly are shown in Figs. 4a/4b and Fig. 5, respectively. The occultation entry and exits will cover all planetary latitudes of the northern and southern hemispheres (Fig. 6).

2.2 Determination of the dielectric properties of the surface (bistatic radar)

The bistatic radar configuration (Fig. 7) is distinguished from the monostatic by spatial separation of the transmitter (on the spacecraft) and the receiver (in the ground station on Earth). It may be used to derive information about surface roughness and slope at scales of the incident wavelength (a few cm). Bistatic radar may also be used to determine properties of the surface material, such as dielectric constant, through differential reflection of orthogonal polarisations. The bistatic radar geometry of an orbiting spacecraft is well suited to probing the surface of planets at a variety of latitude, longitude and incidence angles. Bistatic radar experiments have been conducted at the Moon (e.g. Tyler & Howard, 1973; Nozette et al., 1996), Mars (Simpson & Tyler, 1981; Simpson et al., 1984) and Venus (Pettengill et al., 1997; Kolosov et al., 1979).

The objectives at Mars focus on the polar regions and caps, the volcanic regions and the famous 'Stealth' area south-west of Tharsis (Muhleman et al., 1991; Edgett et al., 1997). The bistatic geometry is well-suited to probing icy surfaces, which are poorly understood on Mars. The fact that the residual south polar cap on Mars has anomalously high backscatter when viewed from Earth, while the northern cap (presumably much more massive) does not stand out, is a continuing mystery. The Stealth region is anomalous in the sense that it yields very weak backscatter when probed from Earth. In both cases, the unique geometry of a bistatic experiment promises a better understanding of both the scattering processes and the underlying surface geology. Selected targets in other areas, such as volcanic plains, will also be studied. Despite similar appearances in orbital images, some plains do not necessarily have the same radar behaviour, again suggesting differences in the underlying surface geology.

For a typical bistatic radar experiment, the radio signal is transmitted from the spacecraft High Gain Antenna (HGA) towards the surface of Mars and is scattered from the surface. Optimising the performance of these bistatic radar experiments requires accurate prediction of the orbiter trajectory in order to formulate antenna pointing strategies as well as to predict signal parameters such as Doppler shift and signal amplitude. In a quasi-specular experiment, the antenna is programmed to follow the locus of points for which surface reflection would be specular if Mars were smooth. From the data recorded along these specular point paths, surface roughness can be inferred from Doppler dispersion of the echo signal; the dielectric constant ϵ of the surface material can be inferred from echo amplitude and/or polarisation properties. Dielectric properties of a lunar basin were obtained by measuring the Brewster angle $\tan^2\phi_B = \epsilon$ (Tyler, 1968b). Similarly, a more general Stokes parameter analysis led to detection of a tellurium-like material in the Venus highlands (Pettengill et al., 1996).

In a spotlight experiment, the antenna is programmed to track a fixed point on the surface, viewing it from a variety of angles. When the configuration passes through the backscatter geometry, coherent backscatter enhancements can be sought in the echo amplitude and polarisation (Hapke, 1990). Clementine spotlight data have been

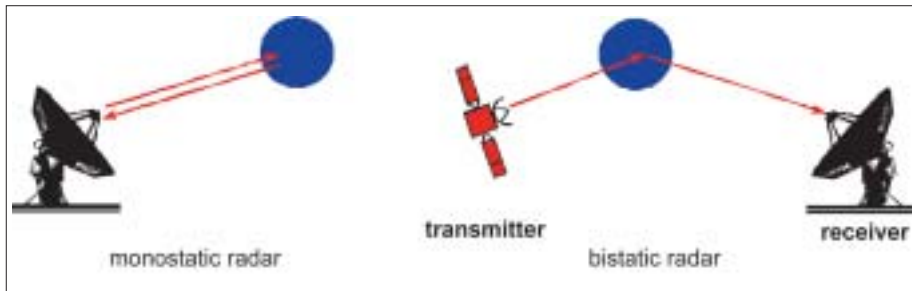


Fig. 7. Bistatic radar configuration is distinguished from the monostatic by the spatial separation of the transmitter (spacecraft) and the receiver (ground station on Earth).

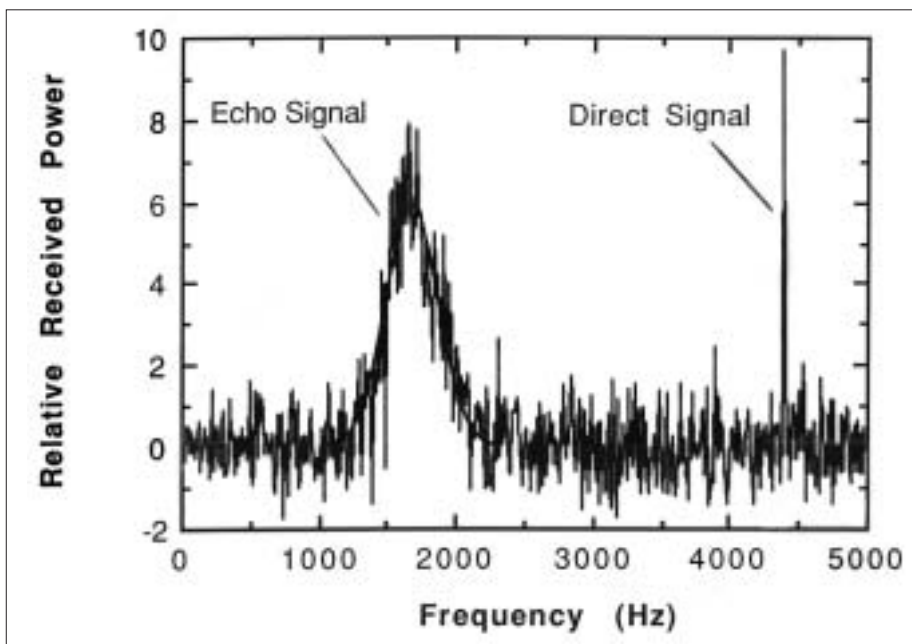


Fig. 8. Typical bistatic radar spectrum showing separation of the echo signal from the direct signal leaking out from the HGA side lobes toward the receiver. The broadening of the echo signal is caused by motion of the specular point over the surface and is related to surface roughness (from Simpson, 1993).

interpreted as suggesting the presence of water ice near the lunar south pole (Nozette et al., 1996; 2001), although that conclusion is not universally accepted (Simpson & Tyler, 1999). Strong backscatter enhancements are the salient features of backscatter from the icy Galilean moons of Jupiter (Eshleman, 1987) and have also been observed in the terrestrial environment of Greenland. Both the mechanism and its expected signature from real targets remain the subjects of active debate (Hagfors et al., 1985; Eshleman, 1987; Peters, 1992). Careful measurement of any observed enhancement magnitude and its angular variation are not available but would be useful.

The radio echo signal is received in the open-loop mode (see below) in two orthogonal polarisations (e.g. Left Circular Polarisation, LCP, and Right Circular Polarisation, RCP), down-converted, sampled and stored for further processing at the investigator's home institution. Fig. 8 shows a typical frequency spectrum of the received radio signal. The direct signal, leaking out from the side lobes of the HGA and reduced accordingly in power, is on the right. The echo signal is on the left and it is Doppler shifted relative to the direct signal according to the change in spacecraft-to-surface-to-Earth distance as a function of time. It is broadened according to the roughness of the surface and the motion of the specular point over the surface (Simpson, 1993).

It is required that the HGA points towards the martian surface. To ensure maximum signal-to-noise ratio in the echo signal received at Earth, the transmission of an unmodulated carrier at the highest feasible power level is also required. Transmission of linear (or elliptical) polarisation offers advantages in detecting differential quasi-

specular polarisation reflections from volcanic plains, while circular (or elliptical) polarisation is preferred for spotlight observations of ice deposits.

2.3 Geophysics: gravity anomalies

The gravity field of a planet is the result of its internal mass distribution and rotational state. Rapidly rotating planets bulge at the equator as a result of centrifugal forces. Consequently, the associated redistribution of mass to the equatorial plane results in a stronger gravitational acceleration of a spacecraft when it is near the pole than when it is at the same altitude located over the equator. Similarly, anomalies in the internal distribution of mass are expressed as departures of the external gravitational field from that of a uniform sphere or a stratified spherical distribution. Space probes in the vicinity of planetary bodies follow trajectories that deviate from the ideal orbits described by Kepler's two-body laws in response to these gravity anomalies.

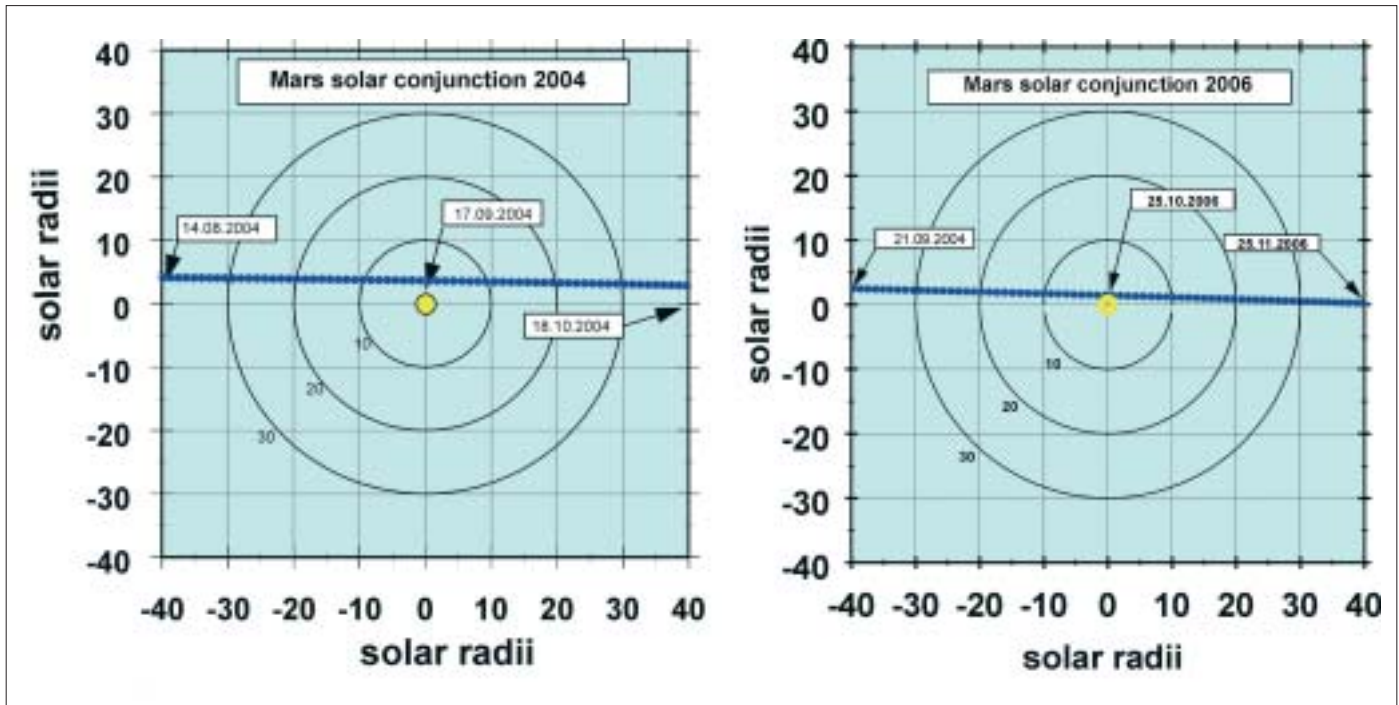
Precision two-way radio tracking provides an accurate measurement of spacecraft velocity along the line-of-sight to the tracking station, with variations attributed to gravitational acceleration owing to mass distribution in the planetary body. The utility of data for studying mass variations depends on the sensitivity of the radio system, the details of the geometry, and the characteristics of the overall spacecraft trajectory. The method is capable of detecting accelerations of the order of 10^{-3} Gal (1 Gal = 10^{-2} m s⁻²; Earth surface gravity is 982 Gal). Such data, through the connection between mass and gravitational force, are used to study planetary interiors. From low altitudes, even relatively minor variations in the mass density of surface and near-surface features are detectable. For example, a reduction in density of about 300 kg m⁻³ (or about a 10% change in the average martian crustal density) of a 50-km cube of rock near the surface is readily measurable.

Combining data from a large number of orbits from the Mariner, Viking and MGS missions has allowed construction of a complete gravity map, with resolution elements of about 2° on the martian surface. Large-scale variations in the strength of gravity correspond to the overall distribution of mass, mostly in the deep interior of Mars, and are relevant to the interpretation of the early history and evolution of the planet. Smaller scale variations, on lateral distances of a few thousand km or less, correspond to mass variations relatively close to the surface. Both large- and small-scale variations must be interpreted in light of the known overall shape of the planet and the variations in the surface elevation since, as in the examples above, topographic and mass density variations can play a similar role in the raw gravity data. Mars Express, as a result of its low periapsis altitude, can improve the present maps by a factor of about two in linear resolution in areas scanned by the evolution of the orbit.

Two gravity field models of degree and order 50 have been derived from radio tracking data of the Viking and Mariner-9 missions (Smith et al., 1993; Konopliv & Sjogren, 1995). The same teams collaborated on a derivation of a gravity field model of degree and order 60 and higher using the Mars Global Surveyor tracking data (Smith et al., 1999; Yuan et al., 2001).

The highly eccentric orbit of Mars Express is not best-suited for a global investigation of the gravity field. The investigation proposed here focuses on specific target areas for the determination of local gravity anomalies. Observations with the HRSC stereo camera will yield the high-resolution 3D topography of the target area. Three data sets (radio science, camera, radar) will be combined to study the state and evolution of the martian crust and lithosphere, with implications for studying the tectonic evolution of Mars.

The targets of investigations are the hot spot areas of Tharsis and Elysium, large single volcanoes, large impact craters and basins, and the highland-lowland boundary. The investigation of impact basins must be seen in the context of similar studies on other planetary bodies, including the Earth, in the sense of comparative planetology and studies of the impact mechanism, which is not fully understood (particularly for



large basins). Studies of the highland-lowland boundary will contribute to the open question of this dichotomy.

Topographic data provide digital terrain models (DTMs) which, in combination with the gravity data, are the basis for crustal density models. The measured line-of-sight free-air gravity anomaly at spacecraft altitudes amounts up to 70 mGal (Janle & Erkul, 1991). A complete density model consists of a topographic model (DTM) and a density model of the subsurface structures (e.g. undulations of the crust/mantle boundary, mantle plume). Variations in gravity of up to about 500 mGal are associated with topography and drive the need for precise and high-resolution topographic data. DTMs are also necessary for bending-stress models of the lithosphere, as demonstrated by Janle & Janssen (1986) for Olympus Mons.

Precise DTMs are required for the lithospheric load of bending-stress models, in particular for the correlation of the lineament distribution with the topography and calculated stresses. The combination of radar altimeter data and stereo images from HRSC will provide DTMs with vertical resolutions of 12-18 m and linear ground resolutions of 20-30 m, which are perfectly suited for bending stress models and geologic interpretations of the lineament distribution.

The expected accuracy of the Mars Express X/X-band two-way radio link is of the order $\ll 100 \text{ mm s}^{-1}$ at 10 s integration time. This translates into an accuracy of gravity accelerations of the order of several mGal, depending on the size and extension of the local topographic features (Tyler et al., 1992).

2.4 Radio sounding of the solar corona

Mars will move into superior conjunction with the Sun in the autumns of 2004 and 2006. Within about 10° elongation with respect to the solar disc in the plane of the sky (Fig. 9), the dispersive effects on the radio signals (propagation time, Doppler shift and Doppler noise) are dominated by the solar corona. It is therefore proposed that this valuable time be used for a thorough investigation of the solar corona to derive electron density profiles in the structured corona, solar wind speed, turbulence spectra in the source regions of fast and slow solar wind streams from coronal holes and streamers, respectively, and to detect, identify and describe the spatial and

Fig. 9. Superior solar conjunction geometry of Mars in the plane-of-sky. Each tick mark represents one day. Mars is within 40 solar radii (circles) from 14 August 2004 to 18 September 2004 (left panel), and from 21 September 2006 to 25 November 2006 (right panel). Within 12 solar radii, telemetry reception will be degraded. No telemetry can be expected within 4 solar radii. An adequate signal-to-noise radio carrier can be received at any time, however.

Fig. 10. The Mars Express radio subsystem. The transponder is redundant and each unit contains an S-band and X-band receiver and transmitter. X-band is amplified by TWTAs to an RF power output of 65 W. The RF distribution unit (RFDU) connects the receivers and transmitters with the antennas. It also contains the S-band amplifiers (5 W RF power output). The HGA receives uplink at either X-band or S-band and radiates simultaneously X-band and S-band downlink. The LGAs receive and transmit at S-band only.

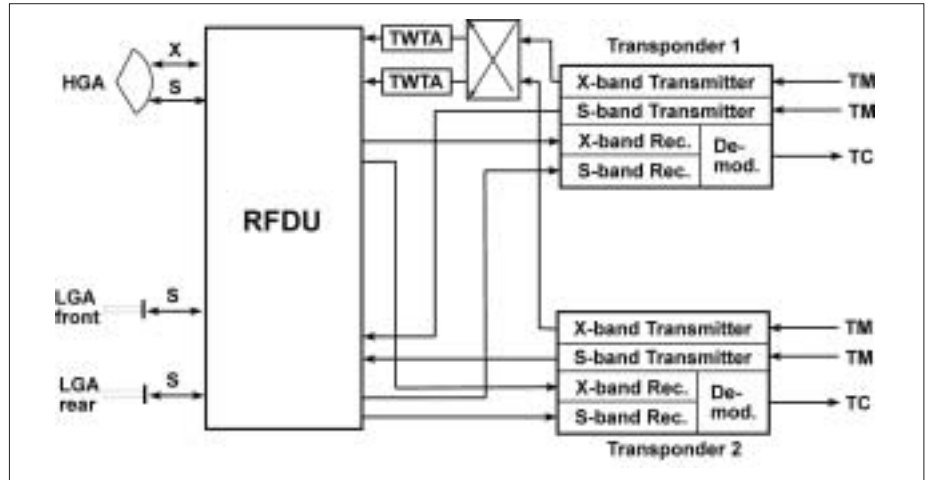


Fig. 11. Mars Express at the time of the release of the Beagle 2 lander descent capsule, showing the fixed HGA, a parabolic dish of 1.60 m diameter. (ESA)



temporal evolution of the shockfronts of coronal mass ejections (Bird et al., 1994; Pätzold et al., 1995; 1996; 1997; Karl et al., 1997). It is highly desirable to carry out these observations simultaneously with SOHO or other solar space observatories to enhance and compare the observations.

The technique of coronal sounding is well established and has been performed by members of the Mars Express team during the superior solar conjunctions of Ulysses (1991, 1995), Magellan (1992), Voyager and Viking (Bird et al., 1992; 1994; 1996; Pätzold et al., 1995; 1996; 1997; Tyler et al., 1977). For Mars Express, a two-way radio link and dual-frequency downlink at S-band and X-band allow separation of the coronal dispersive effects from the classical Doppler shifts. The two-way link is a powerful tool for the derivation of electron density models from observed electron content when propagation time delay, ranging data and dispersive Doppler shifts are compared (Pätzold et al., 1997). Furthermore, it provides the basis for the determination of solar wind speed by correlating uplink and downlink signals (Wohlmuth et al., 1997) and detection of fast outward-propagating density enhancement originating from solar events.

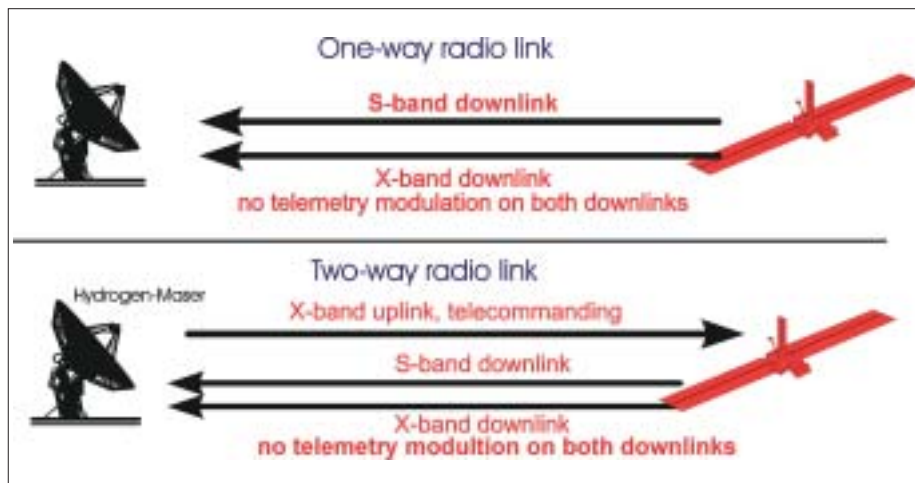


Fig. 12. Radio links between the Orbiter and the Earth station. Upper panel: one-way X-band and S-band downlink for bistatic radar. Lower panel: two-way radio link where the uplink is transponded phase-coherently with dual-frequency downlinks at X-band and S-band. Frequency stability is governed by a hydrogen maser at the ground station.

3.1 Mars Express radio subsystem

Mars Express can receive and transmit radio signals via either of two dedicated antenna systems:

- High Gain Antenna (HGA), a fixed parabolic dish of 1.60 m diameter, antenna gains 40 dBi and 28 dBi at X-band and S-band, respectively;
- two Low Gain Antennas (LGAs).

A block diagram of the characteristic features of the radio subsystem is shown in Fig. 10. Each of the two redundant transponders consist of an S-band and X-band receiver. The X-band transmitter output is amplified by a redundant 65 W Travelling Wave Tube Amplifier (TWTA) and the S-band downlink by a Solid State Amplifier of 5 W RF output. The spacecraft can receive and transmit at S-band (2.1 GHz) via the LGAs, or receive non-simultaneously at either X-band (7.1 GHz) or S-band via the HGA. The right-hand circular polarised downlink signals at S-band (2.3 GHz) and X-band (8.4 GHz) are transmitted via the HGA simultaneously (see an overview of frequencies in Table 1). The HGA (Fig. 11) is the primary antenna for receiving telecommands from and transmitting high rate telemetry in the operational phase. The LGAs are used during the commissioning phase and emergency operations.

MaRS uses two radio link modes (Fig. 12). The coherent two-way radio link is established by transmitting an uplink radio signal either at S-band or X-band to the spacecraft. A received S-band uplink carrier frequency is transponded to downlinks at S-band and X-band upon multiplication by the constant transponder ratios 240/221 and 880/221, respectively, in order to guarantee a ratio of the two downlinks of $880/240 = 11/3$. A received X-band uplink is multiplied by 880/749 and 240/749 to arrive at X-band and S-band downlink frequencies, respectively. Here again, the ratio of both frequencies is $880/240 = 11/3$. The two-way radio mode takes advantage of the superior frequency stability inherent to the hydrogen maser oscillator at the ground station on Earth. This mode is used for sounding the atmosphere and ionosphere, the gravity science applications and the sounding of the solar corona.

The one-way link mode is established by transmitting the X-band and S-band downlink simultaneously and phase coherently. It is used for the bistatic radar experiment.

3.2 Ground segment

Ground stations (Fig. 13) include antennas, associated equipment and operating systems in the tracking complexes of Perth, Australia (ESA, 35 m) and NASA's Deep Space Network (DSN, 34 m and 70 m) in California, Spain and Australia. A tracking

3. Technical Description

Table 1. Carrier frequencies.

	Uplink	Downlink	
S-band	2.1	2.3	GHz
X-band	7.1	8.4	GHz

Fig. 13. ESA and NASA ground station networks. The 15 m ESA antenna at Kourou will be used for the commissioning phase, while the new 35 m antenna near Perth will be the primary antenna. NASA will support specific mission phases and the radio science experiment with its Deep Space Network antennas at Goldstone (California), Canberra (Australia) and Madrid (Spain).

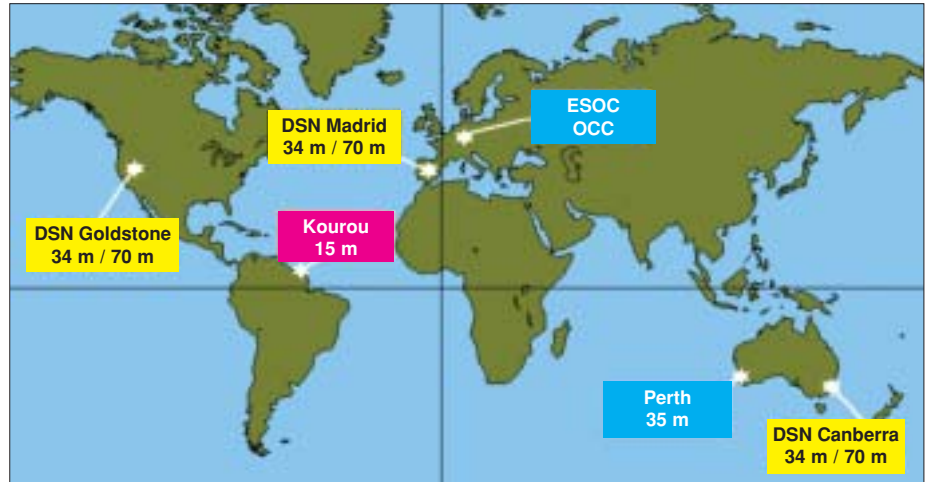


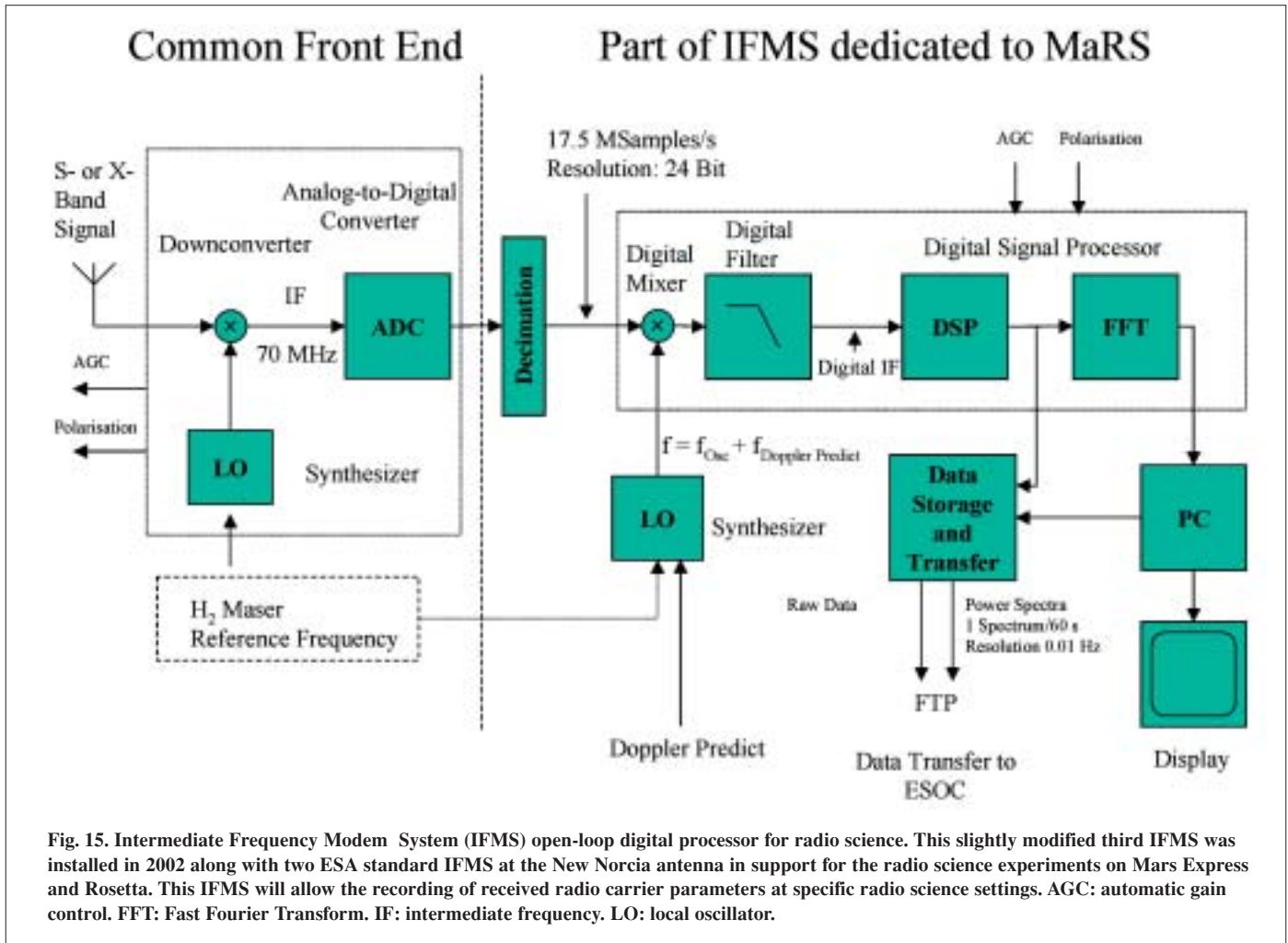
Fig. 14. ESA's new 35 m antenna at New Norcia, Australia.



pass consists of typically 8-10 h of spacecraft visibility and communication at the respective ground station site. Measurements of the spacecraft range and carrier Doppler shift can be obtained whenever the spacecraft is visible and its HGA is pointed towards Earth. The baseline calls for one communication pass at the ESA ground station per day, summarising approximately 1700 tracking passes for radio science (630 gravity passes, 750 occultations, 120 corona soundings, 200 bistatic radar observations). The use of the DSN antennas in California and Spain are under discussion and would usefully increase the number of tracking passes and experiment performance.

In the two-way mode, the ground station transmits an uplink radio signal at either S-band or at X-band and receives the dual-frequency downlink at X-band and S-band. Information about signal amplitude, received frequency and polarisation is extracted and stored as a function of ground receive time.

ESA's new 35 m ground station at New Norcia, Australia, about 200 km north of the older tracking complex in Perth, became operational in summer 2002 (Fig. 14). Its first deep space test with Ulysses was planned for September 2002. The station equipment consist of three identical new receiving systems designated as the Intermediate Frequency and Modem System (IFMS; Fig. 15). One is dedicated for radio science open-loop data recording of the Mars Express radio science



investigations and the Rosetta Radio Science Investigations experiment (Pätzold et al., 2000). This open-loop system will be used specifically for the radio sounding of the atmosphere/ionosphere, bistatic radar and solar corona investigations where closed-loop tracking receivers would typically lose lock. The IFMS operates on a 17.5 Msp/s 24-bit complex baseband stream (containing 12-bit words each for the *I* and *Q* channels) and resulting from filtering and decimating the 280 Msp/s 8-bit stream output data from the Common Front End Analogue-to-Digital Converter. These channels are provided for both RCP and LCP polarisations. The radio science raw data can be directly transferred to a mass storage device and/or processed by a Fast Fourier routine.

The DSN stations (Fig. 16) also provide uplinks at S-band or X-band. Dedicated radio science equipment functionally similar to the IFMS is available at all DSN stations (Asmar & Renzetti, 1993).

Radio science measurements in the ground stations can be done simultaneously on a non-interference basis with the transmission and/or reception of telecommands. However, since the signal-to-noise ratio of the carrier signal is considerably reduced when transmitting telemetry, a non-modulated downlink radio carrier is required in that case.

3.3 Observed quantities

The two data types (closed- and open-loop) can be generated simultaneously

Fig. 16. NASA's 70 m (foreground) and 34 m (background) deep space antennas at the Goldstone complex in the Mojave desert. (NASA)



regardless of the radio link configuration (one- or two-way). The received carrier frequencies, the signal strengths (received total power) and the polarisation of the radio signals are monitored at the ground station. Ground-based radiometric data are recorded using closed-loop receivers:

- amplitude and phase (Doppler) measurements (two- and one-way modes);
- ranging measurements (two-way mode only);
- full polarisation measurements (primarily one-way mode).

3.3.1 Doppler shift

The transmission of dual-frequency phase-coherent downlinks at S-band and X-band with the constant ratio of 11/3 makes it feasible to separate the dispersive from the non-dispersive Doppler effects on the radio link.

The frequency of the radio carrier is shifted according to the relative radial velocity between the transmitter and the receiver (classical Doppler shift). Furthermore, a relative phase shift is experienced when the radio wave propagates through an ionised medium (ionosphere, interplanetary medium, solar corona). Excluding oscillator drifts and instabilities, the frequency shift for a one-way (spacecraft-to-Earth) radio link due to plasma is:

$$\Delta f = f - f_0 = -\frac{f_0}{c} \frac{ds}{dt} + \frac{40.31}{c} \frac{1}{f_0} \frac{d}{dt} \int_{s/c}^{Earth} N_e ds \quad (1)$$

where ds/dt is the rate of change of the distance between transmitter and receiver (relative velocity), c is the speed of light and f_0 is the carrier frequency. The integral of the electron density $N_e(s)$ along the propagation path ds of the radio wave from the spacecraft (s/c) to Earth is also called the columnar electron content, or column density.

The first term on the right hand side of (1) is the classical Doppler shift (linear in f_0) and the second term is the dispersive propagation effect of radio waves in ionised media, which is inversely proportional to f_0 . A larger classical Doppler shift is measured on the X-band, but the lower S-band frequency is more sensitive to dispersive frequency shifts. A change in relative velocity of 2 cm s^{-1} yields a classical Doppler frequency shift of 0.6 Hz at X-band. A dispersive frequency shift of 0.6 Hz at S-band is produced by a change in electron content by one hexem (10^{16} electrons m^{-2}) within 1 s.

It is not possible to separate classical and dispersive frequency shifts from the observed total change in frequency Δf at either f_s or f_x , the S-band or X-band carrier frequency, respectively, alone. However, using Eq. 1 for the two phase-coherent downlinks at X-band and S-band with a constant transponder ratio of $880/240 = 11/3$ and calculating the differential Doppler

$$\Delta f_s - \frac{3}{11} \Delta f_x, \quad (2)$$

where Δf_s and Δf_x are the observed Doppler shifts at S-band and X-band, respectively. According to Eq. 1, it is possible to isolate the dispersive frequency shift:

$$\begin{aligned} \Delta f_s - \frac{3}{11} \Delta f_x &= -\frac{\frac{d}{dt} s}{c} f_s + \frac{40.31}{c} \frac{1}{f_s} \frac{d}{dt} \int_{s/c}^{Earth} N ds + \frac{3}{11} \frac{\frac{d}{dt} s}{c} f_x - \frac{3}{11} \frac{40.31}{c} \frac{1}{f_x} \frac{d}{dt} \int_{s/c}^{Earth} N ds \\ &= \frac{40.31}{c} f_s \left(\frac{1}{f_s^2} - \frac{1}{f_x^2} \right) \frac{d}{dt} \int_{s/c}^{Earth} N ds \end{aligned} \quad (3)$$

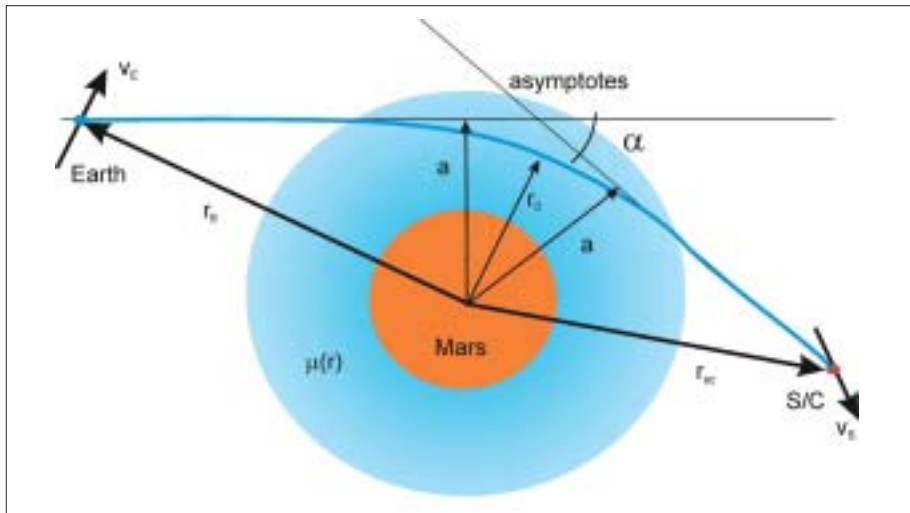


Fig. 17. Radio ray bending in a planetary atmosphere. Refractivity is represented as a function of radius. The bending can be described by the total bending angle α , and the distance of the ray asymptotes, a . In a spherically symmetric atmosphere, the radio path remains in a plane and bends about the centre of the system. The closest approach distance of the ray is r_{01} . The plane is defined by the geometry of the constellation (distance to Earth vector, velocity vector of Earth, distance vector to spacecraft, velocity vector of spacecraft with respect to Mars).

The ‘differential Doppler effect’ (Eq. 3), calculated from the observed frequency shifts, is used to determine the changes in electron content. All oscillator drifts and relative velocities are eliminated in this process. This result can further be used to correct each single classical frequency shift for the dispersive propagation effects.

The example above was derived for a one-way link. It can be shown that the calculation of the differential Doppler of a two-way radio link, when the spacecraft transmitted carrier frequencies are derived coherently from the received (and Doppler-shifted) uplink frequency, leads to exactly the same relation. In either case, Eq. 3 can be used to determine the electron content along the downlink path. Integration of Eq. 3 with respect to time yields the differential phase, which is proportional to changes in electron content along the downlink from the beginning of the tracking pass.

3.3.2 Ranging (propagation delay)

The absolute value of total electron content can be determined from the differential propagation delay by two-way ranging at S-band and X-band:

$$\tau_s - \tau_x = \frac{40.31}{c} \left(\frac{1}{f_s^2} - \frac{1}{f_x^2} \right) \int_{s/c}^{Earth} N ds \quad (4)$$

Typically, the Doppler or phase measurements are more sensitive than the ranging measurements by about two orders of magnitude (Bird, 1982).

3.3.3 Ray bending in atmospheres

Radio occultation studies of atmospheres can be understood in terms of ‘geometric’ or ‘ray’ optics refraction of signals travelling between spacecraft and ground stations. In a spatially varying medium where the wavelength is very short compared with the scale of variation in refractive index, the direction of propagation of an electromagnetic wave always curves in the direction of increasing refractivity. Consequently, in a spherically symmetric atmosphere with gas refractivity proportional to number density constantly decreasing with height, the radio path remains in a plane and bends about the centre of the system. The degree of bending depends on the strength of the refractivity gradient. This simple model approximates a real atmosphere and is useful for understanding the basic phenomena of radio occultation (Fjeldbo, 1964).

The geometry is illustrated in Fig. 17, where the atmosphere is represented by the

Table 2. Doppler velocity error σ_v (mm s⁻¹) for 1 s integration time.

	0.8 AU		2.5 AU	
	S-band	X-band	S-band	X-band
Thermal noise (ground station)	0.9	0.01	2.00	0.03
Transponder phase noise	0.42	0.26	0.42	0.26
Total error (two-way coherent mode)	0.99	0.26	2.04	0.26

refractivity as a function of radius from the centre, $\mu(r_0)$, and the bending can be described in terms of a total bending angle, α , and a ray asymptote, a . The variation of the bending angle, ray asymptote and refractivity are linked through an Abel transform (Fjeldbo & Eshleman, 1964),

$$\alpha(a) = -2a \int_{r=r_0}^{\infty} \frac{1}{\mu} \frac{\partial \mu}{\partial r} \frac{\partial r}{\sqrt{(\mu r)^2 - a^2}} \quad (5)$$

where $r_0 = \frac{a}{\mu(r_0)}$ is the ray periapse and,

$$\mu(r_{01}) = \exp \left\{ -\frac{1}{\pi} \int_{a=a_1}^{a=\infty} \ln \left\{ \frac{a}{a_1} + \sqrt{\left(\frac{a}{a_1}\right)^2 - 1} \right\} \frac{da}{da} da \right\} \quad (6)$$

with $r_0 = \frac{a}{\mu(r_{01})}$.

In this last expression, a_1 represents the asymptotic miss distance for a ray whose radius of closest approach is r_{01} . Thus, for spherical atmospheres, if $\alpha(a)$ is known, then the corresponding refractivity profile can be found exactly. For non-spherical geometry, alternative numerical solutions are available. The bending angle and the ray asymptote can be determined accurately by radio occultation to create an experimentally derived table of α versus a , or $\alpha(a)$.

In order to interpret the refractivity in terms of gas parameters, the pressure and temperature are calculated assuming hydrostatic equilibrium, for example, from

$$p(h) = \langle m \rangle \int_h^{\infty} g(h) N(h) dh \quad (7)$$

and

$$T(h) = \frac{p(h)}{k_B N(h)} \quad (8)$$

where $p(h)$ and $T(h)$ are the pressure and temperature as a function of height h , respectively, g is the acceleration of gravity, k_B is Boltzmann's constant, $\langle m \rangle$ is the mean molecular mass, and $N(h)$ is the molecular number density. Formal use of these equations requires *a priori* knowledge of the atmospheric composition.

3.4 Error budget

The major noise sources contributing to the Doppler velocity error are the thermal noise of the radio receiver on the ground for one-way observations, and both on the ground and aboard the spacecraft for two-way observations. The velocity error σ_v contributed by the ground station is given by

$$\sigma_v = \frac{c}{4\pi f \Delta t} \sqrt{\frac{2BN_0}{C}} \quad (9)$$

and the transponder phase noise σ_ϕ by

$$\sigma_v = \frac{c \sqrt{2}}{4\pi f t} \sigma_\phi \quad (10)$$

where B is the receiver bandwidth, C and N_0 are the received carrier power and the noise power density, respectively. The transponder phase noise σ_ϕ was experimentally determined by Remus et al. (2001) with a transponder electrical qualification model on ground. The total velocity error σ_v is calculated in Table 2 for an integration time Δt of 1 s at S-band and X-band.

Typical integration times for practical observations are in the range 1-10 s, thus yielding 0.26-0.03 mm s⁻¹ Doppler error, respectively, at X-band for 0.8 AU, large solar elongation angles and quiet solar wind conditions. The sensitivity in the electron content from differential Doppler measurements (Eq. 2) at 1 s integration time is computed to be in the order of 0.02 hexem s⁻¹.

References

- Acuna, M.H., Connerney, J.E.P., Wasilewski, P., Lin, R.P., Anderson, K.A., Carlson, C.W., McFadden, J., Curtis, D.W., Mitchell, D., Reme, H., Mazelle, C., Sauvaud, J.A., D'Uston, C., Cros, A., Medale, J.L., Bauer, S.J., Cloutier, P., Mayhew, M., Winterhalter, D. & Ness, N.F. (1998). Magnetic Field and Plasma Observations at Mars: Initial Results of the Mars Global Surveyor Mission. *Science* **279**, 1676-1680.
- Anderson, J.D., Colombo, G., Esposito, P.B., Lau, E.L. & Trager, G.B. (1987). The Mass, Gravity Field, and Ephemeris of Mercury. *Icarus* **71**, 337-349.
- Anderson, J.D., Armstrong, J.W., Campbell, J.K., Eastabrook, F.B., Krisher, T.P. & Lau, E.L. (1992). Gravitation and Celestial Mechanics Investigations with Galileo. *Space Sci. Rev.* **60**, 591-610.
- Anderson, J.D., Lau, E.L., Sjogren, W.L., Schubert, G. & Moore, W.B. (1997). Europa's Differentiated Internal Structure: Inferences from Two Galileo Encounters. *Science* **176**, 1236-1239.
- Asmar, S.W. & Renzetti, N.A. (1993). The Deep Space Network as an Instrument for Radio Science Research. *JPL Publication 80-93, Rev. 1*.
- Barth, C.A., Stewart, A.I.F., Bougher, S.W., Hunten, D.M., Bauer, S.J. & Nagy, A.F. (1992). Aeronomy of the Current Martian Atmosphere. In *Mars* (Eds. H.H. Kieffer, B.M. Jakosky, C.W. Snyder, M.S. Matthews), University of Arizona Press, Tucson, USA, pp1054-1089.
- Bird, M.K. (1982). Coronal Investigations with Occulted Spacecraft Signals. *Space Sci. Rev.* **33**, 99-126.
- Bird, M., Asmar, S.W., Brenkle, J.P., Edenhofer, P., Paetzold, M. & Volland, H. (1992). The Coronal Sounding Experiment. *Astron. Astrophys. Suppl. Ser.* **92**, 425-430.
- Bird, M.K., Volland, H., Pätzold, M., Edenhofer, P., Asmar, S.W. & Brenkle, J.P.

- (1994). The Coronal Electron Density Distribution Determined from Dual-Frequency Ranging Measurements during the 1991 Solar Conjunction of the Ulysses Spacecraft. *Astrophys. J.* **426**, 373-381.
- Bird, M.K., Allison, M., Asmar, S.W., Atkinson, D.H., Edenhofer, P., Heyl, M., Iess, L., Plettemeier, D., Tyler, G.L. & Wohlmuth, R. (1995). The Huygens Doppler Wind Experiment. In *Huygens: Science, Payload and Mission* (Ed. A. Wilson), ESA SP-1177, European Space Agency, pp139-162.
- Bird, M.K., Paetzold, M., Edenhofer, P., Asmar, S.W. & McElrath, T.P. (1996). Coronal Radio Sounding with Ulysses: Solar Wind Electron Density near 0.1 AU during the 1995 Conjunction. *Astron. Astrophys.* **316**, 437-448.
- Edgett, K.S., Butler, B.J., Zimbelman, J.R. & Hamilton, V.E. (1997). Geologic Context of the Mars Radar 'Stealth' Region in Southwestern Tharsis. *J. Geophys. Res.* **102**, 21545-21567.
- Eshleman, V.R., Tyler, G.L., Anderson, J.D., Fjeldbo, G., Levy, G.S., Wood, G.E. & Croft, T.A. (1977). Radio Science Investigations with Voyager. *Space Sci. Rev.* **21**(2), 207-232.
- Eshleman, V.R. (1973). The Radio Occultation Method for the Study of Planetary Atmospheres. *Planet. Space Sci.* **21**, 1521-1531.
- Eshleman, V.R. (1987). The Radar-Glory Theory for Icy Moons with Implications for Radar Mapping. *Adv. Space Res.* **7**, 133-136.
- Fjeldbo, G. (1964). Bistatic Radar Methods for Studying Planetary Ionospheres and Surfaces. Stanford Electronics Laboratory, Stanford University, SU-SEL-64-025.
- Fjeldbo, G. & Eshleman, V.R. (1968). The Atmosphere of Mars Analyzed by Integral Inversion of the Mariner IV Occultation Data. *Planet. Space Sci.* **16**, 1035-1059.
- Gresh, D.L., Marouf, E.A., Tyler, G.L., Rosen, P.A. & Simpson, R.A. (1989). Voyager Radio Occultation by Uranus' Rings. *Icarus* **78**, 131-168.
- Hagfors, T., Gold, T. & Ierkic, H.M. (1985). Refraction Scattering as Origin of the Anomalous Radar Returns of Jupiter's Satellites. *Nature* **315**, 637-640.
- Hapke, B. (1990). Coherent Backscattering and the Radar Characteristics of the Outer Planet Satellites. *Icarus* **88**, 407-417.
- Hinson, D.P., Simpson, R.A., Twicken, J.D., Tyler, G.L. & Flasar, F.M. (1999). Initial Results from Radio Occultation Measurements with Mars Global Surveyor. *J. Geophys. Res.* **104** (E11), 29997-27012.
- Hinson, D.P., Tyler, G.L., Hollingworth, J.L. & Wilson, R.J. (2001). Radio Occultation Measurements of Forced Atmospheric Waves on Mars. *J. Geophys. Res.* **106** (E1), 1463-1480.
- Howard, H.T., Eshleman, V.R., Hinson, D.P., Kliore, A.J., Lindal, G.F., Woo, R., Bird, M.K., Volland, H., Edenhofer, P., Pätzold, M. & Porsche, H. (1992). Galileo Radio Science Investigations. *Space Sci. Rev.* **60**, 565-590.
- Janle, P. & Erkul, E. (1991). Gravity Studies of the Tharsis Area on Mars. *Earth, Moon & Plan.* **53**, 217-232.
- Janle, P. & Janssen, D. (1986). Isostatic Gravity and Elastic Bending Models of Olympus Mons, Mars. *Ann. Geophysicae* **4**, B, 537-546.
- Karayel, E.T. & Hinson, D.P. (1997). Sub-Fresnel-scale Vertical Resolution in Atmospheric Profiles from Radio Occultation. *Radio Sci.* **32**, 411-423.
- Karl, J., Pätzold, M. & Bird, M.K. (1997). Coronal Radio Sounding: Non-Gaussian Turbulence in the Source Regions of the Solar Wind. *Geophys. Res. Lett.* **24**, 2881-2884.
- Kliore, A.J. (1992). Radio Occultation Observations of the Ionospheres of Mars and Venus. In *Venus and Mars: Atmospheres, Ionospheres, and Solar Wind Interaction* (Eds. J.G. Luhmann, M. Tatrallyay & R.O. Pepin), *Geophys. Monograph* **66**, 265-276.
- Kliore, A.J. & Luhmann, J.G. (1991). Solar Cycle Effects on the Structure of the Electron Density Profiles in the Dayside Ionosphere of Venus. *J. Geophys. Res.* **96**, 21281-21289.
- Kliore, A.K., Cain, D.L., Levy, G.S., Eshleman, V.R., Fjeldbo, G. & Drake, F.D.

- (1965). Occultation Experiment: Results of the First Direct Measurement of Mars' Atmosphere and Ionosphere. *Science* **149**, 1243-1248.
- Kliore, A.J., Anderson, J.D., Armstrong, J.W., Asmar, S.W., Hamilton, C.L., Rappaport, N.J., Walquist, H.D., Ambrosini, R., Bertotti, B., Flasar, F.M., French, R.G., Iess, L., Marouf, E.A. & Nagy, A.F. (2002). Cassini Radio Science. *Space Sci. Rev.*, in Press.
- Kolosov, M.A., Yakovlev, O.I., Efimov, A.I., Pavelyev, A.G. & Matyugov, S.S. (1979). Radio Occultation of the Venusian Atmosphere and Bistatic Radar Location of the Surface of Venus using the Venera-9 and Venera-10 Satellites. *Radio Sci.* **14**, 163-173.
- Konopliv, A.S. & Sjogren, W.L. (1995). The JPL Mars Gravity Field, Mars50c, Based upon Viking and Mariner 9 Doppler Tracking Data. *JPL Publication* **95-5**.
- Marouf, E.A., Tyler, G.L. & Rosen, P.A. (1986). Profiling Saturn's Rings by Radio Occultation. *Icarus* **68**, 120-166.
- Muhleman, D.O., Butler, B.J., Grossman, A.W. & Slade, M.A. (1991). Radar Images of Mars. *Science* **253**, 1508-1513.
- Nozette, S., Lichtenberg, C.L., Spudis, P., Bonner, R., Ort, W., Malaret, E., Robinson, M. & Shoemaker, E. (1996). The Clementine Bistatic Radar Experiment. *Science* **274**, 1495-1498.
- Nozette, S. (2001). Spudis, P.D., Robinson, M.S., Bussey, D.B.J., Lichtenberg, C. & Bonner, R. Integration of Lunar Polar Remote-Sensing Data Sets: Evidence for Ice at the Lunar South Pole. *J. Geophys. Res.* **106** (E10), 23253-23266.
- Pätzold, M., Bird, M.K., Volland, H., Edenhofer, P. & Buschert, H. (1991a). Dynamics of the Giotto Spacecraft in the Inner Dust Coma of Comet P/Halley; Part 1: Observations. *Z. Flugwiss. Weltraumforsch* **15**, 89-96.
- Pätzold, M., Bird, M.K., Volland, H., Edenhofer, P. & Buschert, H. (1991b). Dynamics of the Giotto Spacecraft in the Inner Dust Coma of Comet P/Halley; Part 2: Interpretations. *Z. Flugwiss. Weltraumforsch* **15**, 159-164.
- Pätzold, M., Bird, M.K. & Edenhofer, P. (1993). The Change of Giotto's Dynamical State during the P/Grigg-Skjellerup Flyby Caused by Dust Particle Impacts. *J. Geophys. Res.* **98**, A12, 20911-20920.
- Pätzold, M., Bird, M.K., Edenhofer, P., Asmar, S.W. & McElrath, T.P. (1995). Dual-frequency Radio Sounding of the Solar Corona during the 1995 Conjunction of the Ulysses Spacecraft. *Geophys. Res. Lett.* **22**, 3313-3316.
- Pätzold, M., Karl, J. & Bird, M.K. (1996). Coronal Sounding with Ulysses: Phase Scintillation Spectra in Coronal Holes and Streamers. *Astron. Astrophys.* **316**, 449-456.
- Pätzold, M., Tsurutani, B.T. & Bird, M.K., (1997). An Estimate of Large-scale Solar Wind Density and Velocity Profiles in a Coronal Hole and the Coronal Streamer Belt. *J. Geophys. Res.* **102**, 24151-24160.
- Pätzold, M., Neubauer, F.M., Wennmacher, A., Aksnes, K., Anderson, J.D., Asmar, S.W., Tinto, M., Tsurutani, B.T., Yeomans, D.K., Barriot, J.-P., Bird, M.K., Boehnhardt, H., Gill, E., Montenbruck, O., Grun, E., Hausler, B., Ip, W.H., Thomas, N., Marouf, E.A., Rickman, H., Wallis, M.K. & Wickramasinghe, N.C. (2000). Rosetta Radio Science Investigations (RSI). *Research Notes #4*, Institut für Geophysik und Meteorologie, Universität zu Köln.
- Pätzold, M., Wennmacher, A., Häusler, B., Eidel, W., Morley, T., Thomas, N. & Anderson, J.D. (2001). Mass and Density Determinations of 140 Siwa and 4979 Otawara during the Rosetta Flybys. *Astron. Astrophys.* **370**, 1122-1127.
- Peters, K.J. (1992). The Coherent Backscatter Effect: a Vector Formulation Accounting for Polarization and Absorption Effects and Small or Large Scatterers. *Physical Review B* **46**, 801-812.
- Pettengill, G.H., Ford, P.G. & Simpson, R.A. (1996). Electrical Properties of the Venus Surface from Bistatic Radar Observations. *Science* **272**, 1628-1631.
- Pettengill, G.H., Campbell, B.A., Campbell, D.B. & Simpson, R.A. (1997). Surface Scattering and Dielectric Properties. In *Venus II* (Eds. S.W. Bougher, D.M. Hunten & R.J. Phillips), Tucson, University of Arizona Press, USA, p527.

- Remus, S., Häusler, B., Pätzold, M. & Wennmacher, A. (2001). Ergebnisse der Radio Science Testmessungen an den ESA Satelliten Rosetta und Mars Express. Deutscher Luft- und Raumfahrtkongress, 17-20 September 2001, DGLR-2001-022.
- Simpson, R.A. & Tyler, G.L. (1981). Viking Bistatic Radar Experiment: Summary of First-order Results Emphasizing North Polar Data. *Icarus* **46**, 361-389.
- Simpson, R.A., Tyler, G.L. & Schaber, G.G. (1984). Viking Bistatic Radar Experiment: Summary of Results in Near-equatorial Regions. *J. Geophys. Res.* **89**, 10385-10404.
- Simpson, R.A. (1993). Spacecraft Studies of Planetary Surfaces using Bistatic Radar. *IEEE Transactions on Geoscience and Remote Sensing* **31**, 465-482.
- Simpson, R.A. & Tyler, G.L. (1999). Reanalysis of Clementine Bistatic Radar from the Lunar South Pole. *J. Geophys. Res.* **104**, 3845-3862.
- Smith, D.E., Lerch, F.J., Nerem, R.S., Zuber, M.T., Patel, G.B., Fricke, S.K. & Lemoine, F.G. (1993). An Improved Gravity Model for Mars: Goddard Mars Model 1. *J. Geophys. Res.* **98**, 20871-20889.
- Smith, D.E., Sjogren, W.L., Tyler, G.L., Balmino, G., Lemoine, F.G. & Konopliv, A.S. (1999). The Gravity Field of Mars: Results from Mars Global Surveyor. *Science* **286**, 94-97.
- Standish, E.M. (1993). Planet X – No Dynamical Evidence in the Optical Observations. *Astron. J.* **105**(5), 2000-2006.
- Tyler, G.L. (1968a). Oblique-scattering Radar Reflectivity of the Lunar Surface: Preliminary Results from Explorer 35. *J. Geophys. Res.* **73**, 7609-7620.
- Tyler, G.L. (1968b). Brewster Angle of the Lunar Crust. *Nature* **219**, 1243-1244.
- Tyler, G.L. (1987). Radio Propagation Experiments in the Outer Solar System with Voyager. *Proc. IEEE* **75**, No.10, 1404-1431.
- Tyler, G.L. & Howard, H.T. (1973). Dual-frequency Bistatic Radar Investigations of the Moon with Apollos 14 and 15. *J. Geophys. Res.* **78**, 4852-4874.
- Tyler, G.L., Balmino, G., Hinson, D.P., Sjogren, W.L., Smith, D.E., Simpson, R.A., Asmar, S.W., Priest, P. & Twicken, J.D. (2001). Radio Science Observations with Mars Global Surveyor: Orbit Insertion through one Mars year in Mapping Orbit. *J. Geophys. Res.* **106**, E10, 23327-23348.
- Tyler, G.L., Balmino, G., Hinson, D.P., Sjogren, W.L., Smith, D.E., Woo, R., Asmar, S.W., Conally, M.J., Hamilton, C.L. & Simpson, R.A. (1992). Radio Science Investigations with Mars Observer. *J. Geophys. Res.* **97**, 7759-7779.
- Tyler, G.L., Brenkle, J.P., Komarek, T.A. & Zygielbaum, A.I. (1977). The Viking Solar Corona Experiment. *J. Geophys. Res.* **82**, 4335-4340.
- Tyler, G.L., Eshleman, V.R., Fjeldbo, G., Howard, H.T. & Peterson, A.M. (1967). Bistatic-radar Detection of Lunar Scattering Centers with Lunar Orbiter I. *Science* **157**, No. 3785, 193-195.
- Tyler, G.L., Eshleman, V.R., Hinson, D.P., Marouf, E.A., Simpson, R.A., Sweetnam, D.N., Anderson, J.D., Campbell, J.K., Levy, G.S. & Lindal, G.F. (1989). Voyager Radio Science Observations of Neptune and Triton. *Science* **246**, 1466-1473.
- Tyler, G.L., Ford, P.G., Campbell, D.B., Elachi, C., Pettengill, G.H. & Simpson, R.A. (1991). Magellan – Electrical and Physical Properties of Venus' Surface. *Science* **252**, 265-270.
- Wohlmuth, R., Plettemeier, D., Edenhofer, P., Bird, M.K., Pätzold, M. & Asmar, S.W. (1997). Measurement of the Propagation Speed of Plasma Inhomogeneities in the Solar Corona using an Uplink/Downlink Cross-correlation Method. *Radio Sci.* **32**, 617-628.
- Yakovlev, O.I. & Efimov, A.I. (1966). Studies of Reflection of Meter-length Radio Waves. *Dokladi Akademii Nauk SSSR* **174**, 583-584.
- Yeomans, D.K., Antreasian, P.G., Barriot, J.-P., Chesley, S.R., Dunham, D.W., Farquhar, R.W., Giorgini, J.D., Helfrich, C.E., Konopliv, A.S., McAdams, J.V., Miller, J.K., Owen, W.M., Scheeres, D.J., Thomas, P.C., Veverka, J. & Williams, B.G. (2000). Radio Science Results during the NEAR-Shoemaker Spacecraft Rendezvous with Eros. *Science* **289**, 2085-2088.

- Yeomans, D.K., Barriot, J.-P., Dunham, D.W., Farquhar, R.W., Giorgini, J.D., Helfrich, C.E., Konopliv, A.S., McAdams, J.V., Miller, J.K., Owen, W., Jr., Scheeres, D.J., Synnott, S.P. & Williams, B.G. (1997). Estimating the Mass of Asteroid 253 Mathilde from Tracking Data during the NEAR Flyby. *Science* **278**, 2106-2109.
- Yuan, D.-N., Sjogren, W.L., Konopliv, A.S. & Kucinskas, A.B. (2001). Gravity Field of Mars: A 75th Degree and Order Model. *J. Geophys. Res.* **106**, E10, 23377-23402.

Acknowledgements

The Mars Express Orbiter Radio Science (MaRS) experiment is funded by the Deutsches Zentrum für Luft- und Raumfahrt (DLR), Bonn, Germany, and the National Aeronautics and Space Administration (NASA), Washington DC, USA.

Beagle 2: the Exobiological Lander of Mars Express

D. Pullan^{1,4}, M.R. Sims^{1,4}, I.P. Wright^{2,4}, C.T. Pillinger^{2,4} & R. Trautner^{3,4}

¹*Space Research Centre, Department of Physics and Astronomy, University of Leicester, Leicester, UK*
Email: dpu@star.le.ac.uk

²*Planetary and Space Sciences Research Institute, Open University, Walton Hall, Milton Keynes, UK*

³*Research & Scientific Support Department, European Space Agency, ESTEC, Noordwijk, The Netherlands*
⁴*on behalf of the Beagle 2 project*

In late 2003, the Beagle 2 lander component of the Mars Express mission is planned to touch down in the Isidis Planitia region of Mars (265.0°W, 11.6°N). Once safely deployed on the surface, Beagle 2 will conduct an intensive and exhaustive programme of surface operations for about 180 sols (equivalent to about 6 months on Earth). The principal objective is the detection of extinct and/or extant life, or at least to establish if the conditions at the landing site were ever suitable for life to have evolved in the planet's history. To achieve this goal, a systematic set of experiments using a complementary suite of instruments will perform *in situ* geochemical, mineralogical and petrological analysis of selected rocks and soils. Studies of the martian environment will also be conducted via chemical analysis of the atmosphere, local geomorphological assessment of the landing site and measurement/monitoring of dynamic environmental processes, including transient events such as 'dust devils'. Further studies, unique to Beagle 2, include analysis of the subsurface regime using a ground penetration tool and the first attempt at *in situ* isotopic dating of rocks on another planet.

The complete experiment package weighs less than 9 kg and requires less than 40 W of power. With a probe mass limit of 69 kg, imposed by mission constraints, and a landed mass of 33 kg, Beagle 2 thus aims to fly the highest mass ratio of payload-to-support systems of any mission to Mars. This is achievable only by adopting an integrated design approach and employing minimal or zero redundancy.

Beagle 2 is named to honour the ship used in the epic voyage of Charles Darwin and Robert FitzRoy during 1831-1836, which led to publication of Darwin's *On the Origin of Species*. Nearly a century and a half after the publication of the first edition of this volume, Beagle 2 aims to discover whether the theory of evolution extends to a second planet in the Solar System. Darwin's more famous biological works means that the contributions made by him to geology (and those of FitzRoy to meteorology) are often forgotten. Beagle 2, like its predecessor, addresses a wide range of subjects: the life question, of course, but also the geochemical and mineralogical characterisation of the immediate landing site and the chemistry of the atmosphere. To fulfil these goals, Beagle 2 has the following remit:

- geological investigation of the local terrain and rocks, especially their light-element chemistry, composition, mineralogy, petrology and age;
- investigation of the oxidation state of the martian surface within rocks, soils and at protected locations beneath boulders;
- full characterisation of the atmospheric composition to establish the history of the

1. Introduction

- planet and the processes involved in seasonal climatic changes and diurnal cycling;
- search for key criteria deemed to demonstrate that life processes could have operated in the past;
 - determination of trace atmospheric gases, indicative of extant life at some location.

The above list, in many respects, exceeds what has been achieved by previous missions. It goes far beyond the goals stated for other Mars landers under consideration and transcends the Science Definition Team's ambitions for Mars Express itself. Rock dating, atmospheric characterisation, climatic change monitoring and the search for possible biologically-derived trace constituents are all among the most important aspects of the study of Mars, and are envisaged as firsts that could be achieved by Beagle 2. Presumably none of these was thought to be possible or within the scope of small landers, as envisaged at the conception of the Mars Express project.

In its original form, Beagle 2 was conceived as a 'large' (108 kg) lander that carried additional instruments to enable it to act as the third node in a geophysical network. Following the imposition of more stringent mass constraints (60 kg only available for a landing craft), a network of several stations was no longer feasible. As a result, the additional elements of the Beagle 2 payload became redundant and were therefore deleted. Likewise, the earlier version of Beagle 2 had provision for a small rover to transport sampling devices some distance from the lander, but the discovery that the subsurface sampler (the 'Mole') had inherent lateral mobility also allowed that element to be discarded. It is encouraging to note that, throughout the challenging period from proposal to delivery, the scientific goals (reflected in the payload) remained intact. This has been achievable only through the skill and dedication of the Beagle 2 team of engineers and scientists.

1.1 Background

In 1976, two Viking spacecraft landed on Mars with the prime objective of searching for evidence of life on a second planet in the Solar System. Results from a package of biological activity experiments and a pyrolysis gas chromatograph-mass spectrometer (GC-MS) were interpreted, by majority verdict rather than unanimous consent, as negative. The one positive result that suggested operation of a martian metabolism was subsequently interpreted as a chemical artefact. The intervention of an oxidative surface chemistry on the planet rather conveniently explained the inability of the GC-MS to observe any organic matter above the detection levels, in spite of some theories that predict the presence of meteorite debris, and hence carbon compounds, even in a sterile environment.

Although the findings were disappointing, Viking provided the first close-up images of the martian surface, major element chemical analyses of soil samples and meteorological information, a feat duplicated at considerably less cost and with simpler technology 20 years later by Pathfinder. An unexpected bonus of Viking was that an exploratory compositional and isotopic study of the atmosphere enabled a link to be made with a previously poorly understood group of meteorites: the Shergotty, Nakhla and Chassigny association or SNCs (Bogard & Johnson, 1983; Becker & Pepin, 1984; Carr et al., 1985). The number of SNC-class finds has now grown to more than 20 specimens; their genetic relationship has been confirmed by exceedingly precise oxygen isotopic measurements: $\delta^{17}\text{O}$, $\delta^{18}\text{O}$, where $\delta^{17}\text{O} = [({}^{17}\text{O}/{}^{16}\text{O})_{\text{sample}}/({}^{17}\text{O}/{}^{16}\text{O})_{\text{standard}} - 1] \times 1000$, per mil, or ‰; and so on for other δ values. In detail on a plot of $\delta^{17}\text{O}$ versus $\delta^{18}\text{O}$, the so-called 'cap-', 'cap-delta-', or 'big-delta-' ${}^{17}\text{O}$ value ($\Delta^{17}\text{O} = \delta^{17}\text{O} - 0.52 \times \delta^{18}\text{O}$) for martian meteorites is $0.321 \pm 0.013\text{‰}$ (Franchi et al., 1999). The presence in some of the meteorites of six atmospheric species having the same abundance ratios and isotopic systematics (e.g. high $\delta^{15}\text{N}$) as values measured in the martian atmosphere, points indubitably to Mars as a

provenance (Pepin, 1985). The young geological age (1.3 Ga to 180 Ma) of all but one (4.5 Ga) of the SNC meteorites (Wood & Ashwal, 1981; McSween, 1985; 1994) provides circumstantial evidence of their being from a body sufficiently large (planetary-sized) to show recent volcanic activity. Although some scepticism remains, there is almost universal belief that SNCs are martian. Data from SNC research, in conjunction with Viking and Pathfinder results, guided the scientific goals of Beagle 2, which are harmonised rather than being a series of uncoordinated efforts from a group of disparate investigators.

Although all the SNC samples are igneous in origin, Nakhla, EET A79001 and ALH 84001 show good evidence of low-temperature hydrothermal alteration, producing carbonate and other mineral deposits (Carr et al., 1985; Gooding et al., 1988; Wright et al., 1988; Mittlefehldt, 1994). These discoveries have proved highly beneficial to the study of the martian environment and to understanding the chronological sequence of events. For 75 years, however, petrologists failed to recognise the presence of carbonate in these igneous meteorites. In 1985 geochemical analyses (Carr et al., 1985) uncovered the existence of carbonates, a vital facet of martian meteorite research. Eventually, Gooding et al. (1991) demonstrated unequivocally the presence of inclusions microscopically. For a while it was argued that carbonate in martian meteorites must be a terrestrial artefact, but $\delta^{13}\text{C}$ measurements strongly suggest otherwise (Carr et al., 1985; Wright et al., 1988). Interpretations based on the ^{14}C content of carbonates in EET A79001, that such minerals were terrestrial (Jull et al., 1992), may be erroneous owing to experimental problems (Wright et al., 1997a).

Notwithstanding the above, carbonates in ALH 84001 are isotopically distinct from all similar species on Earth, and have $\delta^{13}\text{C}$ values consistent with those expected for the martian atmosphere. Debates concerning their origin have now switched to the interpretation of models used for calculating carbonate formation conditions (Wright et al., 1992). Techniques that rely on major-element abundance, measured by electron microprobe in selected areas, invoke a high-temperature (600°C) formation event (Harvey & McSween, 1996). Bulk oxygen isotope and, to some extent, carbon studies of carbonates by chemical dissolution require a scenario involving liquid water and temperatures in the range 0-80°C (Romanek et al., 1994). Other studies, at high spatial resolution, indicate a mixture of origins at a variety of temperatures, for different generations of carbonate, none of which exceeds 250°C (Valley et al., 1997; Leshin et al., 1998; Saxton et al., 1998).

The origin of the carbonates in SNC meteorites is of vital importance because they are accompanied by organic matter (Wright et al., 1989). Also identified within the mineral, at least in some samples, are features that are interpreted to be nm-sized fossils (McKay et al., 1996). Thus it has been suggested that biological processes have been acting on Mars. A view that all the organics are a result of contaminants derived from percolating Antarctic melt waters (McDonald & Bada, 1995; Bada et al., 1998) can be refuted on a number of grounds. For example, oxygen isotope and D/H results (Wright et al., 1997b) would have been disturbed by inundation; as these remain recognisably different from Earth values, they must be very little affected by terrestrial water exchange. Although each of the martian meteorites contains some Earth-generated contamination, specimens where the organic matter is in excess of 1000 ppm, e.g. EET A79001 (Wright et al., 1989), are considered to host some pre-terrestrial martian carbonaceous material.

Whether the existence of nanofossils or indigenous organic matter in martian meteorites is genuine or not, the inescapable fact remains that conditions conducive to life prevailed on Mars in the past. Furthermore, in the years since Viking, investigations into the viability of terrestrial organisms have demonstrated their adaptability and tenacity. It has been shown that they can thrive and multiply in acid, alkaline and highly saline conditions, apparently unaffected by pressure, capable of living at temperatures ranging from -12°C to 113°C, with the simplest and most ancient forms being the most tolerant (ESA Exobiology Team, 1999). How long

organisms may lie dormant and survive at even greater extremes, particularly at the low-temperature end of the scale, is unknown. Microorganisms have been shown to inhabit Antarctic dry valleys, the nearest equivalent on Earth to martian conditions. It follows that the decision to conclude that Mars is totally hostile to life, on the basis of the very preliminary results from Viking, was premature.

According to theories proposed after Viking, a problem that must be considered with respect to carbonaceous matter is its survival on the surface. The planet's regolith is highly oxidised, a property believed to arise from hydrogen peroxide in the atmosphere. Models exist relating to this question (Bullock et al., 1994; Stoker & Bullock, 1997; Zent & McKay, 1994). One suggests penetration of the oxidant to less than a few metres in soil, the other assumes a vast turnover so that all material down to 150 m is oxidised. The martian rocks examined by the Alpha Proton X-ray Spectrometer (APXS) on Pathfinder's Sojourner rover showed evidence for a weathering rind (Rieder et al., 1997) but the depth of this layer was not ascertained, and the oxidation state was not recorded. One way to address this issue would be through an *in situ* investigation that determines the concentrations of certain components (especially oxidation-sensitive organic compounds) with depth in the regolith.

Unfortunately, SNC meteorites, being of deep-seated mafic origin, are not able to elucidate directly the problem of oxidation within the regolith. However, we note here that martian soils are sulphur-rich, possibly due to volcanic exhalations, and that SNC meteorites contain sulphides and sulphates (Burgess et al., 1989) and even nitrates (Grady et al., 1995). Furthermore, from geochemical data it appears that SNCs and the Viking and Pathfinder soils are related, possibly two-component mixing, with one end-member being SNC-like and the other being andesitic.

It should be borne in mind that all the rocks investigated by Pathfinder were igneous and of the same petrological type, with the exception of one 'rock' that was possibly a soil clod. This was disappointing because it was thought that the Pathfinder landing site (a washout area) would be a good place to find rocks of sedimentary origin. Perhaps Pathfinder was unlucky; future missions should continue to search for rock types from sedimentary formations. Note that the Pathfinder APXS attempted to measure carbon abundance, and hence recognise carbonates (widely thought to be present at, or near, the martian surface) but none was found. The problem with this approach is that atmospheric CO₂ intervenes between the uneven rock surfaces and the detector, resulting in a major background signal. Furthermore, although some close-up images of rocks were taken by the camera on Sojourner (Smith et al., 1997), these were obscured by dust, which also affected the APXS data. As yet, no microscopic imaging studies have ever been made on Mars.

Although regions on the martian surface have been assigned relative ages derived from crater counts, the only absolute dates available for martian rocks come from SNC meteorites, and, of course, *their* exact provenance on Mars is unknown. In this respect, it should be noted that the APXS made measurements that revealed the average potassium content of the 'soil-free rock' to be $0.7 \pm 0.1\%$; the age of such a rock could have been estimated from a knowledge of the ⁴⁰Ar content had the noble gas abundance been measured.

While the abundance and isotopic compositions of martian atmospheric constituents have been used to such good effect in identifying martian meteorites, these values, particularly the isotopic ratios, are not well constrained. The data quoted for ¹⁴N/¹⁵N (165, $\delta^{15}\text{N} = +650\%$) and ¹²C/¹³C (88, $\delta^{13}\text{C} = +11\%$) were for a limited number of measurements, which were made using an instrument that was never envisaged as a dedicated isotope mass spectrometer or, indeed, calibrated in this respect. In consequence, there is a $\pm 50\%$ to $\pm 100\%$ (i.e. $\pm 5\%$ to $\pm 10\%$) error attached to the figures. Neither the ill-fated Mars Polar Lander (including the Deep Space 2 microprobes) nor the Mars Surveyor mission carried a mass spectrometer that could have provided more precise data. A totally independent assessment of the full isotopic composition of carbon dioxide on Mars, both its carbon and oxygen, is still required

employing instrumentation designed for that purpose. The same applies to the crucial measurements of $\delta^{15}\text{N}$ and $\delta\Delta$.

The noble gas isotope ratios of martian atmospheric constituents are even less well defined than those for carbon and nitrogen. A key value for argon, the third most abundant constituent in the atmosphere of Mars, is $4 \leq {}^{36}\text{Ar}/{}^{38}\text{Ar} \leq 7$, described by some authors as matching the terrestrial value, which happens to be 5.3, conveniently around the mean of the Viking measurements. Quite unaccountably, SNC meteorites have a ${}^{36}\text{Ar}/{}^{38}\text{Ar}$ of 4.1 ± 0.2 (Wiens et al., 1986), a value distinct from all other meteorites and hence a possible diagnostic indicator of a martian provenance. Other intriguing noble gas results from Viking and the meteorite clan concern ${}^{40}\text{Ar}/{}^{36}\text{Ar}$ (3000 ± 500 , c.f. Earth 296) and ${}^{129}\text{Xe}/{}^{132}\text{Xe}$ (2.5 ± 2 , c.f. Earth 0.97). Both ratios imply a much greater abundance of radiogenic elements (${}^{40}\text{K}$ and ${}^{129}\text{I}$, respectively) in the martian surface than Earth, or that an early martian atmosphere was lost and replenished from crustal outgassing.

Water is another intriguing trace constituent (volume mixing ratio 3.0×10^{-4} mol.) in the martian atmosphere. No D/H ratios were measured by Viking, but some have been afforded by astronomical observations at infrared wavelengths from ground and airborne telescopes, and the ratio is believed to be about 5.0 ± 0.2 times the terrestrial value of 1.6×10^{-4} . The quoted error, if applied to the Earth, would suggest all terrestrial D/H ratios were the same, which is not true; D/H on Earth varies in a predictable way and reveals much about the hydrological cycle. Measurement of the equivalent parameter on Mars has the potential to provide information on equivalent planet-wide phenomena, including seasonal climatic effects, and addresses the issue of Mars' warmer and wetter past.

Looking in greater detail at the effects of fluids on Mars, the oxygen isotopic composition of water released from the hydrated silicates of martian meteorites (Karlsson et al., 1992; Baker et al., 1998) do not fall on the Mars line defined by high-temperature minerals. The results predict that water in the martian atmosphere is not in equilibrium with the surface of the planet and has been, or is being, isotopically affected by photolytic or exospheric loss processes. Clearly this needs to be studied further by future space missions.

Quite apart from the major and minor constituents of the martian atmosphere (CO_2 , N_2 , Ar, O_2 , CO, H_2O , Ne, Kr and Xe in abundance order) there are also likely to be important trace constituents. So far, only upper limits can be placed on these (Owen, 1992; Owen et al., 1997). It is vital that the minor and trace species on Mars are measured. The abundance and, where possible, isotopic information for trace atmosphere gases could be the best possible indicators of contemporary biological activity on the planet. The equilibrium composition of Earth's atmosphere, for example, is dictated by the delicate balance of biological production on the ground and chemical destruction above it. Sampling Earth's atmosphere anywhere on the planet will lead to the detection of species that could not be there but for biology. The same would probably be true for Mars if life exists; even a remote subterranean lifeform might be recognised from the identification of a gaseous by-product of its metabolism, i.e. a species out of chemical equilibrium. The best chance in this respect would appear to be methane: it is produced on Earth by a great variety of primitive organisms, is chemically short-lived, being destroyed by photolytic oxidation but stable to gas-solid degradation reactions, and detectable at high sensitivities. Since biological processes tend to impart large isotopic fractionations during methane production from its precursors, this parameter may be useful in the preliminary hunt for extant life on Mars.

1.2 The Beagle 2 investigation

The main focus of the Beagle 2 scientific payload is to establish whether there is convincing evidence for past life on Mars or to assess if the conditions were ever suitable. Beagle 2 also plans a globally responsive test to see if there is any present-day biological activity on Mars.

Fig. 1. A fully deployed model of the Beagle 2 lander showing the arrangement of solar arrays (four petals plus the lid). The base unit (diameter ~66 cm) accommodates GAP and the lander systems, including batteries and transceiver. The PAW is shown deployed and making contact with a sample under investigation. *All Rights Reserved, Beagle 2*



In 1996/97, ESA's Directorate of Manned Spaceflight and Microgravity commissioned a study into the search for life in the Solar System. The final report (ESA Exobiology Team, 1999) concluded that, despite Viking results, Mars represented the best immediate opportunity for searching for life beyond the Earth. The presence, or recognition, of any, or all, of the following were considered to be important indicators of biology:

- water;
- appropriate inorganic minerals (e.g. carbonates);
- carbonaceous debris;
- organic matter of complex structure;
- chirality;
- isotopic fractionation between reservoirs (e.g. organics and carbonate).

No other Mars mission yet plans such a comprehensive and complete investigation. Furthermore, martian sample-return missions, once the preserve of NASA, but increasingly seen as likely to be driven by a European-led effort, are unlikely to yield results before 2015. However, none of the above tests provides an unambiguous answer alone. It is therefore the key objective of Beagle 2 to perform a programme of experiments using compatible and synergistic instrumentation capable of addressing five of the above six indicators.

At the centre of the Beagle 2 scientific payload is a miniaturised chemical laboratory, the Gas Analysis Package (GAP), designed to make quantitative and stable isotopic measurements of gases such as H₂, N₂, O₂ and CO₂. GAP includes a 6 cm-radius magnetic sector mass spectrometer, which can be operated in either static or dynamic modes, and the supporting equipment to analyse atmospheric, rock and soil samples from the surface of Mars. The system can process and determine some of the noble gases (Ne, Ar and Xe; including some isotopic measurements) as well as anticipated trace constituents such as CH₄. The search for chirality was omitted from the Beagle 2 programme on the grounds that the most interesting molecules require the complex step of derivatisation; it would seem prudent to confirm their existence before including the necessary processing steps that would complicate the instrumentation.

To assist in the primary mission objective and provide essential context, the Beagle 2 payload incorporates a set of deployable *in situ* instrumentation. The payload therefore incorporates an arrangement of imaging devices, field spectrometers, sampling tools and environmental sensors in order to characterise fully the landing site in terms of geology and environment. By definition, this array of diverse yet complementary instrumentation provides a degree of scientific redundancy to a mission with minimal or zero engineering redundancy. Furthermore, even if the main exobiological objective of the mission proves inconclusive or the negative results of Viking are confirmed, a wealth of novel science will be conducted with the Beagle 2 payload.

The individual experiments on Beagle 2 are described in detail in later sections; here, the payload is considered in a general sense. The lander configuration is shown in Fig. 1; its mass breakdown is given in Table 1. Together, the GAP and the lander service systems (electronics, batteries, transceiver etc) occupy two-thirds of the lander base. The *in situ* instruments and sampling tools are located on the Position Adjustable Workbench (PAW), effectively the ‘hand’ at the end of a robotic manipulator that unstows when the lander is unfolded on the surface. During transit to Mars, these items occupy the remaining recessed third of the lander base. Finally, the majority of environmental sensors are strategically located about the lander.

Other novel elements of the *in situ* payload include a ‘torch’: a cluster of LEDs for white-light illumination of surface materials to determine the true colour of the martian surface; and a ‘spoon’: a simple soil acquisition-device to act as a backup for the Mole.

As with any lander-based mission, the camera system on Beagle 2 plays a crucial role in both the engineering and the science. Shortly after the lander is deployed on the surface, a panoramic view of the site will be provided by one of the cameras with the aid of the Wide Angle Mirror (WAM), a device attached to the PAW. This will allow the mission planners to unstow the PAW safely subsequently and avoid any obstacles that may be present. The complete scientific investigation of the landing site with the stereo cameras using the spectral filters will be accumulated systematically over the primary mission period because of the data volumes involved, communications constraints and other experiment requirements. However, an early priority for the cameras is to image the area within reach of the PAW and allow a Digital Elevation Model (DEM) of the surface to be constructed. Such a model is vital for planning the *in situ* analysis and sampling activities of candidate rocks and soils. In addition to assessing their morphologies and spatial distribution, rocks within reach of the PAW and the sampling Mole will be imaged through various filters to determine their composition remotely. A set of candidate sites for detailed

Table 1. Beagle 2 mass budget (kg).

<i>Scientific Payload</i>	
GAP and local electronics	5.74
PAW	2.75
BEEST	0.250
ESS	0.156
<i>Subtotal</i>	<i>8.896</i>
<i>Lander Engineering</i>	
Structure (base and lid)	11.972
including main hinge, etc	
Solar panels including hinges	3.21
ARM	2.11
Transceiver	0.65
Battery	2.63
Electronics and memory	3.02
Miscellaneous (cabling, bracketry, MLI etc)	0.692
<i>Subtotal</i>	<i>24.284</i>
<i>Lander total (landed mass)</i>	<i>33.18</i>
<i>Probe Engineering</i>	
Structure (heatshield and back cover)	17.81
Parachutes	3.26
Airbags and gas generator	14.59
<i>Subtotal</i>	<i>35.66</i>
<i>Probe total</i>	<i>68.84</i>

investigation will be selected based on the remote-sensing data and engineering parameters. The cameras also play an important role in understanding the absorption properties of the atmosphere, in particular with respect to dust and water vapour.

Close-up imaging of rocks and soils will be done initially using one of the stereo cameras, configured to emulate a hand-lens by selecting the appropriate 'secondary optic' filter. Observations at higher magnification are achieved by the self-illuminating microscope, which requires contact to be made with the surface to establish a fixed stand-off distance. Both activities will provide important data on the texture of the rock/soil and nature of the particulates on the surface of the sample under investigation. Any remnant microstructures, if present (and visible) and not destroyed by erosion or the sample preparation process, should be resolvable. The microscope will also provide spectral information on individual grains and identify any fluorescing minerals or materials.

The *in situ* spectrometers will analyse specified areas of each candidate rock or soil patch, previously imaged with the cameras, to determine elemental chemistry and iron mineralogy. A range of major and trace element abundances will be determined by the X-ray spectrometer (XRS) and the iron-bearing minerals in the sample will be identified by the Mössbauer spectrometer. Because the penetration depths of the analysing fluxes for both these techniques are low, the true chemical and mineralogical nature of the fresh material can be determined only by removing any weathering/alteration rind and adhering soil/dust veneers. Mechanical sample preparation is therefore necessary by the PAW Rock Corer Grinder tool. The other function of this tool is to acquire solid samples from rocks in the form of chippings for analysis by GAP.

There is much synergy between experiments in the payload. For example, GAP in conjunction with XRS will be the first to attempt to date rocks on the surface of another planet by radiometric means. To perform a crude radiometric age estimate requires a precise measurement of potassium content in a sample made by XRS and a precise measurement of argon made by GAP from the same sample. GAP will also attempt to derive an exposure age of the surface material by analysing neon isotopic compositions (^{20}Ne , ^{21}Ne , ^{22}Ne).

In the search for organics, the philosophy adopted by Beagle 2 is that unoxidised soil material is most likely to be either at depth, below the superoxidised horizon, or alternatively located under relatively large (~1 m) boulders, which may have lain undisturbed for aeons. The strategy for retrieving such specimens uses the Mole, the primary soil sampling tool deployed from the PAW. The device has the ability to propagate itself directly into the soil to depths up to 1.5 m or crawl across the surface and be diverted under boulders to acquire material from these protected regimes. Elemental chemical analysis performed by GAP (light elements) and XRS (major and trace elements), together with Mössbauer analysis, of such material will provide a route to testing the oxidation hypothesis and developing meaningful models of martian surface environmental conditions.

The quantity of organic matter in acquired samples, if present at all, could be small or highly cross-linked, approximating to elemental carbon (as in some of Earth's most ancient rocks) because of chemical processing. The search for organics will, therefore, be conducted by stepped combustion, a technique that distinguishes carbon species by the temperature at which they burn or degrade in oxygen. Similar experiments have been performed on Earth using many hundreds of meteorite samples and terrestrial rocks, all of which show some trace of organic matter either indigenous to the specimen or from terrestrial biogenic sources. This sort of contamination, which causes difficulties for some research on Earth, could be invaluable on Mars. The stepped combustion method when applied to martian soils and rocks will confirm whether there are any indigenous forms of carbon with the appropriate combustion temperatures for them to be organic. Combustion, of course, converts all carbon entities into CO_2 , each with 100% efficiency, unlike pyrolysis which represents only a partial conversion of some components.

The stepped combustion technique that converts organic carbon to CO_2 also allows the measurement of the isotopic composition. Indigenous organic matter on Mars might have a diagnostic $\delta^{13}\text{C}$; indeed, the $\delta^{13}\text{C}$ values of organic matter in martian meteorites hint that it might be slightly different from that on Earth, but all experiments are confused by terrestrial contamination. If bulk organic matter and carbonates are found adjacent in rocks on Mars, then measurement of the isotopic difference between them will be essential. On Earth, at least, a 30‰ fractionation between inorganic and organic carbon is the most general signature of biosynthesis and has been observed in 10 000 examples all the way back in history, from present day until 3.8 Ga (Schidlowski, 1997); only biology is able to impose such an effect. Such is the ubiquity of terrestrial biology that there is no such thing on Earth as a rock without organic material. Even rocks carefully collected on the Moon, protected and preserved on Earth, show that Earth's biological activity is impossible to exclude. Rocks collected and returned to Earth from Mars would almost certainly be susceptible to such effects. Therefore it is imperative that stepped combustion, with attendant isotopic measurements, be performed *in situ* on Mars to establish a true positive or negative for the presence of organic matter.

Unlike organic matter, carbonates should be totally immune from degradation by oxidants. Given that soils are the weathering products of rocks, thoroughly mixed by aeolian processes, then fine particles represent the best route to locating martian carbonates and measuring their geochemical parameters, e.g. isotopic compositions. GAP is able to measure the abundance of carbonate in soil and rocks at levels well beyond the capability of spectrometric methods.

Since the separation schemes needed for studying the constituents of rocks are the same as those needed for the characterisation of the martian atmosphere, the gas analysis package on Beagle 2 is admirably suited for direct analysis of the major martian atmosphere component CO_2 and for minor constituents, particularly CO , H_2O , N_2 , the noble gases and minute amounts of hydrocarbons. Beagle 2 could thus be expected to provide a detailed and comprehensive study of the constitution of the atmosphere with precise isotopic data for major, minor and trace components. It would follow some constituents during diurnal cycling and as a function of the mission duration to investigate daily and longer-term climatic processes on Mars.

In respect of methods for separating trace components, procedures to extract and purify methane, originally developed to provide isotopic information about the sources of this harmful greenhouse component in Earth's atmosphere, are included as part of GAP. A confident detection of methane on Mars, a species that would be out of chemical equilibrium, would have enormous repercussions for deciding if there is still an active biology on the planet.

The payload (Fig. 2) on Beagle 2 can be divided into three categories:

- the Gas Analysis Package occupies about 33% of the lander base section and requires samples, including atmospheric gases, to be delivered via an inlet system. GAP is the primary science experiment on Beagle 2; its lead institute is the Open University;
- a collection of *in situ* investigation instruments and tools located on the PAW, an integrated structure attached to the end of the Anthropomorphic Robotic Manipulator (ARM). The tools are used to prepare the surfaces of samples for study by the *in situ* instruments and to extract cores from these samples for analysis by GAP. The Mole ground penetration tool is deployed from the PAW. The lead institute for the PAW is the University of Leicester; individual instruments are supplied by various institutions (see later);
- a suite of sensors for dynamically monitoring the martian environment. These are located both on the PAW and about the lander. The lead institute for the environmental sensors is the Open University.

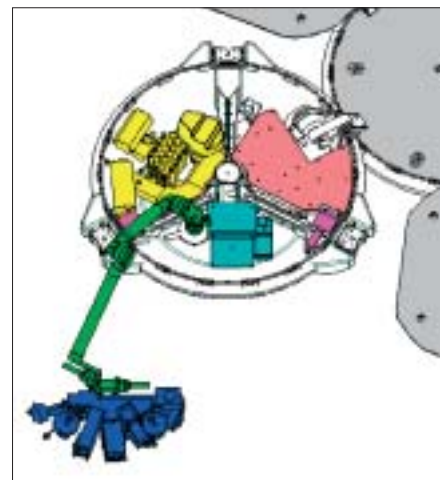


Fig. 2. Location of key elements of the Beagle 2 lander. Thermal insulating foam is removed for clarity. The GAP (yellow) and lander support systems (pink) occupy complete 120° sectors of the base. The PAW (dark blue) houses all the *in situ* instrumentation and is manoeuvred by the ARM (green). Some instruments on the PAW have associated electronics housed in the lander base (light blue). A few environmental sensors are also visible (purple).
All Rights Reserved, Beagle 2

2. The Beagle 2 Scientific Payload

2.1 Gas Analysis Package

GAP (Fig. 3) has three modes of operation: quantitative analysis, qualitative analysis and precise isotopic measurement. Instrument modes will be decided according to the type of investigation required. There will be three main types of study:

- search for organic matter;
- stepped combustion for total light element content and speciation;
- atmospheric analysis.

In all cases of isotope ratio measurements, the principles of GAP are derived from MODULUS (Methods of Determining and Understanding Light elements from Unequivocal Stable isotopic compositions), a concept developed for the Rosetta mission (Wright & Pillinger, 1998a) and expanded to include Mars (Wright & Pillinger, 1998b). Specific chemical reactions appropriate to martian species, e.g. CO₂, CO, H₂O have been worked out to afford full C, O and H isotopic characterisation without the necessity of having to resolve isobaric interferences. This philosophy incorporates real-time calibration of the instrument using a variety of reference gases, e.g. a reference CO₂ used during ¹³C/¹²C measurements, etc. In consequence, stable isotope ratio measurements will be quoted to high precision relative to internationally accepted standards.

GAP is fed either by direct atmospheric sampling, or via one of 12 ovens mounted on a carousel. Material acquired by the sampling tools, in the form of soil or rock chippings, is deposited via an inlet system into one of the ovens, which is then rotated to a tapping station to connect the oven to GAP. The ovens withstand temperatures up to 1000°C, although in practice 700°C will be adequate for most analyses. Only the sample container will be heated. This consists of a platinum liner heated by a Pt-Rh filament directly wound on to the container. Electrical insulation between the liner and the filament is secured by a thin layer of aluminium oxide deposited on the outer surface. Thermal losses in the oven are reduced by means of an internal radiation shield, and conductive heat losses are cut down by using ceramic support structures with low heat conductivity.

GAP is designed to make quantitative and stable isotopic measurements of gases such as H₂, N₂, O₂ and CO₂. The system can also process and determine some of the noble gases (Ne, Ar and Xe) as well as anticipated trace constituents such as CH₄. It operates in one of two ways, either analysing gases directly (such as those present in the atmosphere, or which can be liberated from samples by heating), or producing appropriate analyte gases (e.g. CO₂) by chemical processing (e.g. conversion of organic compounds to CO₂ by oxidation). In this way, GAP is tremendously flexible, being able to investigate processes of atmospheric evolution, circulation and cycling, the nature of gases trapped in rocks and soils, low-temperature geochemistry, fluid processes, organic chemistry, formation temperatures, surface exposure ages, assist in isotopic rock dating, etc.

At the heart of the GAP system is a 6 cm-radius magnetic sector mass spectrometer, which operates in both dynamic and static modes, i.e. continuously pumped and isolated, respectively. The mass spectrometer includes six ion beam detectors. The main unit is a triple-collector array for the determination of N₂ (*m/z* 28, 29, 30), O₂ (*m/z* 32, 33, 34), and CO₂ (*m/z* 44, 45, 46). A spur in the flight tube of the instrument includes a double-collector for measurement of D/H ratios (H₂⁺ and HD⁺ at *m/z* 2 and 3, respectively). A further detector mounted on the high-mass side of the triple-collector comprises a pulse-counting electron multiplier for measurements of trace gases. When operated dynamically, the mass spectrometer should be able to measure stable isotope ratios to high degrees of precision and accuracy (±0.1‰ when expressed as a δ-value). In contrast, static operation will allow high levels of sensitivity albeit with some reduction in precision of the isotopic measurements.

As an illustration of instrument performance, note that when Viking test equipment analysed two different Antarctic soils, each containing 300 ppm carbon, they were

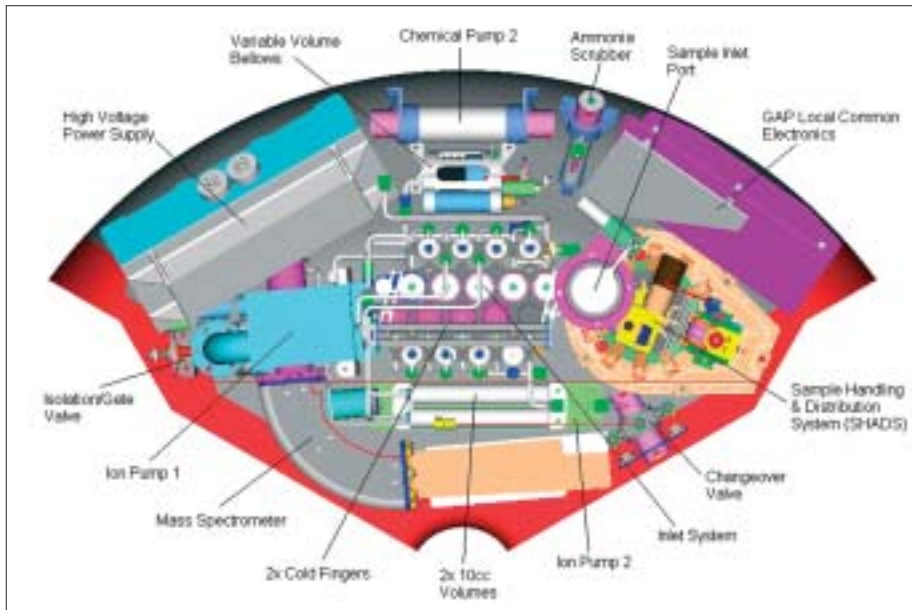
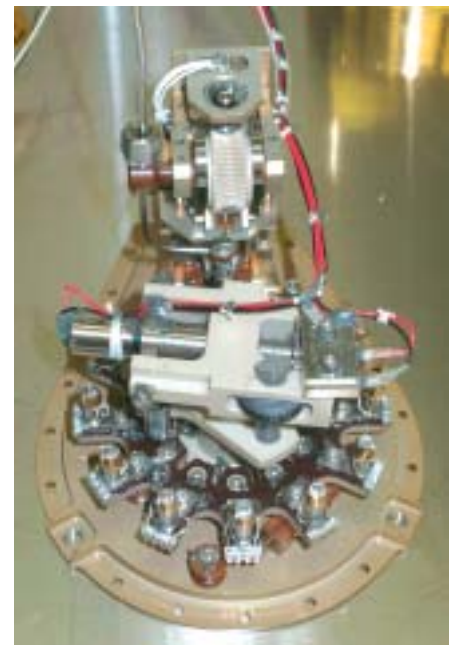


Fig. 3. The Gas Analysis Package, the primary experiment that occupies a complete 120° sector of the lander base. All the key components are annotated. Below left: the Flight Model GAP in transportation case before final sterilisation. Below right: the Sample Handling and Distribution System (SHADS), showing the carousel of ovens (lower part of assembly) and tapping station (to rear). *All Rights Reserved, Beagle 2*



determined to have about 5 ppm and 0.01 ppm C as organic carbon. This probably reflects the low yield of pyrolytic reactions from highly cross-linked carbonaceous materials. Had materials of equivalent character been analysed on Mars by Viking, the latter of these would not have yielded any carbon above background, even though a significant fraction of the 300 ppm total carbon may have been non-pyrolytically degradable organic matter. Laboratory analyses of carbon in SNC meteorites by a system similar to GAP is regularly used to measure carbon contents of 250 ppm, or less, from a few milligrams of sample. Thus GAP should provide meaningful data from samples where Viking would have detected nothing. The mass spectrometer on GAP has been designed to measure, quantitatively and isotopically, nanogram quantities of carbon in any form. For a 50-100 mg sample (the target for Beagle 2 operations on Mars), this translates to a detection limit for carbon of 0.02-0.01 ppm.

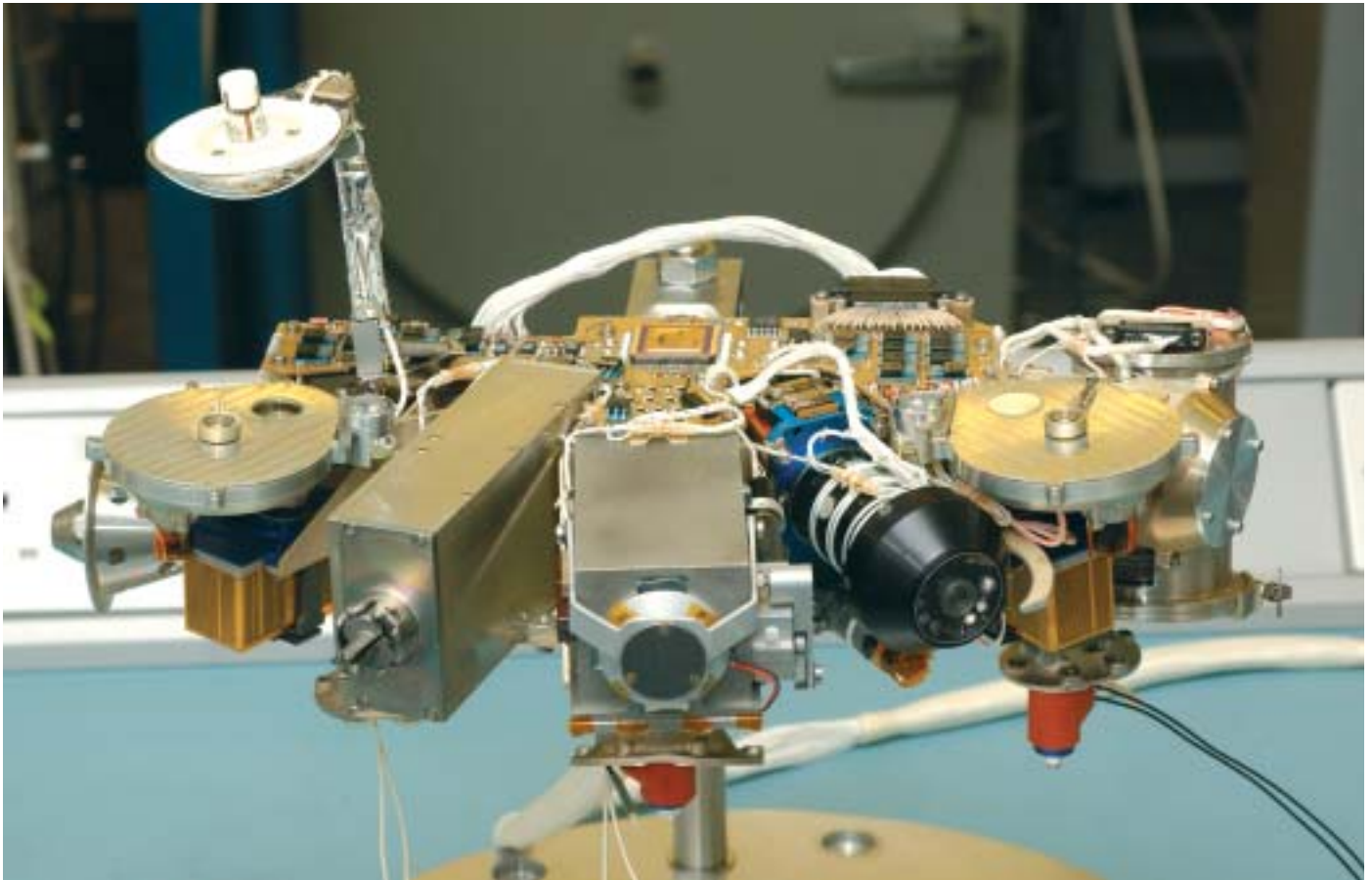


Fig. 4. The PAW FM, fully assembled and ready for sterilisation, November 2002. Two of the three Frangibolt actuators are visible under the mounting feet.

All Rights Reserved, Beagle 2

This represents a very significant advance on previous *in situ* investigations of Mars, and opens up the possibility of a serious reappraisal of the presence of organic materials on the planet.

2.2 PAW subsystem

The PAW (Figs. 4 & 5) is a highly optimised and compact integrated suite of scientific instruments, sample acquisition and preparation tools, deployed by the ARM for *in situ* investigation of the surface. All the lander imaging systems and field spectrometers are housed on the PAW and rely on the versatility of the ARM for essential categorisation of the landing site. In addition, GAP, as Beagle 2's primary scientific experiment, relies on the PAW-ARM to deliver solid samples for isotopic analysis.

The majority of instruments and tools on the PAW are serviced by the PAW electronics. Complex ARM harnessing between the PAW instruments and the lander support systems is kept to a minimum by the inclusion of an FPGA within the PAW electronics. The fully equipped PAW is 38 cm at its widest point and has a mass of only 2.75 kg.

During cruise and coast to Mars, the PAW-ARM is stowed within a recess in the lander base. The PAW is attached to the ARM via a right-angle bracket and is held down to the lander base by three feet that secure the system during launch and other extreme environmental conditions. The baseline release mechanism is to have one Frangibolt actuator per foot; these are operated prior to initial deployment of the PAW and the beginning of surface operations. Once deployed, the PAW does not return to the stowed configuration.

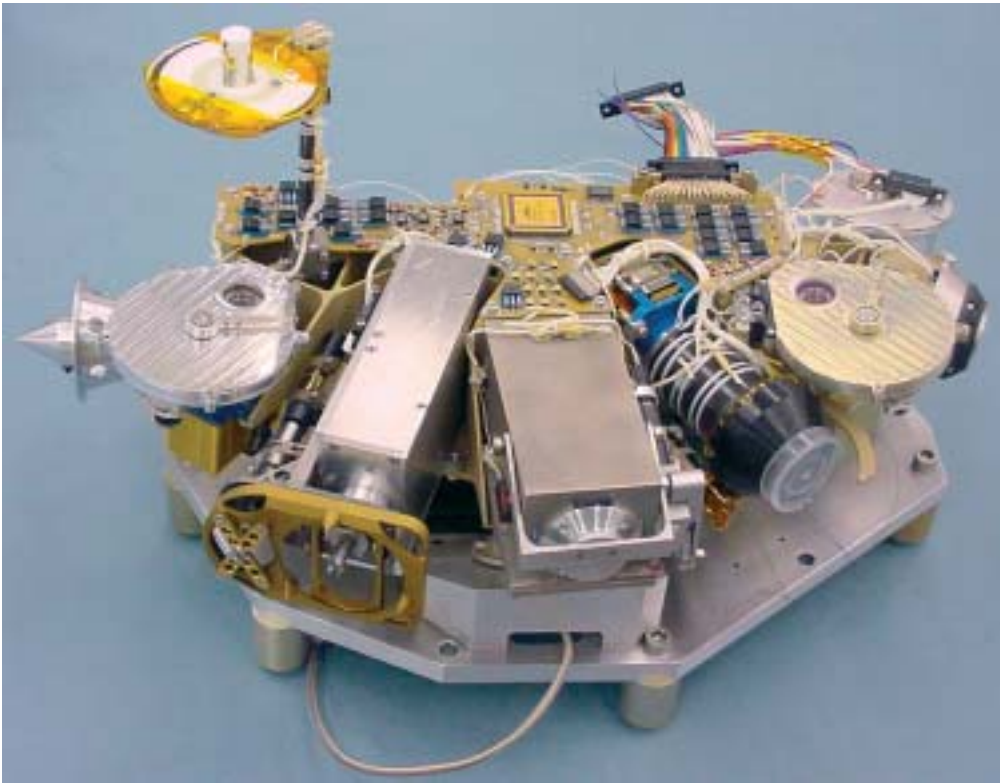
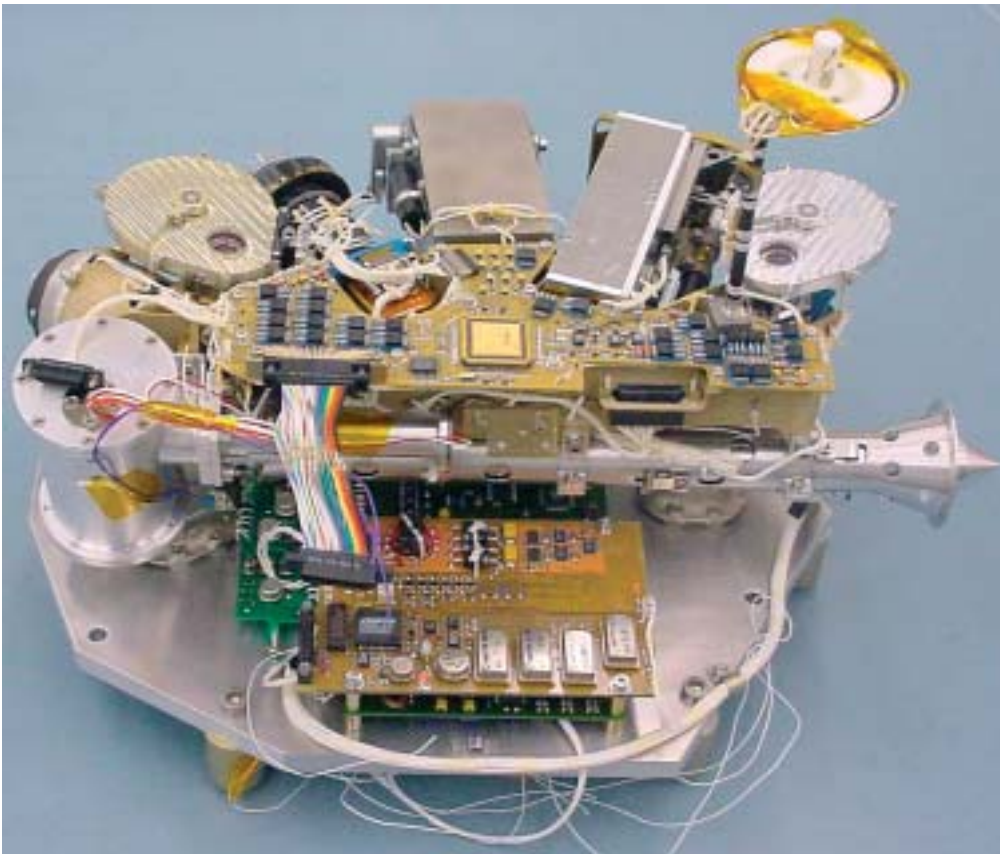


Fig. 5: The PAW Qualification Model (QM) and Back End Electronics Stack (BEEST) mounted on the combined assembly plate. Note that the Rock Corer Grinder QM is equipped with a translation table, an assembly subsequently deleted from the Flight Model (see Section 2.2.6). *All Rights Reserved, Beagle 2*



The principal objectives of the PAW-ARM subsystem are:

- multispectral stereo imaging of the immediate area around the lander;
- Digital Elevation Model (DEM) construction of the landing site (especially the 1 m² PAW-ARM working zone);
- multi-instrument *in situ* rock/soil analysis;
- wind measurements at various heights about the martian surface;
- acquisition of core samples from rocks;
- acquisition of soil samples (Mole or spoon) from the subsurface;
- delivery of solid (core or soil) samples to GAP via the inlet port;
- dust-removal from lander surfaces, if possible;
- pre-PAW-ARM deployment hazard mitigation via the WAM

In addition, the following are worthy of inclusion in extended operations:

- analysis of soil samples with *in situ* instruments, being considered for the primary mission because it provides for complete assessment of samples acquired from the subsurface. This applies to samples acquired by the Mole and spoon and deposited on a suitable surface on the lander. Possible determination of super-oxidation depth if this is present within the top 2 m of the regolith;
- analysis of uncovered soil surfaces with spectrometers. This requires the top layer of soil to be scraped off by the PAW; this may also apply to semi-consolidated blocks if there are any at the landing site. Measurements made in contact with the soil surface (contamination issues);
- imaging of the Mole-hole. Examination of the hole left by the Mole after penetration will provide information on various geotechnical properties of the surface and near-surface materials. The hole, if it remains intact, will also be useful for imaging diurnal frost deposition and particle-settling processes.

Several lead institutes were involved in supplying hardware to the PAW:

- X-ray Spectrometer (XRS): University of Leicester, UK;
- Mössbauer Spectrometer (MBS): University of Mainz, D;
- Stereo Camera System (SCS): Mullard Space Science Laboratory, UK;
- Microscope (MIC): Space Research and Planetary Sciences Div., Physikalisches Institut, Bern, CH (PI formally at Max Planck Institute for Aeronomy, Lindau, D);
- camera heads for SCS/MIC and primary optics and close-up lens for SCS: Space-X (formerly a division of CSEM), CH;
- Planetary Underground Tool (PLUTO) and the Sampling Mole: DLR, Cologne, D;
- Rock Corer Grinder (RCG): Hong Kong Polytechnic University, China;
- Wind Sensor: Oxford University, UK;
- Wide Angle Mirror (WAM), torch, spoon: University of Leicester, UK.

All the other elements of the PAW, including the control electronics, mechanical structure and harnessing, were designed and supplied by the University of Leicester as part of the PAW lead activity.

2.2.1 X-ray Spectrometer

The X-ray Spectrometer (XRS; Fig. 6, Table 2) is loosely based on the successful APXS experiment flown on Pathfinder Sojourner but favouring the excitation method used by the Viking spectrometers. Like the APXS, the primary goal of XRS is to determine, *in situ*, the elemental composition, and, by inference, the geochemical composition and petrological classification, of the surface material at the landing site. Major elements (Mg, Al, Si, S, Ca, Ti, Cr, Mn, Fe) and trace elements up to Nb are detectable with XRS. The exclusion of a proton mode offered by APXS is offset by the greater sensitivity of GAP in determining light-element abundance. However, a



Table 2. XRS engineering parameters.

Mass*	154 g (DHA 56 g; BEE 98 g)
Dimensions	DHA 47 mm diam. x 47 mm; BEE 120 x 81 x 15 mm
Power	PPS +6 V (BEE); TCS (BEE heaters). Nominal current 450 mA; current limit after switch-on for 5 s followed by 660-625 mA for ~12 s. BEE provides all power directly to DHA
Data volume	32 kb (MCA mode (default); histogram fixed size); <<1Mb (diagnostic mode; count rate and integration time dependent)

*excluding DHA housing, which is part of the PAW structure
PPS: Payload Power Supply. TCS: Thermal Control System.

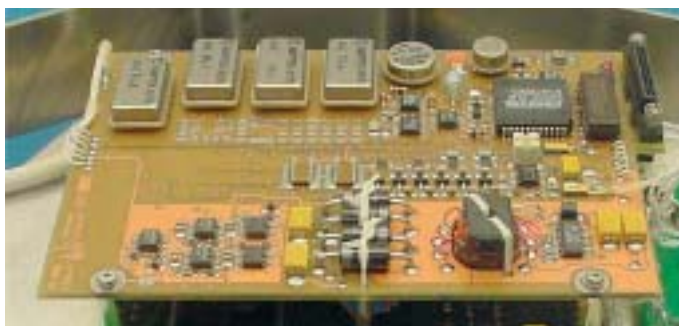


Fig. 6. QM of the X-ray spectrometer. Above left: the Detector Head Assembly is carried on the PAW. The conical carbon-fibre reinforced plastic stand-off cone is gold-flashed and contains the excitation sources and the detector element. Left: the Back End Electronics is located at the base of the ARM in the relatively warmer environment of the lander base.

All Rights Reserved, Beagle 2

more ambitious and unique application of XRS is to use the precise measurement of elemental abundance in conjunction with measurements made by GAP to attempt a crude radiometric age determination.

XRS employs X-ray fluorescence spectrometry to determine the elemental constituents of rocks (Rieder et al., 1997). The principal components of the instrument are a set of four radioisotope sources, two ^{55}Fe and two ^{109}Cd , to excite the sample via primary X-rays at 5.90, 6.49, 22.16 and 24.94 keV, arranged around a Si PIN diode X-ray detector. A 7.5 mm-thick Be window over the diode permits detection of fluorescent X-rays down to 1 keV. The energy resolution of the detector (~300 eV) is sufficient to resolve all lines of interest. The lower energy cut-off of the Be window transmission is well matched to the X-ray opacity of a 6 mbar CO_2 martian atmosphere. The instrumental resolution requirement is ~25 eV across a 24 keV range (1-25 keV detector bandpass). Data are digitised using a 16-bit analogue-to-digital converter for good differential non-linearity performance and binned to 12 bits for onboard storage. Further binning to 10 bits on the ground will provide ~23 eV resolution.

Crude radiometric dating of martian rocks *in situ* will be by the $^{40}\text{K} \rightarrow ^{40}\text{Ar}$ method. For this, XRS needs to make a precise measurement of K on a fresh sample of rock. Preparation of the surface for XRS is performed by the Rock Corer Grinder housed on the PAW. It is essential that the surface for XRS is both flat and free from weathered rind because both factors will compromise the performance and results. The Ar component is determined by GAP as part of a suite of experiments performed on a core sample extracted later from the same specimen. The target performance of XRS is to provide a determination of K with a relative precision of better than ~5% in silicate rocks with K_2O levels of 0.2% by weight or greater.

2.2.2 Mössbauer Spectrometer

Mössbauer spectroscopy is an extremely useful tool for quantitative analysis of Fe-bearing materials and is therefore particularly suited for *in situ* studies on the surface

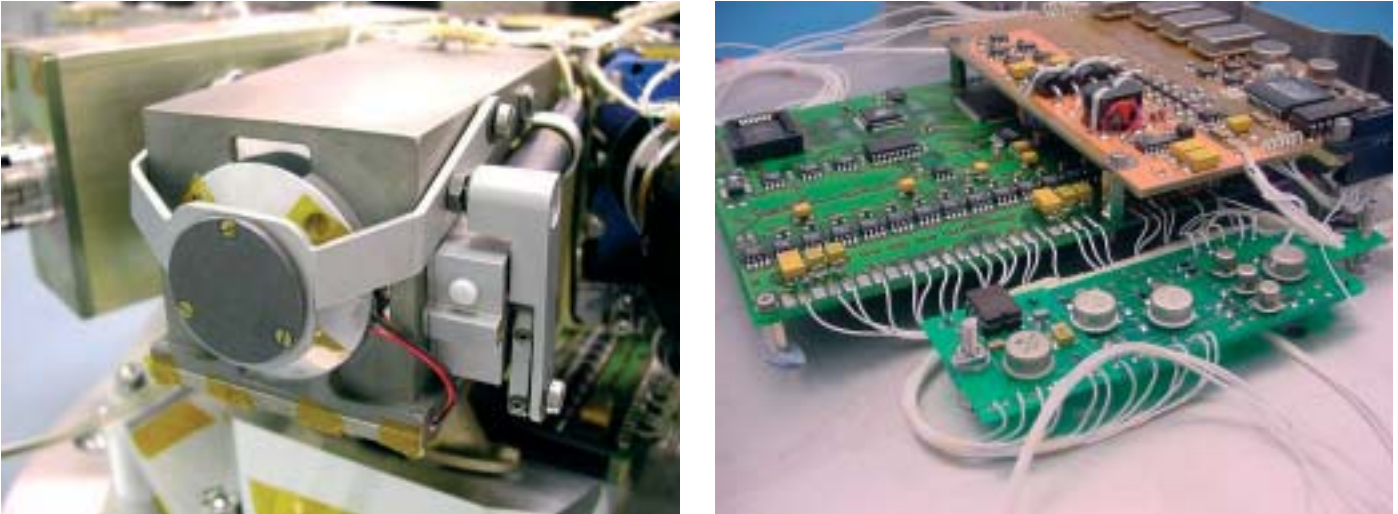


Fig. 7. The Mössbauer spectrometer. **Left:** the Detector Head Assembly (DHA) is located on the PAW and contains the radioactive sources and detectors. A mechanical shutter blocks the primary beam when the instrument is not in use. **Right:** the Back End Electronics (BEE; the larger circuit board to the left) is located at the base of the ARM in the relatively warmer environment of the lander base. The image also shows the XRS BEE (top right) and Wind BEE (foreground). *All Rights Reserved, Beagle 2*

of Mars. The Fe-rich nature of martian deposits enables relative proportions of Fe in olivine and pyroxene to be determined using the Mössbauer technique, together with magnetite in basalts. In conjunction with the X-ray Spectrometer, the Mössbauer complements the *in situ* geochemical and petrological work, and provides support for the measurements made by GAP. For example, a pure carbonate (other than siderite) gives almost no Mössbauer signal because the technique is specific to Fe mineralogy; such a signal may favour a candidate rock over another worthy of isotopic analysis.

The Mössbauer effect provides information about the iron content of mineral samples by measurement of the Doppler shift in the velocity (or energy spectrum) of gamma-rays emitted by a stationary target bombarded by an isotopically equivalent gamma-ray source (Klingelhöfer et al., 1996; Klingelhöfer, 1998). Thus the instrument uses gamma rays from the decay of ^{57}Co to ^{57}Fe . The electronic environment of atoms in a sample dictates the absorption characteristics and thus they give spectra dependent on their valence state and bonding. The strength of the signals is quantifiable, so the instrument can characterise the mineralogical makeup of the rocks and soils, and hence help to identify the petrological classification. Its ability to measure valence states provides important information about oxidation, and therefore relative changes in the rocks and soils can provide a detailed understanding of the weathering environment.

The principal scientific objectives of the Mössbauer Spectrometer (MBS; Fig. 7, Table 3) are:

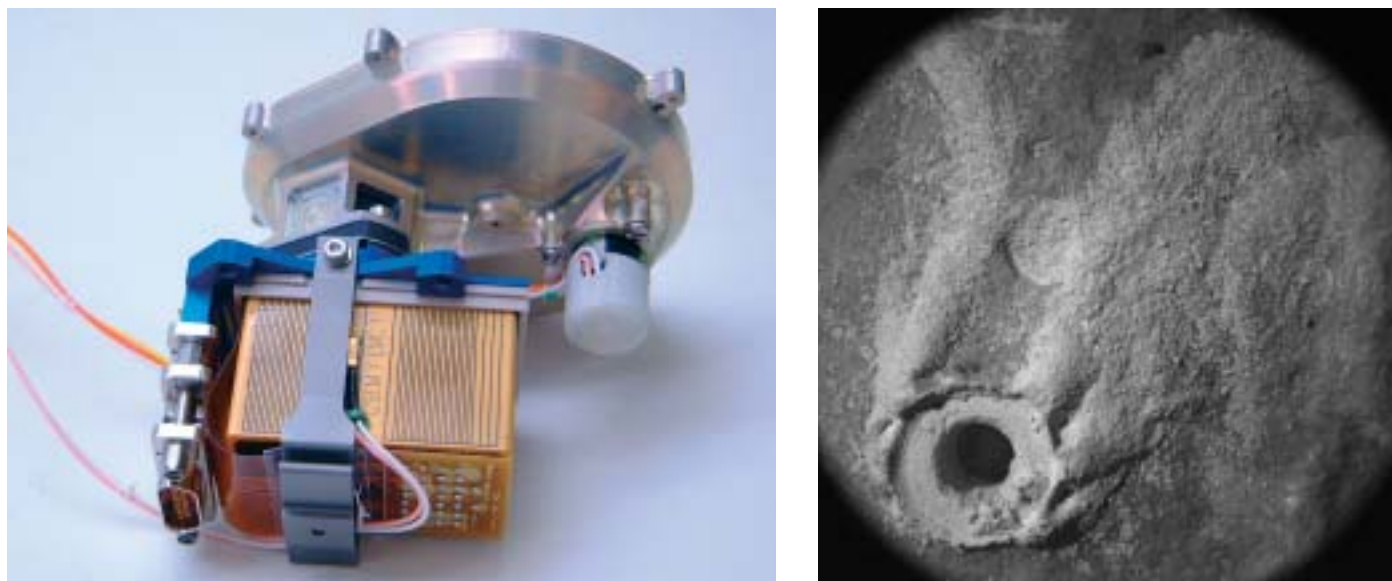
- identification of Fe-bearing phases with low detection limits;
- determination of the oxidation state of iron-bearing minerals;
- identification of Fe carbonates, sulphates, nitrates etc. that may provide information on early martian environmental conditions;
- determination of Fe oxides and the magnetic phase in martian soil;
- detection of nanophase and amorphous hydrothermal Fe minerals that could preserve biological materials.

Table 3. MBS engineering parameters.

Mass	DHA 438 g; BEE 102 g
Dimensions	DHA: 45 x 50 x 90 mm; BEE: 100 x 160 x 30 mm
Power	PPS +6 V; 3 W
Data volume	130 kbit

The footprint of the instrument is circular, with a diameter of about 1.5 cm. The average information depth is of the order 100-200 mm. The extent of dust layering found on rocks during the Viking and Pathfinder missions may exceed these values, and the thickness of weathering rinds may be even greater.

The Mössbauer parameters are temperature-dependent and under certain circumstances the Mössbauer spectra may change drastically with temperature. This



is particularly relevant for small particles exhibiting superparamagnetic behaviour (e.g. nanophase Fe oxides). The observation of such changes will help in determining the nature of the iron-bearing phases. Therefore, Mössbauer measurements will be performed at different temperatures. Ideally, these should span both the highest temperatures (during the day) and lowest temperatures (during the night).

2.2.3 Stereo Camera System

The Beagle 2 Stereo Camera System (SCS) is designed to perform a similar function to the Imager for Mars Pathfinder (IMP). Indeed, IMP was the baseline for many of the SCS design features, including the spectral coverage, and operating procedures. The major design difference is that, while IMP created stereo images by using mirrors to fold the light from two windows onto different halves of a single detector chip, SCS consists of two identical CCD cameras and integrated filter wheels (Table 4). Another important difference is that IMP was mounted on a deployable mast 1.75 m above the surface, while SCS is mounted on the PAW on the end of the ARM. The stereo baseline is 195 mm and each camera is mounted to provide a toe-in angle of 4.65° for the required stereo coverage.

A primary engineering objective of SCS is the construction of a DEM of the landing site, in particular the area within reach of the ARM, from a series of overlapping monochromatic (670 nm) stereo pair images. The DEM is reconstructed on Earth and used to position the PAW against target rocks and soils. In addition, a wide range of other imaging studies of the landing site and atmospheric/astronomical observations is possible. The following studies are baselined:

- 360° panoramic imaging to characterise the landing site and, depending on the topography, allow the location of the landing site to be determined with respect to orbital images;
- multi-spectral imaging of rocks and soils to determine mineralogy (if not completely obscured by aeolian dust);
- close-up imaging of rocks and soils using the right-hand camera (equipped with appropriate secondary optics as part of the filter set). This feature emulates the field geologist's hand-lens (Table 4);
- observations of the Sun to measure absorption of specific solar wavelengths by water vapour;
- observations of the Sun and general sky brightness at several times during the day

Fig. 8: Left: FM stereo camera, showing the camera head and Filter Wheel Assembly (FWA). The filter wheel itself is driven via a stepper motor shown protruding from the back of the FWA. Right: laboratory image acquired with the Development Model camera and filter R1 (close-up lens; see text and Table 4). The sample is a quartzose sandstone previously prepared with the QM Rock Corer Grinder (see Fig. 12).

All Rights Reserved, Beagle 2.

Table 4. The Stereo Camera System filter set.*

		λ (nm)**	Shape	Application
R 1	CLOSE-UP LENS; x6.4 magnification	Wide	curved	Geology
R 2	Ferric oxyhydroxide (local maximum)	600	flat	Geology
R 3	Maghemite (local maximum)	800	flat	Geology
R 4	Goethite, enstatite & hypersthene	900	flat	Geology
R 5	Ferrous silicates	965	flat	Geology
R 6	Diopside & fosterite	1000	flat	Geology
R 7	NEAR STEREO; Ferric oxides/oxyhydrides & Fe Silicates	670	flat	DEM/Geology
R 8	FAR STEREO; Ferric oxides/oxyhydrides & Fe Silicates	670	curved	Stereo/Geology
R 9	BLUE; Ferric oxides/oxyhydrides	440	curved	Colour/Geology
R 10	GREEN; haematite, d-FeOOH, goethite & lepidocrocite	530	curved	Colour/Geology
R 11	Dust Opacity	450	flat	Dust
R 12	HOME; Dust Opacity	670	flat	Dust
L 1	Discriminate crystalline hematite, crystalline goethite & nanophase ferric oxide	480	flat	Geology
L 2	BLUE; Ferric oxides/oxyhydrides	440	flat	Colour/Geology
L 3	GREEN; haematite, d-FeOOH, goethite & lepidocrocite	530	flat	Colour/Geology
L 4	Ferric oxides (local maximum) oxyhydroxide minerals	750	flat	Geology
L 5	Haematite, Pyroxenes & Olivines	860	flat	Geology
L 6	Low-Ca clinopyroxenes	930	flat	Geology
L 7	NEAR STEREO; Ferric oxides/oxyhydrides & Fe Silicates	670	flat	DEM/Geology
L 8	FAR STEREO; Ferric oxides/oxyhydrides & Fe Silicates	670	curved	Stereo/Geology
L 9	Continuum Band	925	flat	Water
L 10	Water Absorption	935	flat	Water
L 11	Continuum Band; Dust Opacity	990	flat	Water/Dust
L 12	HOME; Continuum Band; Dust Opacity	880	flat	Water/Dust

*the majority of filters used on Pathfinder appear here, albeit shared between two cameras. A secondary optic for close-up work (R1) is included. The long-wavelength solar filters are selected during periods of non-use to minimise exposure of the CCDs to UV during the day.

**centre wavelength. Passbands vary per filter ranging from 17 nm to 42 nm for geology, 4nm to 6 nm for dust/water, and 560 nm for the close-up lens.

to allow the determination of atmospheric optical density and aerosol (dust and water ice) properties;

- astronomical observations of Phobos and Deimos (spectral characteristics) and bright stars to allow night-time optical density to be determined. There are also ‘public awareness’ opportunities to image the Earth-Moon pair (maximum 3-pixel separation, at beginning of mission) from the martian surface;
- observations of lander surfaces and, if possible, air bags and landing scuff marks in soil to determine dust properties;
- if sufficient bandwidth is available, to return full-frame solar images (IMP solar images were 31 x 31-pixel sub-frames), unique ‘Sun dogs’ and other halo effects arising from CO₂ ice crystals may be observable.

Additional possible observations include looking for transitory or seasonal changes (dune migration, surface frosts) at the landing site or in the sky (clouds, haloes, dust devils?).

Table 5. SCS engineering parameters.

Mass	174.5 g (SCS-L); 175.5 g (SCS-R)
Dimensions (per camera)	79 x 63 x 75 mm
Power (per camera)	PPS +15 V (CCH); PPS +5 V (CCH); PPS +15 V (FWA). Nominal currents: 70mA (CCH); 40mA (FW moving)
Data volume	10 Mb (uncompressed) or 1 Mb (compressed) per image

The camera system must focus over a wide range of distances to achieve the scientific objectives. To keep the design simple, a fixed objective lens is used. This was designed to produce an optimum focus between 0.6 m and 1.2 m to support stereo pair imaging/DEM generation for the surface within reach of the ARM. To focus out to greater distances, curved filters provide optimum focus at distances between 1.2 m and infinity. Each camera is equipped with 48° optics allowing for 100% overlap at 1.2 m distance. The inclusion of a secondary optic in the filter set for the right-hand camera allows for inspection of materials at approximately 100 mm distance with this camera. The CCDs allow for an exposure range of 1 ms to 65 000 ms.

The imager on Pathfinder had a sufficiently large depth-of-focus to perform all the landing site imaging at a single fixed focus. The fact that the SCS has two working distances complicates filter selection for Beagle 2 somewhat. Potentially the size of the filter set would need to be doubled if it were required to do all science at each working distance. Given these constraints, two assumptions are made:

- imaging of the area within reach of the PAW is critical for DEM generation but stereo imaging of the rest of landing site is less important;
- best-resolution images are required of potential targets of interest for the *in situ* instruments. However, spectral properties of rocks and soils more than 1.2 m from the cameras can be retrieved from slightly out-of-focus images, albeit at reduced resolution.

All of the imaging systems used on the PAW (both stereo cameras and the microscope) use common camera head (CCH) technology consisting of a micro-integrated electronics cube and a CCD detector (1k x 1k frame transfer device). These camera heads were produced by Micro-cameras and Space Exploration SA (Space-X), formerly a division of Centre Suisse d'Electronique et de Microtechnique SA (CSEM) under a Technology Research Programme (TRP) contract to ESA (11233/94/NL/FM(SC)). For the SCS, this company also provided the primary optics and the close-up lens.

2.2.4 Microscope

The microscopic imager (Fig. 9, Table 6) on Beagle 2 will investigate the nature of martian rocks, soils and fines at the particulate scale. Such studies will provide important data in support of the exobiological objective in the form of direct evidence of fossils, microtextures and mineralisation of biogenic origin if these are present. In addition, the physical nature and extent of weathering rinds/coatings on rocks and soils will benefit the *in situ* geological investigations. Atmospheric and global planetary studies will also benefit from detailed knowledge of dust morphology.

Given that the discovery of martian biota will be of major scientific, if not philosophical, importance, minimisation of ambiguity is vital. Thus, several methods of investigation of a sample are needed to corroborate that a martian deposit is indeed biogenic. Therefore, in support of the exobiological objective, the microscope will seek evidential data in the form of preserved fossils in whatever form. Sedimentary pyrite and, in particular, framboidal textures are frequently observed in recent and ancient sediments on Earth. Although examples exist for a purely inorganic origin, the

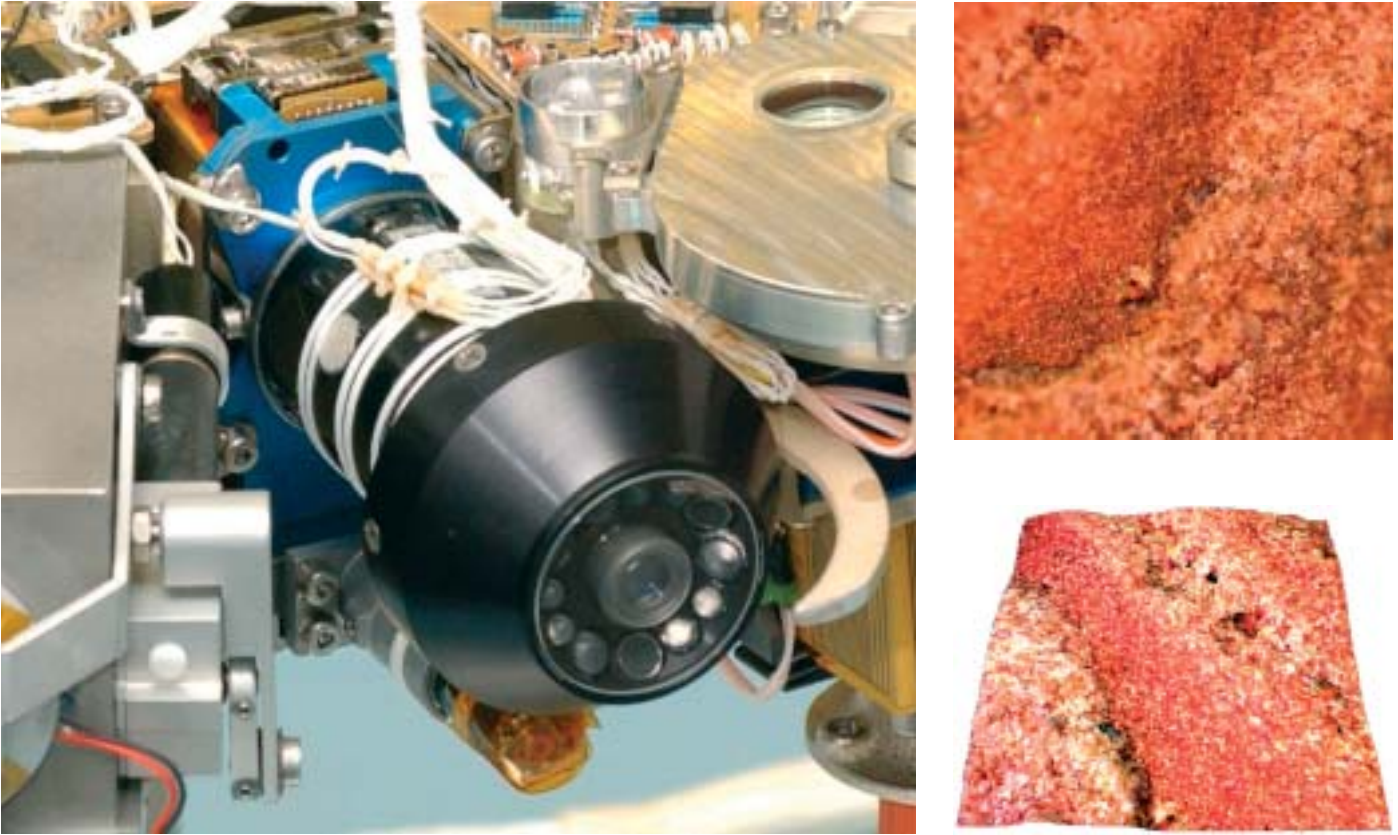


Fig. 9. The FM microscope, showing the camera head (detector and electronics), optical tube and LED illumination system. The standoff ‘thumb’, part of the PAW structure, is at the right of the image; it provides a fixed stand-off distance of 12 mm. The point of contact of the thumb and the PAW orientation are optimised after SCS imaging. Upper right: a colour composite image acquired with the microscope. The sample is a layered limestone from Piz Alv, Switzerland. A 3D reconstruction of the sample’s surface is shown below. Entropy analysis determined the depth of the scene from 60 images at different focus positions. The layering is clearly evident in this isometric view. *All Rights Reserved, Beagle 2*

Table 6. MIC engineering parameters.

Mass	151 g excluding focusing mechanism (53.7 g), which is part of the PAW assembly
Dimensions	111.58 mm x 45.24 mm (max. dia. of optical head)
Power	PPS +15 V (CCH); PPS +5 V (CCH); PPS +15 V (LEDs); PPS +15 V (Focusing mechanism)
Data volume	10 Mb (uncompressed) or 1 Mb (compressed) per image. Default mode is single best focused image plus depth map derived via onboard algorithm in LSW.

presence of framboidal pyrite in sedimentary systems is overall considered as evidence for a biological origin. In that respect, microscopic examination of the martian surface and, in particular subsurface material, for pyrite as a potential biogenic mineral might provide important evidence in the search for extinct life.

One of the major drawbacks of the Pathfinder mission was the uncertainty concerning the extent to which the APXS experiment was affected by a possible silicate-bearing weathering rind on the surface of sampled rocks. There is now no evidence that the APXS ever sampled unweathered material. The surfaces of many rocks facing north-east at the Pathfinder landing site appeared less red in the initial panorama. However, it has been recently shown that the remarkable brightness of the sky produced by airborne dust affects the illumination of the surface in such a way that rocks appear redder when in shadow or oblique sunlight. The initial interpretation of the less red faces of rocks as dust-scoured (and hence unweathered) surfaces must therefore be questioned and cannot be justified without a more sophisticated treat-

ment of the illumination. Argument about contamination of sampled materials will always occur unless the sampling strategy provides a method of exposing fresh (unaltered and unweathered) material. Detailed microscopic study of rock and soil surfaces will be an important factor in the *in situ* investigations.

Apart from being a potential barrier for *in situ* geological study, martian dust plays a key role in the atmospheric energy budget. Material in suspension in turn controls the global circulation and the present climate. It is also suspected that the martian dust has had a major influence on the evolution of the surface and the long-term evolution of the planet's climate. To date, properties of the dust particles have been inferred from remote sensing from Earth, Mars orbit and landed craft. A major contributor to the overall dynamic, thermal and radiative properties of the martian atmospheric dust is particle morphology. A thorough understanding of the physical nature of this material has wide-reaching consequences for planetary scientists. The Beagle 2 microscope will be the first attempt to image and assess individual particles directly of sizes close to the wavelength of scattered light.

The microscope consists of a camera head identical to that used by the stereo cameras and a 10-fold magnifying lens system of 20 mm focal length. The depth of field is 40 mm and the image size is 4.1 x 4.1 mm; thus the scale is 4 μm /pixel (at 12 mm distance. Focusing is achieved by moving the whole assembly in and out (total travel 6 mm) with a stepper motor-driven translation table secured to the PAW structure. Spectral information can be gathered by using an illumination system consisting of a concentric set of super-bright LEDs around the lens system, uniformly illuminating the field of view. Four wavebands, each with a bandwidth of 30 nm, are accommodated (642, 523, 466, 373 nm).

Materials exposed on the surface of Mars, including rocks, soils and drifts, are known to be highly irregular at all scales. The microscope has a small depth of field so the acquisition of focused images of irregular surfaces ideally requires many individual images to be taken at various delta stand-off distances from the target. Single 'snapshot' images obtained with the microscope are likely to have little scientific value. Arrays of images at coarse stand-off distances are undesirable because subtle morphological and textural features, which may be significant, would not be resolvable. A complete set of individual images obtained at each stand-off position is achieved via the focusing mechanism on the PAW.

Generally, individual images compress well because they are usually dominated by out-of-focus areas (although scene-dependent, estimated compression on Beagle 2 is about 10:1). Unfortunately, the number of these 'image layers' can be as large as 60-100 per illumination configuration. By applying a focusing algorithm to a set, a single in-focus image derived from all stepper motor positions plus a depth map for 3D reconstruction map can be compiled. This process can either be done *in situ* or back on Earth. However, a single in-focus image plus map (i.e. two images) is much more efficient in terms of data volume. For this reason, the onboard software includes a focusing algorithm.

2.2.5 PLUTO and the Sampling Mole

It is of prime importance to supply GAP with material from rocks and soils to realise the mission's primary objective. The Planetary Underground Tool (PLUTO; Fig 10, Table 7) subsurface soil sampling device provides samples of soil from depths down to 1.5 m and, depending on the terrain, from under a large boulder. Both activities have never been attempted on Mars. The Viking missions had access to depths of only 20 cm in the surface soil, which proved to be still within a layer of presumably highly oxidised material with no measured concentrations of organic matter. It is expected that the top metre of bulk soil on Mars has in the past been exposed by aeolian mixing processes to the atmosphere and UV flux, and thus subjected to oxidation and irradiation processes that destroyed any organic matter over a scale of decades. If biological activity ever existed on Mars, then decomposition products in the form of biomarkers would best be preserved at depth in the bulk soil or within rocks.

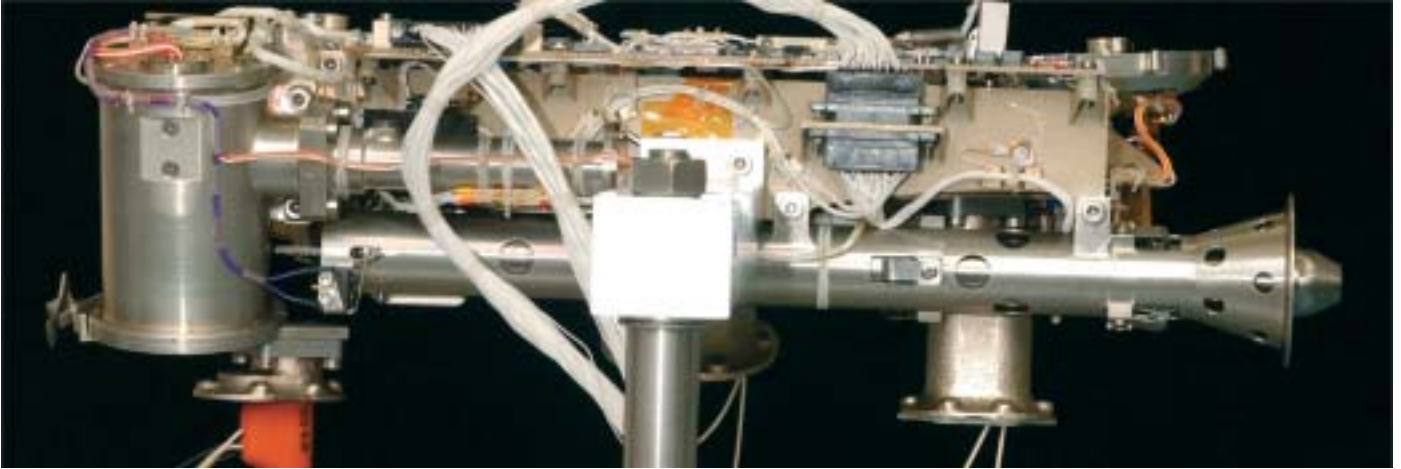


Fig. 10. The PLUTO FM mounted on the PAW FM. The Mole is just visible at the right, protruding from the launch tube (minus the sampling head, which is fitted as late as possible to avoid biological contamination). The winch housing is the cylindrical object on the left. *All Rights Reserved, Beagle 2*

Table 7. PLUTO engineering parameters.

Mass	340 g (Mole); 550 g (deployment unit); total 890 g
Dimensions	approx. envelope ~380 x ~90 x ~80 mm (Mole = 280 mm long)
Power	3 W (17 W for pin-puller release after landing)
Data volume	~ kb (HK only)

PLUTO employs a self-penetrating sampling Mole tethered to a support mechanism attached to the PAW. The Mole is the primary soil-sampling device. It is based on a Russian self-burying penetrometer; a scaled-down version of the original device was developed within an ESA TRP activity specifically for space applications (Re et al., 1997). It requires no reaction force from the lander once a small initial penetration is achieved: the Mole proceeds into the subsurface, connected by a tether for power (for the inertial hammering mechanism) and can reach depths several times the length of its casing.

At the tip of the Mole is a sampling mechanism that can be commanded to open at the appropriate sampling depth to acquire some 0.20 cm³ of soil. Once secured by closing the mechanism, the sample is delivered to GAP by retrieving the Mole, retracting the tool into the 'launch tube' and moving the ARM back to the GAP inlet port on the lander. Samples are released by opening the mechanism again once in position, docked to the inlet. With one shock occurring every 5 s, it may take 30 min to 1 h to reach a vertical depth of 1 m under Mars gravity and the estimated soil resistance.

In addition to serving as a soil sample-acquisition device, the Mole provides a platform for *in situ* temperature measurements as a function of time and depth while embedded in the subsurface. Moreover, soil mechanical properties and layering will be estimated from the ground intrusion behaviour.

For retrieval from the subsurface, the cable reel operates in reverse, pulling the device back into the launch tube on the PAW, the latter remaining in position throughout the entire operation. The Mole retraction manoeuvre has been extensively tested on a variety of analogous materials. Retraction can also be aided by operating the hammering mechanism while rewinding the cable, an activity more likely to be considered for deep sampling. Once back inside its tube housing, the Mole is ready to discharge its cargo into the GAP sampling inlet.

The Mole can also be deployed laterally across the surface, away from the lander and towards a suitably sized boulder beyond the reach of the PAW, using the shocks

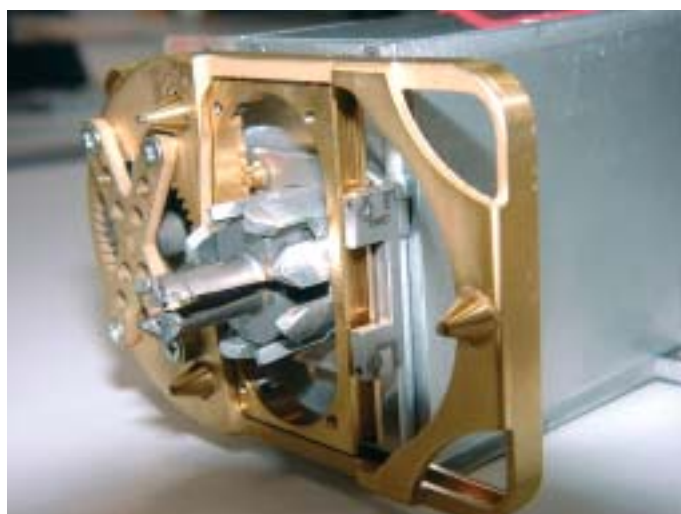


Fig 11. Upper left: the Rock Corer Grinder FM. Note the dual functionality and shape of the sampling tip. Right: results of coring into a field sample of quartzose sandstone with a case-hardened thin (~1 mm) weathering rind (Planetary Science Sample Library 146/274). Lower left: the RCG QM equipped with the Translation Table (TT) for transcribing the tool-head during grinding. The TT was not fitted to the FM following an engineering and scientific assessment on the effectiveness of the device. *All Rights Reserved, Beagle 2*

Table 8. RCG engineering parameters.

Mass	348 g (FM without Translation Table)
Dimensions	approx. envelope ~30 x ~60 x ~100 mm
Power	6 W
Data volume	~ kb (HK only)

from its hammering mechanism for forward motion, at a rate of about 10 mm travel for each percussive stroke. Such hammering perpendicular to the local gravity vector had already been verified during an early ESA TRP activity. Once the Mole encounters a large rock with an overhang, it will be diverted downward to initiate soil penetration under the rock, thereby allowing access to protected samples.

2.2.6 Rock Corer Grinder

It is a scientific requisite that all the PAW instruments have access to fresh, unweathered/unaltered material in order to avoid the effects of surface weathering rinds thought to be prevalent on all exposed material on Mars. In addition, the spectrometers require a prepared flat area of optimum size to counter geometric effects that can seriously compromise instrument performance. To address these requirements, the PAW is equipped with a combined Rock Corer Grinder (Fig. 11, Table 8) tool.

The grinding action of the RCG removes as much weathering rind material as possible, up to 6 mm, by producing individual or an array of flat, 10 mm-diameter

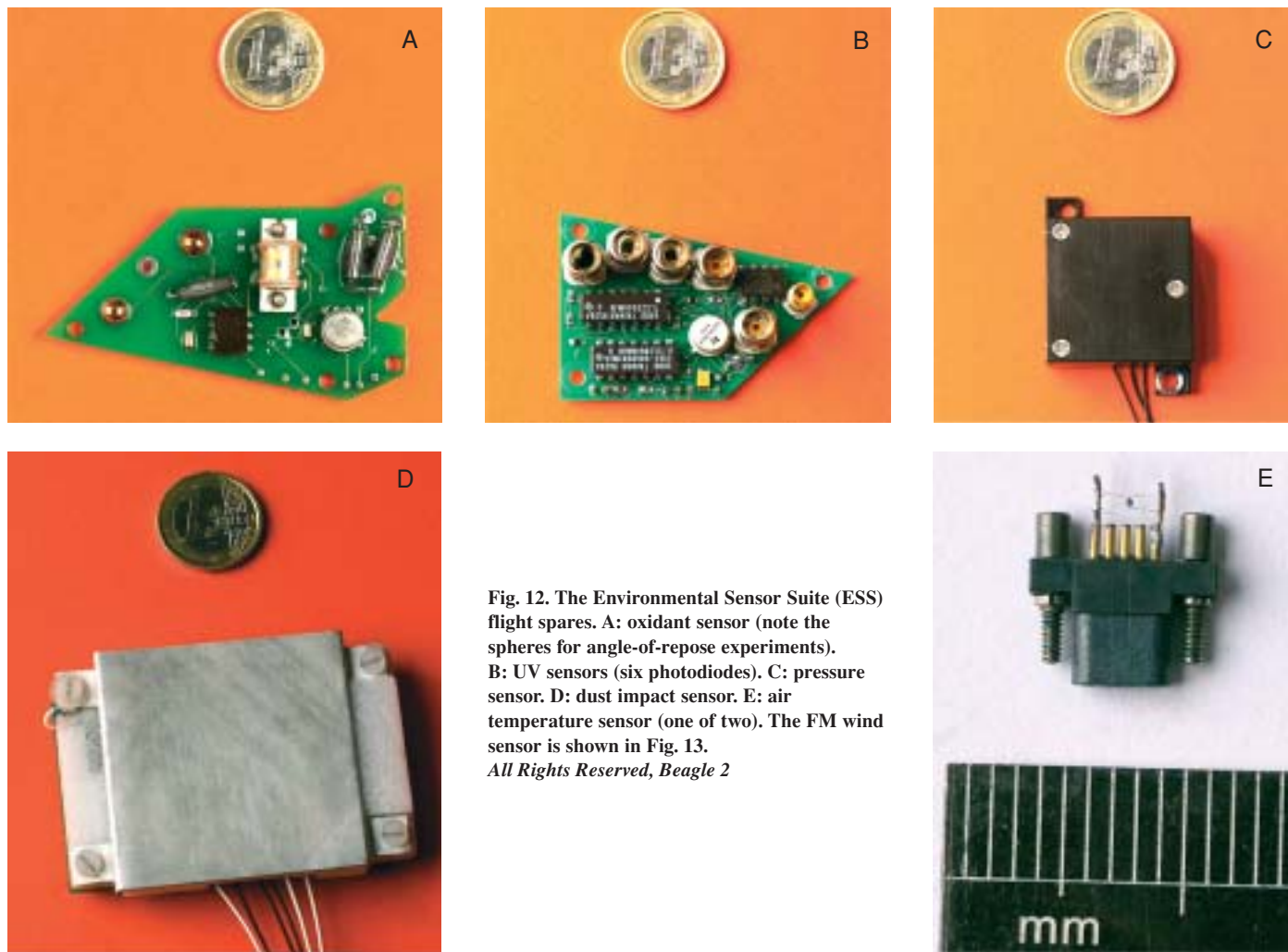


Fig. 12. The Environmental Sensor Suite (ESS) flight spares. A: oxidant sensor (note the spheres for angle-of-repose experiments). B: UV sensors (six photodiodes). C: pressure sensor. D: dust impact sensor. E: air temperature sensor (one of two). The FM wind sensor is shown in Fig. 13. All Rights Reserved, Beagle 2

fresh surfaces suitable for the spectrometer instruments. A translation table mechanism was developed for the RCG QM to transcribe the tool-head over the surface of a sample to produce a flat area of ~30 mm diameter. However, for mass and other reasons, this facility was not adopted for flight. After all *in situ* analyses have been completed, a sample from the ground patch is extracted by using the coring action of the device and delivered to GAP via an inlet port on the upper part of the lander. Coring is achieved by a hammering/rotating action of the main drive where material is retained within the Micro End Effector (MEE) jaw-type device. Cores, or more precisely a collection of rock chippings, obtained by this tool are of reproducible volume suitable for the GAP ovens.

2.3 Environmental Sensor Suite

Beagle 2 is equipped with a complementary set of environmental sensors (Fig. 12) to assist in both the prime objective, characterisation of the landing site and meteorological studies. Measurement of the UV and radiation flux (a RadFET within the lander electronics measures total dosage) at the surface together with the oxidising capability of the soil and air provides direct input into the astrobiological investigations. In addition, measurement of atmospheric temperature, pressure, wind speed/direction, dust saltation and angle-of-repose will complement the *in situ* experiments. Dynamic studies such as dust devil profiling will also benefit assessments of aeolian

erosion rates, as will an understanding of the boundary layer wind regime using the wind sensor on the PAW.

The mass of the complete suite of sensors is 156 g. Each sensor is powered via the lander Auxiliary Power Supply (APS) and typically has a 0-5 V analogue output. Depending on the sampling rate adopted during operations, the environmental sensors can generate between kilobytes of data (low rate typically one reading from each sensor every 10 min) through to megabytes (high rate typically 4 Hz).

2.3.1 Oxidant sensor

One controversial issue arising from the Viking results is the postulated presence of hydrogen peroxide or other oxidising compounds in the soil, used in several cases to explain the results of the experiments designed to detect martian life. The Beagle 2 oxidant sensor is a one-shot measurement, in which a sensitive titanium film is exposed to the atmosphere and its resistance is monitored as it oxidises. It is not, however, H_2O_2 -specific but will also detect other oxidising species, such as O_3 . By simultaneously monitoring the UV and dust sensor, it is hoped to shed some light on the processes generating any oxidants. At the end of the mission, the PAW will be used to deposit quantities of soil onto the film, and to monitor the response. The sensor is located near the rim of the lander base.

2.3.2 Ultraviolet sensor

Short-wavelength UV, such as UVB and UVC, are harmful to life and can directly damage DNA. The UV environment on Mars is known to be harsh, and it is unlikely that life can survive on the surface, but subsurface life may still be possible. This sensor will produce a 5-point spectrum in the range of 200-400 nm, covering UVA (320-400 nm) and UVB (280-320 nm) over seasonal and daily time-scales. At wavelengths below 204 nm, the CO_2 atmosphere is strongly absorbing, partially blocking the UVC band (100-280 nm). The sensor is located near the rim of the lander base.

The unit uses six photodiode sensors, each with a particular bandpass filter:

- 210 nm: main TiO_2 dust absorption band;
- 230 nm: biologically damaging and rapidly time-varying regime;
- 250 nm: secondary TiO_2 band;
- 300 nm: mid-UVB;
- 350 nm: mid-UVA;
- 200-400 nm (no filter): calibration channel.

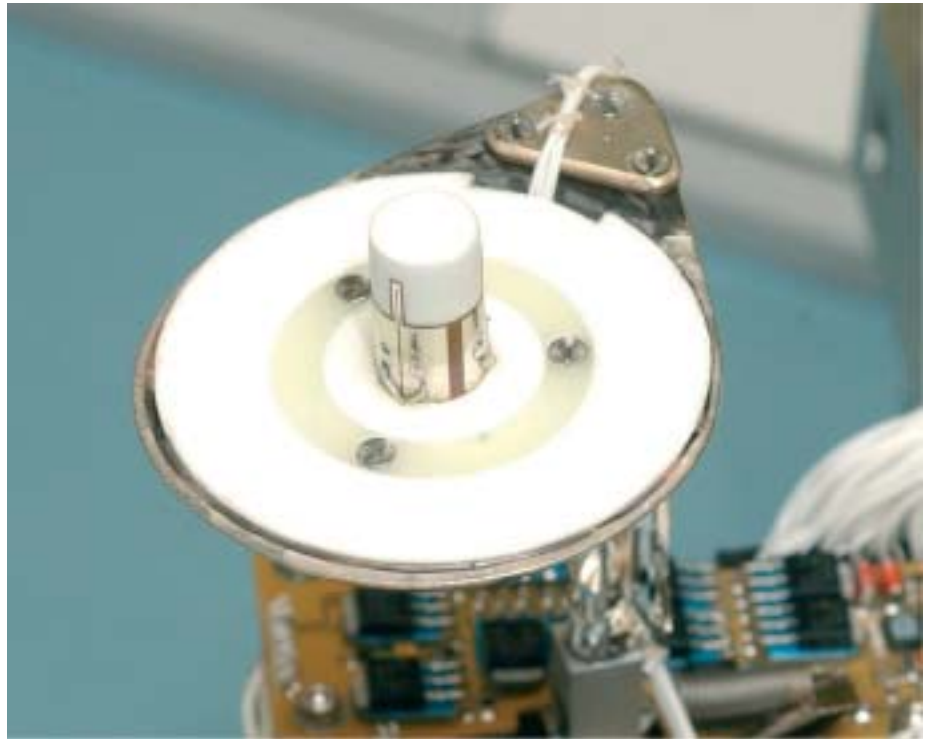
2.3.3 Wind sensor

A hot-film wind sensor (Fig. 13) was supplied by Oxford University (UK). It is mounted with an associated air-temperature sensor on the PAW. The difference in heat transfer coefficients between the three films can be used to calculate a 2D wind vector perpendicular to the axis of the wind sensor. In its normal orientation, the sensor measures a horizontal wind vector. The sensor is calibrated for the range $0.3\text{-}30\text{ m s}^{-1}$ though wind speeds above this range can also be measured. There are several sensor-specific goals and activities:

- obtain a long-term meteorological record of wind speed and direction, and air temperature at the landing site;
- obtain higher frequency data ($\sim 1\text{ Hz}$) at various times of the day to enable characterisation of boundary-layer turbulence and fluxes;
- detect and observe dust devils;
- characterise the vertical profile of air temperature and wind speed at different times of the day, by taking measurements with the sensor head at different heights above the surface.

At times, the top surface of the lander can be up to 80°C hotter than the surround-

Fig. 13. Wind Sensor FM integrated with the Wide Angle Mirror during final assembly of the PAW FM. For an alternative view, see Fig. 4. All Rights Reserved, Beagle 2



ing surface, giving rise to a convective plume. This plume, which affects meteorological measurements made directly above it, will be studied by moving the temperature and wind sensors into different positions above the lander. Such a plume was seen by the Viking landers (Ryan & Lucich, 1983), and the effect should be stronger on Beagle 2 because of its geometry.

2.3.4 Air pressure

The Barobit pressure sensor was supplied to Beagle 2 by the Finnish Meteorological Institute. It uses the same Barocap sensing element as in the Meteorology Instrument System aboard the Mars-96 small stations and penetrators (Harri et al., 1998) and within the MVACS package on the Mars Polar Lander. Barocap is a capacitive absolute pressure sensor based on a thin silicon diaphragm. The Barobit design is based on the EGA-P experiment flown aboard Mars Polar Lander. Barobit electronics and Beagle 2 data-handling capability limit the measurement accuracy down to about 0.006 hPa and resolution to 0.003 hPa. The sensor is located in the lander base.

2.3.5 Air temperature

Air temperature will be monitored at two locations using commercial 0.3 mm-diameter bead platinum resistors. The sensor is optimised to give the highest sensitivity and accuracy of better than 0.01K over the range -10°C to -60°C . At the extremes of the operating temperatures (less than -100°C and greater than 10°C), the accuracy is reduced to about 0.1K. One sensor is mounted at a fixed height of around 0.05 m above the ground, on the edge of one of the solar panel sheets, in an attempt to isolate it thermally from the effects of the hot lander body. An identical sensor is mounted as part of the wind sensor assembly on the PAW, allowing air temperature measurements at heights of up to 0.6 m.

2.3.6 Dust impact monitor

A dust impact monitor, located near the rim of the lander base, will measure the

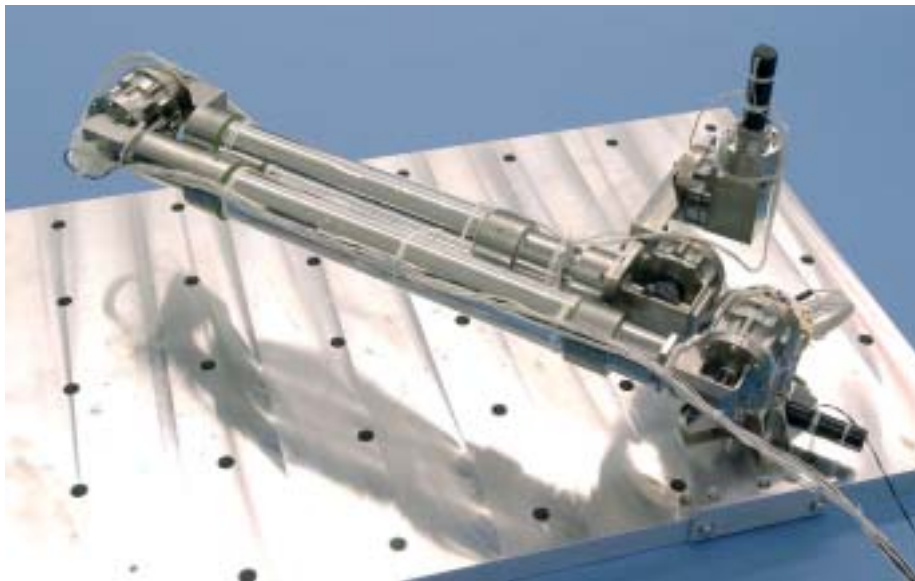


Fig. 14: The ARM Development Model.
All Rights Reserved, Beagle 2

impact rate and magnitude of wind-blown dust, providing information about the regolith transport and mixing mechanisms on the surface. The sensor is mounted horizontally, near the rim of the probe, and will listen continuously for dust impacts. It consists of a simple aluminium sheet, 0.25 mm thick, with a polyvinylidene fluoride (PVDF) piezoelectric film on the rear face. PVDF films such as this have been used on several missions, most recently on the high-rate detector within the CDA instrument aboard Cassini (Tuzzolino, 1995). Maximum sensitivity of the device is $1 \times 10^{-10} \text{ kg m s}^{-1}$ (equivalent to a 0.2 mm glass bead dropped from 10 mm height on Earth); the sensor records the magnitude and time of an impact.

3.1 Anthropomorphic Robotic Manipulator (ARM)

The Beagle 2 ARM (Fig. 14) is a 5-degree-of-freedom manipulator, with the PAW permanently attached to the wrist. The fully extended ARM is 109 cm long, measured from the centre of the body joint to the centre of the PAW wrist joint. Each joint comprises a DC brushed motor driving through a 100:1 harmonic gearbox. Joint position is detected by a potentiometer mounted directly onto the output shaft. A typical joint speed is 0.6° s^{-1} (axes 1-3 only).

The ARM's primary purpose is to position and orientate the PAW so that the instruments and tools can perform their tasks. Requirements imposed on the ARM by the PAW include:

- working zone DEM (0.6 m to 1.2 m near-stereo) requires PAW/ARM to view the scene from as many perspectives as possible – at least two or three – while maintaining targets of interest in focus;
- 360° multi-spectral panorama (including > 1.2 m far-stereo) requires PAW/ARM pointing straight up for maximum height advantage and rotation about this axis. The relative position of the Sun with respect to the viewing scene needs to be considered for optimal illumination and direct solar avoidance during geological imaging;
- close-up lens for imaging rocks, coarse detritus and large clasts at a working distance of ~80 mm requires optimum PAW orientation to avoid navigational hazards, including contamination from the surface.

It is proposed that a number of positions be selected within the sphere of PAW/

3. Surface Operations

Fig. 15. The ARM FM equipped with a one-third mass PAW during calibration work. The configuration shows the sampling Mole docked to a representative (in terms of mechanical interface and location) GAP inlet.
All Rights Reserved, Beagle 2



ARM operations that are deemed to be 'safe points'. These are configurations that can be returned to at any time without risk of collision and from which a series of pre-set manoeuvres can be initiated.

Those operations requiring actual contact to be made with a sampling surface or activities with the Mole need special attention and are discussed in the following sections. Most imaging tasks do not require contact with the sample under investigation but some scenarios involving close-up work will require careful navigation to avoid local collisions with objects on the surface. A complete and accurate DEM of the area reachable by the PAW/ARM and PLUTO sampling Mole, and an initial characterisation of potential sampling targets contained within the zone, is an early priority. Only when this has been done can the majority of PAW/ARM operations commence.

3.2 Positioning

During initial positioning, the location of the spot where the PAW comes into contact with the candidate sample is not expected to be very precise. A suitable goal is to achieve initial contact within ± 5 mm of a nominated position, based on the working zone DEM and the capabilities of the ARM. Angular contact should be within 5° of the average normal to the chosen spot. Once initial contact has been made, then this point becomes the reference datum and subsequent positioning will be relative, and therefore more accurate, albeit subject to surface roughness constraints.

The requirement for lateral positioning of the RCG for coring and the instruments is ± 2 mm from the centre of ground patch. This is primarily to ensure that the instruments view the same spot within the prepared area. Along with this tighter positional alignment, it is required that the ARM can position a tool or instrument within 1° of a nominal perpendicular to a face. This is required in particular for spectrometer positioning, because any angular misalignment alters the distance between the detectors and surface. It is expected that if this angle is achieved then the action of applying a longitudinal force coupled with the compliance of the ARM would remove any angular error anyway.



Fig. 16. Sampling operations at the Lander Operations Control Centre, Univ. Leicester (UK) during early December 2003. The lander Ground Test Model, equipped with the DM ARM, is deploying the QM PAW and performing a sampling operation with the Rock Corer Grinder. The sample itself, in this case a fissile shale, is seated in a bed of coarse sand and within the working zone of the PAW/ARM defined by the raised area. *All Rights Reserved, Beagle 2*

The only instrument that requires more precise positioning is the microscope, which needs to be positioned longitudinally to an accuracy of $40\ \mu\text{m}$ for focusing. This means that some device is required to move the microscope over a range of $\pm 3\ \text{mm}$ to within an accuracy of $40\ \mu\text{m}$. A separate actuator on the PAW provides this.

There is no precise positioning requirement for the PLUTO sampling Mole. It is expected that positioning within $\pm 3\ \text{mm}$ in any axis and within 5° of a nominal 'launch' angle will be acceptable.

For the wind sensor to be maintained horizontally with respect to the martian surface requires the PAW/ARM subsystem to account for relative lander orientation. The latter will be determined via the onboard accelerometers if they survive the landing shock. Alternatively, some estimate may be achieved via the stereo cameras.

3.3 Approach technique

Once a sampling spot has been identified on the candidate rock, the ARM will orientate the PAW to align the RCG as orthogonal to the sampling surface as possible and advance the PAW along the RCG axis towards the surface (Fig. 16). The RCG is proposed for all initial contacts with candidate samples, because it is more robust than other instruments, to establish a reference point from which all subsequent positioning can be performed with more accuracy. Furthermore, the first operation in the analysis cycle involves imaging the weathered surface with the close-up lens. This requires a PAW reorientation anyway, so nothing is gained by placing one of the longitudinal instruments against the sample first. Advancement in this way proceeds until contact has been detected or a predetermined timeout has expired. In the latter case, some sort of corrective action will have to be applied that may involve aborting the sequence and moving to a safe/default position, branching to another activity.

The final approach prior to making contact may be achievable by operating a single joint other than the wrist. For example, if the elbow joint is considered, and the forearm/PAW length is $400\ \text{mm}$, then the PAW needs to sweep forward up to $5\ \text{mm}$ in the worst case, to prepare the surface with the RCG. This equates to an angle of about 0.7° swept by the RCG during operation, compatible with the accuracy of surface preparation achievable by the RCG.

On the approach to the rock, if not during the whole of the movement, the ARM movement will be stopped as soon as a sufficient contact force has been reached. This

is sensed by a piezoelectric force load washer (sensitivity 3 pC N^{-1}) that generates an electrical signal upon contact with a resistive surface: a rock, instrument calibration target on the Calibration Target, GAP inlet or sample dish. Forces required by the various instruments and tools are determined from this point as a function of ARM velocity, direction and time. Suitable choice of sampling site can utilise the weight of the PAW or vertical component thereof. A different contact strategy will be required for investigations of rocks and unconsolidated materials.

The piezoelectric sensor will not normally give any charge output while the PAW is being moved around gently during normal ARM movements. The primary mode of operation is to use the sensor to detect the moment when the PAW comes into contact with the rock. The ARM is then allowed to continue to drive for a given time after contact has been detected, determined by the stiffness of the arm joints. The ARM will stop advancing shortly ($\sim 102 \text{ ms}$) after contact has been detected. The exact length of time depends on the instrument or tool being positioned and the anticipated orientation of the PAW with respect to the contact surface.

The ARM must operate with a degree of autonomy owing to the limited communication periods available with Earth. However, it is not intelligent but follows predetermined manoeuvres or strategies, which then allow it and the associated PAW to survey the martian surface and analyse the rocks.

3.4 Nominal rock analysis cycle

Given the constraints of the surface operations timeline and scientific requirements, only a small number of rocks (~ 3) are expected to be fully investigated *in situ*. Assuming that a number of appropriately sized rocks lie within reach of the PAW/ARM, each potential candidate for detailed analysis will have to be assessed based on bulk spectral properties, morphology and PAW/ARM accessibility. Once a candidate has been chosen, the full suite of analysis will be performed *in situ* by the PAW instruments and by GAP on the same material. Of course, this modus operandi may change on arrival at Mars, especially if the landing site yields unexpected or scientifically interesting diversity.

The list below describes a typical analytical sequence after a candidate rock has been selected for detailed study:

Assessment

Image the candidate rock from various angles using geology and stereo filters.
Select an area of rock for investigation (constrained by ARM, PAW access, surface morphology and spectra).

Analysis (weathered surface)

Obtain close-up images of the selected surface using hand-lens and microscope.
Perform detailed measurements with the spectrometers.

Surface preparation

Grind away the surface weathering rind and create a flat working surface.

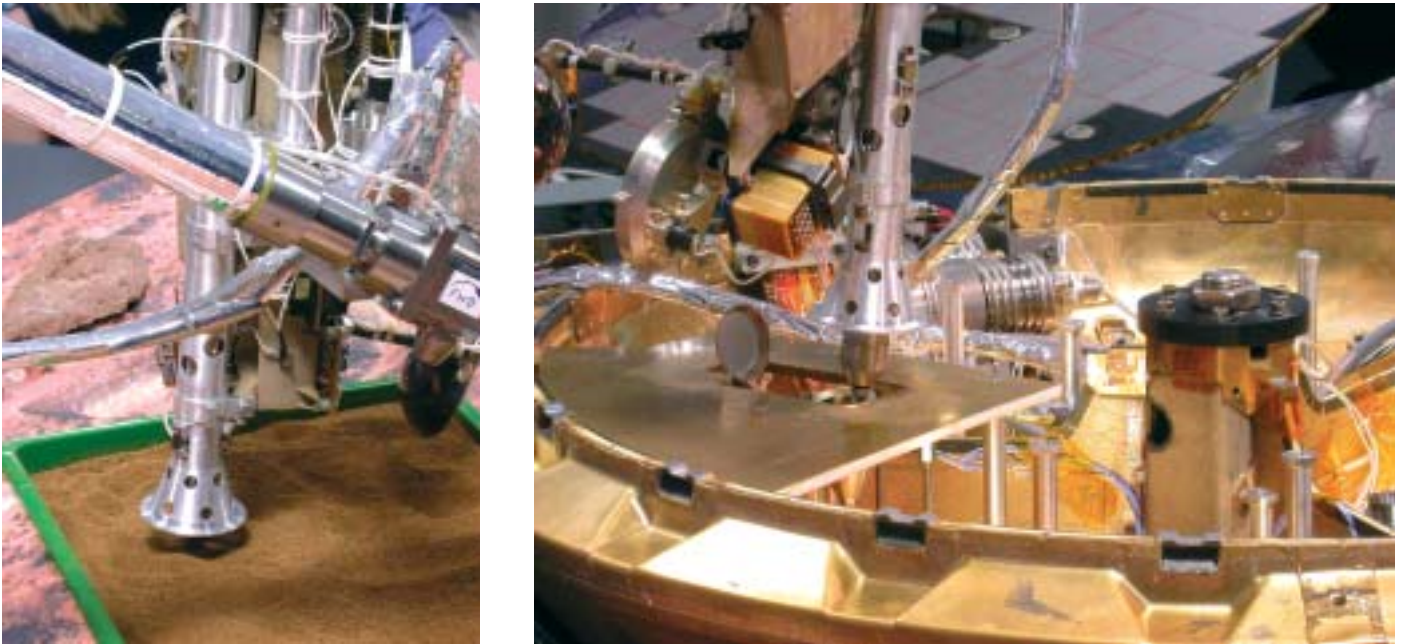
Analysis (fresh surface)

Obtain close-up images of the prepared surface using hand-lens and microscope.
Perform detailed measurements with the spectrometers.

Sample acquisition and disposition

Extract a core from the centre of the sampling area.
Obtain close-up images of sampling area using hand-lens and microscope.
Deliver core (chippings) to GAP via the inlet port.

This sequence is based on fundamental field practice but may have to be modified as a result of surface operations and constraints.



3.5 PLUTO (Mole) and spoon operations

The Mole (Fig. 17) is deployed in one of two ways. In the vertical mode, the sampling Mole penetrates the regolith to a specified depth (maximum 1.5 m baselined), from where a sample is retrieved. Temperature measurements are obtained at various depths (maximum 1.25 m). In the horizontal mode, the Mole crawls across the surface towards a candidate rock and is potentially diverted to retrieve a sample from a sheltered zone under a boulder. The number of samples acquired by the Mole during the primary mission will be restricted to about three.

The uppermost zone of the martian regolith is probably heterogeneous and chaotic. Suspended rocks and pebbles may deviate (or impede) the Mole, thereby contributing to an error in the depth measurement. Mole operations will be progressively more ambitious during the course of surface activities in order to minimise the risk to the scientific objectives of all instrumentation dependent on the device.

The PAW is also equipped with a ‘spoon’ as a backup method of sampling unconsolidated soil. The design ensures that no more than 20 mm³ of material is collected, thereby avoiding the risk of overfilling the sample ovens.

3.6 *In situ* calibration and validation

Once Beagle 2 has finally come to rest on the surface of Mars and fully deployed itself, the PAW is ready to obtain the first image of the landing site. This is achieved via the Wide Angle Mirror, which moves into the FOV of the right-hand stereo camera when the pre-tensioned spring holding it down is released by the opening of the lid and solar panels. The figure of the WAM is designed to provide a 360° view of the landing site that includes the horizon. Fig. 18 shows simulated and actual views using the WAM.

Immediately after PAW/ARM release and deployment, a programme of calibration and verification will be initiated. Each instrument will undergo a predefined checkout and *in situ* calibration sequence as soon as possible. This will avoid possible erroneous effects caused by degradation of the data from the targets owing to dust accumulation etc. Recalibration will also occur throughout the surface mission to monitor any changes and, if necessary, for instrument diagnostic reasons.

The lander is equipped with a Calibration Target (CT) consisting of individual targets specific to or shared by the deployable instruments. Each instrument’s CT will

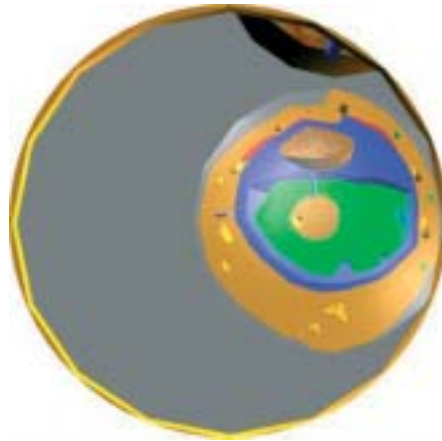
Fig. 17: PLUTO sampling operations at the Lander Operations Control Centre, Univ. Leicester (UK) during early December 2003. The lander Ground Test Model, equipped with the DM ARM is being used to deploy the QM PAW and perform shallow soil sampling operations with the Mole. Left: the sample being acquired from unconsolidated coarse sand (JSCMars1). Right: the sample being deposited into the GAP inlet port; note the inlet cover and funnel in the representative section of the lander deck.

All Rights Reserved, Beagle 2



Fig. 18. Imaging with the Wide Angle Mirror. Right: early simulated view of a rock-strewn landing site prior to PAW/ARM deployment via the WAM and right-hand stereo camera. The scene is made up of sky (grey), lander structure (blue/green) and a martian surface (brown). Far right: image taken with the DM Stereo Camera and a spherically figured WAM. Camera is visible in centre of image together with the structural & thermal model PAW and lander model. The WAM mast is clearly visible in the lower half of the image. Above: processed version of the far-right image courtesy of Joanneum Research, Austria.

All Rights Reserved, Beagle 2



be 'known' by the onboard software and flagged as a designated point. The position of the CT has been chosen to allow PAW optimal viewing of the imaging targets and provide access for physical contact to be made by the spectrometers and the microscope. The latter case requires some structural support beneath the CT to accommodate the weight of the PAW.

4. Spacecraft Engineering

The 69 kg Beagle 2 is a highly sophisticated spacecraft (Figs. 19 & 20), which uses advanced technologies and very limited redundancy in order to meet the tight mass restrictions dictated by the Mars Express spacecraft requirements. Beagle 2 will be ejected from the orbiter before the Mars orbit insertion, and enter the planet's atmosphere on 25 December 2003 after a coast phase of about 6 days. The entry, descent and landing system will deliver it to the martian surface, where the nominal science operations phase will begin after an initial commissioning phase. The nominal lifetime of Beagle 2 is 6 months. The following sections provide an overview of the technical aspects of the Beagle 2 lander.

In addition to the Beagle 2 Flight Model, a number of system and subsystem models were built to support the lander test activities. The Beagle 2 programme delivered the following models to Mars Express:

- the protoflight model (PFM) to be integrated to the orbiter on the launch site;
- the electrical test model (ETM) for software and interface tests;
- two mass/stiffness models (MSM#1 and #2) for mechanical testing, one equipped with a QM Spin-Up and Eject Mechanism (SUEM).

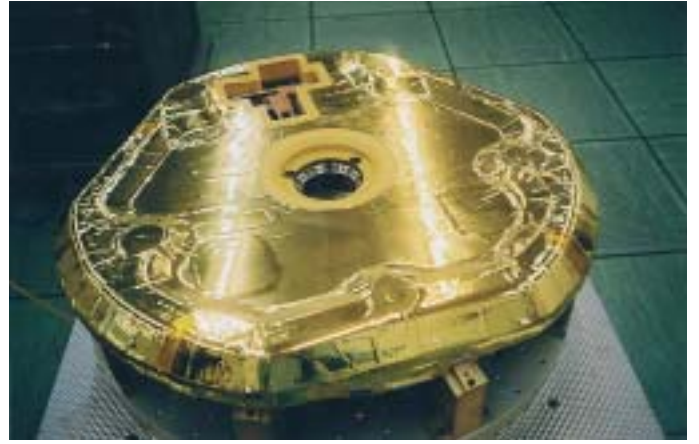
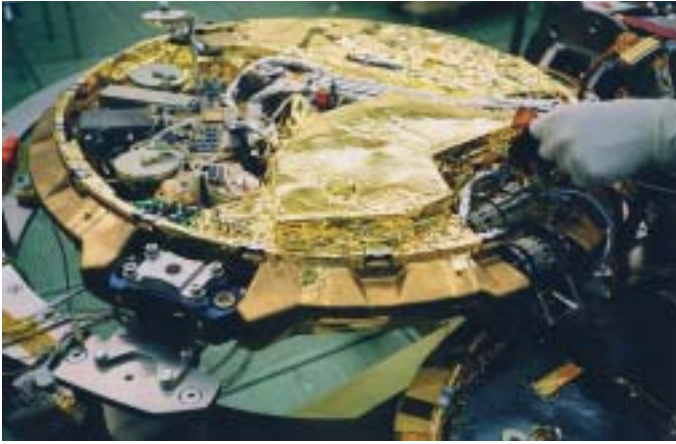


Fig. 19. The Beagle 2 Flight Model during final assembly in the aseptic clean room at the Open University, Milton Keynes, UK. Note that the Wide Angle Mirror on the PAW is held down under spring tension when the lander lid is closed. Above is the the closed lander, ready for integration into the descent capsule. *All Rights Reserved, Beagle 2*



Fig. 20. Below: the fully assembled and encapsulated Beagle 2 probe, ready for delivery. Left: enshrouded in thermal insulation and integrated on Mars Express. *All Rights Reserved, Beagle 2*



- the volume interface model for mechanical integration tests;
- two pyro and frangibolt units (1 FM and 1 EQM).

A number of additional models (aeroshell assembly model, Development Model, SUEM QM #2, common electronics development model) were built for test purposes but not delivered to Mars Express.

The Beagle 2 lander comprises a number of subsystems on the landing module, and some support systems that remain on the Mars Express orbiter. The Beagle 2 system components are described briefly below.

The Entry, Descent and Landing System (EDLS) will decelerate Beagle 2 during atmospheric entry and deliver the lander to the surface of Mars. The entry sequence is controlled by onboard accelerometers and fixed time offsets and delays derived from modelling of the entry phase. The aeroshell, comprising a thermal protection system, an ablative front shield and a back cover, will decelerate the lander and protect it during the initial atmospheric entry. It will reduce the probe's speed from Mach 31.5 to Mach 1.5. Before entering the transonic region, the pilot parachute is deployed. After reaching subsonic speed, pyrotechnic bolts release the back cover and the front shield. The parachute system consists of a pilot 'chute and a main 'chute. The pilot 'chute decelerates the lander to subsonic speed. After the release of the back cover and front shield, the main 'chute is deployed, which is released on impact on the ground. The main parachute's deceleration of the lander also automatically releases the front aeroshell, which is held in place by aerodynamic pressure following release of the bolts. Once the probe is 200 m above the surface, detected by a radar altimeter, the airbag system is activated. It absorbs the remaining speed of $\sim 17 \text{ m s}^{-1}$ in a series of 10-20 bounces. When the probe finally comes to rest, the lacing that holds the airbags together is released, forcing the segments apart via their internal gas pressure and allowing the 33 kg lander to drop to the ground, where it finally deploys itself (Fig. 1).

At the end of the cruise phase, the capsule is released from Mars Express using the spring-powered spin-up and eject mechanism. This provides the probe with the correct axial velocity and spin rate for stability during the coast phase until entry. The capsule aeroshell is made of carbon fibre with a surface layer of powdered cork (Norcoat) tiles impregnated with phenolic resin for thermal protection during entry. The back cover is made of carbon fibre with titanium stringers again covered with Norcoat tiles. These structures act as a bioshield, enveloping and protecting the lander, airbag system and parachute from all the environments the probe encounters en route to Mars and pre-launch following sealing of the probe.

The lander structure consists of an upper (lid) and lower (base) shell, which are held closed by a clamp band until after landing. The shells are made of Kevlar, providing both energy absorption during impact with the ground and thermal protection during surface activities. The inner structure of the lander comprises carbon fibre skins on an aluminium honeycomb core. The lander outer structure contains a crushable honeycomb designed to deform around small rocks while still protecting the integrity of the payload and systems.

A main hinge mechanism allows the shells to open and provides self-righting by shifting the centre of gravity (dominated by the base) if the lander lands the wrong way up. The lander lid houses the solar panels, which are deployed via electrically-powered hinges. The base shell accommodates the robotic arm, which allows the PAW instruments to be deployed.

Beagle 2 is powered via a 42-cell lithium ion battery that is kept warm by the thermal insulation and by heater power during the martian night. When Beagle 2 is deployed on the surface, power to charge the battery and/or supply daytime experiments is provided by four deployable solar panels of total effective area of about 1 m^2 . The panels employ high-performance triple-junction gallium arsenide cells mounted on germanium substrates. The electronics module of the lander provides power distribution, conditioning and management.

The lander common electronics consists of a number of circuit boards, forming the

electronics module (ELM). A local common electronics module (LCE) that supports GAP is accommodated separately. The lander electronics provide the following functions:

- onboard processor (ERC32) and data handling;
- power conditioning, distribution and management;
- interfaces to instruments and equipment.

An interface to the lander electronics is provided via the probe umbilical. The ERC32 processor is controlled by the onboard software, which consists of four basic modules:

- the Bootstrap Loader (BL), which resides in a PROM. It contains the programs run initially after power-on (mission phase detection, execution of application software image);
- the Common Software (CSW), which provides low-level hardware drivers and utilities;
- the Probe Software (PSW), which provides the functionality required for entry, descent and landing, as well as for handover to Lander Software functionality;
- the Lander Software (LSW), which provides the lander subsystem control and instrument and experiment functionality for the surface operations.

The CSW, PSW and LSW are stored in EEPROM and loaded into and executed from RAM memory.

The Beagle 2 communication system provides the means for bi-directional UHF radio communication with the Mars Express orbiter and NASA's Mars Odyssey. It consists of the following:

- transceiver (transponder and interface digital baseband circuits);
- diplexer, power divider and radio-frequency cables;
- receive and transmit antenna integrated into the lander lid structure.

The data rates provided on the forward link (Mars Express to Beagle 2) are 2 kbit s⁻¹ and 8 kbit s⁻¹. The return link data rates are 2-128 kbit s⁻¹.

Under the UN COSPAR regulations for planetary protection, planetary landers carrying life-detection instrumentation (designated as category 4B) are subject to sterilisation procedures, which have a major impact on probe design and assembly, integration and verification. In order to meet these requirements, the Beagle 2 Planetary Protection Plan was implemented, ensuring that both the protection of the martian environment and the life-detection capabilities of Beagle 2 were not compromised. The FM lander/capsule was assembled in an Aseptic Assembly Facility (Fig. 19). All components were sterilised and cleaned before integration. After lander integration was completed, measures were taken to prevent any contamination during tests and on the way to the launch pad.

The Beagle 2 mission can be divided into five phases:

- cruise and coast following deployment from Mars Express;
- descent;
- initial lander operations (status and integrity checkout);
- primary (baseline) mission (landing to +180 sols);
- extended mission, subject to additional funding becoming available (+180 to +669 sols, i.e. martian year).

An operations team with varying levels of involvement will support all phases of

5. Flight Operations

the mission. Most operations will be conducted remotely from the UK via data links, with only a small team at ESOC for critical operations. Data will be released at intervals to the public via project-controlled web sites and the media centre, consistent with the ESA mission publicity and information plan.

Surface operations will be dictated by the ability to communicate with either Mars Express or Mars Odyssey. The telecommunications system is designed to relay at least 10 Mbits per day. Communication sessions are dictated by the landing site, Mars Express orbit, availability of relays via the NASA Mars Odyssey mission, etc.

Beagle 2 remained passive for long periods of the cruise phase. At two intervals during cruise, the probe was checked out and the battery charged. The data and command interface with Mars Express allowed reprogramming of the onboard common electronics in Beagle 2, which will control the descent sequence, had it proved necessary to redefine the landing sequence time delays. Temperature and heater power for the Beagle 2 probe were monitored throughout the cruise phase.

The descent will be fully controlled by the processor within the common electronics. This will be powered up via a hardware timer ~60 min before atmosphere entry in order to avoid depleting the battery. The onboard processor will continue to control Beagle 2 until the first communication session is held via either Mars Express or a relay via Mars Odyssey.

The following operations, which will be initiated following release of the gas-filled landing bags and impact with the surface, will be performed automatically:

- deploy solar panels;
- start battery charging (for the remainder of the day);
- obtain monochromatic image with right-hand stereo camera and WAM. WAM will automatically be positioned in the field of view;
- initiate overnight low-power mode if no contact occurs on sol 1;
- continue low-power mode and daytime battery charging until communication possible.

Following first contact and evaluation of the lander status, including analysis of the first image, the following operations will be commanded:

- deploy the PAW-ARM subsystem to a safe/default configuration;
- begin the initial imaging phase. An early priority is to provide sufficient stereo coverage of the PAW-ARM working zone for DEM construction.

Once the area within reach of the PAW-ARM has been modelled, the following activities dominate the rest of the primary phase of the mission:

- communication sessions;
- accumulation of multispectral images of the landing site and atmosphere;
- PAW-ARM activities, including target assessment, selection, *in situ* analysis, surface preparation and sample acquisition;
- extended sampling activities with the Mole;
- gas analysis of samples acquired by the PAW or directly from the atmosphere;
- battery charging.

To conserve power, ARM positioning and GAP processes will be performed during the day, whereas low-resource activities such as spectrometry and microscopy will be done at night. Obviously there is some logical and/or priority order to some of the activities listed above. Furthermore, much is dependent on what Beagle 2 is presented with at the landing site. It is estimated that an ideal (complete) sampling cycle will take tens of sols. Assuming a baseline of 5-6 samples is available for analysis, the primary mission will last ~80-100 sols plus additional time for early operations. Given these factors, a target primary mission lifetime of up to 180 sols is assumed.

The majority of an extended mission, if funded, will be devoted to atmospheric science because it is expected that available solar power will be reduced by dust settling on the solar panels and hence a low-power mode will be implemented. The following operations are expected during the extended mission:

- communication sessions;
- occasional imaging of the landing site and lander targets to monitor for seasonal and other changes;
- repetition of atmospheric analyses, i.e. daily, seasonal and other changes;
- *in situ* analysis of other rocks and soils;
- additional sample analysis by GAP, if resources permit and ovens are available.

Three locations on Mars had been visited by landers before 2003. The Viking and Pathfinder sites had in common their rock-strewn landscapes; at the Pathfinder site, coverage by fragments of ~3 cm was ~16% (Golombek et al., 1997). Size-frequency data suggest that there should be three specimens larger than 10 cm m⁻² of surface, one of which would be ~20 cm. Boulders like Pathfinder's Yogi (> 1 m) occur at a rate of one per 100 m², so an individual rock of such proportions might be found 5-6 m from Beagle 2 at any landing locality similar to that of Viking or Pathfinder. The soil consistency on Mars is sandy and the presence of rounded pebbles in the Ares Vallis confirmed that water and wind had probably once modified the terrain (Smith et al., 1997). The Pathfinder location was specifically chosen because it was likely to have been a flood region; the success of this prediction means that similar sites can readily be selected for Beagle 2, especially given the availability of Mars Global Surveyor images to guide decisions.

The Beagle 2 team identified a number of sites that were considered to fit the mission objectives and constraints (within ±35° of the martian equator and below the datum). Candidate sites fell into three categories:

- craters in highland terrain with evidence of runoff channels around their margins, e.g. Gusev (15°S, 185°W), Becquerel (22°N, 8°W);
- regions near the highland/lowland boundary, e.g. Elysium basin (0-20°N, 170-210°W) and the margin of Amazonis (4°N, 150-151°W);
- previous landing sites: Viking-1 in Chryse Planitia (22.4°N, 48°W) and Pathfinder in Ares Vallis (19.5°N, 32.8°W).

While all candidate sites, with the possible exception of the Viking-1 site, show evidence of flooding in the past and hence possible sedimentary deposits, the highland region was discounted because of the incompatibility with the expected size of the landing ellipse (~250 x 30-50 km). Further work on site selection followed analysis of data from Mars Global Surveyor, resulting in the identification of three suitable regions: the Maja Vallis channel area in Chryse, Tritonis Lacus on the margin of the Elysium Plains, and Isidis Planitia.

6.1 Isidis Planitia

The landing site for Beagle 2 was eventually chosen as the area around 265.0°W and 11.6°N within Isidis Planitia (Bridges et al., 2002). The site satisfies the safety requirements for landing (average slope of 0.57° and a low elevation, being more than 3.6 km below the martian datum) and provides an environment with good exobiological potential. The rock abundance is estimated at about 2-17% (mean 11%) and, in addition, Isidis shows evidence for the concentration and remobilisation of volatiles.

In a regional sense, the pattern observed in thermal inertia data suggests that sedimentary materials have been added to the landing site area from the Noachian units around the southern half of the basin. At the same time, a variation in the degree

6. Landing Site Selection

to which tuff cones have been eroded suggests that they formed intermittently over a long period of time (within the Amazonian period, and possibly Hesperian as well). The whole area has also been resurfaced in relatively recent times by aeolian deposition and/or erosion, which is highlighted by a deficit in impact craters larger than 120 m diameter.

In conclusion, Isidis Planitia represents an opportunity for sampling a set of martian materials not previously encountered by other missions. These include Noachian rocks from Libya Montes, rocks from below tuff cones (which might show evidence of geological activity involving CO₂-H₂O fluids) and rocks from some of the local impact craters (Bridges et al., 2002).

7. Scientific Analysis

In addition to the instrument experimenters, the Beagle 2 project has set up a group of adjunct scientists under the Chairmanship of the Associate Science Leader, Dr. A. Brack (Centre de Biophysique Moléculaire, Orleans, F). These investigators, who have no hardware role, work in a great variety of disciplines; their theoretical input and background laboratory experience will greatly enhance the interpretation of the returned data and contribute to the overall success of the mission.

References

- Bada, J.L., Glavin, D.P., McDonald, G.D. & Becker, L. (1998). A Search for Endogenous Amino Acids in Martian Meteorite ALH 84001. *Science* **279**, 362-365.
- Baker, L., Franchi, I., Wright, I.P. & Pillinger, C.T. (1998). Oxygen Isotopes in Water from Martian Meteorites. *Meteoritics Planet. Sci.* **33**, A11-A12.
- Becker, R.H. & Pepin, R.O. (1984). The Case for a Martian Origin of the Shergottites: Nitrogen and Noble Gases in EET A79001. *Earth Planet. Sci. Lett.* **69**, 225-242.
- Bogard, D.D. & Johnson, P. (1983). Martian Gases in an Antarctic Meteorite. *Science* **221**, 631-634.
- Bridges, J.C., Seabrook, A.M., Rothery, D.A., Kim, J.-R., Pillinger, C.T., Sims, M.R., Golombek, M.P., Duxbury, T., Head, J.W., Muller, J.-P., Moncrieff, C., Wright, I.P., Mitchell, K.L., Grady, M.M. & Morley, J.G. (2002). Selection of the Landing Site in Isidis planitia of Mars Probe Beagle 2. *J. Geophys. Res.* (in press).
- Bullock, M.A., Stoker, C.R., McKay, C.P. & Zent, A.P. (1994). A Coupled Soil-Atmosphere Model H₂O₂ on Mars. *Icarus* **107**, 142-154.
- Burgess, R., Wright, I.P. & Pillinger, C.T. (1989). Distribution of Sulphides and Oxidised Sulphur Components in SNC Meteorites. *Earth Planet. Sci. Lett.* **93**, 314-320.
- Carr, R.H., Grady, M.M., Wright, I.P. & Pillinger, C.T. (1985). Martian Atmospheric Carbon Dioxide and Weathering Products in SNC Meteorites. *Nature* **314**, 248-250.
- The ESA Exobiology Team (1999). Exobiology in the Solar System and The Search for Life on Mars. (Ed. A. Wilson). ESA SP-1231, ESA Publications Division, Noordwijk, The Netherlands.
- Franchi, I.A., Wright, I.P., Sexton, A.S. & Pillinger, C.T. (1999). The Oxygen-Isotopic Composition of Earth and Mars. *Meteoritics Planet. Sci.* **34**, 657-661.
- Golombek, M.P., Cook, R.A., Economou, T., Folkner, W.M., Haldemann, A.F.C., Kallemeyn, P.H., Knudsen, J.M., Manning, R.M., Moore, H.J., Parker, T.J., Rieder, R., Schofield, J.T., Smith, P.H. & Vaughan, R.M. (1997). Overview of the Mars Pathfinder Mission and Assessment of Landing Site Predictions. *Science* **278**, 1734-1748.
- Gooding, J.L., Wentworth, S.J. & Zolensky, M.E. (1988). Calcium Carbonate and Sulphate of Possible Extraterrestrial Origin in the EET A79001 Meteorite. *Geochim. Cosmochim. Acta* **52**, 909-915.
- Gooding, J.L., Wentworth, S.J. & Zolensky, M.E. (1991). Aqueous Alteration of the Nakhla Meteorite. *Meteoritics* **26**, 135-143.

- Grady, M.M., Wright, I.P. & Pillinger, C.T. (1995). A Search for Nitrates in Martian Meteorites. *J. Geophys. Res.* **100**, 5449-5455.
- Harri, A.-M., Linkin, V., Pollko, J., Marov, M., Pommereau, J-P., Lipatov, A., Siili, T., Manuilov, K., Lebedev, V., Lehto, A., Pellinen, R., Pirjola, R., Carpentier, T., Malique, C., Makarov, V., Khloustova, L., Esposito, L., Maki, J., Lawrence, G. & Lystev, V. (1998). Meteorological Observations on Martian Surface: Met-Packages of Mars-96 Small Stations and Penetrators. *Planet. Space Sci.* **46**, 6/7, 779-793.
- Harvey, R.P. & McSween, H.Y. (1996). A Possible High-Temperature Origin for the Carbonates in Martian Meteorite ALH 84001. *Nature* **382**, 49-51.
- Jull, A.J.T., Donahue, D.J., Swindle, T.D., Burkland, M.K., Herzog, G.F., Albrecht, A., Klein, J. & Middleton, R. (1992). Isotopic Studies Relevant to the Origin of the 'White Druse' Carbonates on EET A79001. *Lunar Planet. Sci.* **XXIII**, 641-642.
- Karlsson, H.R., Clayton, R.N., Gibson, E.K. & Mayeda, T.K. (1992). Water in SNC Meteorites: Evidence for a Martian Hydrosphere. *Science* **255**, 1409-1411.
- Klingelhöfer, G. (1998). In-situ Analysis of Planetary Surfaces by Mossbauer Spectroscopy. *Hyperfine Interact.* **113**, 369-374.
- Klingelhöfer, G., Fegley, B., Morris, R.V., Kankeleit, E., Held, P., Evlanov, E. & Priloutskii, O. (1996). Mineralogical Analysis of Martian Soil and Rock by a Miniaturized Backscattering Mossbauer Spectrometer. *Planet. Space Sci.* **44**, 1277-1288.
- Leshin, L.A., McKeegan, K.S., Carpenter, P.K. & Harvey, R.P. (1998). Oxygen Isotopic Constraints on the Genesis of Carbonates from Martian Meteorite ALH 84001. *Geochim. Cosmochim. Acta* **62**, 3-13.
- McDonald, G.D. & Bada, J.L. (1995). A Search for Endogenous Amino Acids in the Martian Meteorite EET A79001. *Geochim. Cosmochim. Acta* **59**, 1179-1184.
- McKay, D.S., Gibson, E.K., Thomas-Keprta, K.L., Vali, H., Romanek, C.S., Clemett, S.J., Chillier, X.D.F., Maechling, C.R. & Zare, R.N. (1996). Search for Life on Mars: Possible Relic Biogenic Activity in Martian Meteorite ALH 84001. *Science* **273**, 924-930.
- McSween, H.Y. (1985). SNC Meteorites: Clues to Martian Petrologic Evolution? *Rev. Geophysics* **23**, 391-416.
- McSween, H.Y. (1994). What We Have Learned about Mars from SNC Meteorites. *Meteoritics* **29**, 757-779.
- Mittlefehldt, D.W. (1994). ALH 84001, a Cumulate Orthopyroxinite Member of the Martian Meteorite Clan. *Meteoritics* **29**, 214-221.
- Owen, T. (1992). The Composition and Early History for the Atmosphere of Mars. In *Mars* (Eds. H.H. Kieffer, B.M. Jakosky, C.W. Snyder & M.S. Mathews), University of Arizona Press, Tuscon, 818-834.
- Owen, T., Biemann, K., Rushneck, D.R., Buller, J.E., Howarth, D.W. & LaFleur, A.L. (1997). The Composition of the Atmosphere at the Surface of Mars. *J. Geophys. Res.* **82**, 4635-4639.
- Pepin, R.O. (1985). Evidence of Martian Origins. *Nature* **317**, 473-475.
- Re, E., Kochan, H., Magnani, P.G. & Ylikorpi, T. (1997). Small Sample Acquisition/Distribution Tool (SSA/DT). Final Report ESTEC Co. No. 11485/95 NL PP(SC), Milano.
- Rieder, R., Economou, T., Wänke, H., Turkevich, A., Crisp, J., Brückner, J., Dreibus, G. & McSween, H.Y. (1997). The Chemical Composition of Martian Soil and Rocks Returned by the Mobile Alpha Proton X-ray Spectrometer: Preliminary Results from the X-ray Mode. *Science* **278**, 1771-1774.
- Romanek, C.S., Grady, M.M., Wright, I.P., Mittlefehldt, D.W., Socki, R.A., Pillinger, C.T. & Gibson, E.K. (1994). Record of Fluid-Rock Interactions on Mars from the Meteorite ALH 84001. *Nature* **372**, 655-657.
- Ryan, J. A. & Lucich, R. D. (1983). Possible Dust Devil Vortices on Mars. *J. Geophys. Res.* **88**, 11005-11011.
- Saxton, J.M., Lyon, I.C. & Turner, E. (1998). Correlated Chemical and Isotopic Zoning in Carbonates in the Martian Meteorite ALH84001. *Earth Planet. Sci. Lett.* **160**, 811-822.

- Schidlowski, M. (1997). Application of Stable Carbon Isotopes to Early Biochemical Evolution on Earth. *Ann. Rev. Earth and Planet. Sci.* **15**, 47-72.
- Smith, P.H., Bell, J.F., Bridges, N.T., Britt, D.T., Gaddis, L., Greeley, R., Keller, H.U., Herkenhoff, K.E., Jaumann, R., Johnson, J.R., Kirk, R.L., Lemmon, M., Maki, J.N., Malin, M.C., Murchie, S.L., Oberst, J., Parker, T.J., Reid, R.J., Sablotny, R., Soderblom, L.A., Stoker, C., Sullivan, R., Thomas, N., Tomasko, M.G., Ward, W. & Wegrzyn, E. (1997). Results from the Mars Pathfinder Camera. *Science* **278**, 1758-1765.
- Stoker, C.R. & Bullock, M.A. (1997). Organic Degradation under Simulated Martian Conditions. *J. Geophysical Res.* **102**, 10881-10888.
- Tuzzolino, A.J. (1995). Applications of PVDF Dust Sensor Systems in Space in-situ Impact Detection Techniques, Interplanetary Dust, and Future Mars Exploration. *Adv. Space Res.* **17** (12): 123-132.
- Valley, J., Eiler, J.M., Graham, C.M., Gibson, E.K., Romanek, C.S. & Stolper, E.M. (1997). Low-Temperature Carbonate Concentrations in the Martian Meteorite ALH 84001: Evidence from Stable Isotopes and Mineralogy. *Science* **275**, 1633-1638.
- Wiens, R.C., Becker, R.H. & Pepin, R.O. (1986). The Case for a Martian Origin of the Shergottites. II Trapped and Indigenous Gas Components in EET A79001 Glass. *Earth Planet. Sci. Lett.* **77**, 149-158.
- Wood, C.A. & Ashwal, C.D. (1981). SNC Meteorites: Igneous Rocks from Mars? In *Proc. Lunar Planet. Sci. Conf.*, 12th, 1359-1375.
- Wright, I.P., Grady, M.M. & Pillinger, C.T. (1988). Carbon, Oxygen and Nitrogen Isotopic Compositions of Possible Martian Weathering Products in EET A79001. *Geochim. Cosmochim. Acta* **52**, 917-924.
- Wright, I.P., Grady, M.M. & Pillinger, C.T. (1989). Organic Materials in a Martian Meteorite. *Nature* **340**, 220-222.
- Wright, I.P., Grady, M.M. & Pillinger, C.T. (1992). Chassigny and the Nakhilites: Carbon-bearing Components and their Relationship to Martian Environmental Conditions. *Geochim. Cosmochim. Acta* **56**, 817-826.
- Wright, I.P., Grady, M.M. & Pillinger, C.T. (1997a). Evidence Relevant to the Life on Mars Debate. (1) ^{14}C Results. *Lunar Planet. Sci.* **XXVIII**, 1585-1586.
- Wright, I.P., Grady, M.M. & Pillinger, C.T. (1997b). Evidence Relevant to the Life on Mars Debate (2) Amino Acid Results. *Lunar Planet. Sci.* **XXVII**, 1587-1588.
- Wright, I.P. & Pillinger, C.T. (1998a). Modulus – An Experiment to Measure Precise Stable Isotope Ratios on Cometary Materials. *Adv. Space Res.* **21**, 1537-1545.
- Wright, I.P. & Pillinger, C.T. (1998b). Mars, Modulus and MAGIC. The Measurement of Stable Isotopic Compositions at a Planetary Surface. *Planet. Space Sci.* **46**, 813-823.
- Zent, A.P. & McKay, C.P. (1994). The Chemical Reactivity of the Martian Soil and Implications for Future Missions. *Icarus* **108**, 146-157.

Acknowledgements

The Beagle 2 consortium has a large industrial component concerned with the engineering aspects of the programme; we gratefully acknowledge the involvement of everyone in the team. In addition, the authors would like to express their gratitude to the European Space Agency (ESA), the UK Particle Physics and Astronomy Research Council (PPARC), EADS Astrium, the Wellcome Trust and the British National Space Centre (BNSC).

US PARTICIPATION

US Participation in Mars Express

A.D. Morrison¹, T.W. Thompson¹, R.L. Horttor¹, C.H. Acton¹, Jr., S. Butman¹, J.K. Campbell¹, P.L. Jepsen¹, W.T.K. Johnson¹, J.D. Winningham², J.J. Plaut¹ & A. Vaisnys¹

¹*Jet Propulsion Laboratory, California Institute of Technology, 4800 Oak Grove, Pasadena, CA 91109, USA*
Email: Andrew.D.Morrison@jpl.nasa.gov

²*Southwest Research Institute, 6220 Culebra Road, San Antonio, TX 78228, USA*

This paper describes US participation in the Mars Express mission, in which NASA is a supporting partner.

In December 1997, ESA issued an Announcement of Opportunity for experiments to be included in the Mars Express mission. Mars Express is flying refurbished European instruments developed for the Russian-led Mars-96 mission, plus an advanced radar sounder capable of characterising the martian subsurface to a depth of several kilometres. US scientists who had been appointed Mars-96 Participating Scientists by NASA were invited to propose as instrument Co-Investigators (Co-Is). NASA and the Italian Space Agency (ASI) submitted a joint experiment proposal for the subsurface sounder: the Mars Advanced Radar for Subsurface and Ionosphere Sounding (MARSIS).

NASA Headquarters was represented in the ESA selection process. Eleven US proposers were selected by ESA as instrument Co-Is. The selected investigators subsequently submitted proposals and proposed budgets to NASA and were appointed by NASA. The NASA/ASI MARSIS sounder was selected over a competing proposal prepared by a German-led consortium. J. Plaut, of the Jet Propulsion Laboratory (JPL), is the MARSIS Co-Principal Investigator (Co-PI) and W.T.K. Johnson was named as Instrument Manager. NASA is also funding hardware development, data reduction and archiving tasks for the Analyser of Space Plasma and Energetic Atoms (ASPERA-3) instrument via the agency's Discovery Mission of Opportunity. Two of ASPERA-3's four data-gathering sensors, the Electron Spectrometer and the Ion Mass Analyser, were built by the Southwest Research Institute (SwRI).

Table 1 lists the Mars Express experiments and their US Investigators. Table 2 lists the key US personnel.

US participation primarily consists of the Mars Express/NASA Project, managed by JPL. The contribution to ASPERA-3 is supported by the Discovery Program, managed by the NASA Management Office, also located in Pasadena.

2.1 Mars Express/NASA Project

The structure of the Mars Express/NASA Project is shown in Fig. 1. It includes the US role in MARSIS, support for the US investigators and a Telecommunications and Interoperability Task to study communications between elements of Mars Express and US assets at Mars. In addition, the Deep Space Network (DSN) will provide tracking support.

1. Introduction

2. US Participation

Country	Instrument	PI	US Hardware	US Co-Is
I/US	MARSIS	G. Picardi, Univ. of Rome Co-PI, J.J. Plaut	W.T.K. Johnson, JPL/ D. Gurnett, Univ. of Iowa RF subsystems and Sounder antenna	J. Plaut, JPL D. Gurnett, Univ. of Iowa E. Stofan, Proxemy Research Inc
I	PFS	V. Formisano, Instituto Fisica Spazio Interplanetario		S. Atreya, Univ of Michigan
D	HRSC	C.G. Neukum, DLR Institut für Planetenerkundung		M. Carr, USGS R. Kirk, US Geological Survey T. Duxbury, JPL R. Greeley, Univ. of Arizona J. Head, Brown Univ. T. McCord, Univ. of Hawaii S. Squyres, Cornell Univ. L. Tyler, Stanford Univ.
D	MaRS	M. Paetzold, Univ. of Cologne		W. Sandel, Univ. of Arizona A. Stern, SwRI
F	SPICAM	J.L. Bertaux, Service d'Aéronomie, Verrières-le-Buisson		
F	OMEGA	J.P. Bibring, Institut d'Astrophysique Spatiale		
S	ASPERA-3	R. Lundin, Swedish Institute of Space Physics	D. Winningham, SwRI Electron Spectrometer and portions of the Ion Mass Analyser	C. Curtis, Univ. of Arizona K.C. Hsieh, Univ. of Arizona J. Kozyra, Univ. of Michigan J. Luhmann, Univ. of California E. Roelof, Johns Hopkins Univ. B. Sandel, Univ. of Arizona J. Sharber, SwRI R. Frahm, SwRI D. Williams, Johns Hopkins Univ.
UK	Beagle 2	C. Pillinger, Open Univ.		M. Sinha, JPL

<i>Mars Express/NASA Project Manager:</i> Richard L. Horttor (richard.l.horttor@jpl.nasa.gov)
<i>Mars Express/NASA Project Science Manager:</i> Thomas W. Thompson (thomas.thompson@jpl.nasa.gov)
<i>MARSIS Instrument Manager:</i> William T.K. Johnson (wtk.johnson@jpl.nasa.gov)
<i>Mars Express/NASA Project Telecommunications and Interoperability Task Manager:</i> Stanley A. Butman (stanley.butman@jpl.nasa.gov)
<i>MARSIS Co-PI:</i> Jeffrey J. Plaut (plaut@jpl.nasa.gov)
<i>ASPERA-3 ELS PI:</i> J. David Winningham (david@cluster.space.swri.edu)
<i>Discovery Program Manager:</i> John B. McNamee (john.b.mcnamee@jpl.nasa.gov)
<i>NASA Headquarters Program Executive:</i> David Lavery (dave.lavery@hq.nasa.gov)
<i>NASA Headquarters Program Scientist:</i> Catherine Weitz (cweitz@hq.nasa.gov)

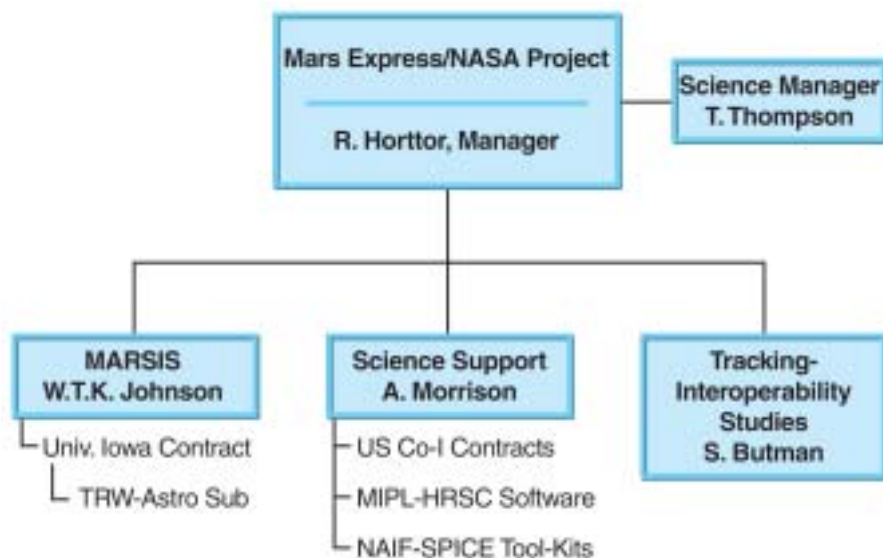


Fig. 1. The structure of the Mars Express/NASA Project.

Specific goals of the Mars Express/NASA Project are:

- to support the science objectives of HRSC (High Resolution Stereo Camera), OMEGA (IR mapping spectrometer), MaRS (Mars Radio Science), PFS (Planetary Fourier Spectrometer), SPICAM (UV atmospheric spectrometer), ASPERA-3 and MARSIS instruments by providing US Co-I support;
- to provide information and advice on navigation and mission operations that could be used by Mars Express;
- to provide the Radio Frequency (RF) subsystem for MARSIS, including the integrated transmitter, antenna and receiver;
- to plan for relaying communications to and from Beagle-2 and any potential European 2005 landers using NASA and ESA orbital assets;
- to coordinate US planning inputs to Mars Express orbiter observations and secure support from JPL's Telecommunications and Mission Operations Directorate for tracking and navigation support for Mars orbit insertion;
- to archive a copy of the science investigation data in a Planetary Data System (PDS)-compatible format, as specified in the international agreements;
- to support the HRSC investigation with adaptation of NASA/JPL image processing software;
- to deploy the Spacecraft, Planet, Instrument, C-matrix, Events (SPICE) ancillary information system.

The Mars Express/NASA Project completed the transition from Phase-B (Planning) into Phase-C/D (Implementation) in September 2000. Launch initiated mission operations.

2.2 MARSIS

The MARSIS Program is funded by both NASA and ASI. ASI maintains the science leadership through the Principal Investigator (PI), Giovanni Picardi of the INFOCOM Department of the University of Rome, while NASA maintains the instrument leadership through JPL. The US MARSIS Team provided the antennas and the receiver and transmitter subsystems; Alenia Spazio, Rome had responsibility for the digital subsystem and instrument integration and test, under direction of the JPL Instrument Manager. The Co-PI serves as the lead scientist for the NASA side of the joint experiment.

The University of Iowa, under contract to JPL, constructed the antenna subsystem,

working with their subcontractor, TRW-Astro, Inc., of Carpinteria, CA. The University of Iowa, under contract to JPL, built the transmitter subsystem; JPL built the receiver subsystem. JPL integrated the antenna, transmitter and receiver subsystems into a single RF subsystem that was delivered to Alenia Spazio, who integrated it with their digital electronic system and delivered an integrated MARSIS instrument to ESA (Astrium) for mating to the spacecraft.

2.3 Science Support Task

The Science Support Task (SST) comprises three Sub-Tasks: the Co-I Sub-Task, the HRSC-Multimission Image Processing Laboratory (MIPL) Sub-Task, the Navigation and Ancillary Information Facility (NAIF)-SPICE Sub-Task and several ancillary activities, including possible US navigation contributions to the mission.

The Co-I support activity funds and manages the Co-PI and Co-Is. With the exception of OMEGA, all Orbiter instruments have one or more US Co-Is. The SST will support OMEGA Co-Is, once selected. The MARSIS Co-PI is also supported by the SST.

US Co-Investigators will provide instrument calibration, data validation and data archiving support to their respective Instrument PIs and Teams to help ensure that the data products meet the objectives of the mission. Co-Investigators are expected to publish the results of their scientific analysis and provide their data products to the PDS. Interdisciplinary and Participating Scientists, when selected, will also be supported by the Co-I support activity.

The Co-I activity also supports obtaining DSN tracking and data communication through Mars Express Project Service Level Agreements (PSLAs), approved Letters of Agreement (LOAs) and Memoranda of Understanding (MOUs), allowing technical exchange between the US Co-Is and their European colleagues and JPL navigation support to the mission.

The HRSC/MIPL telemetry software development activity is similar to that for Mars-96. The basic HRSC instrument is the same except that the wide-angle camera was deleted and a Super-Resolution Channel (SRC) added. With those exceptions, the instrument formats are the same, including the data compression. The spacecraft is completely different, as are the telemetry systems.

MIPL developed the HRSC telemetry processing software. This will convert the HRSC data as they are received in Berlin (D) from ESA into a format compatible with existing image processing software for further processing. The telemetry processing includes a telemetry processor and data-merge and decompression programs.

After using the telemetry processor on its data, DLR will distribute this processed imagery daily to its Co-Is, so that the US HRSC Co-Is can support Mars Express mission operations, as well as meet their individual commitments as described in their proposals. As part of this distribution activity, MIPL will receive these processed data electronically on behalf of the HRSC Co-Is and then distribute them directly to the US Co-Is.

MIPL will maintain approximately 60 days of the most current HRSC Mars Express data online, with the remainder held in an offline store. The data will be provided to the US HRSC Co-Is automatically through a subscription service or on a request basis. They will have access to the data in level 1 or 2 format, such as the decompressed version of the level 0 image product, or the radiometrically corrected version of level 1. The radiometric correction software and calibration files will be provided to MIPL by DLR.

MIPL will also develop PDS generation and validation software to convert the HRSC processed imagery into a PDS-compatible format. DLR will then use this software to place its HRSC data on archive volumes for delivery to the PDS imaging node at JPL. There will also be sustaining support for the JPL-developed software for the first 6 months after orbital insertion.

NASA's SPICE system was conceived to provide planetary scientists with a standard, flexible and proven method of obtaining and properly using the suite of

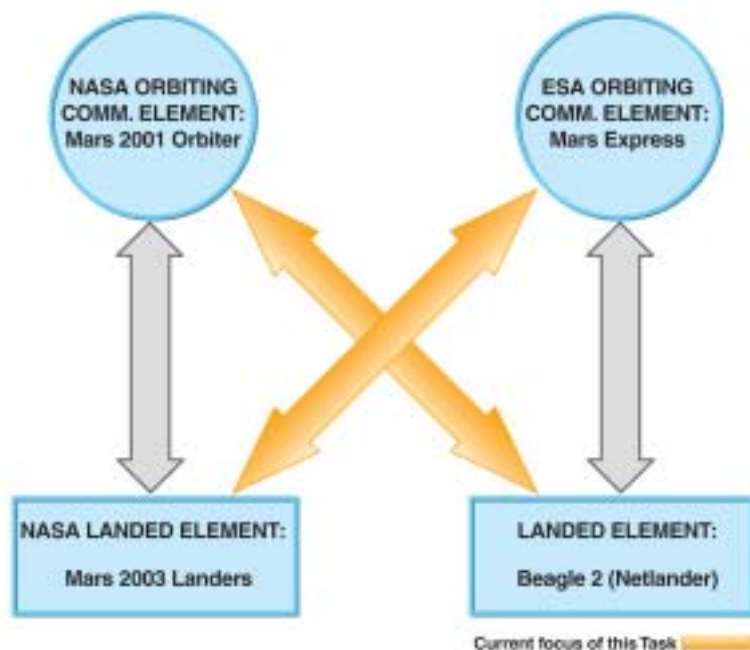


Fig. 2. Mars telecommunications interoperability.

ancillary and engineering data needed for conceptualising and evaluating mission designs, planning scientific observations, analysing scientific data and comparing results obtained from multiple instruments and multiple spacecraft. To this end, SPICE is used – or being adapted for use – on all NASA planetary missions, including the full suite of JPL's Mars Exploration Program missions. NASA's SPICE system will be deployed to support the US Co-Is, the HRSC team operations, and the other instrument teams as interested. SPICE was developed and is maintained by JPL's NAIF.

In particular, JPL provided the SPICE Tool Kit software and documentation to ESTEC and Mars Express PI and Co-I teams and team members who will be involved in producing and using SPICE data components. The latest versions were delivered in November 2000, June 2001 and June 2002. In conducting its work, the SPICE Sub-Task is striving to achieve as much commonality as possible with the use of SPICE by NASA Mars missions.

2.4 Relay communications and tracking interoperability

Another ESA-NASA area of cooperation involves tracking and telecommunication interoperability. NASA is supporting efforts to establish and demonstrate communications and tracking interoperability between the various orbiting and landing elements of NASA and ESA. Starting with the Mars 2001 Orbiter and the 2003 Landers, NASA plans to launch a series of orbiting and landing/roving elements, with the eventual goal of returning rock and soil samples to Earth. With all these assets, including Mars Express, in Mars orbit and on the surface, it is desirable to provide communication and navigation cross-support between the NASA and ESA elements. This support may be highly desirable during certain critical mission events such as orbit insertion or landing. Fig. 2 shows the potential combinations of cross-support at Mars for Mars Express and other elements in the 2001-2005 time frame.

Achieving interoperability requires several steps:

- determine the interface characteristics of each pair of elements;
- if compatible, proceed to write the Interface Control Documents (ICDs);
- if not compatible, propose design changes to one or both elements;
- write ICD to define interface to be tested;

- write test plan and schedule test;
- perform interface test and document results.

2.5 Navigation and orbit insertion

When the Mars Express spacecraft arrives at Mars, it will deliver the Beagle-2 lander and brake into an elliptical orbit about the planet. Achieving the operational orbit might involve aerobraking. Coordination between the ESA/ESOC Flight Dynamics Division and the NASA/JPL Navigation Section will improve understanding of the mission constraints and risks. This follows the path pioneered by previous joint ESA-NASA missions such as Giotto, Ulysses and Mars Pathfinder. Comparison of navigation results from techniques and procedures developed by each agency is the primary objective of a series of workshops starting in September 2000 on navigation collaboration for Mars Express.

2.6 The Discovery Program and ASPERA-3

NASA's Discovery Program is supporting ASPERA-3 as a Discovery Mission of Opportunity, which is not a complete Discovery Mission but rather a portion of a larger mission. In this case, it gives the US scientific community the chance to participate in a mission of a non-US government agency. For ASPERA-3, the Discovery Program is funding both hardware development and data reduction, and the PDS archiving tasks being performed by the SwRI.

The Swedish Institute of Space Physics headed the development of ASPERA-3. The instrument has four sensors, along with the data processing unit and the scanning platform. Two of the sensors, the Electron Spectrometer (ELS) and the Ion Mass Analyser (IMA), are funded by NASA as a Discovery Mission of Opportunity. ELS and IMA were built by SwRI, led by D. Winningham as PI and J. Scherrer as Project Manager. The instrument was built by an international team of 15 groups from 10 countries.

ASPERA-3's scientific objectives are to study the interaction between the solar wind and the atmosphere of Mars and to characterise the plasma and neutral gas environment in near-Mars space. It uses Energetic Neutral Atom (ENA) imaging to visualise the charged and neutral gas environments around Mars. ASPERA-3 will make the first ever ENA measurements at another planet. These studies will address the fundamental question of how strongly interplanetary plasma and electromagnetic fields affect the martian atmosphere, which is directly related to the many questions about water on Mars.

Acknowledgement

The work described in this paper was performed at the Jet Propulsion Laboratory, California Institute of Technology, under a contract with the National Aeronautics and Space Administration.

ACRONYMS & ABBREVIATIONS

AAF	Aseptic Assembly Facility (Beagle 2)	EQM	Electrical Qualification Model
ADU	analogue to digital conversion unit	ESA	European Space Agency; electrostatic analyser
AIV	assembly, integration and verification	ESAC	European Space Astronomy Centre, Villafranca (Spain)
AO	Announcement of Opportunity		
AOTF	acousto-optical tunable filter	ESOC	European Space Operations Centre, Darmstadt (Germany)
APS	Auxiliary Power Supply		
APXS	Alpha Proton X-ray Spectrometer (NASA Mars Pathfinder)	ESS	Environmental Sensor Suite
		ESTEC	European Space Research and Technology Centre, Noordwijk (The Netherlands)
ARM	Anthropomorphic Robot Manipulator (Beagle 2)		
ASI	Italian space agency	ETM	Electrical Test Model
ASIC	Application Specific Integrated Circuit	EUV	extreme ultraviolet
ASPERA	Analyser of Space Plasma and Energetic Atoms (Mars Express)	EW	equivalent width
AU	Astronomical Unit		
		FFT	Fast Fourier Transform
		FIR	far-infrared
BEE	Back End Electronics	FM	flight model
BEEST	Back End Electronics Stack (Beagle 2)	FOV	field of view
BL	bootstrap loader	FPGA	field programmable gate array
		FUV	far-ultraviolet
		FW(A)	filter wheel (assembly)
		FWHM	full width at half maximum
CCD	Charge Coupled Device		
CCH	Common Camera Head		
CDPU	Command & Data Processing Unit		
CNES	Centre National d'Etudes Spatiales	GaAs	gallium arsenide
CNR	Consiglio Nazionale della Ricerca (Italy)	GAP	Gas Analysis Package (Beagle 2)
CNRS	Centre National de la Recherche Scientifique (France)	GCM	general circulation model
		GC-MS	gas chromatograph-mass spectrometer
CMOS	Complementary Metal Oxide Semiconductor	GDS	global dust storm
Co-I	Co-Investigator	GTM	Ground Test Model
COSPAR	UN Committee on Space Research		
CSW	common software		
CT	Calibration Target (the Damien Hirst 'spot' painting on Beagle 2)	HK	housekeeping
		HRSC	High Resolution Stereo Camera (Mars Express)
CUL	close-up lens		
		IAS	Institut d'Astrophysique Spatiale, Orsay (France)
DCT	Discrete Cosine Transform	ICA	Ion Composition Analyser (Rosetta)
DEM	Digital Elevation Model	ICD	Interface Control Document
DES	Digital Electronic Subsystem	IDS	Interdisciplinary Scientist
DESPA	Observatoire de Paris, Département de Recherches Spatiales (France)	IF	Improvement Factor
		IFMS	Intermediate Frequency and Modem System
DHA	Detector Head Assembly	IFSI	Istituto di Fisica dello Spazio Interplanetario (Italy)
DLR	Deutsches Zentrum für Luft- und Raumfahrt	IKI	Institute for Space Research (Russia)
DM	Development Model	IFOV	instantaneous field of view
DN	Data Number (pixel intensity on scale of 0-255)	IMA	Ion Mass Analyser (ASPERA)
DSN	Deep Space Network (DSN)	IMEWG	International Mars Exploration Working Group
DTM	Digital Terrain Model; data-transmission mode	IMI	Ion Mass Imager (Nozomi)
DVD	digital versatile disk	IMIS	Ion-Mass Imaging Spectrometer (Mars-96)
		IMP	Imager for Pathfinder
		IR	infrared
EDLS	Entry, Descent and Landing System	ISM	imaging spectrometer (Phobos mission)
EEPROM	electrically erasable programmable read-only memory	ISO	Infrared Space Observatory (ESA)
EGSE	electrical ground support equipment		
ELS	Electron Spectrometer (ASPERA)	JPL	Jet Propulsion Laboratory (NASA)
ELM	Electronics Module		
ENA	Energetic Neutral Atom (ASPERA)		
EPROM	erasable programmable read-only memory	LEC	local common electronics

LCP	left-hand circular polarisation	PSA	Planetary Science Data Archive
LOA	Letter of Agreement	PSLA	Project Service Level Agreements
LOC	Lander Operations Centre	PSSL	Planetary Science Sample Library
LOS	line of sight	PST	Project Scientist Team
LSW	Lander Software (Beagle 2)	PSW	Probe Software (Beagle 2)
LTE	local thermodynamic equilibrium	px	pixel
LUT	look-up table		
LW	long wavelength		
		QM	Qualification Model
MaRS	Mars Radio Science (Mars Express)		
MARSIS	Mars Advanced Radar for Subsurface and Ionosphere Sounding (Mars Express)	RCL	Recognised Cooperating Laboratory
		RCG	Rock Corer Grinder (Beagle 2)
MBS	Mössbauer Spectrometer (Beagle 2)	RCP	right-hand circular polarisation
MCA	Multi-Channel Analyser (Beagle 2)	RFS	Radio Frequency Subsystem
MCO	Mars Climate Orbiter (NASA)	rms	root mean square
MCP	micro-channel plate		
MEDUSA	Miniaturized Electrostatic DUal-top-hat Spherical Analyzer	SCS	Stereo Camera System (Beagle 2)
MEE	Micro-End Effector (Beagle 2)	SHADS	Sample Handling and Distribution System (Beagle 2)
MELACOM	Mars Express Lander Communications subsystems		
MEP	Mars Exploration Program (NASA)	S/N	signal-to-noise ratio
MGS	Mars Global Surveyor (NASA)	SNC	Shergottite-Nakhilite-Chassignite meteorite
MGSE	mechanical ground support equipment	SOWG	Science Operations Working Group
MIC	microscope	SPICAM	Spectroscopy for the Investigation of the Characteristics of the Atmosphere of Mars (Mars Express)
MIPL	Multimission Image Processing Laboratory (JPL)		
MLI	multi-layer insulation		
MOC	Mission Operations Centre; Mars Observer Camera	SPICE	Spacecraft, Planet, Instrument, C-matrix, Events system
MOCAD	Monolithic Octal Charge Amplifier/Pulse Discriminator		
		SRC	Super-Resolution Channel (HRSC)
MOLA	Mars Orbiter Laser Altimeter (MGS)	SST	Science Support Task
MOU	Memorandum of Understanding	SUEM	Spin-Up and Eject Mechanism (Beagle 2)
MPF	Mars Pathfinder (NASA)	SW	short wavelength
MSM	Mass Stiffness Model	SWIR	short wavelength infrared
MSP	Master Science Plan	SWS	Short Wavelength Spectrometer (ISO)
Msps	Megasamples per second		
		TCS	Thermal Control System
NAIF	Navigation and Ancillary Information Facility (JPL)	TES	Thermal Emission Spectrometer (Mars Global Surveyor)
NEB	noise equivalent brightness		
NPD	Neutral Particle Detector (ASPERA)	TGCM	thermospheric general circulation model
NPI	Neutral Particle Imager (ASPERA)	TICS	Three-dimensional Ion Composition Spectrometer (Freja)
		TMOD	Telecommunications and Mission Operations Directorate (JPL)
OBDM	onboard data management		
OMEGA	Observatoire pour la Minéralogie, l'Eau, les Glaces et l'Activité (Mars Express)	TOF	time-of-flight
		TT	Translation Table (Beagle 2)
		TTL	transistor-transistor logic
		TWTA	travelling wave tube amplifier
PAW	Position Adjustable Workbench (Beagle 2)		
PDS	Planetary Data System		
PFM	Proto Flight Model	VMC	Visual Monitoring Camera
PFS	Planetary Fourier Spectrometer (Mars Express)	VNIR	visible & near-infrared
PG	Pattern Generator		
PLUTO	Planetary Underground Tool (Beagle 2)		
POS	Payload Operations Service	WAM	Wide Angle Mirror (Beagle 2)
PPS	Payload Power Supply (Beagle 2)		
PRF	Pulse Repetition Frequency		
PROM	programmable read-only memory	XRS	X-Ray Spectrometer (Beagle 2)